

STUDY OF ARGON FROM UNDERGROUND  
SOURCES FOR DIRECT DARK MATTER  
DETECTION

JINGKE XU

A DISSERTATION  
PRESENTED TO THE FACULTY  
OF PRINCETON UNIVERSITY  
IN CANDIDACY FOR THE DEGREE  
OF DOCTOR OF PHILOSOPHY

RECOMMENDED FOR ACCEPTANCE  
BY THE DEPARTMENT OF  
PHYSICS

ADVISOR: FRANK P. CALAPRICE

SEPTEMBER 2013

© Copyright by Jingke Xu, 2013.

All Rights Reserved

# Abstract

There has been accumulating evidence for the existence of dark matter in the universe, but its nature remains a deep mystery. Weakly Interacting Massive Particles (WIMPs) are likely dark matter candidates, which may scatter with nuclei and get detected. Several experiments have been launched in attempts to detect WIMP-induced nuclear recoils, but no conclusive detection has been confirmed. Now it is generally believed that ton-scale detectors are required for sensitive WIMP detection, and this may go beyond the reach of traditional low background technologies. Detectors using noble liquids such as argon offer this desired scalability, and argon has also been shown to have excellent background rejection power from scintillation pulse shape analysis. The problem with argon, however, lies in the cosmogenic  $^{39}\text{Ar}$  isotope in atmospheric argon; it restricts the ultimate size of argon Time Projection Chambers (TPCs) and also reduces the detectors' WIMP sensitivity.

The DarkSide collaboration has successfully located underground sources of argon with extremely low  $^{39}\text{Ar}$  levels that are below the sensitivity of all known measurement techniques. Therefore, we developed a low background liquid argon detector to measure the  $^{39}\text{Ar}$  concentration in this underground argon. The detector was constructed with radio-clean materials and was carefully shielded from backgrounds. Using the data acquired in an underground laboratory ( $\sim 1450$  m.w.e.) combined with Monte Carlo techniques, we obtained an  $^{39}\text{Ar}$  limit in samples of underground argon at  $\sim 0.65\%$  of the concentration in atmospheric argon,  $\sim 10$  times better than the previously best result. This measurement demonstrates the possibility of achieving ultra-low background levels in argon-based detectors, and may extend the mass limit of argon TPCs by  $\sim 45$  times. Multi-ton detectors using underground argon are expected to cover a large fraction of the WIMP parameter space predicted by popular WIMP theories. I also discuss the possible application of the underground argon in the detection of low mass WIMP interactions and coherent neutrino scattering.

# Acknowledgements

First I am extremely grateful to my adviser Prof. Frank Calaprice for offering me the excellent opportunity to work on the low level  $^{39}\text{Ar}$  measurement project. It is an integrated project that involves detector designing, hardware construction, system operation, data acquisition, data analysis and Monte Carlo simulation. Such a joined training experience is not always available in contemporary particle physics experiments, and is very precious for a young researcher. Frank is knowledgeable, patient, and encouraging. He always encourages students to carry out independent researches and to think about the big picture; at the same time, he provides insightful directions and suggestions to his students. I learned not only scientific knowledges from him, but also valuable advices in future career development.

Next I want to acknowledge Dr. Alexander Wright for his generous help on every aspect of this project during the last a few years. He comes up with a lot of great ideas on how to operate and improve the detector; he has also been actively involved in the specific tasks of the experiment, for example, commissioning and operating the detector underground. I would like to thank Prof. Cristiano Galbiati and Prof. Peter Meyers for their continuous support to this project and the insightful discussions I had with them. I acknowledge Engineer David Montanari and Dr. Henning Back for their efforts on extracting argon from underground gas wells and making the underground argon gas available for this measurement.

For the final low background  $^{39}\text{Ar}$  measurement to take place at the Kimballton Underground Research Facility (KURF), Prof. R. Bruce Vogelaar and Dr. S. Derek Rountree from the Virginia Polytechnic Institute and State University played a critical role in initializing and maintaining the KURF laboratory, and in offering lab space to this project. They also helped us coordinate with the Kimballton Mine administrative to solve problems that the experiment ran into due to the special underground environment. I am indebted to our technical specialist Allan Nelson for



designing and machining the detector parts flawlessly, and for his critical help on operating the detector in both surface and underground campaigns. I thank Dave Holtz and Geoffrey Lou Guray for their important contributions in building and running this experiment, and thank Mark Luxbacher, Chris Campbell, Wesley Johnson, Drew Taylor, Stephanie O’Neil, Colletta Mabry and other Lhoist Kimballton mine staff for their hospitality and support to the experiment at the Kimballton mine.

I would also like to acknowledge Dr. Stephen Pordes from Fermilab and Prof. C. Jeff Martoff from Temple University for generously loaning the scintillator veto chamber and associating electronics to this experiment. I thank Dr. Ben Loer for his continuous support on the data acquisition system in both hardware and software issues, and thank Pablo J. Mosterio and Dave Holtz for their help on building and maintaining the detector monitor system. I appreciate the helpful discussion that I had with Dr. Richard Saldahna and Dr. Alvaro Chavarria on physics topic and beyond in the past years. And it has been a very pleasant experience to work with Jason Brodsky, Charles Huajie Cao, Emily Shields, Shawn Westerdale, Guangyong Koh, and Hao Qian in the Princeton nuclear astro-particle physics group. I want to give my special thanks to our group assistant Helen Ju for her patient help on our purchases, trips, and celebrations; chaos would definitely result without her.

Last, but certainly not least, I would like to thank my parents for their unconditional love and constant support during all my education experiences. This thesis would definitely not have been possible without their support. I am grateful to my wonderful fiancée, Dan Xie, for her company and encouragement while I work on this thesis. I thank all my friends in Princeton and outside Princeton who have helped make my life in graduate school less dreary and more enjoyable.

# Contents

Abstract . . . . .	iii
Acknowledgements . . . . .	iv
<b>1 Introduction to Dark Matter</b>	<b>1</b>
1.1 Evidence for Dark Matter . . . . .	1
1.1.1 Galaxy Rotation Curves . . . . .	1
1.1.2 Gravitational Lensing Measurements . . . . .	3
1.1.3 Cosmic Microwave Background Radiation . . . . .	5
1.2 Candidates of Dark Matter . . . . .	9
1.2.1 MOND and MACHOs . . . . .	9
1.2.2 Standard Model Neutrinos . . . . .	10
1.2.3 Weakly Interacting Massive Particles . . . . .	12
1.2.4 The Axion . . . . .	15
1.3 WIMP Dark Matter Detection . . . . .	16
1.3.1 Basic Theories in Direct WIMP Search . . . . .	17
1.3.2 General Discussions on Direct WIMP Searches . . . . .	24
1.3.3 Direct WIMP Search Experiments and Results . . . . .	27
1.3.4 Indirect Search and Accelerator Search of WIMPs . . . . .	34
<b>2 Underground Argon for Direct Dark Matter Search</b>	<b>37</b>
2.1 Characteristics of Argon as a Scintillator . . . . .	38

2.1.1	The Scintillation Mechanism . . . . .	39
2.1.2	The Scintillation Quenching Effects . . . . .	42
2.2	Argon-Based Dark Matter Detectors . . . . .	48
2.3	Discovery of Underground Argon . . . . .	51
2.3.1	The $^{39}\text{Ar}$ Problem . . . . .	51
2.3.2	Search for low- $^{39}\text{Ar}$ Argon underground . . . . .	55
2.3.3	Argon Collection from Underground Sources . . . . .	59
2.3.4	Early $^{39}\text{Ar}$ Activity Measurements . . . . .	62
2.4	The DarkSide Program . . . . .	65
2.4.1	The Two-Phase Argon TPC . . . . .	65
2.4.2	The Active Neutron Veto Detector . . . . .	68
<b>3</b>	<b>The Low Background Liquid Argon Detector</b>	<b>72</b>
3.1	Inner Detector Components . . . . .	74
3.1.1	Wavelength Shifter and Reflector . . . . .	74
3.1.2	PhotoMultiplier Tube . . . . .	80
3.1.3	High Voltage and Signal Readout System . . . . .	84
3.2	Shielding from Backgrounds . . . . .	91
3.2.1	Gamma Ray Shielding . . . . .	91
3.2.2	Muon Veto . . . . .	93
3.2.3	KURF Laboratory . . . . .	96
3.3	Preparation of Argon for Measurements . . . . .	99
3.3.1	Purification of Underground Argon . . . . .	99
3.3.2	The Detector Gas Handling System . . . . .	101
3.4	Data Acquisition System . . . . .	105
<b>4</b>	<b>Measurements and Results</b>	<b>109</b>
4.1	Preliminary Studies . . . . .	110

4.1.1	Background Study with Pseudocumene . . . . .	111
4.1.2	First Direct Evidence of $^{39}\text{Ar}$ Depletion . . . . .	113
4.2	Detector Upgrading . . . . .	118
4.2.1	Upgrade to Cryogenic PMTs . . . . .	118
4.2.2	Light Collection Study . . . . .	119
4.2.3	Investigation of Neutron Backgrounds . . . . .	122
4.3	Data Analysis in the Main Measurements . . . . .	124
4.3.1	Energy Calibration and Light Yield . . . . .	124
4.3.2	Study of Slow Argon Scintillation . . . . .	131
4.3.3	Data Quality and Cuts . . . . .	138
4.3.4	Monte Carlo Simulation . . . . .	143
4.4	The Main Measurement Campaign . . . . .	145
4.4.1	The Measurement at Surface . . . . .	146
4.4.2	Measurement at KURF - 2011 . . . . .	154
4.4.3	Measurement at KURF - 2012 . . . . .	162
4.5	$^{39}\text{Ar}$ Analysis . . . . .	166
4.5.1	External Background Study . . . . .	167
4.5.2	Radioactivity in the Argon Sample . . . . .	172
4.5.3	$^{39}\text{Ar}$ Limits with Background Subtracted . . . . .	175
<b>5</b>	<b>Discussion on the low-<math>^{39}\text{Ar}</math> Argon</b>	<b>177</b>
5.1	Implication for Dark Matter Experiments . . . . .	177
5.1.1	Pulse Shape Discrimination in Argon . . . . .	178
5.1.2	Event pile-up in Two Phase Argon TPCs . . . . .	183
5.1.3	Improved WIMP sensitivity in Argon Detectors . . . . .	186
5.1.4	Argon in Light WIMP Detections . . . . .	189
5.2	Potential Application in CNS Detection . . . . .	191
5.3	Discussion on Argon Isotopes . . . . .	195

<b>Appendices</b>	<b>199</b>
<b>A Surface Background Study</b>	<b>200</b>
A.1 Surface Alpha Decay Backgrounds . . . . .	200
A.2 WLS Scintillation . . . . .	202
A.2.1 Room Temperature Measurements . . . . .	203
A.2.2 Cryogenic Measurements . . . . .	206
A.3 Surface Background Measurements . . . . .	208
A.3.1 Radon Collection . . . . .	209
A.3.2 Bi-Po Coincidence Measurements . . . . .	211
A.3.3 Summary . . . . .	214
<b>B Evaporation Procedures</b>	<b>216</b>
<b>C Useful Online Resources</b>	<b>220</b>

# Chapter 1

## Introduction to Dark Matter

Since the beginning of twentieth century, there has been accumulating evidence for the existence of non-luminous matter, or dark matter, in the universe. Recent cosmic microwave background observation has confirmed that such dark matter outweighs luminous matter that largely makes up our known universe by a factor of  $\sim 5$ . Though immune to electromagnetic interactions, dark matter played an important role in the formation and evolution of the “luminous world”. Various candidates for dark matter have been proposed by physicists, and the search for dark matter via non-gravitational approaches has become a flourishing field with rich physics.

### 1.1 Evidence for Dark Matter

#### 1.1.1 Galaxy Rotation Curves

In the year of 1933, when Swiss astronomer Fritz Zwicky was examining the Coma galaxy cluster, he found that the galaxies’ mass implied by luminosity didn’t match the mass predicted by the virial theorem. He concluded that some non-luminous matter must exist in the cluster of galaxies and account for the majority of the mass distribution [1]. These non-luminous matter was named “dunkle Materie”, or dark

matter, by Zwicky.

It was not the first time unobserved mass was predicted in the history of astronomy. In 1846, French mathematician Urbain Le Verrier proved that the hypothetical existence of a new celestial object could explain the deviation of the Uranus orbit from that predicted by the gravitational laws. Following Verrier's instructions, Johann Gottfried Galle, director of the Berlin Observatory, discovered the planet Neptune in the predicted region of the sky [2].

Zwicky's estimate of dark matter density was later found to be inaccurate, but the existence of mass other than luminous matter in the universe was confirmed by many following observations. An important example is the discovery by Babcock. In 1939 Babcock observed that stars in M31 galaxy were exhibiting an unexpectedly high rotation velocity around the galaxy center, which could allow the stars to escape the gravitational pull if only luminous matter existed [1].

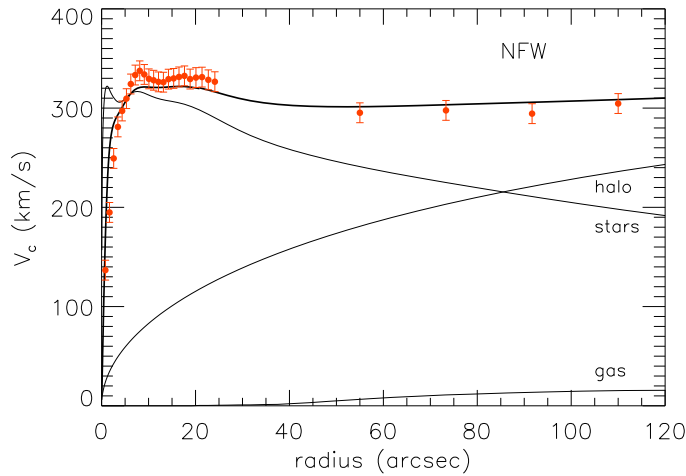


Figure 1.1: The rotation curve of NGC 2974 (120 arcsec  $\sim$  12 kpc) [3].

Rotation curves of spiral galaxies have been extensively studied. For the majority of the observed spiral galaxies, the velocity of stars remains approximately constant even outside the optical disk where few stars exist. This observation holds true at a radius as large as 12 kpc (1 kpc  $\approx$  3.26 light-years) in some galaxies. Fig. 1.1 shows

the measured rotation curve in the elliptical galaxy NGC 2974 compared with that calculated based on the luminous mass distributions [3]. The gravitational force due to stars and gases does not suffice to keep the galaxy bound, while the addition of non-luminous matter could effectively compensate the difference. According to Newtonian physics, the rotation velocity of celestial objects would drop as  $1/\sqrt{R}$  outside the matter distribution, so the observed rotation curve indicates that more mass exist beyond the optical disk. The estimated mass density needs to vary as  $1/R^2$  at large radii<sup>1</sup> to produce a flat rotation curve.

### 1.1.2 Gravitational Lensing Measurements

The general theory of relativity states that the presence of matter warps the local space-time structure, so the path of light can be significantly deflected in strong gravitational fields. This effect is called gravitational lensing and can be used to map out the mass distribution of celestial objects. Techniques such as strong lensing, statistical weak lensing and time-dependent micro-lensing have been developed and are widely used in astronomy. For example, Abell 1689 is one of the most massive objects in the universe, and its mass distribution has been derived from the gravitational lensing effects measured using light from distant stars [4]. The enormous gravity produces curved and/or multiple images of background objects, which could not be explained by the observed galaxies and other visible matter. This discrepancy suggests that non-luminous matter may exist in this galaxy cluster.

Another famous evidence for dark matter provided by gravitational lensing measurements comes from the galaxy cluster 1E 0657-56 [5], which is better known as the Bullet cluster because of the shape of its X-ray image. The Bullet cluster consists of two colliding sub-clusters, and the different matter components exhibit strikingly different spatial distributions in the collision, as illustrated in Fig. 1.2. The stars

---

<sup>1</sup>In this case the mass of a galaxy (halo) within a certain radius is proportional to the radius.



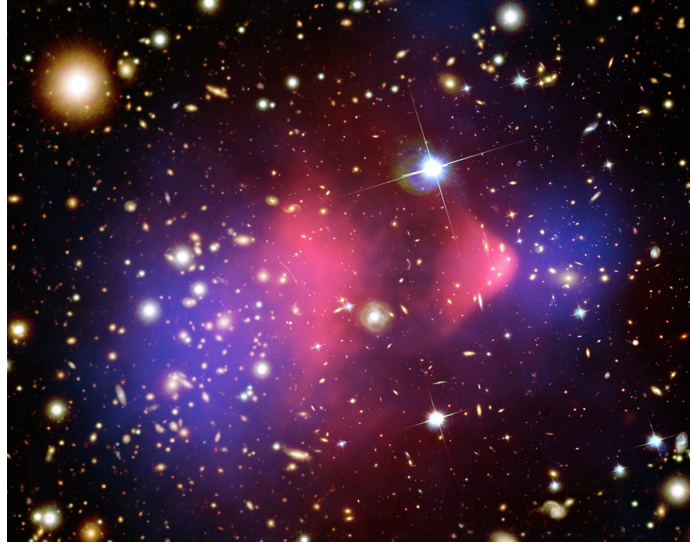


Figure 1.2: The mass distribution of the Bullet Cluster; this plot includes optical image of the galaxies, X-ray telescope data for the hot gas clouds (red) and gravitational lensing results for total mass (blue).

of the galaxies, seen in optical image data, mostly pass through the collision site without being significantly affected because of the gigantic intergalactic space; the hot ionized gas clouds (shown in red), on the contrary, are seriously deterred due to electromagnetic interaction in the collision, according to X-ray telescope images [6]. Gravitational lensing measurements, however, indicate that the center of the total mass (shown in blue) approximately coincide with the galaxies, instead of with the more massive intergalactic gases. In addition, the total mass around the galaxies out-weights the mass of galaxies by orders of magnitude, and this matter content doesn't seem to be seriously slowed down by the collision.

The Bullet cluster is a very convincing piece of direct evidence for the existence of dark matter. It shows that the dominant mass of some galaxy clusters couldn't be directly detected by optical techniques or X-ray telescopes, and it is free of collision with luminous matter or with its own specie. This heavy and non-interactive matter, again, matches the expected properties of dark matter. Although dark matter appears to be isolated from the luminous world, it manifests itself by the enormous

gravitational attraction that holds together the galaxies clusters.

### 1.1.3 Cosmic Microwave Background Radiation

In 1964, when Bell Lab scientists Arno Penzias and Robert Wilson studied the noise in a radio-wave antenna receiver, they found a mysterious microwave background [7]. This background persisted day and night, and was isotropic in the sky. It couldn't be explained by human activities as radio broadcasting or radar, and didn't seem to come from the Earth, the Sun, or the Milky Way. This background was later attributed to the thermal relics of the big bang, usually referred to as the Cosmic Microwave Background (CMB) radiation. The accidental detection of CMB radiation made one of the greatest scientific discoveries in the twentieth century.

The big bang theory, which is the standard framework for modern cosmology, states that our universe started from a singularity. All the fundamental particles were contained in an extremely small region in a hot and dense state. As this high energy density drove the universe to expand, the temperature dropped and the energies of particles decreased. When the temperature of the universe came down to the level of 1-10 eV, protons started to combine with electrons and form neutral hydrogen atoms because photons at this time did not have enough energy to re-ionize them. As the recombination process completed, the universe became transparent to light, and the relic photons have been freely propagating ever since<sup>2</sup>. The photons got fainter and fainter due to expansion, and form the  $\sim 2.7$  K background radiation in the microwave region that we observe today.

Because the CMB photons have been traveling nearly free after decoupling, the current CMB image provides a snapshot of the early universe, and information of the decoupling era can be retrieved. For example, the CMB energy distribution is found to agree excellently with the black body radiation, which suggests, along with other

---

<sup>2</sup>CMB photons are only approximately free of collisions, because they can also scatter off free electrons during and after the re-ionization epoch.

facts, that radiation photons were once in thermal equilibrium with matter. Another important characteristic of the CMB radiation is that the radiation is isotropic up to the level of one part in 10,000 after the Doppler shift from the Earth's motion is corrected, which provides a direct validation of the homogeneous universe hypothesis (the cosmological principle).

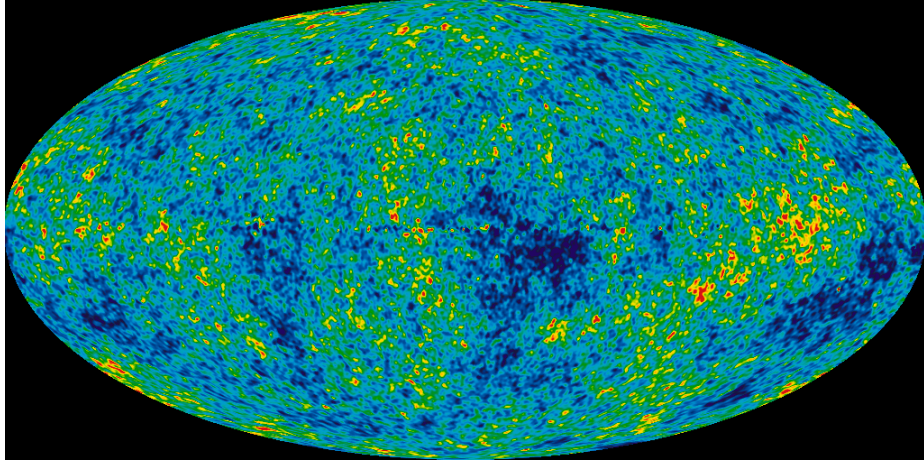


Figure 1.3: The fluctuation in the observed CMB temperature; the homogeneous background and the Doppler effects from the Earth's motion have been subtracted [8].

The anisotropy of the CMB, as graphically illustrated in Fig. 1.3, however, yields more important information about the universe's evolution. Shortly after the big bang, the universe was considered perfectly homogeneous and every part of it was in causal contact. But during the inflation epoch, the dramatic inflation caused the loss of causal connection and amplified the minute quantum fluctuations of the universe into slight over-densities and under-densities. An over-dense region can grow by attracting more mass, but the increased radiation pressure from photons tends to resist the infall; as a result, an acoustic baryonic oscillation could form in regions where causal contact was regained [9, 10]. This oscillation continued and increased in size until the photons decoupled and the photon pressure vanished. During this period, regions could have undergone different numbers of compression and rarefaction cycles, and have different oscillating amplitudes, for varying sizes of over-densities and

under-densities. Many cosmological parameters, including the universe expansion rate and the matter/dark matter density played a role in this process.

The anisotropy of the CMB radiation provides a way to investigate the acoustic oscillation states right before decoupling, and to restrict the values of some cosmological parameters. The temperature variation shown in Fig. 1.3 can be represented by its decomposition into the spheric harmonics series [9, 10].

$$\Theta_{lm} = \int Y_{lm}^*(\hat{n}) \frac{T(\hat{n}) - \langle T \rangle}{\langle T \rangle} d\Omega \quad (1.1)$$

For a temperature field arising from Gaussian fluctuations, all the field information is contained in the angular power spectrum, or equivalently in the two-point temperature correlation function,  $C_l$ , defined as

$$\langle \Theta_{l'm'}^* \Theta_{lm} \rangle = \delta_{l'l} \delta_{m'm} C_l \quad (1.2)$$

This angular power spectrum tells how much the CMB temperature varies from point to point in the sky, and the value of  $C_l$  quantitatively describes the strength of a fluctuation mode that appears  $l$  cycles across the whole sky. The degree  $l$  represents a characteristic angular size of  $\sim 180^\circ/l$  for a fluctuation mode; the order parameter  $m$  describes the angular orientation, which is irrelevant here since there is no preferred direction in our universe. The recent result of the CMB power spectrum measured by the WMAP team [11] is shown in Fig. 1.4.

Since many cosmological parameters functioned in the formation of the CMB anisotropy, their values can be estimated from the CMB power spectrum. Some of the fit values in the  $\Lambda$ CDM cosmological model by the WMAP experiments [11] are listed in Tab. 1.1. Baryonic matter, including galaxies and intergalactic gases, is estimated to account for only 4.6% of the total mass-energy of the universe, while cold dark matter outweighs baryonic matter by a factor of  $\sim 5$ . The rest of the universe is

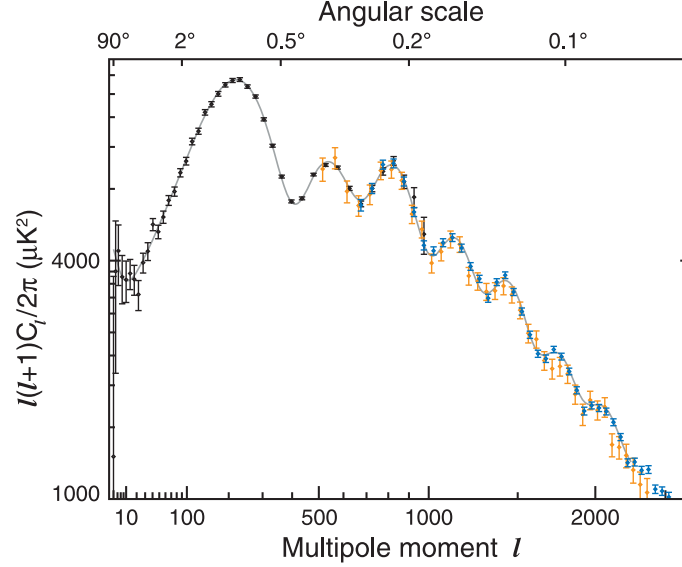


Figure 1.4: The angular power spectrum of CMB measured by WMAP (9 years' data).

dominated by dark energy that is little understood today.

Parameter	Symbol	Value	Unit
baryon density	$\Omega_b$	0.046	$\Omega_0$ , the critical density <sup>3</sup>
cold dark matter density	$\Omega_c$	0.24	$\Omega_0$
dark energy density	$\Omega_\Lambda$	0.71	$\Omega_0$
Hubble constant	$H_0$	69.3	km/s/Mpc
age of the universe	$t_0$	13.8	Gyr

Table 1.1: A selection of the cosmological parameters by fitting the WMAP CMB power spectrum to the cold dark matter cosmology model with a cosmological constant [11].

The Planck experiment revealed their CMB analysis based on 15.5 months measurements in March 2013 and provided the most up-to-date CMB power spectrum [12]. Although there is some tension between the Planck measurement and the WMAP results, they agree in general. These CMB observations provide some of the strongest evidence for the existence of dark matter in the universe, and also yields the best estimate of its average density.

<sup>3</sup>The critical density,  $\Omega_0 = 3H_0^2/8\pi G$ , is the average density at which the universe geometry is flat.

## 1.2 Candidates of Dark Matter

It has been indicated that a variety of cosmological observations can not be explained by known luminous matter in the Newtonian physics framework, while invoking non-luminous dark matter has successfully reconciled the discrepancies. The nature of dark matter, however, remains a deep mystery. Various models have been brought up to explain the origin of dark matter, but none have been confirmed.

### 1.2.1 MOND and MACHOs

Although dark matter is the focus of this thesis, it is worth noting that alternative possibilities exist. Since the discrepancies rise in the Newtonian framework, it might be possible to modify the physics to reconcile with the observations. A somewhat successful example is Modified Newtonian Dynamics (MOND) [13]. MOND requires the gravitational acceleration  $g$  to asymptotically approach  $\sqrt{g_n a_0}$  in the low acceleration limit, where  $g_n$  is the Newtonian acceleration and  $a_0 \approx cH_0/6$  is a new cosmological parameter with units of acceleration. In high acceleration regimes  $g_n \gg a_0$ , MOND returns to Newtonian dynamics  $g \approx g_n$ . With this empirical modification, the rotation curve of all galaxies become flat at sufficiently large radii ( $g = \sqrt{GMa_0}/r = v^2/r$ ), which also agrees with the galaxy luminosity observations  $M \propto v^4$ . Despite its successes, MOND remains as an empirical modification and lacks physical basis in a theoretical framework. In addition, MOND may have difficulties explaining phenomena such as the bullet cluster collision<sup>4</sup> and the structure formation of the universe. So more work has to be done to make MOND competitive to the dark matter hypothesis as an explanation of the observed discrepancies.

If dark matter does exist, it is natural to ask the question whether it can be non-luminous baryonic matter. Massive Astrophysical Compact Halo Objects (MACHOs),

---

<sup>4</sup>Some authors argue that MOND is not ruled out by the offset between the total mass distribution and the luminous mass distribution in the bullet cluster because the lensing analysis doesn't include MOND modification, which has not been developed.

or celestial objects that are difficult to detect, are such a possibility. They include black holes that are too dense for any light to escape, neutron stars and white dwarfs that glow only faintly, and brown dwarfs and gas giants that are not massive enough to start hydrogen fusion. If MACHOs are present in large quantities in the universe, they may account for some of the missing matter. However, the overall baryonic matter content in the universe is restricted by the big-bang nucleosynthesis analysis that is restricted by the observed deuterium abundance relative to hydrogen, as well as by the CMB observations [11,12]. Baryonic matters are also expected to participate in the gravitational infall during structure formation, and thus are unlikely to remain in the extended dark halo of galaxies. In addition, MACHO objects can be detected by gravitational lensing effects, but not enough of them have been observed [14]. As a result, MACHOs may not be a valid dark matter candidate.

Generally speaking, competitive dark matter candidates are assumed to be fundamental particles that are only subject to gravitational interaction and weak (scale) interactions. They are expected to be produced in the early universe and remain at high density in the universe today. We will review a few of these particle candidates in the following sections.

### 1.2.2 Standard Model Neutrinos

If the dark matter content of the universe is made of non-baryonic, weakly interacting, stable fundamental particles, the only candidate offered by the standard model of particle physics is the neutrino [15]. Neutrinos don't carry any electric charge so they don't emit or absorb light, and thus are dark; they only interact with matter weakly so they can easily escape detection; they are predicted to be massless by the standard model, but there has been strong evidence that neutrinos have a finite mass. So Neutrinos appear to be a plausible candidate for dark matter.

As in the case of CMB photons, neutrinos were also created in the early universe.

Electrons and positrons collided and annihilated into neutrino and antineutrino pairs; neutrinos and antineutrinos similarly annihilated into electron-positron pairs; a thermal equilibrium state may be maintained when the universe was hot. But as the universe cooled down to the level of a few MeV, the annihilation processes ceased to happen because of the low particle density, low collision energy and low interaction cross section. As a result, neutrinos decoupled from the rest of the universe and evolved independently after this point. Using a similar argument to that of CMB photons, the remaining neutrino density in the present universe is estimated to be  $\sim 100/\text{cm}^3$ , which is a few times lower than that of CMB photons ( $\sim 400/\text{cm}^3$ ) [16]. We comment that when neutrinos were in thermal equilibrium with electrons in the early universe, the neutrino densities were estimated to be comparable to that of photons; but as the temperature of the universe dropped below  $\sim 1$  MeV, the neutrino number had been frozen while the photon content got boosted by the annihilation of residual electrons and positrons.

At this number density, the total mass of all light neutrino species has to be at the order of tens of electron-volts to account for the estimated dark matter density. However, various neutrino mass measurements have suggested much smaller values for neutrino mass; this rules out light neutrinos as major constituents of cosmic dark matter. Moreover, when neutrinos decoupled from the universe ( $T \sim \text{MeV}$ ), they were still relativistic and would stream freely; they could iron out the primordial density fluctuations of the universe and made structure formation difficult. It has been estimated that if the dark matter particles were mainly relativistic at decoupling, the primordial density fluctuations of the universe would have to be a few orders of magnitudes higher than what is indicated by the CMB observations ( $\delta T/T \sim 10^{-5}$ ). Therefore, it is unlikely for relativistic particles to account for a large fraction of dark matter, and the majority of it has to be non-relativistic, or cold at decoupling.

Hypothetical heavy neutrinos with conventional weak interactions could decouple



from the universe at non-relativistic velocities. However, neutrino masses of  $\gtrsim \text{MeV}$ - $\text{GeV}$  would result in unpractically high relic neutrino density in the current universe and thus are not possible [16]. The well-measured Z boson decay processes by LEP has also excluded the existence of any non-standard model neutrinos with masses below half of that of Z boson ( $\sim 45 \text{ GeV}$ ). Heavier Dirac neutrinos ( $< 1.4 \text{ TeV}$ ) are expected to have a relatively strong coupling to nucleus and have been ruled out by early direct detection experiments [17, 18].

### 1.2.3 Weakly Interacting Massive Particles

Probably the most plausible particle candidate for dark matter is Weakly Interacting Massive Particles (WIMPs). WIMPs are expected to interact with matter weakly and gravitationally, and have masses at the level of  $\text{GeV}$  to  $\text{TeV}$ . Besides the motivation from dark matter, WIMP-like particles are also naturally predicted by many theoretical extensions to the standard model, such as supersymmetric particle physics<sup>5</sup> [17].

Supersymmetry, or fermion-boson symmetry, was brought up as a solution to the fine-tuning problem of the standard model. In a perturbative theory, the calculation of the self energy of a scalar particle like Higgs boson usually leads to divergent results if radiative loop corrections are included, and the coupling constant has to be fine-tuned to avoid this difficulty. However, if all the particles appear in supersymmetric multiplets, i.e. every fermion has a boson partner and vice versa, the radiative corrections of supersymmetric partners would (mostly) cancel<sup>6</sup> and the divergence can be softened or removed. Supersymmetric partners of standard model particles have not been observed in any experiments, so they are usually believed to be very massive or immune to electromagnetic and strong interactions. In addition, heavy supersymmetric particles are expected to decay to light ones, while the lightest is required to

---

<sup>5</sup>We comment that WIMPs also exist in other theories than supersymmetry, like the Kaluza-Klein(K-K) resonance particles in the Universal Extra Dimension theory [19], and brane fluctuations (branons) in some brane-world theories [20].

<sup>6</sup>In perturbative theories, a fermion loop carries a factor of -1 compared to boson loops.

be stable by conservation laws. As a result, if supersymmetry exists, the universe would be highly populated with a stable, massive particle that rarely interacts with matter; this makes a well motivated dark matter candidate.

If such WIMP particles exist, they can be produced in the big bang along with baryonic particles. When the universe was hot (the temperature  $T$  was greater than the WIMP mass  $m_\chi$ ), WIMPs were expected to be continuously created and annihilated during collisions, and they may reach a thermal equilibrium with the rest of the universe. But as the universe expanded and cooled down, heavy WIMPs were no longer being produced, and at a certain time the WIMP density became so low that they also stopped annihilating. As a result the total number of WIMPs in the universe would freeze out and the rest may remain in the universe today. At a certain time the WIMP number density  $n$  is determined by the WIMP creation rate, annihilation rate, and the expansion rate of the universe.

$$\frac{dn}{dt} + 3Hn = \frac{d(na^3)}{a^3 dt} = \langle\sigma v\rangle(n_{eq}^2 - n^2) \quad (1.3)$$

where  $a$  is the scale factor of the universe,  $H = (da/dt)/a$  is the Hubble constant denoting the expansion rate of the universe,  $\langle\sigma v\rangle$  is the thermally averaged WIMP annihilation cross section<sup>7</sup>, and  $n_{eq}$  is the equilibrium WIMP number density in case of strong couplings (at high temperatures) [21].  $n_{eq}^2\langle\sigma v\rangle$  determines the production rate of WIMPs at a certain temperature;  $n_{eq} \propto T^3$  for relativistic WIMPs at high temperature ( $T \gtrsim m_\chi$ ) and  $n_{eq} \propto (m_\chi T)^{3/2} e^{-m_\chi/T}$  for non-relativistic WIMPs ( $T \lesssim m_\chi$ ) in the late universe.

Eq. 1.3 can be approximately solved on the assumption of entropy conservation throughout the evolution of the universe [22]. The result shows that the WIMP density  $n$  closely follows the equilibrium density  $n_{eq}$  until the temperature of the universe dropped below  $\sim 1/10$  of the WIMP mass. After this point the WIMP

---

<sup>7</sup>This quantity is usually believed to be largely independent of WIMP energy.

number was frozen out, and the WIMP density was exclusively determined by the expansion of the universe. As illustrated in Fig. 1.5, the relic density of the WIMP particles strongly depends on the annihilation cross section  $\langle\sigma v\rangle$ . For a certain WIMP mass, a larger cross section (stronger coupling) indicates that the WIMP density would follow the equilibrium density  $n_{eq}$  for a longer period, which decays exponential with time, and thus the value gets highly suppressed.

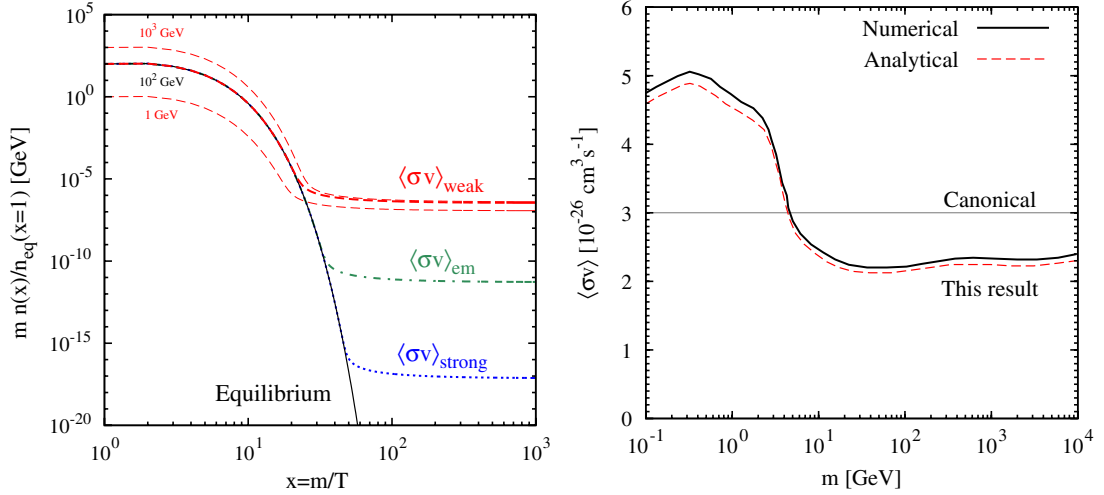


Figure 1.5: Left: an illustration of the WIMP decoupling from the rest of the Universe assuming different masses and different interaction cross sections; Right: the required WIMP annihilation cross section to account for the estimated dark matter density today [22].

The annihilation cross section  $\langle\sigma v\rangle$  required to produce the current dark matter density is estimated to be  $2.2 \times 10^{-26} \text{ cm}^3/\text{s}$  for WIMP mass from 10 GeV up to 10 TeV, and the value is approximately  $5 \times 10^{-26} \text{ cm}^3/\text{s}$  for WIMP masses below 1 GeV, as shown in Fig. 1.5. The drop between 1 GeV and 10 GeV WIMP mass is a result of the QCD transition in the universe when the temperature was at the QCD scale (0.1-1 GeV). The WIMP creation and annihilation rate is expected to scale with the degree of freedoms of the relativistic particles (the equilibrium part of the universe); as the QCD transition took place a lot of degrees of freedom (quarks) were eliminated and the WIMP decoupling around this time was strongly affected. The appearance of the WIMP annihilation cross section at the weak scale is sometimes called the WIMP

Miracle; just starting from the basic requirements that dark matter particles should be massive and weakly interacting (hopefully, otherwise they can not be detected), the remaining WIMP density from the big bang amazingly matches the expected dark matter density today.

We comment that the lightest supersymmetric particle is sometimes assumed to be a linear combination of the super-partners of photons, Higgs and Z bosons. The mass is estimated to be associated to the weak scale, while the annihilation cross section can be affected by many free parameters in supersymmetry theories. As a result, much flexibility remains for the supersymmetric WIMP particles to make up an important fraction of the dark matter content in the current universe.

### 1.2.4 The Axion

Another feasible dark matter candidate is the axion, which, unlike WIMPs, is a very light particle but qualifies for cold dark matter [23]. The axion was invented to solve the strong CP problem, or why strong interactions conserve CP symmetry while the CP violation can be arbitrarily large<sup>8</sup>. Peccei and Quinn proposed a P-Q symmetry that is spontaneously broken and leads to CP conservation; the axion is the psuedo-Goldstone boson associated with this symmetry [24]. The mass of the axion, as well as its coupling strength to quarks, electrons and photons, is predicted to depend on a single parameter  $f$  [15].

$$m_a \sim \frac{10^6 GeV}{f} eV, \quad g \propto \frac{1}{f} \quad (1.4)$$

The value of  $f$ , and thus the mass of the axion, is mainly constrained by cosmological considerations [25]. Heavy axions can be produced at relatively high rate in the cores of stars, but their coupling to matter is not strong enough to be contained in the

---

<sup>8</sup>For example, the neutron electric dipole moment is measured to be several orders of magnitude smaller than the predicted value in the absence of CP conservation.

stars. This heat loss from stellar cores would shorten stellar lifetimes and result in fewer stars. Cosmological observations have put an upper limit of  $\sim 10^{-2}$  eV on the estimated axion mass [26].

Though they have a tiny mass, the axions may have decoupled non-relativistically from the early universe and fall into the category of cold dark matter. The axions are expected to be produced when the temperature of the universe approached the QCD scale  $T \sim 0.1\text{--}1$  GeV. At this temperature the phase  $\theta$  in the P-Q order parameter  $\langle\phi\rangle = fe^{i\theta}$  prefers the  $\theta=0$  CP-invariant value, while it takes random values at higher temperatures. In this way the P-Q symmetry is broken and the axions are produced non-thermally; they receive a small mass by mixing with other neutral pseudo-scalar mesons [24]. Due to the weak coupling, the axion condensate is expected to decouple from the universe before it could reach a thermal equilibrium. Therefore, the axions may have remained non-relativistic during the structure formation of the universe. The residual axion content in the current universe is estimated to be  $\Omega_a \sim f/10^{12}$  GeV, which puts a lower limit of  $10^{-5}$  eV on the axion mass in a flat universe  $\Omega_a < \Omega \approx 1$  [15].

To sum up, the axion mass needs to fall in a region of  $10^{-5}$  eV– $10^{-3}$  eV to be a valid dark matter candidate. Several ongoing experiments, such as ADMX [27], attempt to search for the axion through axion conversion into photons in strong magnetic fields. An axion mass sensitivity at the level of  $10^{-6}$  eV may be expected.

### 1.3 WIMP Dark Matter Detection

Of all dark matter candidates, WIMPs are particularly attractive to physicists because they are well motivated and have the properties required by cosmological considerations. In addition, WIMPs, if they exist, may interact with baryonic matter weakly and get detected with technologies that are already existing or being currently de-

veloped. Several experiments using a wide range of technologies have been launched in attempts to directly or indirectly detect WIMP dark matter. Though the nature of dark matter still remains unknown, much progress has been made toward setting limits on WIMP model parameters.

### 1.3.1 Basic Theories in Direct WIMP Search

The hypothesis that high-density WIMP particles travel at galactic velocities in the vicinity of the Earth provides the possibility of direct detection of dark matter. A WIMP could transfer part of its kinetic energy to atomic matter during collisions, and the energy transfer may produce ionizations and excitations that are detectable with particle detectors. For large WIMP masses, the target particles typically gain a velocity at the same level of WIMP velocity during elastic collisions; this velocity corresponds to an energy of a few keV to hundreds of keV for heavy target particles like nuclei. Contemporary direct dark matter experiments usually look for nuclear recoils as a possible signature of WIMP dark matter interactions.

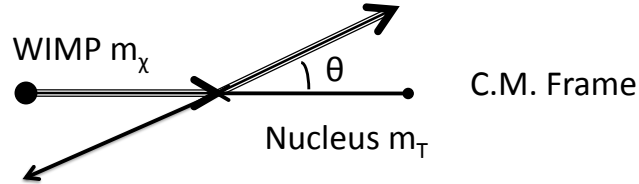


Figure 1.6: An illustrative WIMP interaction with matter in the center of momentum frame.

Typical nuclear energy levels are at MeV scales and are not excited in low energy WIMP scattering processes, so the collisions are usually taken as elastic. The energy transfer to a target nucleus (mass  $m_T$ ) during an elastic WIMP (mass  $m_\chi$ ) collision, usually called the WIMP-induced nuclear recoil energy  $E_R$ , can be obtained:

$$E_R = E_\chi r \frac{1 - \cos \theta}{2} \quad (1.5)$$

where  $E_\chi = m_\chi v^2/2$  is the incident energy of the WIMP particle,  $r = 4m_T m_\chi/(m_T + m_\chi)^2$  is a constant kinematic factor, which is related to the reduced collision mass  $\mu = m_T m_\chi/(m_T + m_\chi)$  by  $4\mu^2 = m_\chi m_T r$ ,  $\theta$  is the WIMP scattering angle in the center of momentum frame. We primarily follow the conventions defined in Ref. [28] in this analysis. It is obvious from Eq. 1.5 that the maximum recoil energy is:

$$E_R \leq E_\chi r = \frac{1}{2} m_T v^2 \left( \frac{2m_\chi}{m_\chi + m_T} \right)^2 \quad (1.6)$$

In the case of heavy WIMPs,  $m_\chi \gg m_T$ , the recoil nucleus acquires a velocity twice of that of the WIMP particle, and the maximum nuclear recoil energy scales up with the target nucleus mass.

For low energy  $s$ -wave elastic scattering, the scattered final states are usually isotropic in the center of momentum frame, which means the differential interaction cross section doesn't explicitly depend on the scattering angle.

$$\frac{d\sigma}{d\Omega} = \frac{\sigma_0}{4\pi}, \quad \frac{d\sigma}{d\cos\theta} = \frac{\sigma_0}{2} \quad (1.7)$$

where  $\sigma_0 = \int d\sigma$  is the total cross section for all scattering angles. This total cross section is determined by the type of interaction and is model dependent, but a general form can be written as  $\sigma_0 \propto \mu^2 G^2$  at 0 energy transfer [25, 29], where the reduced mass  $\mu$  arises from the kinematics and  $G$  is the coupling constant between WIMPs and nuclei. In the case of  $W$  boson-mediated weak interactions, the coupling constant is the Fermi constant of  $G_F \propto 1/m_W^2$  and  $m_W$  is the mass of  $W$  boson.

The differential cross section with respect to the recoil energy in the lab-frame

can be obtained by combining Eq. 1.7 and the derivative of Eq. 1.5.

$$\begin{aligned} dE_R &= -\frac{E_\chi r}{2} d\cos\theta \\ \frac{d\sigma}{dE_R}(E_\chi) &= \frac{\sigma_0}{E_\chi r} \Theta(E_\chi r - E_R) \end{aligned} \quad (1.8)$$

where  $\Theta(x)$  is the Heaviside step function which takes the value 1 for  $x > 0$  and vanishes for  $x < 0$ . The energy spectrum is flat below the maximum allowed energy transfer in a single scattering.

We have assumed a mono-energetic WIMP flux in the above discussions, and the WIMP energy distribution has to be considered to obtain the experimental nuclear recoil energy spectrum. Suppose the WIMP velocity follows a distribution,

$$dn = f(\vec{v}) d^3\vec{v}$$

and the integral over all WIMP velocities yields the estimated WIMP number density  $n_0 = \int dn \sim 0.3 \text{ GeV}/m_\chi/\text{cm}^3$ ; here we assume that one specie of WIMP particle is responsible for the expected dark matter density in the Earth's vicinity. Then the nuclear recoil event spectrum can be calculated as:

$$\begin{aligned} \frac{dR}{dE_R} &= \int \frac{d\sigma}{dE_R} v dn = \int \frac{\sigma_0}{E_\chi r} \Theta(E_\chi r - E_R) v dn \\ &= \int_{v \geq v_{min}} \frac{\sigma_0}{E_\chi r} v f(\vec{v}) d^3\vec{v} \end{aligned} \quad (1.9)$$

where  $v_{min}$  is the minimum WIMP velocity to produce nuclear recoils at energy  $E_R$ :

$$E_\chi = \frac{1}{2} m_\chi v^2 > E_R/r, \quad v \geq v_{min} = \sqrt{\frac{2E_R}{m_\chi r}}$$

And the integration needs to be carried out over all possible WIMP velocities below



the maximum velocity

$$v \leq v_{esc}$$

$v_{esc}$  is the velocity at which the WIMP particle would overcome the gravitational pull of the galaxy and escape.

The velocity distribution of the WIMP particles is not known, but it is usually assumed to be a Maxwell-Boltzmann distribution with a most probable velocity of  $v_0$  in the galactic frame,

$$dn = \frac{n_0}{(\sqrt{\pi}v_0)^3} e^{-\frac{v^2}{v_0^2}} d^3\vec{v} = n_0 \frac{4}{\sqrt{\pi}} \frac{v^2}{v_0^3} e^{-\frac{v^2}{v_0^2}} dv \quad (1.10)$$

For experiments installed on the Earth, the relative WIMP velocity is modulated by the Earth's motion in the galaxy. So the nuclear recoil event rate becomes:

$$\begin{aligned} \frac{dR}{dE_R} &= \int_{|\vec{v}-\vec{v}_E| > v_{min}}^{v_{esc}} \frac{\sigma_0}{E_{\chi,Er}} |\vec{v} - \vec{v}_E| \frac{n_0}{(\sqrt{\pi}v_0)^3} e^{-\frac{v^2}{v_0^2}} d^3\vec{v} \\ &= \int_{|\vec{v}-\vec{v}_E| > v_{min}}^{v_{esc}} \frac{8}{\sqrt{\pi}} \frac{n_0\sigma_0}{m_\chi r v_0^3} \frac{v^2}{|\vec{v} - \vec{v}_E|} e^{-\frac{v^2}{v_0^2}} dv \end{aligned} \quad (1.11)$$

In the simplest case of a WIMP detector at rest in the WIMP halo bombarded by WIMPs with infinite escaping velocity, the integration can be carried out analytically and yields the famous exponentially decaying nuclear recoil energy spectrum,

$$\begin{aligned} \frac{dR}{dE_R} &= \frac{2}{\sqrt{\pi}} \frac{n_0 v_0 \sigma_0}{E_0 r} e^{-\frac{E_R}{E_0 r}} \\ &= \frac{R_0}{E_0 r} e^{-\frac{E_R}{E_0 r}} \end{aligned} \quad (1.12)$$

where  $R_0$  is the total event rate over all nuclear recoil energies  $R_0 = 2n_0 v_0 \sigma_0 / \sqrt{\pi}$ , and  $E_0 = m_\chi v_0^2 / 2$  is the WIMP kinetic energy at the most probable velocity. The spectral shape is smoothly decreasing and featureless, which adds to the difficulties of direct WIMP detection experiments.

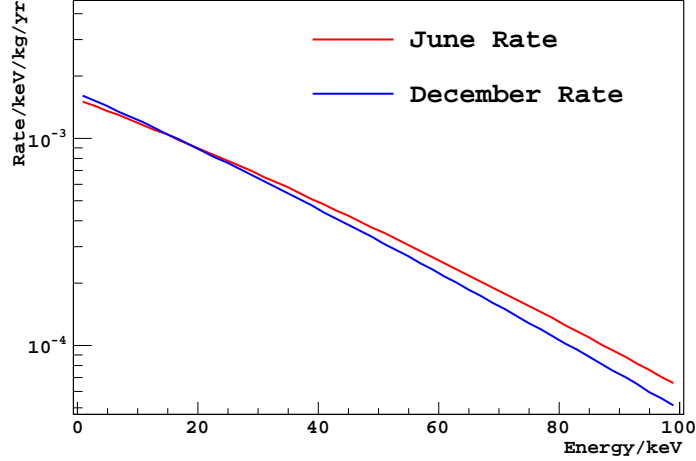


Figure 1.7: The hypothetical WIMP induced argon nuclear recoil spectra in June (high Earth velocity) and in December (low Earth velocity). A WIMP nucleon interaction cross section of  $10^{-45} \text{ cm}^2$  and a WIMP mass of 100 GeV is assumed in the calculation.

Since the Earth orbits the Sun with a period of one year, its velocity relative to the galactic WIMP halo oscillates with time. The time-dependent velocity can be practically parameterized as [30]

$$v_E = (244 + 15 \sin(2\pi t)) \text{ km/s}$$

The velocity takes its maximum value in June when the Earth's orbital velocity is in the same direction to that of the Sun, and the effective WIMP flux seen by a detector is the largest. As a result, the overall WIMP interaction rate increases in June and decreases in December, the rate of modulation is approximately 3% [30]. However, this rate modulation amplitude changes sign with energy<sup>9</sup>, as illustrated in Fig. 1.7, so the relative amplitude can be larger than 3% for binned data.

To compare the results of dark matter search with different target nuclei, it is usually convenient to report the cross section measurement of WIMP-nucleon scattering  $\sigma_{n,p}$  instead of WIMP-nucleus cross section  $\sigma_0$ . During a WIMP-nucleus collision, the

---

<sup>9</sup>This may be approximately taken as a variation in  $E_0$  in Eq. 1.12 (we note the formula does not apply exactly to this case), the increased  $E_0$  value in June would require the differential rate to decay more slowly and the low energy rate would decrease.

WIMP may interact with any of the  $A$  nucleons, and the scattering amplitudes may add coherently.

$$\sigma_0 \propto \left| \sum_{i=1}^A f_i(\vec{p}, \vec{p}') e^{-i(\vec{p}' - \vec{p}) \cdot \vec{r}_i} \right|^2 \sim \left( (Zf_p + (A - Z)f_n) F(\vec{q}) \right)^2 \quad (1.13)$$

where  $f_i$  is the scattering amplitude of WIMP with a nucleon, and the factor  $F(\vec{q})$  describes the interference between nucleons due to their relative positions.  $F(\vec{q})$  is called the nuclear form factor and is defined as:

$$F(\vec{q}) = \sum_j \rho_j e^{i\vec{q} \cdot \vec{R}_j} = \int \rho(\vec{x}) e^{i\vec{q} \cdot \vec{R}} d^3\vec{R} \quad (1.14)$$

In this definition the interaction charge density  $\rho_i$  has been normalized to have unit sum for the whole nucleus.

In the low momentum transfer limit, the De Broglie wavelength at the momentum transfer  $q = \sqrt{2E_R M_T}$  can be large compared to the size of a nucleus ( $R \sim \text{fm}$ ), or  $qR \sim 0$ . In this case the nuclear form factor approaches to unit  $F(\vec{q}) \sim 1$ ; the WIMP collision with different nucleons is indistinguishable and adds constructively. If we further assume the WIMP interaction strengths with protons and neutrons are the same, the WIMP-nucleus scattering amplitude is simply  $A$  times larger than the WIMP-nucleon scattering amplitude, and the cross section is  $A^2$  times larger.

$$\sigma_0 \propto ((Zf_p + (A - Z)f_n) F(\vec{q}))^2 = (A f_{n/p})^2, \quad \sigma_0 \propto A^2 \sigma_{n,p} \quad (1.15)$$

Though equal WIMP interaction strengths with neutrons and protons are usually assumed in direct dark matter search experiment, it has been suggested by some authors that different WIMP-neutron coupling from WIMP-proton coupling might help solve contradictory experimental observations [31]. So a general formulation of

the WIMP-nucleus interaction cross section is:

$$\frac{\sigma_0}{\mu^2} = \frac{\sigma_n}{\mu_n^2} \left( \frac{f_p}{f_n} Z + (A - Z) \right)^2 F^2(\vec{q}) \quad (1.16)$$

The WIMP-nucleus reduced mass  $\mu$  and WIMP-nucleon reduced mass  $\mu_n$  are divided by the cross section because they rise from the kinematic factors in the cross section calculation instead of from the scattering amplitude. A relative ratio of  $f_n/f_p \sim 0.7$  is suggested by Ref. [31] for 10 GeV WIMPs. We comment that the WIMP-neutron scattering cross section  $\sigma_n$  is usually assumed to be proportional to the WIMP-neutron reduced mass and the WIMP-neutron coupling strength. For example, the coherent cross section for a non-relativistic Dirac neutrino scattering is calculated to be

$$\sigma_{\nu_D} = \frac{G_F^2}{8\pi\hbar^4} \mu^2 \left( (A - Z) + (1 - 4\sin^2\theta_W)Z \right)^2 \quad (1.17)$$

where  $G_F$  is the Fermi weak coupling constant and  $\theta_W$  is the Weinberg weak mixing angle. The WIMP interaction with protons and neutrons are distinctively different; actually the value of the Weinberg angle  $\sin^2\theta_W \sim 0.24$  causes the cross section to be approximately proportional to the neutron number instead of the nucleon number.

To sum up, the total spin-independent WIMP interaction rate with a target nucleus can be estimated as

$$R_0 \sim n_0 \sigma_0 v_0 \sim \frac{\rho_\chi}{m_\chi} \frac{\mu^2}{\mu_n^2} \sigma_n v_0 \left( \frac{f_p}{f_n} Z + (A - Z) \right)^2 \quad (1.18)$$

where we have set the nuclear form factor  $F(\vec{q})$  to be unit as we are working in the low energy transfer limit, and we ignore the detailed structure of the WIMP velocity distribution. The rate for a certain sensitive mass  $M$  of a target specie can be obtained

by multiplying with the number of target atoms.

$$\begin{aligned}
R_M &\sim \frac{MN_A}{m_T} \frac{\rho_\chi}{m_\chi} \frac{\mu^2}{\mu_n^2} \sigma_n v_0 \left( \frac{f_p}{f_n} Z + (A - Z) \right)^2 \\
&\sim \left( \frac{MN_A \rho_\chi}{\mu_n^2} \sigma_n v_0 \right) \left[ r \left( \frac{f_p}{f_n} Z + (A - Z) \right)^2 \right]
\end{aligned} \tag{1.19}$$

The target-independent factors (first term) and the target-dependent factor (second term) have been separated. Therefore, the unit mass WIMP interaction rate from different experiments can be compared after the second term is taken care of.

Beside spin-independent interactions, WIMP and nuclei could also undergo spin interactions. In this case, the sum over the scattering amplitudes from individual nucleons gets complicated by the spin distribution inside a nucleus. The simplest model assumes that the scattering amplitudes from nucleons with opposite spin states cancel, and only unpaired nucleons contribute to the total cross section. However, this simplified method doesn't yield the correct nuclear properties for most nuclei, especially for those far away from closed shells. More sophisticated models have been developed, and the readers are referred to Ref. [32] for detailed discussions.

### 1.3.2 General Discussions on Direct WIMP Searches

With the basic theory of WIMP interaction with matter discussed in Sec. 1.3.1, the WIMP event rate in a direct detection dark matter detector can be estimated. We will compare this rate with the expected background rate, and discuss the general requirements for WIMP detectors.

Current direct dark matter search experiments have reached a sensitivity beyond  $10^{-44} \text{ cm}^2$  with no conclusive detection of WIMPs, and in this section we will assume a hypothetical WIMP-nucleon interaction cross section of  $10^{-45} \text{ cm}^2$  at a WIMP mass of 100 GeV. The WIMP halo parameters will take the standard values: the WIMP density  $\rho \approx 0.3 \text{ GeV/cm}^3$  in the vicinity of the Earth, the average WIMP velocity

$v_0=220$  km/s, the local escape velocity  $v_{esc}=600$  km/s, and the velocity of the solar system is  $v_0=230$  km/s. The ILIAS dark matter online tool [33] and the nuclear form factors provided by Ref. [30] are used in the calculation of WIMP interaction rates.

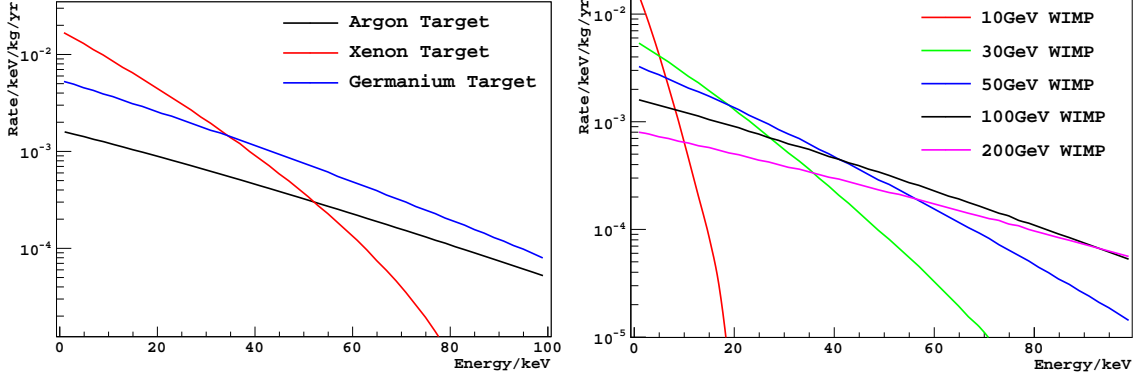


Figure 1.8: Left: the expected nuclear recoil spectra induced by 100 GeV WIMPs through spin-independent interactions with different target materials; Right: the argon nuclear recoil spectra induced by WIMPs of different masses. The WIMP nucleon interaction cross section is assumed to be  $10^{-45}$  cm<sup>2</sup> in both plots.

The expected WIMP induced nuclear recoil spectra in commonly used detector targets are shown in Fig. 1.8. These spectra approximately resemble the exponentially decaying spectral shape in the case of perfect Maxwellian WIMP velocity distribution (Eq. 1.12). Heavy nuclei like xenon typically have a high WIMP interaction rate because of the coherent factors of  $A^2$  and the kinematic factor of  $\mu^2$  (reduced mass), but the rate decays fast at high energy due to the nuclear form factors  $F(q)$  ( $q \sim \sqrt{2m_T E}$ ). The integrated WIMP interaction rates with Xe, Ge and Ar at different energy thresholds are summarized in Tab. 1.2. As for WIMPs of different masses, heavy WIMPs tend to produce high energy nuclear recoils, but the total interaction rate is suppressed by the low WIMP flux (the total WIMP density  $\rho \sim m_\chi n_\chi$  is fixed). On the contrary, light WIMPs may produce very high nuclear recoil rates but they are concentrated in the low energy regions; as a result, an argon-based detector with a typical nuclear recoil energy threshold above  $\sim 20$  keV would essentially have no sensitivity to  $<10$  GeV light WIMPs.

Target Atom	Rate(/kg/yr) 0-100 keV	Rate(/kg/yr) 10-100 keV	Rate(/kg/yr) 20-100 keV	Rate(/kg/yr) 30-100 keV
Argon	$3.3 \times 10^{-2}$	$2.1 \times 10^{-2}$	$1.2 \times 10^{-2}$	$6.8 \times 10^{-3}$
Germanium	$1.3 \times 10^{-1}$	$7.7 \times 10^{-2}$	$4.2 \times 10^{-2}$	$2.2 \times 10^{-2}$
Xenon	$5.9 \times 10^{-1}$	$2.6 \times 10^{-1}$	$1.1 \times 10^{-1}$	$4.5 \times 10^{-2}$

Table 1.2: The expected interaction rate of 100 GeV WIMP with argon, germanium, and xenon targets at nucleon interaction cross section of  $10^{-45} \text{ cm}^2$  in 1 kg-yr exposure.

Compared to the extraordinarily low WIMP interaction rate, the cosmic ray background and environmental radioactivity background are enormous at the Earth's surface. Take 1 kg of typical crustal rock [34] as an example, the event rate due to U, Th, K in a year is estimated in Tab. 1.3. We also estimate the background from cosmic rays (CRs), where we use a dimension of  $7.5 \text{ cm} \times 7.5 \text{ cm} \times 7.5 \text{ cm}$  for this 1 kg rock sample (assuming a rock density of  $2.4 \text{ g/cm}^3$ ). The cosmogenic  $^{39}\text{Ar}$  activity in argon extracted from the atmosphere is also listed.

Background Sources	Concentration or Rate	Events in a year	Additional Comments
U(rock)	1.7 ppm	$6.6 \times 10^8$	In secular equilibrium, each $^{238}\text{U}$ decay includes several alphas, gamma rays, and electrons
Th(rock)	8.5 ppm	$1.1 \times 10^9$	similar to the U case
K(rock)	2.1%	$2.1 \times 10^{10}$	
CR Muon	$100\text{-}200/\text{m}^2/\text{s}$	$2.7 \times 10^7$	$1 \times 10^7$ neutrons, $7 \times 10^6$ electrons and other cosmic ray particles
$^{39}\text{Ar}$ (argon)	1 Bq/kg	$3.2 \times 10^7$	

Table 1.3: The estimated background rate from U, Th, K decays in 1 kg of crustal rock in a year; sea level cosmic ray radiation and  $^{39}\text{Ar}$  in atmospheric argon are also listed.

As can be seen, the background rate can be many orders of magnitude higher than that of the expected WIMP interactions. So effective background suppression

methods have to be developed for a sensitive WIMP detection. The basic requirements for a feasible WIMP experiment would include:

1. Low radioactivity materials have to be used in the detector, especially for the sensitive volume. High purity crystals and noble liquids are widely used.
2. The experiment needs to be installed deep underground to reduce cosmic rays backgrounds, and has to be shielded (actively/passively) from residual backgrounds. Besides suppressing backgrounds, active shielding can also provide in situ measurements of the background.
3. Event discrimination methods are desired to separate the WIMP-induced nuclear recoil events from the prevalent electron recoil backgrounds.
4. A dark matter detector needs to be sensitive to low energy nuclear recoil events, especially for light WIMP detection.

### **1.3.3 Direct WIMP Search Experiments and Results**

Several low background experiments have been launched in attempts to detect WIMP interactions with nuclei. We will briefly review the search techniques and physical results of the major experiments.

A long standing claim of positive evidence for dark matter interactions is made by the DAMA collaboration. The DAMA experiment is located in the Gran Sasso Laboratory, 3800 meters of water equivalent (m.w.e.) underground; it uses a scintillating crystal NaI (Tl) to look for low energy WIMP interactions [35]. The original DAMA/NaI setup consisted of nine 9.7kg crystals, and each of them was seen by two PMTs through low radioactivity light guides. The detectors were contained in a well shielded copper box and were continuously purged with high purity nitrogen gas to suppress radon backgrounds. These NaI crystals did not distinguish between nu-



clear recoil events and electron recoil backgrounds, but had moderate rejection power against electronic noise based on pulse shape information.

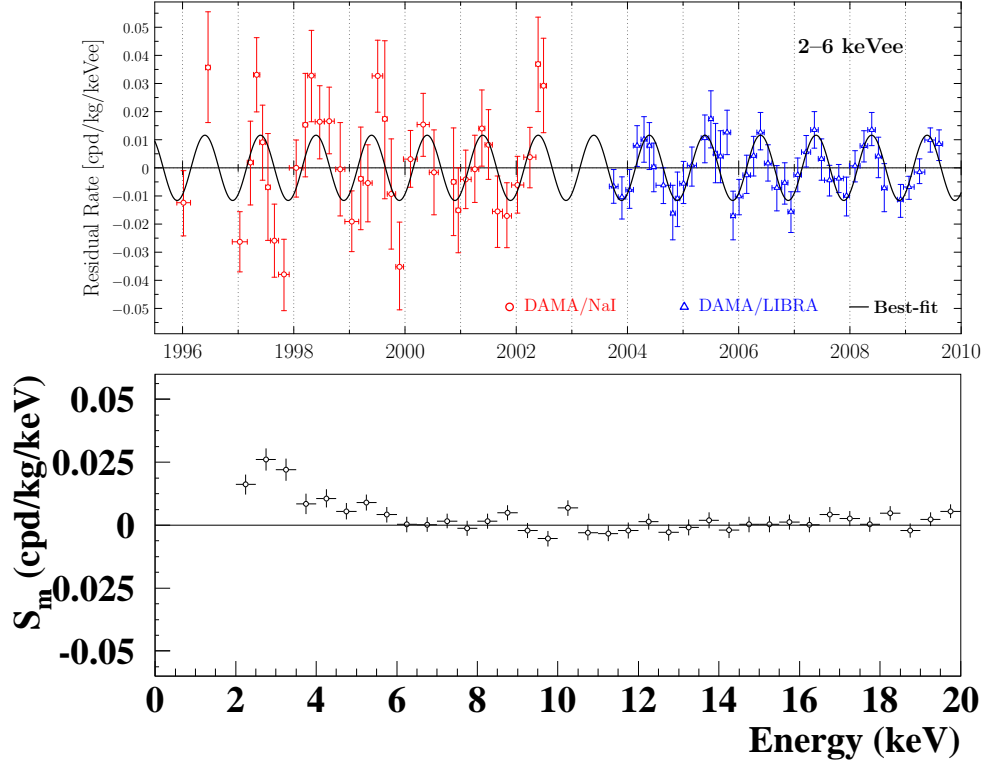


Figure 1.9: The rate modulation analysis of the DAMA experiment. Top: the modulation of the residual event rate between 2–6  $\text{keV}_{ee}$  in DAMA/NaI and DAMA/LIBRA [36–38]; Bottom: the modulation amplitudes at different energy ( $\text{keV}_{ee}$ ).

In 1998, DAMA/NaI reported the first evidence of event rate modulation between 2  $\text{keV}_{ee}$  and 6  $\text{keV}_{ee}$  at a 99.6% confidence level [37]. This result was obtained based on a total exposure of 41  $\text{kg}\cdot\text{yr}$ , and events that had interactions with multiple crystals excluded from the analysis. This modulation behavior was reproduced with high statistics by the DAMA/LIBRA experiment [39], which is the successor of DAMA/NaI. The combined exposure of  $\sim 1.2$  ton-year from both DAMA/NaI and DAMA/LIBRA revealed a significance of  $8.9\sigma$  for the annual modulation hypothesis over the null result [38]. In addition, the phase of the modulation matches what is expected from the motion of Earth in the dark matter halo. The DAMA result, if can be

confirmed, would provide a model-independent evidence for WIMP dark matter interactions. Other explanations of the modulation, including cosmogenic backgrounds<sup>10</sup> and radon-induced backgrounds, were all refuted by DAMA modulation [41].

The DAMA claim of dark matter evidence was not supported by other direct dark matter search experiments until 2011, when the Coherent Germanium Neutrino Technology (CoGeNT) experiment reported an excess of low energy events beyond the identified backgrounds. The CoGeNT experiment uses of a 440 g p-type point contact (PPC) germanium crystal to look for low energy ionization events in the Soudan underground laboratory ( $\sim 2100$  m.w.e.) [42]. The PPC crystal is maintained at liquid nitrogen temperature and is reported to have a modest electronic noise level at a relatively large mass. The detector’s response to nuclear recoils was calibrated with a 24 keV neutron beam [43], but it is not capable of differentiating between nuclear recoils and electron recoils. Surface contaminations, on the contrary, may be rejected using the time profile of the ionization signals.

In 2011, CoGeNT reported an event rate excess in the energy window of 0.4-3.2 keV<sub>ee</sub> based on  $\sim 18.5$  kg·days (8 weeks) of data, after the X-rays and Auger electrons backgrounds from Ge, Cu, Ga isotopes were subtracted [44]. If these events originated from WIMP interactions, they would correspond to a spin-independent WIMP-nucleon scattering cross section of  $\sim 6.7 \times 10^{-41}$  cm<sup>2</sup> for (7-12) GeV WIMPs. This rate excess was confirmed with a longer exposure ( $\sim 150$  kg·days or 442 live days), and the analysis result is shown in Fig. 1.10. The new CoGeNT data also suggest a possible rate modulation [45]. The period of the modulation is estimated to be  $347 \pm 29$  days, and its amplitude was very significant, approximately 16.6% of the overall residual rate. The significance of the modulation is 99.4%, or  $2.8 \sigma$ , over null hypothesis. Although CoGeNT and DAMA reported similar signals, the dark matter interpretation of the two experiments do not coincide in the standard dark matter

---

<sup>10</sup>The peak time of cosmic muon flux at LNGS is measured to be  $\sim 1$  month later than that of DAMA by the Borexino collaboration [40].

picture. The WIMP mass and interaction cross section predicted by the two experiments have little overlap, and CoGeNT observes the peak of event rate approximately one month earlier than that of DAMA (Early June). CoGeNT later reported a high rate of surface events contamination at low energy, and this brought the estimated WIMP interaction cross section to  $1\text{--}3 \times 10^{-41} \text{ cm}^2$  [46].

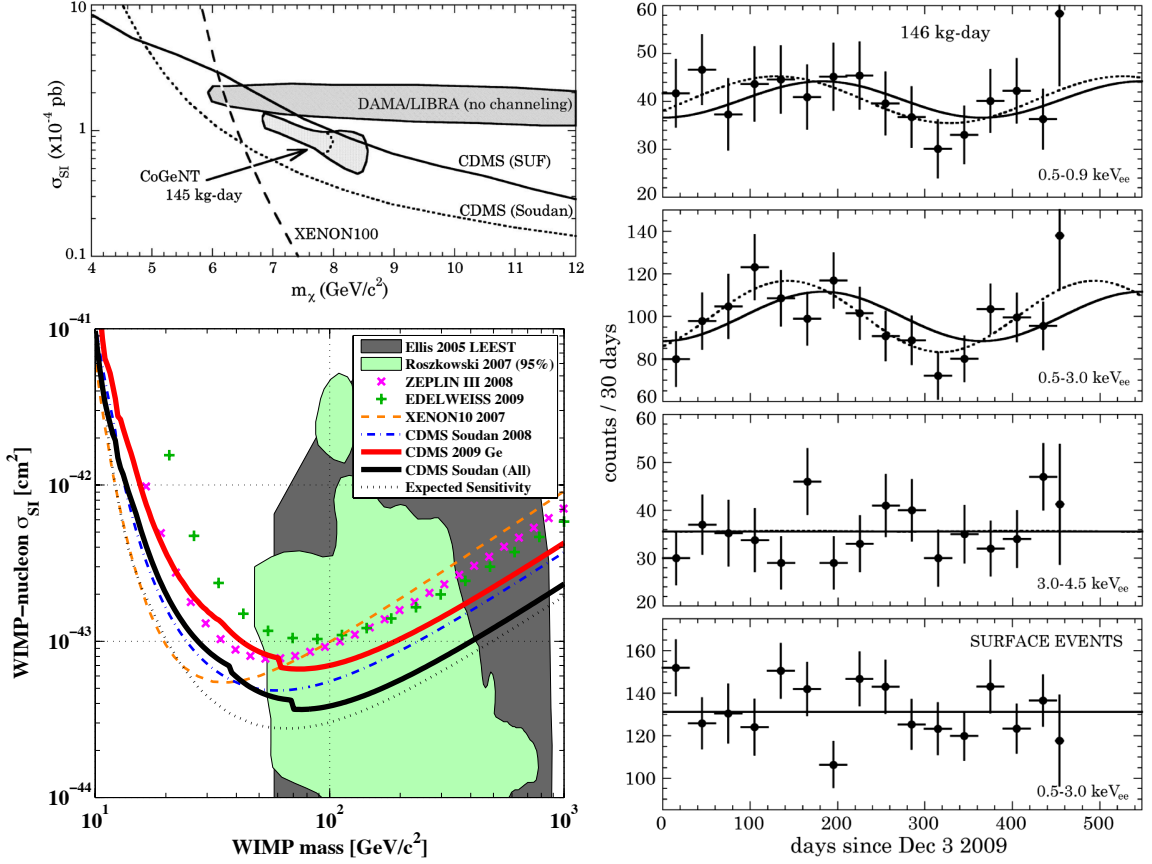


Figure 1.10: top left: Spin-independent WIMP sensitivity curve for the 2011 CoGeNT data; right: rate modulation in the CoGeNT data; bottom left: Spin-independent WIMP sensitivity curve of the 2009 CDMSII-Ge results.

Another germanium-based dark matter experiment is the Cryogenic Dark Matter Search (CDMSII) [47, 48]. CDMS uses an array of 19 germanium detectors ( $\sim 230 \text{ g}$  each) and 11 silicon detectors ( $\sim 105 \text{ g}$  each) to detect low energy nuclear recoil events in the Soudan mine. The detectors are maintained at  $\sim 50 \text{ mK}$  and instrumented with both phonon sensors and charge electrodes. Comparison of the phonon signal with the

ionization signal provides a powerful discrimination between nuclear recoil signals and gamma ray backgrounds ( $>99.99\%$  above the 10 keV nuclear recoil energy threshold). The pulse shape of the phonon signals is also used to reject surface background events<sup>11</sup> at an efficiency of  $>96\%$ . The probability of misidentifying electron recoil events as nuclear recoils is estimated to be less than  $10^{-6}$ .

In 2009, CDMSII reported two suspicious events in 612 kg-days exposure ( $\sim 1$  yr) of Ge data [49]. The probability for the 2 observed events to be backgrounds was  $\sim 23\%$ , so they were not interpreted as significant evidence for WIMP interactions. This observation set an upper limit of  $7.0 \times 10^{-44} \text{ cm}^2$  on the spin-independent WIMP-nucleon interaction cross section for 70 GeV WIMP at 90% confidence level<sup>12</sup>, as shown in Fig. 1.10 (bottom left). The DAMA favored parameter space of WIMP-interactions was largely ruled out. In 2011 CDMSII revealed a low energy analysis (2 keV nuclear recoil energy threshold), but did not observe any excess of events beyond the expected backgrounds; a conservative limit obtained by attributing all residual events to WIMP interactions ruled out the original CoGeNT dark matter interpretation [50]. In addition, the CDMS data did not have any significant event rate modulation above 5 keV nuclear recoil energy [51], as shown in Fig. 1.11. However, in 2013, CDMSII reported 3 candidate events for dark matter interactions with the Si detectors, which could translate to a WIMP-nucleon interaction cross section of  $1.9 \times 10^{-41} \text{ cm}^2$  for 8.6 GeV WIMPs [52]. This result approximately agreed with that of CoGeNT with surface background correction [46].

Different from the crystal experiments, the Xenon experiment makes use of the scintillating noble gas xenon to detect low energy nuclear recoils in the Gran Sasso Laboratory. The Xenon100 detector contains  $\sim 60$  kg (40 kg fiducial) of liquid xenon in its sensitive volume, with another  $\sim 100$  kg in an outer cylinder functioning both as shielding and as a veto [53]. The inner detector is designed to be a two phase

---

<sup>11</sup>Surface events may be misidentified as nuclear recoils because of incomplete charge collection.

<sup>12</sup>This limit was pushed down to  $3.8 \times 10^{-44} \text{ cm}^2$  for all CDMS Ge data combined.

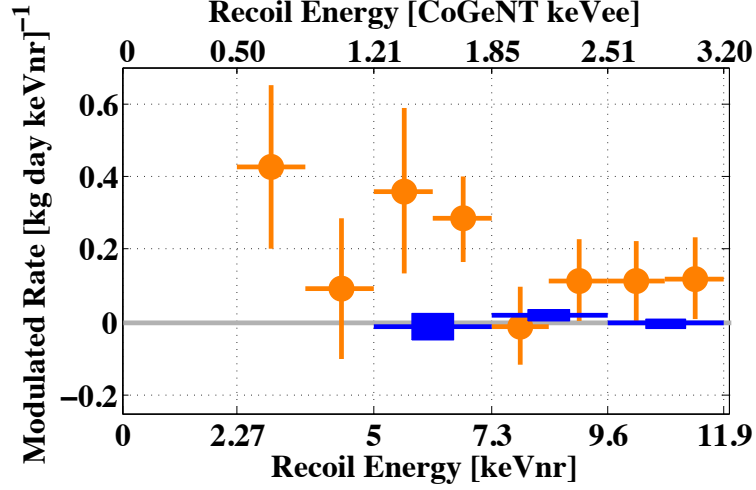


Figure 1.11: Modulation analysis of CDMSII data (blue), compared to CoGeNT (orange).

Time Projection Chamber (TPC) and collects both the scintillation and ionization signals. Comparison of the scintillation to ionization signal amplitudes provides a powerful discrimination between nuclear recoil events and electron recoil backgrounds; the rejection efficiency is reported to be  $\sim 99.5\%$  in the WIMP search window. The ionization signals are also used to reconstruct the event positions in three dimensions, which helps the rejection of surface-related backgrounds.

The most recent Xenon100 analysis revealed two candidate nuclear recoil events in the energy window of 6.6 - 30.5 keV in 7.6 ton-days (225 live days) of data [54]. The background rate was estimated to be  $1.0 \pm 0.2$ . This observation set a limit of  $2 \times 10^{-45} \text{ cm}^2$  on the WIMP-nucleon interaction cross section for 55 GeV WIMPs; the full 90% confidence level sensitivity curve is shown in Fig. 1.12. At the low mass WIMP region, Xenon excluded the WIMP parameter space favored by DAMA and CoGeNT using data from the Xenon10 detector [55], as is shown in Fig. 1.12. A low energy threshold of  $\sim 1.4 \text{ keV}$  was obtained in this analysis by only using the ionization signals.

The experiment CRESST (in Gran Sasso) has also reported observation of low energy events that could not be explained by identified backgrounds [56]. The

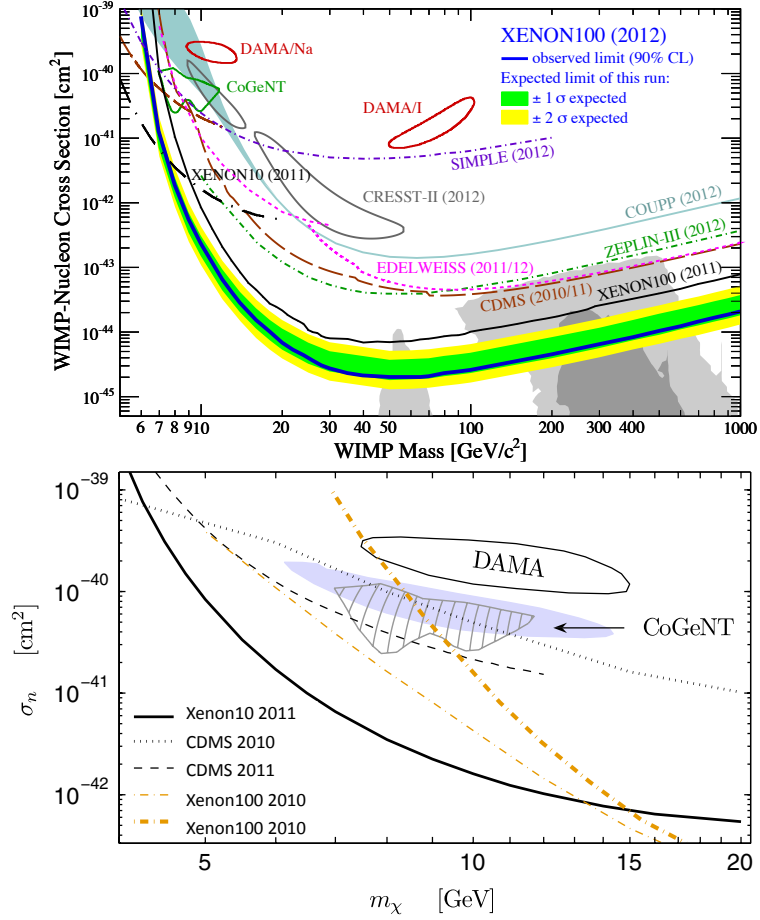


Figure 1.12: The 90% confidence limit on the spin-independent WIMP-nucleon scattering cross section from the Xenon experiment. Top: limit derived from 225 days of Xenon100 data; bottom: low energy analysis of Xenon10 data; the two 2010 Xenon100 limits come from different quenching factors at low energy.

CRESSTII detector is a cryogenic thermometer based on  $\text{CaWO}_4$  crystals that collect both the phonon signals and the scintillation signals. The energy of ionization events is determined by the thermal channel, while the relative ratio of the scintillation signal is used in nuclear recoil events identification. The observed excess of low energy events may be interpreted as light WIMPs ( $< 50$  GeV) interactions with oxygen, and it is approximately consistent with the CoGeNT results.

We comment that several other dark matter experiments, including ZEPLIN [57], EDELWEISS [58] and WArP [59], have also set limits on the spin-independent inter-

actions of WIMPs; experiment like Xenon [60], Picasso [61] and COUPP [62] have also made progresses in measurements of spin-dependent WIMP interactions. The interpretations of some of these experiments appear contradictory, but they may get reconciled by the large uncertainties in the WIMP model, and by the specific detector backgrounds. A few examples of such flexibilities include local substructure of the WIMP halo [36,46], inelastic WIMP-nucleus scattering [63], non-equal WIMP-proton and WIMP-neutron interactions [31], and channeling effects in crystals [64].

### 1.3.4 Indirect Search and Accelerator Search of WIMPs

In addition to searching for WIMP-nucleon collisions, WIMPs may also be detected by the observation of WIMP annihilations or WIMP-pair productions. These possibilities motivate the indirect search and the accelerator search of WIMPs.

Although the WIMP annihilation rate is usually considered to be insignificant after the WIMP-decoupling, WIMPs may still annihilate in highly concentrated regions like in the center of galaxies. WIMP particles may fall into gravitational wells and gradually lose kinetic energy by collisions; eventually they could get trapped by gravity and create high concentration regions. When these WIMPs annihilate, charged cosmic rays, gamma rays or neutrinos may be produced; once detected, they can provide indirect evidence for WIMP dark matter.

An excess of high energy cosmic electron/positron was observed by the balloon-borne experiment ATIC [66], and was later confirmed by the space-based measurements of Fermi-LAT [67], PAMELA [68], AMS-II [69] and ground-based HESS [70], some of which are shown in Fig. 1.13. ATIC observed a broad bump around 300-800 GeV in the energy spectrum, and the AMS-II data also indicated a possible leveling of the positron fraction between 250 GeV and 350 GeV in the spectrum. Cosmic positrons are usually attributed to interactions of cosmic rays with interstellar materials, and the positron fraction  $R = [e^+]/([e^+] + [e^-])$  is expected to be monoton-

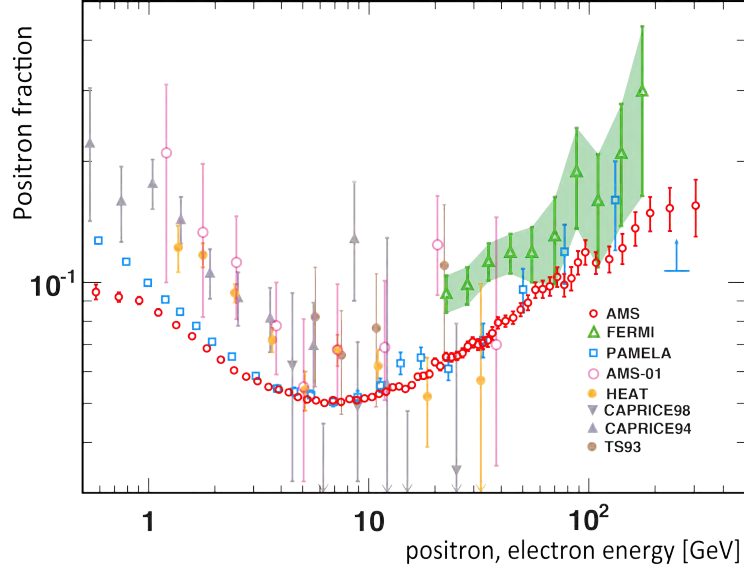


Figure 1.13: The positron fraction out of total electrons and positrons [65]. It is expected to be decreasing for positrons produced by cosmic ray interaction with interstellar medium.

ically decreasing; so this excess of positrons may be considered as evidence for WIMP annihilation in nearby regions<sup>13</sup>. However, this dark matter interpretation has to assume a WIMP annihilation cross section that is 2-3 orders of magnitudes larger than the expected value, and it could not explain the trivial result in the antiproton measurement of PAMELA<sup>14</sup>. In addition, alternative explanations of the positron excess exist; for example, the synchrotron radiation of pulsars may be energetic enough to produce electron-positron pairs but not for proton-antiproton pairs [71, 72]. As a result, the WIMP interpretation of this positron measurements remains inconclusive.

Besides charged particles, gamma rays and neutrinos are also of great interest in WIMP annihilation searches. Although some authors reported that a  $\sim 130$  GeV gamma line from the galactic center is indicated by Fermi-LAT data [73], it largely remains unconfirmed. It is generally agreed that no significant anomaly in cosmic gamma rays has yet been confirmed in experiments. The upper limits on the WIMP

<sup>13</sup>Electrons and positrons can suffer significant energy loss during propagation in the galaxies.

<sup>14</sup>We note that some dark matter interaction models may explain the preferred lepton decays of WIMP dark matter in an ad hoc way.



annihilation processes set by the gamma ray observations have highly constrained the WIMP interpretation of the positron measurements [74]. Compared to charged particles and gamma rays, neutrinos are expected to be a more powerful probe into the high density regions of the universe because they almost don't get scattered by stellar matter. No excess of high energy neutrinos has been observed from the Sun or from the galactic center according to ICECUBE [75] and SuperKamiokande [76]. Besides putting tight constraints on the WIMP annihilation cross section, the neutrino observation may also constrain the WIMP-nucleon scattering cross section because this scattering processes largely determines the slow-down rate and capture rate of WIMPs. In the assumption of equilibrium between WIMP capture and WIMP annihilation, the annihilation neutrino flux is solely determined by the WIMP capture rate, or equivalently, by the WIMP-nucleon scattering cross section.

To the contrary of annihilation processes, WIMPs may be produced in pairs in high energy colliders. A higher rate of events with missing transverse energy than what is predicted by the Standard Model could indicate WIMP productions. The ALEPH experiment reported no observation of the Lightest Supersymmetric Particle (LSP) in the large Electron-Positron collider (LEP) at center of momentum energy up to 209 GeV and placed a mass limit of  $>43$  GeV on LSP in the MSSM model [77]. The  $p\bar{p}$  collider Tevatron [78,79] and  $pp$  collider LHC [80,81] have reached TeV level of center of momentum energy, and no excess beyond the Standard Model backgrounds has been found.

## Chapter 2

# Underground Argon for Direct Dark Matter Search

Technologies of particle detection using noble elements have made much progress in the past a few decades. The properties of argon and other noble gases have been extensively studied, and they exhibit many attractive features to rare-event detection experiments such as dark matter searches.

1. Extraordinarily high purity levels have been reached in noble gas detectors due to their unique chemical properties. They can be free of long-lived primordial U, Th, and K contaminants<sup>1</sup>.
2. Copious light can be emitted by noble liquid; the light yield of noble elements is comparable to that of alkali halide crystals.
3. Noble gases scintillation rises from the relaxation of molecular excimers instead of atomic excitons, so self-absorption of noble element scintillation is minimal.
4. Ionization electrons in noble liquid can remain free and be drifted over long

---

<sup>1</sup>Radon and its progeny could exist in noble gases, but can get highly suppressed by distillation techniques. <sup>39</sup>Ar and <sup>85</sup>Kr may also be considered backgrounds in some experiments.

distances with an external electric field, which makes large scale Time Projection Chambers (TPCs) possible.

5. Noble liquid technologies that work at a small scale can be adopted in large scales. This scalability is required by contemporary dark matter searches.
6. The scintillation and ionization signals of noble liquids can be used for event identification, and provides background rejection power.
7. Unlike crystal detectors, noble element detectors don't form defects after excitations or ionizations, and can have relatively stable performance over time.

Several low background experiments use noble liquid as the detection medium. For example, the Xenon experiment has been leading the search for WIMP dark matter for many years, and a few other xenon-based experiments are also under development. Liquid argon technology is relatively new for dark matter applications, but it has been drawing increasing attention from researchers after its excellent pulse shape discrimination power was revealed. The work of this thesis is to demonstrate that argon detectors can be very competitive in future dark matter search experiments with argon of extremely low  $^{39}\text{Ar}$  radioactivity levels.

## 2.1 Characteristics of Argon as a Scintillator

Argon is a bright scintillator. Approximately 50,000 photons can be emitted for 1 MeV energy deposited by heavy relativistic particles [82], which is very close to that of NaI crystals. The argon scintillation spectrum exhibits a broad peak structure around 128 nm (the second continuum); this feature is observed in liquid, solid argon, and also in high density gaseous argon. In argon gas discharge experiments, scintillation peak around 110 nm (the first continuum) may also be observed.

### 2.1.1 The Scintillation Mechanism

Although most ongoing argon detectors use liquid argon as the detection medium, the argon scintillation mechanisms are primarily studied in solid and gaseous argon. The property of liquid argon scintillation is believed to be similar to that of solid argon though temperature dependence may exist [83,84].

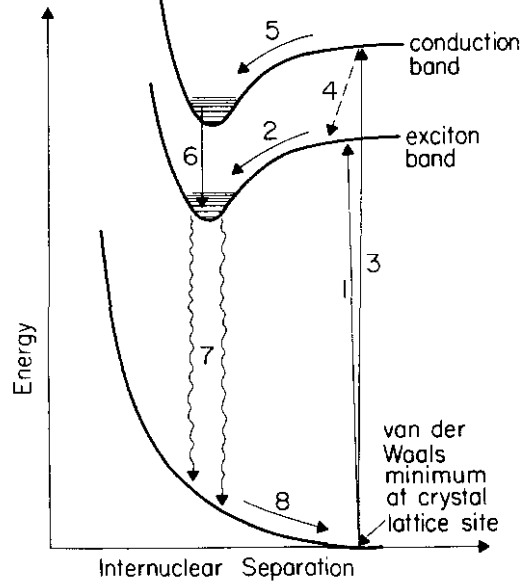


Figure 2.1: Schematic energy levels of diatomic argon molecules (also applies to other rare gases); the possible excitation/relaxation processes are also shown (see text) [83].

As an inert gas, argon atoms have a closed atomic shell. Neighboring atoms are held together by a weak van der Waals force, and the binding is minimal even in argon solids. However, once ionized argon will have a halogen-like shell structure and can form strong covalent bonds with neighboring atoms. For example, a positive  $\text{Ar}^+$  ion can share an orbital electron with a neutral argon atom and form a diatomic molecular ion  $\text{Ar}_2^+$ . The binding energy is at the level of  $\sim 1$  eV, and the levels are schematically illustrated in Fig. 2.1 [83]. Argon atoms in the excited states can form diatomic argon molecules (dimers) in a similar way. The diatomic argon molecules have a potential curve and well depth like that of molecular ions because the excited

electron is only loosely bounded to the diatomic ion core, as in Rydberg atoms.

With the strong bonds to neutral argon atoms, the argon ions and excitons can no longer freely migrate in argon crystals, and thus get self-trapped. This process has been thoroughly studied with alkali halide crystals [85], in which closed shells are formed at each lattice site, similar to that in an argon crystal. Lattice excitons relieve the closed shell condition and opens up the possibility of covalent binding with nearby lattice sites. This covalent interaction leads to a strong local deformation of the lattice structure, and the excitons get trapped by their own distorted field. As a result, covalent bonds are formed in a non-covalent solid, which can affect the luminescence and energy transportation properties of a crystal.

The self-trapping process plays a key role in producing excited argon molecules. Diatomic argon excimers can decay non-radiatively to the lowest excited electronic energy level with the lowest vibrational energy, which don't have other significant decay channels than photon emission. The relaxation from this state to the continuously repulsive electronic ground state produces photons with a continuous spectrum, which is usually known as the second continuum. The emitted photons are in the vacuum ultraviolet (VUV) region with a wavelength around 128 nm, and this energy is below the lowest atomic energy level of argon atoms. This offset in energy is a result of the released binding energy and the elevated ground state energy, both rising from the contracted internuclear distance in the diatomic molecules. Because the internuclear distance changes with density and temperature, the second continuum peak position varies with experimental conditions [84].

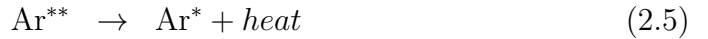
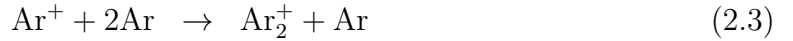
The lowest electronic energy level of diatomic argon can have two spin states: a spin singlet state  $^1\Sigma_u$  and a spin triplet state  $^3\Sigma_u$ . The energies of the two states are very close and can not be resolved in the emitted light due to the spread in the repulsive ground state. The singlet state decays (E1 transition, allowed) quickly to the ground state, and the lifetime is measured to be around 6-7 ns. The decay of the

triplet state to the ground state (M1 transition, hindered) is nominally “forbidden” by spin selection rules, but can happen at a much larger time scale. The triplet lifetime is reported to be  $\sim 1.6 \mu\text{s}$  in liquid argon [86] and  $\sim 3.2 \mu\text{s}$  in gaseous argon at 1 atmospheric pressure [87]. The two decay components are usually referred to as the fast component and the slow component, and they make up most of the argon scintillation light.

To sum up, the covalent bond formation and the scintillation process for argon excitations can be expressed as



As for argon ionizations, the electrons have to first thermalize and recombine with the ions to produce argon excitations



These processes are illustrated in Fig. 2.1 [83]. (1) Ground state atom is excited to the exciton band; (2) exciton self-traps to form dimer in the lowest electronic energy level; (3) ground state atom is excited to the conduction band; (4) conduction state captures electron and form exciton state; (5) formation of self-trapped diatomic ions; (6) diatomic ion captures an electron to form dimer; (7) ultraviolet photon emission; (8) the two atoms in the ground state fly apart. Since both excitation and ionization can be produced by charged particles in argon, the argon scintillation light includes contributions from both the excitation band and the conduction band. The ratio of

excitation to ionization has been estimated to be  $\sim 0.2$  in liquid argon, which was confirmed by a series of measurements [82].

In low density argon gas, inefficient argon atom collision could lead to photon emission from high vibrational states of the lowest electronic energy level in biatomic argon molecules, and give rise to the first continuum, with an wavelength around 110 nm [87]. In high pressure gas or in the condensed phases, excited diatomic molecules quickly relax to the lowest vibrational states and the second continuum dominates the emission spectrum. We comment that a third continuum emission is also reported in argon gas excited by heavy ions [88]. The wavelength is measured to be around 200 nm and the lifetime ranges from nanoseconds to hundred nanoseconds depending on the gas pressure.

### 2.1.2 The Scintillation Quenching Effects

Although argon has a high scintillation efficiency, the observed light yield values are subject to various factors including the linear energy transfer(LET), the electric field, and the impurity level. These factors can act in different stages of the scintillation process and may quench the scintillation light output.

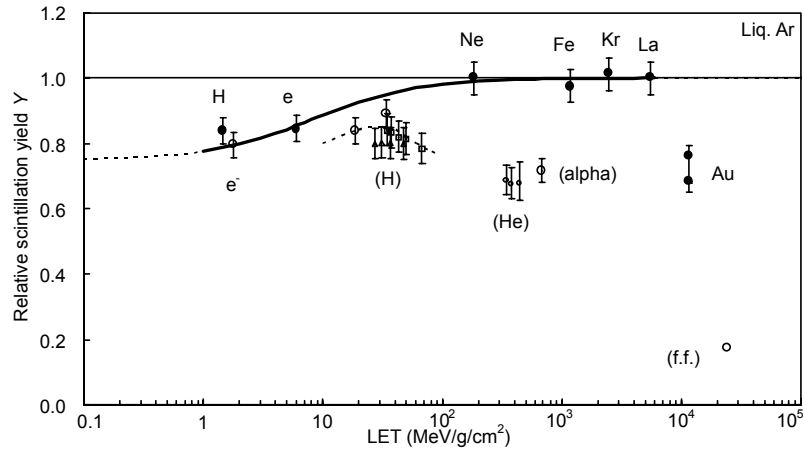


Figure 2.2: The relative light yield of liquid argon with different ionizing particles [82]; closed markers stand for relativistic particles and open ones show non-relativistic particles.

The scintillation efficiency of liquid argon has been studied with many ionizing particles. Fig. 2.2 shows a summary of the relative light yield values, where the closed markers show the measurements with relativistic particles and the open markers represent that for non-relativistic ones [82]. The highest light yield is achieved with relativistic ions of medium mass and is scaled to unit. Relativistic and non-relativistic electrons, which are commonly used in the energy calibration of argon detectors, have a relative light yield of  $\sim 80\%$ . Alpha particles, as that from radioactive alpha decays, have a relative scintillation efficiency of  $\sim 70\%$ , slightly lower than electrons. The scintillation of fission fragments is highly quenched, with an efficiency approximately 20% of that of heavy relativistic particles.

The light yield dependence on the LET value can be partially explained by the recombination efficiency of argon ions with ionization electrons. As is discussed in Sec. 2.1.1, the number of argon excitation produced by charged particles is only  $\sim 20\%$  of that of ionizations, so a large fraction of the scintillation light is resulted from recombined ionizations. In low LET tracks such as that of electrons and protons, the ionization electrons may travel too far away from their associated ions as they scatter and thermalize; as a result they can escape the (geminate) recombination process. In high ionization tracks, on the contrary, the electrons may combine with other ions (homogeneous recombination) and make scintillation light. The thermalization time of ionization electrons can be as large as  $\sim 0.9$  ns in liquid argon [89], and they can travel up to a few microns before reaching thermal energy [82].

The hypothesis of argon scintillation loss due to inefficient recombination can be tested by combining the scintillation signals with the ionization signals. The amplitudes of the combined scintillation-ionization signals for some particles are summarized in Fig. 2.3 [82]. Compared to Fig. 2.2, Fig. 2.3 the electron and proton measurements now have a consistent value, which confirms the competition between the scintillation process and residual ionization signals. We comment that for two phase



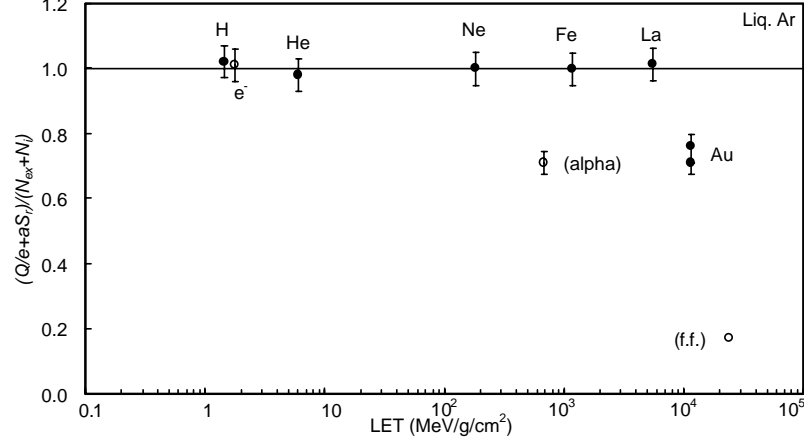


Figure 2.3: The combined scintillation yield and ionization yield in liquid argon [82].

argon Time Projection Chambers (TPCs), the collection of ionization signals using an electric field would lead to the loss of scintillation light yield. In the DarkSide-10 detector, the measured light yield for electron recoil events dropped by a factor of  $\sim 2$  at a drift field of 1 kV/cm.

However, the low light yield values for alpha particles, Au ions and fission fragments remain unexplained. Another hypothesis, called the bi-excitonic quenching effect, was developed to address this problem [90]. This theory predicts that in cases of very high ionization density, free argon excitons may diffuse and collide before bi-atomic excitons are formed.



In this process, two argon excitons are quenched into one<sup>2</sup>; the remaining energy is carried away by the free electron, and is subsequently lost into heat by collision with argon atoms. This bi-excitonic collision process can take place in the core of high ionization tracks (also in the penumbra region for extremely high ionization tracks like that of fission fragments, but not always), and causes the light yield to drop. For

<sup>2</sup>The excitation energy of argon is very close to the ionization energy.

particle tracks with the same LET value, the energy partitions between the core and the penumbra may be different, and this explains the reason why the light yield is not a simple function of LET.

The ionizing particle specie not only affects the light yield, but also determines the relative intensity between the fast and slow argon scintillation components. The fast to slow scintillation ratio has been measured to be for  $\sim 0.3$ ,  $\sim 1.3$  and  $\sim 3$  for  $^{207}\text{Bi}$  electrons,  $^{210}\text{Po}$  and  $^{252}\text{Cf}$  alphas, and  $^{252}\text{Cf}$  fission fragments respectively [86]. This trend is opposite to that of organic scintillators, which typically have larger triplet component for heavier ionizations. The spin relaxation time of thermal electrons is usually estimated to be much larger than the recombination time, and thus the total spin of the electron-ion pair is conserved. In this scenario, the spur recombination model predicts that singlet formation is preferred in low ionization tracks, while the singlet and triplet ratio in heavy ionization tracks would approach the statistical value of 1:3 because electrons and ions can recombine randomly [91]. This theory obviously doesn't explain the case for argon scintillations.

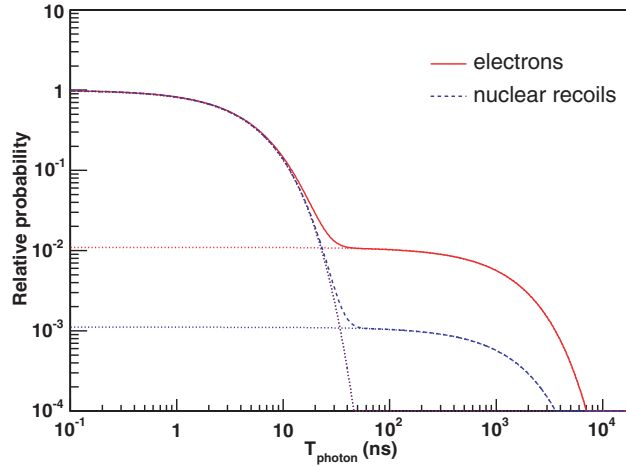


Figure 2.4: The scintillation waveform of electron recoils and nuclear recoils in liquid argon [92]; the dotted lines show the singlet and triplet components.

Fig. 2.4 shows the liquid argon scintillation waveforms excited by electrons and by fission fragments, which are normalized to have equal amplitudes of the fast com-

ponent. In an argon-based dark matter detector, the expected nuclear recoil signals induced by WIMP collisions would have a fission fragment signature, while the prevailing gamma ray and  $^{39}\text{Ar}$  backgrounds would produce electron recoil waveforms. The big difference in the scintillation waveforms offers the possibility of pulse shape discrimination to reject electron recoil backgrounds in dark matter searches. The background discrimination power has been predicted to be  $10^8$  or higher [92], which lays the foundation for argon-based dark matter searches.

The exponential decay lifetimes of the two states, however, are observed to not vary with the particle species. The values are measured to be  $\sim 7\text{ ns}$  for the fast (singlet) component and  $\sim 1.6\text{ }\mu\text{s}$  for the slow (triplet) component in liquid argon ( $\sim 3.2\text{ }\mu\text{s}$  in gaseous argon). The constant lifetime values indicate that the process to form singlet and triplet dimer spin states completes at a time scale smaller than the fast component lifetime. Otherwise, if the spin states can be created or altered as the photon emission process goes on, the exponential shape of the two components may be biased and the observed lifetime value may vary. A plausible process to explain the abnormal spin state statistics is the super-elastic scattering between argon excimers and thermalized electrons [86, 93].

$$^1\Sigma_u + e^- \rightarrow ^3\Sigma_u + e^- \quad (2.7)$$

This process can convert an argon excimer in the singlet state into the triplet state and thus enhance the triplet scintillation. The recombination time for low ionization tracks as that for electrons is relatively long, so the super-elastic collision of thermalized electrons is enhanced and the triplet component is boosted.

In addition to the argon exciton quenching and argon dimer quenching processes, the presence of certain impurities in argon can also quench the scintillation light output. Ideally pure argon is transparent to its scintillation light because the scintil-

lation energy of the second continuum light is below the atomic energy level; however, the absorption spectrum of some impurities such as water and oxygen may overlap with the scintillation spectrum of argon and absorb the scintillation light. In addition, electronegative impurities like nitrogen [94] and oxygen may undergo destructive collision with the argon excimers and cause non-radiative relaxations to the ground state. Therefore, the number density of argon excimers would undergo a faster decay compared to the case of no electronegative impurities.

$$\frac{d [\text{Ar}_2^*]}{dt} = -\left(\frac{1}{\tau} + F([X])\right)[\text{Ar}_2^*] \quad (2.8)$$

where  $[\text{Ar}_2^*]$  is the concentration of argon excimers,  $\tau$  is the lifetime of the argon excimer states without impurity, and  $F([X])$  is the quenching probability for an impurity level of  $[X]$  [95]. This is equivalent to an effective lifetime of  $1/\tau' = 1/\tau + F([X])$ , or  $\tau' = \tau/(1 + F([X])\tau)$ , which indicates that the observed lifetime of argon scintillation would decrease as the impurity level increases. The fraction of light loss (non-radiative argon excimer relaxation) is  $F([X])\tau$ .

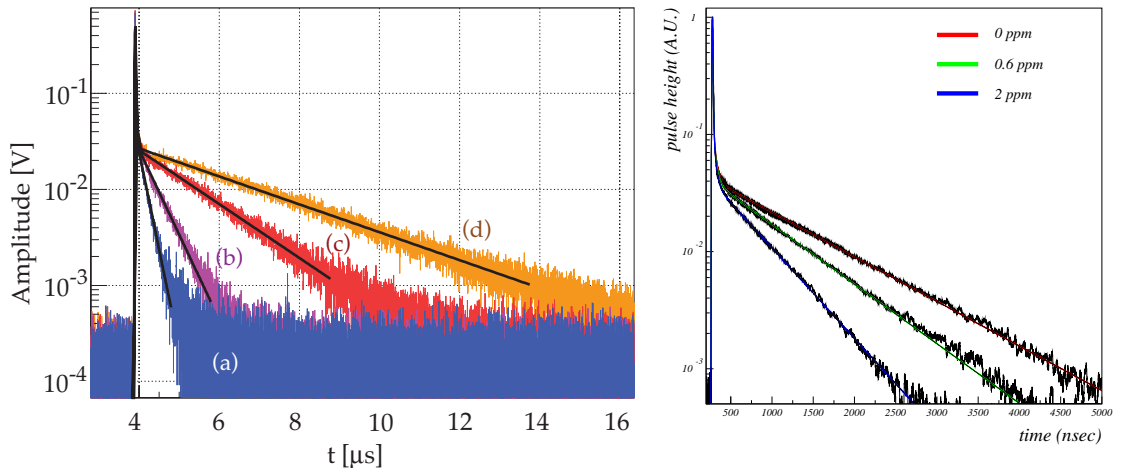


Figure 2.5: Average argon scintillation waveforms with different levels of contaminants. Left: air contaminants in gaseous argon, (a)  $10^{-2}$  mbar, (b)  $10^{-3}$  mbar, (c)  $10^{-4}$  mbar, (d)  $10^{-5}$  mbar. [96]; Right: oxygen contaminant in liquid argon [95].

This quenching effect has been studied by introducing controlled amount of elec-

tronegative impurities into gaseous argon [96] and liquid argon [97]. The averaged scintillation waveforms with different levels of contaminants are shown in Fig. 2.5. The loss of lifetime and scintillation light is minimal in the fast component of argon scintillation due to the small value of  $F([X])\tau$ , while the quenching effect of the slow component is dramatic. Therefore, the slow component lifetime of argon scintillation can be used to monitor the argon purity, and its value can be used to correct the light yield loss. We comment that in a two phase argon Time Projection Chamber (TPC) the ionization electrons can also be captured by electronegative impurities, so it is critical for an argon-based detector to achieve a high purity level.

## 2.2 Argon-Based Dark Matter Detectors

Because of the excellent properties of argon, it is used, or to be used, in many rare-event detection experiments including dark matter searches. Some experiments rely on the argon scintillation signals to reconstruct physical events, some collect the ionization signals in Time Projection Chambers (TPCs), and others may combine both scintillation and ionization for an analysis.

The ICARUS experiment [98], although it is not a dark matter experiment, has made great contribution to the noble liquid technology that is currently used in many direct dark matter search experiments. ICARUS aims to detect solar neutrinos, atmospheric neutrinos, supernovae neutrinos, and accelerator neutrinos via various neutrino interactions with argon atoms. When ionization tracks are produced by neutrino induced interactions in the liquid argon volume, the residual ionization electrons that escape the recombination process are drifted towards the anode by an uniform electric field<sup>3</sup>. The drifted charge signals are then collected by parallel wire planes with different orientations to get comprehensive projections of the ionization tracks. The track information of ionization density, particle range, and event position can be extracted

---

<sup>3</sup>The electric field also prevents some electrons to be recombined.

and used for event identifications. The argon scintillation signals are also detected by WLS-coated PMTs to produce a start signal used in drift time calculations. The ICARUS T600 detector, which has a sensitive mass of 500 tons of liquid argon, is the the largest LAr-TPC ever built; it has been in operation in the Laboratori Nazionali del Gran Sasso (LNGS) laboratory since 2010.

The WIMP Argon Project (WArP) [59] uses a two-phase argon TPC to detect elastic WIMP collisions with argon atoms. The WArP detector takes a new TPC design and collects both the scintillation and ionization signals using photomultiplier tubes (PMTs). Similar to ICARUS, an electric field is used to drift the ionization electrons towards the TPC anode, where, on the contrary, a thin layer of argon gas is maintained to amplify the ionization signals. The ionization electrons are first extracted into the gas by a strong electric field, and then are accelerated to collide with argon atoms and create scintillation light. The distribution of the secondary scintillation light across the PMT array is used to reconstruct the x-y position of the primary ionizations, while the time interval between the scintillation and ionization signals tells the z position of the event. Because the argon scintillation light is in the Vacuum UltraViolet (VUV) region, a wavelength shifting flour, TetraPhenyl Butadiene (TPB), is coated on the reflector and on the PMT windows to convert the light into the visible region. Both the scintillation and ionization signals are used for energy estimation and event identifications. A 2.3 L prototype TPC [99] was operated at LNGS and provided important R&D studies on the argon scintillation properties and the scintillation-to-ionization discrimination method. A 100 L detector with an active argon veto system was also constructed in LNGS, but the project was discontinued due to technical issues.

The DarkSide experiment [100] shares the fundamental principles with WArP, but uses more innovative techniques to further suppress the backgrounds. For example, the DarkSide detector is going to use low- $^{39}\text{Ar}$  argon as the detection medium, which

is critical for ton-scale TPC-type dark matter detectors such as the DarkSide-G2 detector to operate without serious pile-up. The DarkSide experiment implements a liquid scintillator detector to efficiently detect neutrons, which are the most dangerous backgrounds in direct dark matter detection, and also a water Cherenkov detector surrounding the scintillator veto to tag cosmic ray events. In addition, extraordinarily low radioactivity cryogenic PMTs are under development with a collaborative effort between the DarkSide collaboration and the Hamamatsu Corp, Japan. The DarkSide experiment will be discussed in detail in Sec. 2.4.

ArDM [101] is another double phase argon TPC that collects both the scintillation and ionization signals from WIMP induced argon nuclear recoils. But different from WArP and DarkSide, ArDM extracts the ionization electrons into the gas phase and collects them with Large Electron Multiplier (LEM) detectors. The LEM units are expected to amplify the electron signal by  $\sim 4$  orders of magnitude, and are sensitive to position, allowing the primary ionization position to be estimated. As for the scintillation signal collection, the wavelength shifter TPB is coated on the inner surface of the reflectors and also on the PMT window to enhance light collection; due to the installation of LEM detectors in the top of the detector, the scintillation light is only collected by PMTs at the bottom. A 3L prototype detector has been constructed and tested, and a 1 ton dark matter detector is under development.

The DEAP/CLEAN experiments [102, 103] take a single phase design and only collect the liquid argon/neon scintillation light produced by WIMP interactions. Both experiments build detectors with a spherical sensitive volume viewed in  $4\pi$  by PMTs and WLS-coated reflectors, and will use the pulse shape discrimination method to reject electron recoil backgrounds. Based on the study with a 7 kg prototype DEAP detector, a 3,600 kg detector is being developed by the DEAP collaboration and will commission soon, expecting a WIMP sensitivity as low as  $10^{-46} \text{ cm}^2$ . The CLEAN experiment also plans to switch to liquid neon target for background measurement in

addition to operating with liquid argon target for dark matter detection. The estimated WIMP interaction rate with neon is approximately 5 times lower than that of argon above a certain energy threshold, so by changing the target materials the WIMP interaction channels could be effectively “switched on or off”. The MiniCLEAN detector will host 500 kg of liquid argon in its sensitive volume, and a water shielding will be installed to function as an active veto system. The projected sensitivity is at the level of  $10^{-45} \text{ cm}^2$ , and a ton scale CLEAN detector is under consideration.

Besides the dark matter detectors, many neutrino detection experiments like ICARUS also use, or plan to use, liquid argon technology, like LBNE [104], LArTPC [105], Glacier [106], ArgoNeuT [107], and microBooNE [108]. The readers are referred to the references for detailed information about these argon-based experiments.

## 2.3 Discovery of Underground Argon

### 2.3.1 The $^{39}\text{Ar}$ Problem

As has been discussed, argon is a promising target for direct dark matter detection experiments. It has high scintillation light yield and exhibits an extraordinarily high discrimination power between WIMP induced nuclear recoils and electron recoil backgrounds. In addition, as required by modern dark matter searches, argon-based particle detection technology can be scaled to large masses, and more importantly, large quantities of high purity argon are commercially available at low costs. Argon makes up approximately 1% of the atmosphere and can be extracted and purified industrially by liquid air distillation techniques.

Argon-based dark matter experiments, however, must confront the presence of the intrinsic  $^{39}\text{Ar}$  background. The  $^{39}\text{Ar}$  isotope is a beta emitter with an endpoint



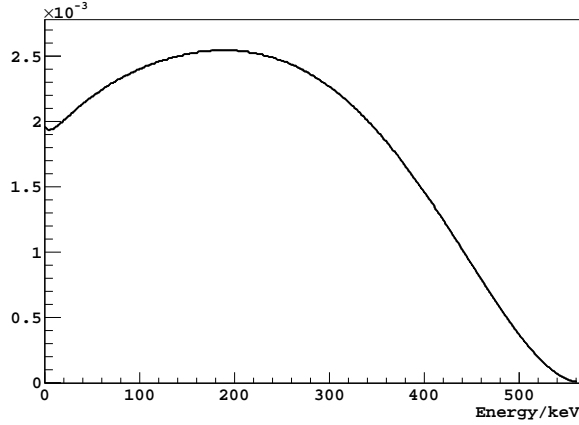
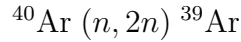


Figure 2.6: The  $^{39}\text{Ar}$  decay electron energy spectrum; data from LBNL.

energy of 565 keV and half life of 269 yr.



The decay electron energy spectrum is shown in Fig. 2.6.  $^{39}\text{Ar}$  is present at an activity of  $\sim 1$  Bq/kg in commercial argon derived from the atmosphere; the corresponding isotope abundance ratio is  $^{39}\text{Ar}/^{40}\text{Ar} \sim 8 \times 10^{-16}$  [109]. As  $^{39}\text{Ar}$  decays in the atmosphere, its concentration is maintained at a stable level by cosmogenic neutron activation on the stable argon isotope  $^{40}\text{Ar}$ .



Human activities, such as nuclear bomb tests and nuclear power plants, also contribute to the production of  $^{39}\text{Ar}$ , but this contribution is estimated to be relatively small compared to the cosmogenic. The  $^{39}\text{Ar}$  activity in pre-nuclear age samples has been compared to that in modern air and an upper limit of 5% was set on the relative abundance of anthropogenic  $^{39}\text{Ar}$  activity in the atmosphere [110].

Although the relative  $^{39}\text{Ar}$  abundance of  $\sim 8 \times 10^{-16}$  appears small, the background due to  $^{39}\text{Ar}$  decay electrons in a large scale detector using atmospheric argon can be

enormous. For example, the  $^{39}\text{Ar}$  decay rate in a 1 ton of atmospheric argon is approximately  $3 \times 10^{10}$  in one year. Meanwhile, the expected WIMP induced signal rate is at the level of 10/ton/yr above a 20 keV energy threshold, assuming that the dark matter density of  $\sim 0.3 \text{ GeV}/\text{cm}^3$  in the Earth's neighborhood can be attributed to 100 GeV mass WIMPs, and we have assumed that the WIMP-nucleon elastic scattering cross section is  $10^{-45} \text{ cm}^2$  [30]; This estimate leads to a signal-to-background ratio close to  $10^{-10}$  and challenges argon-based direct dark matter searches.

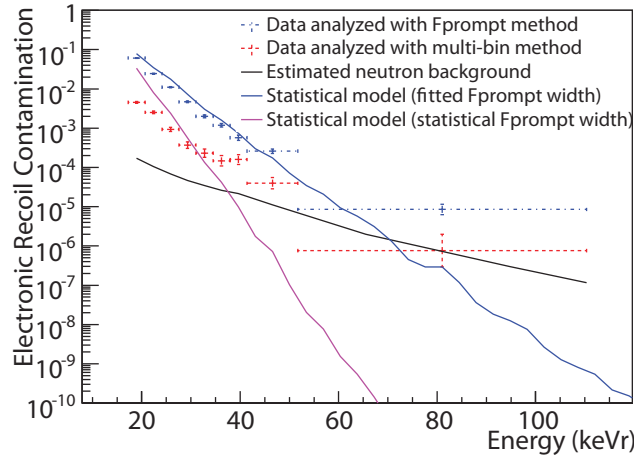


Figure 2.7: The probability of misidentifying an electron recoil as nuclear recoil in the pulse shape discrimination, measurement by the microCLEAN experiment [111].

The pulse shape discrimination of argon scintillation has the potential to suppress the  $^{39}\text{Ar}$  background rate within a certain energy window to a very low level [92]. However, the power of the pulse shape discrimination method decreases dramatically at low energies, as illustrated in Fig. 2.7 [111]; meanwhile, the expected WIMP events are highly populated in the low energy windows (exponential-like spectral shapes). As a result, the WIMP sensitivity of argon-based dark matter detectors is compromised due to the presence of the  $^{39}\text{Ar}$  backgrounds. Tab. 2.1 shows the reported/expected energy thresholds of different dark matter experiments, where we can see argon detectors typically have high energy threshold values.

Detection Technology	Experiment	Energy Threshold
Germanium Bolometer	CDMS [48]	$\sim 10 \text{ keVr}$ <sup>4</sup>
	CoGeNT [44]	$0.4 \text{ keV}_{ee} \sim 2 \text{ keVr}$ <sup>5</sup>
NaI Crystal	DAMA [38]	$2 \text{ keV}_{ee} \sim 7 \text{ keVr}$ <sup>6</sup>
CaWO <sub>4</sub> Crystal	CRESST [56]	$\sim 12 \text{ keVr}$ <sup>7</sup>
Noble Liquid	Xenon [112]	$\sim 2 \text{ keV}_{ee}, \sim 7 \text{ keVr}$
	ArDM [101]	$30 \text{ keV}_{ee} \sim 100 \text{ keVr}$ <sup>8</sup>
	DEAP [102]	$20 \text{ keV}_{ee} \sim 70 \text{ keVr}$

Table 2.1: The reported/expected energy thresholds of a few dark matter experiments.

An additional approach to seek a higher background rejection power is to collect the ionization signals (using time projection chambers) and take advantage of the scintillation-to-ionization discrimination method. This method is expected to yield an electron recoil background rejection power of 10-100 in addition to the pulse shape discrimination. Unfortunately, the  $^{39}\text{Ar}$  activity in atmospheric argon also restricts the ultimate size of argon TPC detectors. A TPC uses an electric field to drift and collect the ionization electrons; the drift velocity in liquid argon at a medium field of a few kV/cm is a few millimeters per microsecond [113], so the drift time is a ton scale detector ( $\sim 1 \text{ m}$  dimension) is estimated to be  $\sim 500 \mu\text{s}$ . At an  $^{39}\text{Ar}$  activity of  $\sim 1 \text{ Bq/kg}$ , the expected  $^{39}\text{Ar}$  rate in such a detector would be  $\sim 1000 \text{ Hz}$ , which means  $\sim 50\%$  of the  $\sim 500 \mu\text{s}$  electron drift windows would contain one or more  $^{39}\text{Ar}$  decay signals. This “pile-up” problem is expected to cause a serious dead time issue and also other difficulties in such experiments, and thus restricts the size of argon-based TPC detector to below  $\sim 1 \text{ ton}$ .

---

<sup>4</sup>The CDMS experiment uses an energy threshold of  $10 \text{ keVr}$  in their dark matter analysis, but also did a  $2 \text{ keVr}$  low threshold analysis to cross check with CoGeNT and DAMA [50].

<sup>5</sup>The  $2 \text{ keVr}$  value of the CoGeNT threshold is estimated from the CDMS values.

<sup>6</sup>The nuclear quenching factors of NaI(Tl) are 0.3 and 0.09 for Na and I respectively [35].

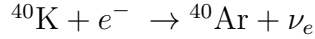
<sup>7</sup>The nuclear quenching factors in CaWO<sub>4</sub> crystal are reported to be 0.1, 0.06, 0.04 for O, Ca, and W respectively [56].

<sup>8</sup>We use a nuclear quenching factor of 0.29 to estimate the nuclear recoil energy based on electron recoil energy for argon scintillation detectors [111].

### 2.3.2 Search for low- $^{39}\text{Ar}$ Argon underground

The  $^{39}\text{Ar}$  problem in dark matter searches can be mitigated if argon with low  $^{39}\text{Ar}$  content is available at large quantities. Two traditional methods have been established for isotope separation: centrifugation and thermal diffusion [114]. However, both approaches become prohibitively expensive and time-consuming on a multi-ton scale. We have pursued naturally occurring sources of low  $^{39}\text{Ar}$  argon instead.

Most of the stable argon isotope  $^{40}\text{Ar}$  in the Earth's atmosphere was produced by the electron capture decay of the long-lived  $^{40}\text{K}$  nuclide present in natural potassium within the bulk earth, which then emerged to the Earth surface.



It has been estimated that the atmosphere contains approximately half of the  $^{40}\text{Ar}$  that has been produced by  $^{40}\text{K}$  decays since the Earth's accretion [115], while the rest is still present underground and can be found in gas wells at useful concentrations. The argon at underground sites is also shielded from cosmic rays, which are primarily responsible for the  $^{39}\text{Ar}$  production in the atmosphere. Therefore, it is expected that argon from underground sources may have a low  $^{39}\text{Ar}$  radioactivity.

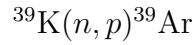
Argon samples extracted from ground water at a number of locations have been studied [110, 116]. In some cases the  $^{39}\text{Ar}$  activity was measured to be very low ( $<5\%$  atmospheric), and some were comparable to the atmospheric value, while others contain significantly more  $^{39}\text{Ar}$  (up to 16 times higher) than that in the atmosphere. A compilation of the measurements are shown in Tab. 2.2. The specific  $^{39}\text{Ar}$  activity is observed to vary dramatically from location to location, and the aquifer types also play an important role.

The large variation of the  $^{39}\text{Ar}$  activity in the underground argon samples indi-

Location	Aquifer	Sample	$^{39}\text{Ar}$ ‰modern
Stripa mine, Sweden	Granite	Borehole N1	1600
		Borehole V1	330
Augraben, Germany	Karstic	-	61
Krautbuckel, Germany	Karstic	-	31
Buscheletten, Germany	Karstic	1	<6.8
		2	<4.7
Lincoln, UK	Triassic sandstone	5 samples	< 5
		3 samples	55-95
Zurzach, Switzerland	Granite	1 (1976)	375
		2 (1976)	380

Table 2.2: The  $^{39}\text{Ar}$  activity in argon samples extracted from ground water [110,116].

cates that significant  $^{39}\text{Ar}$  production is present under the Earth’s surface. Ref. [117] estimates that  $^{39}\text{Ar}$  can be efficiently produced by the stopped muon capture process on  $^{39}\text{K}$  at shallow depths, although the hadronic component of cosmic rays is heavily attenuated; the relative  $^{39}\text{Ar}$  concentration from shallow underground sites could be up to 100 times higher than the atmospheric value. At large depth ( $>1,800$  m.w.e.), the muon flux is highly reduced, and the production of  $^{39}\text{Ar}$  from the (n, p) reaction on stable potassium dominates [116,118].



Neutrons at deep underground locations are produced mainly by radioactivities of primordial U and Th<sup>9</sup>. U and Th can produce neutrons in two ways: 1) alpha decays from the U, Th chains can produce neutrons by the ( $\alpha$ , n) reactions on light nuclei, and 2) spontaneous fission decay of U and other heavy nuclide. For typical crust compositions [34], it is estimated that approximately 4,500 ( $\alpha$ , n) neutrons ( $\sim 1,500$  from U chain and 3,000 from Th chain, both assuming chain secular equilibriums) are produced in 1 kg of crustal rock per year [120], and the spontaneous fission process

---

<sup>9</sup>The cosmic ray muon spallation on heavy nuclei is more important at shallow depth ( $<100$ ) [119]

of U contributes another  $\sim 700$  neutrons/kg/yr. It has been estimated that the  $^{39}\text{Ar}$  concentration in argon of deep crustal origin could be lower than the atmospheric value by from a few times to a few hundred times [117].

Due to the underground production of  $^{39}\text{Ar}$  the search for low- $^{39}\text{Ar}$  argon was very difficult. We studied the argon samples extracted from several gas fields, of which the National Helium Reserve was found to be a promising source [121]. The crude helium gas at this site was separated in the production of natural gas and contained argon in a relatively pure state. The argon component was then extracted from this crude gas with a zeolite gas separation system in Princeton University, as will be discussed in Sec. 3.3.1. The  $^{39}\text{Ar}$  activity in the purified gas was measured with a low background gas counter in the Bern University, Switzerland, and no evidence of  $^{39}\text{Ar}$  was reported at a detection sensitivity of 5% atmospheric [122]. For technical reasons, however, air was used to burn residual methane and hydrogen in the crude helium production plant, and in doing so, the underground argon was subject to contamination of  $^{39}\text{Ar}$  from the atmosphere. The crude helium would have to be purified directly to avoid air contact. Because of this complication, the National Helium Reserve was not pursued.

Compared to the Earth's crust, which has uranium and thorium at ppm levels, the Earth's mantle is expected to contain these elements at the ppb level, as compared in Tab. 2.3 [34, 123]. As a result the neutron flux from the  $(\alpha, n)$  process would be greatly reduced<sup>10</sup>; the neutron yield of average mantle rock is estimated to be 30 n/kg/yr, which is more than two orders of magnitude lower than the crust values.

The  $^{39}\text{Ar}$  production rate from the  $(n, p)$  process is determined by the neutron flux, and thus by the concentration of alpha emitters (uranium and thorium), as well

---

<sup>10</sup>The composition of the light elements does not differ by orders of magnitude in the crust and in the mantle.

Element	Continental Crust	Earth Mantle
U	1.7 ppm	8ppb
Th	8.5ppm	29ppb
K	2.14%	550ppm

Table 2.3: Concentrations of radioactive elements in the Earth’s crust and mantle [34,123].

as by the potassium concentration,

$$[^{39}\text{Ar}] \propto \Phi(n) \times [\text{K}] \propto \{[\text{U}], [\text{Th}]\} \times [\text{K}]$$

whereas production rate of  $^{40}\text{Ar}$  only depends on the potassium concentration.

$$[^{40}\text{Ar}] \propto [\text{K}]$$

Therefore, the relative  $^{39}\text{Ar}$  isotope abundance highly depends on the concentration of the alpha emitters uranium and thorium,

$$\frac{[^{39}\text{Ar}]}{[^{40}\text{Ar}]} \propto \Phi(n) \propto \{[\text{U}], [\text{Th}]\}$$

and it should be 2-3 orders of magnitude lower for mantle gas compared to deep crustal gas. Combining with the previous analysis for crustal gas, it is expected that the mantle argon could have an  $^{39}\text{Ar}$  concentration 1,000 lower than that of the atmospheric argon.

Based on helium, neon, argon, krypton and xenon measurements, the gas in the CO<sub>2</sub> gas fields in the US southwest is believed to be derived from the Earths upper mantle [124–126]; these fields should therefore be a good source of argon low in  $^{39}\text{Ar}$ . Argon samples from the Reliant Dry Ice facility on the Bravo Dome CO<sub>2</sub> gas field in Bueyeros, New Mexico were investigated. First samples showed no evidence of  $^{39}\text{Ar}$ , but later measurements yielded increased  $^{39}\text{Ar}$  levels, possibly due to the decrease

in well pressure as the CO<sub>2</sub> deposit at that site was consumed. The Kinder Morgan CO<sub>2</sub> extraction facility in Cortez, Colorado, was then studied and has been shown to be a reliable source of argon with low <sup>39</sup>Ar radioactivities.

### 2.3.3 Argon Collection from Underground Sources

The concentrations of argon in the underground gas streams range from tens of ppm to hundreds of ppm, and it has to be enriched for any practical use. The low concentration levels also require large quantities of crude gas to be processed, and industrial scale processing plants have to be used.

A Pressure Swing Adsorption (PSA) plant was developed by the Princeton group at the Kinder Morgan CO<sub>2</sub> plant in Cortez, Colorado to concentrate the argon content in the crude CO<sub>2</sub> gas [127]. A PSA system uses an adsorbent material to separate a certain gas specie from a gas mixture based on the gas's affinity for the adsorbent. When the adsorbent bed is in contact with the gas mixture, it selectively retains a certain gas specie. After the adsorbent reaches its maximum retaining capacity it can be regenerated by lowering the absorbed specie's partial pressure and the adsorbed gas will be released. If two adsorption units are operated 180 degrees out of phase, the regeneration of one unit and the adsorption processes of the other unit can take place in parallel, so a near-continuous gas production can be realized. A schematic of such a PSA cycle is shown in Fig. 2.8 [128].

A PSA system is also called a VPSA system if it uses (partial) vacuum for the adsorbent to release the withheld gas. The VPSA plant used for the argon extraction operates with a pressure of ~23 psia for gas processing and a partial vacuum of ~30 - 50 mbar absolute for adsorbent bed regeneration. The system consists of two stages in series, with each stage composed of two adsorption columns operated 180° out of phase. The first stage is to remove CO<sub>2</sub> that dominates the input gas stream, and the adsorbent, zeolite NaX, has a high selectivity for CO<sub>2</sub> over argon. The output gas



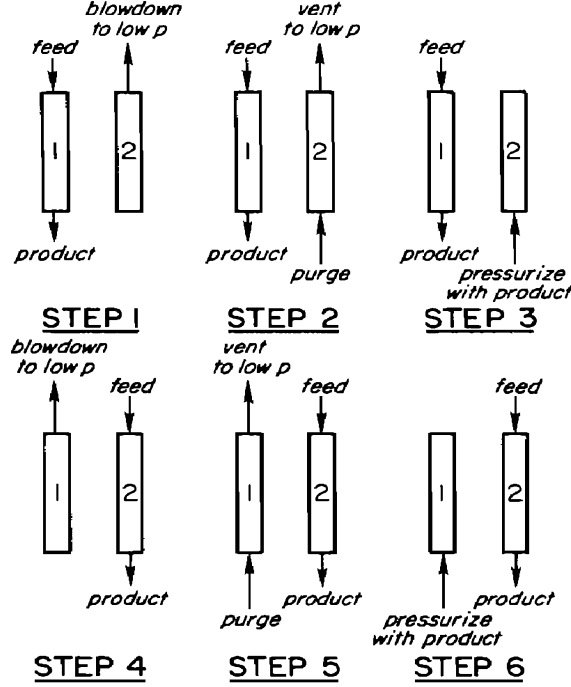


Figure 2.8: An illustration of the operating cycle of a two-bed PSA processing unit [128]. Gas processing in one column and regeneration of the other column are in parallel.

stream from the first stage is enriched in argon, but is dominated by  $N_2$ . This gas is then stored a buffer tank at  $\sim 40$  psig before being processed in the next stage. The second VPSA unit utilizes zeolite Li-LSX as the absorbent, which exhibits optimal selectivity for nitrogen over argon, in order to remove the nitrogen content.

The argon concentration can be increased to  $\sim 5\%$  in the VPSA product gas stream from the original value of 600 ppm. Helium is the dominant contamination because it doesn't get suppressed in either stage of the plant; nitrogen is the next dominant although it has been strongly reduced. A summary of the gas concentrations can be found in Tab. 2.4. The VPSA plant has a processing capacity of 0.5 kg argon per day, and as of early 2013, more than 135 kg of underground argon has been collected from the Kinder Morgan plant at Cortez, CO. This gas will be used in the DarkSide-50 dark matter detector, which will be the first argon-based dark matter detector utilizing low- $^{39}\text{Ar}$  activity argon.

Gas Specie	Original Concentration	VPSA Output	Distillation Output
CO <sub>2</sub>	96%	~0	~0
N <sub>2</sub>	2.4%	40%	~1,000 ppm
He	4,300 ppm	55%	~0
Ar	600 ppm	5%	99.9%

Table 2.4: The composition of the underground argon gas at each purification stage.

The helium and nitrogen content of the collected underground argon gas was then suppressed using a cryogenic fractional distillation column [129] constructed at Fermilab, Chicago, IL. A distillation column uses the differences in the liquids' volatilities to separate a certain component from a liquid mixture. The temperature in a distillation column is tuned to boil off the liquid mixture at the bottom (re-boiler), and to condense the vapor at the top (condenser). The vapor created at the liquid-gas interface consists of that of each components<sup>11</sup>, but as it ascends, the less volatile components preferably get condensed and the concentrations of the more volatile components increase with height. A distillation column can be divided to many stages by installing condensing plates, where the less volatile gas condenses and the released heat will re-vaporize the condensed more volatile liquids. As this process goes on, the vapor on the top would eventually consists solely of the most volatile component, while the liquid at the bottom mainly contains the least volatile component. Therefore, the separation of the liquid mixture is realized.

The cryogenic distillation column in our underground argon purification system is illustrated in Fig. 2.9. It consists of a 318 cm long stainless steel tube filled with a packing material (Sulzer Chemtech, EX Laboratory Packing), making it equivalent to 58 distillation stages. The whole system is contained in a double wall cryostat, and the thermal gradient is maintained by a cryocooler at the top and a heater at the bottom. The crude argon gas from the VPSA plant is liquified by another cryocooler

---

<sup>11</sup>The vapor composition is determined by the Raoult's law in the ideal case.

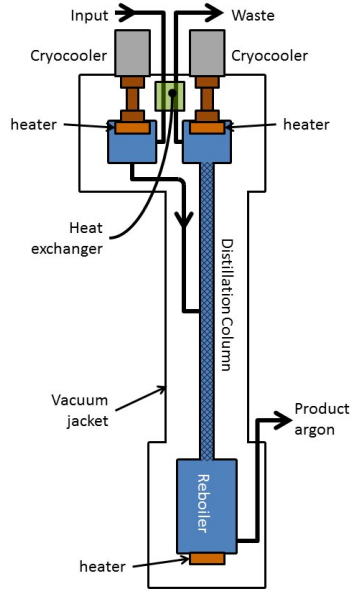


Figure 2.9: A schematic of the cryogenic distillation column used for argon purification.

before being injected into the distillation column; the product argon is collected at the re-boiler at the bottom and the nitrogen and helium are exhausted at the top. This system can be operated in two modes: the continuous mode and the batch mode. In the continuous mode a steady gas flow is fed into the column and a high processing capacity is obtained, while in the batch mode the input flow is turned off, so a high purity can be achieved through iterative distillations.

The distillation system is capable of reducing the nitrogen content in the crude argon by more than 3 orders of magnitude and reducing helium by more than 5 orders of magnitude. The collection efficiency of argon is estimated to be  $\sim 70\text{-}80\%$ . The processing capacity is approximately 1 kg of argon product per day, which matches the argon production rate in Cortez, CO.

### 2.3.4 Early $^{39}\text{Ar}$ Activity Measurements

During the search for low- $^{39}\text{Ar}$  argon, the  $^{39}\text{Ar}$  activities in the collected underground argon gas samples were measured using a low background gas proportional counter

at the Low Level Counting Underground Laboratory [122] in the University of Bern, Switzerland. The laboratory is located 35 m below the Earth's surface (70 m.w.e.), where the cosmic ray muon flux is reduced by a factor of  $\sim 10$ .

Fig. 2.10 (left) illustrates the experimental setup for the  $^{39}\text{Ar}$  measurement. The gas proportional counter was constructed with high-conductivity oxygen-free (OFHC) copper and other low-radioactivity materials. It was shielded from external backgrounds by a 5 cm thick low-radioactivity ancient-lead cylinder, which, in turn, was contained by another gas proportional detector operated in the anti-coincidence mode. The whole setup was surrounded by 12 cm of lead shielding and 40 cm low radioactivity concrete (the wall of the laboratory). During the measurements, the gas counter was filled with  $\sim 100\text{ cm}^3$  of argon gas at a pressure of 10 bar. The energy deposition of the  $^{39}\text{Ar}$  decay electrons in the sensitive volume was typically below 35 keV due to the compact size. The collected anode charge signal was digitized by a 7-bit Multi-Channel Analyzer (MCA), and the data between the channels 20-127 were used in the  $^{39}\text{Ar}$  analysis [121].

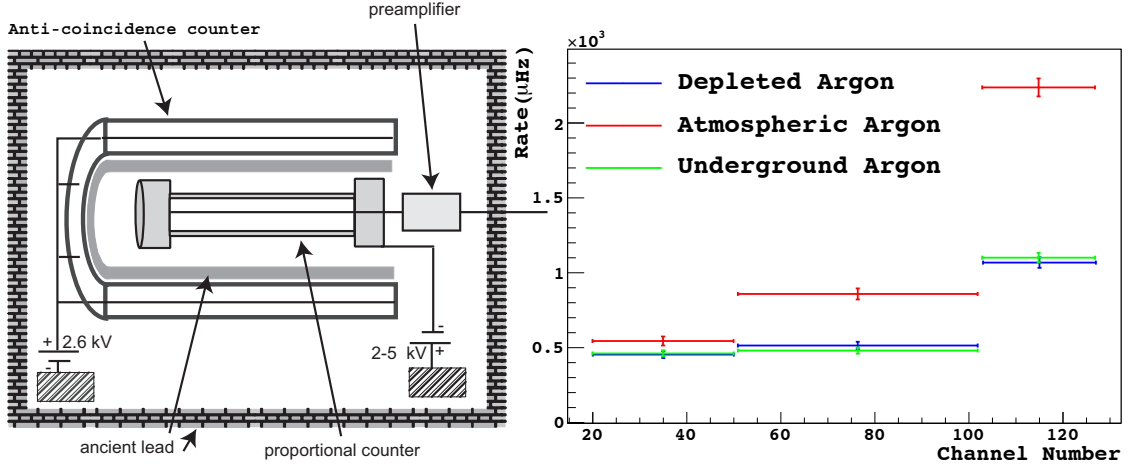


Figure 2.10: Left: an illustration of the low background gas proportional counter used for the  $^{39}\text{Ar}$  activity measurement at the University of Bern; Right: the counting rates in the digitizer channels, where the maximum energy deposition is  $\sim 35$  keV.

The residual background of the proportional counter was evaluated with an argon

sample depleted of  $^{39}\text{Ar}$  through differential thermal diffusion, which was estimated to have less than 3% of  $^{39}\text{Ar}$  compared to atmospheric. This observed background rate was subtracted from the atmospheric argon rate and the underground argon rate, which were then compared to determine the relative  $^{39}\text{Ar}$  level in the underground samples. The system had an sensitivity of  $\sim 5\%$  atmospheric  $^{39}\text{Ar}$  level, and it represented the best  $^{39}\text{Ar}$  decay measurement at that time. The argon samples extracted from the National Helium Reserve and from the Kinder Morgan  $\text{CO}_2$  plant both showed no evidence of  $^{39}\text{Ar}$  at this sensitivity.

The  $^{39}\text{Ar}$  sensitivity of the Bern facility was restricted by the relatively high background level and the small sample size, which were difficult to improve. Therefore, alternative technologies were investigated to seek a better  $^{39}\text{Ar}$  sensitivity. The Accelerator Mass Spectrometry (AMS) method was reported to have a sensitivity around  $\sim 5\%$  atmospheric value in  $^{39}\text{Ar}$  counting [130]; so an effort was made to improve the AMS sensitivity but the background from  $^{39}\text{K}$  couldn't get efficiently reduced. Recently, Atomic Trap Trace Analysis (ATTA) has obtained  $^{39}\text{Ar}/^{40}\text{Ar}$  sensitivity below the atmospheric level, and the authors expect to increase the sensitivity to the level of 0.1% atmospheric with improvements in the future [131], but large uncertainty remains in this schedule.

Limitation in the existing  $^{39}\text{Ar}$  measurement techniques motivates the work of this thesis. A customized, low background, liquid argon detector is proposed to pursue a sensitivity of  $^{39}\text{Ar}$  level below 1% atmospheric value in kilogram size samples. This project is expected to exploit the potential power of argon-based dark matter detectors. It will also provide insights on the PMT background study, wavelength shifter study, reflector study, and the impurity quenching effects, which are important for all argon-based scintillation experiments.

## 2.4 The DarkSide Program

DARCSiDE (commonly referred to as DarkSide) is the acronym for Depleted Argon Chamber for Scintillation and Drifted Electrons. The experiment aims to detect, or set limit on, the WIMP dark matter interactions with argon. The DarkSide collaboration involves 26 research groups and Universities from 7 countries: 12 institutions from the USA, 6 from Italy, 4 from Russia, 1 each from China, Poland, Ukraine and the United Kingdom [132].

Because the WIMP interaction rate with matter is expected to be very low, the background in a dark matter detector has to be suppressed to extremely low levels for sensitive dark matter detections. In addition to exclusively using low radioactivity materials to construct the detector, the DarkSide experiment also uses a few innovative technologies to reduce the background levels, including using the low- $^{39}\text{Ar}$  underground argon as the target, combining the pulse shape discrimination of argon scintillation with the scintillation-to-ionization discrimination to reject electron recoil backgrounds, and implementing a high efficiency neutron veto detector [133] to suppress the most dangerous neutron background. All DarkSide detector aim to achieve background-free operations in a few years's exposure.

### 2.4.1 The Two-Phase Argon TPC

The most prevailing background in an argon-based dark matter detector is the  $^{39}\text{Ar}$  decay electrons; the  $^{39}\text{Ar}$  activity in atmospheric argon ( $\sim 1 \text{ Bq/kg}$ ) is several orders of magnitude higher than the estimated WIMP interaction rate. This background is suppressed in the DarkSide experiment by 3 approaches: 1) the low- $^{39}\text{Ar}$  activity underground argon is used as the target, 2) the argon scintillation light is collected and the pulse shape discrimination method is used to reject electron recoil backgrounds, 3) the ionization electrons are also collected and the scintillation-to-ionization ratio

supplies additional rejection power against electron recoils.

The DarkSide detector is designed to be a two phase argon TPC. It contains a liquid bulk at the bottom as the target for WIMP interaction, and a thin layer of argon gas at the top for ionization electron detection. When a WIMP particle collides with an argon atom, the recoil argon nucleus produces scintillation light. Some electrons in the argon nucleus ionization track may escape the electron-ion recombination process, and are drifted towards the gas phase with a uniform electric field. At the liquid-gas interface, a strong electric field is applied to extract the electrons into the gas, accelerate them and produce argon gas scintillation. The distribution of the secondary scintillation light, along with the electron drift time, gives an estimate of the scintillation event position. To efficiently collect the argon scintillation light, a wavelength shifting fluor, TetraPhenyl Butadiene (TPB), is used to convert the light into the visible range for better reflection and detection.

A 10 kg prototype of the DarkSide detector, usually referred to as DarkSide-10, has been constructed and used to study the performance of this specific TPC design. As illustrated in Fig. 2.11, the DarkSide-10 detector contains  $\sim 10$  kg of atmospheric argon in its sensitive volume, which is seen by  $7 \times 2$  low-radioactivity PMTs (Hamamatsu R11065) from the top and from the bottom. The sensitive volume is surrounded by high reflectivity materials (3M Vikuiti specular reflector film in some runs and high-crystalline PTFE in other runs), which are coated with the TPB wavelength shifter. A quartz diving bell is mounted on the top of the sensitive volume and maintains the gas pocket using a heater (resistor) in a boiling arm. The electric field is defined by transparent cathode/anode plates (quartz, coated with the conductor Indium-Tin-Oxide) and parallel field rings with increasing high voltage. The anode/cathode plates are also coated with the wavelength shifter.

The DarkSide-10 detector has been operated both in a ground level laboratory in Princeton University and deep underground in the LNGS laboratory in Gran Sasso,

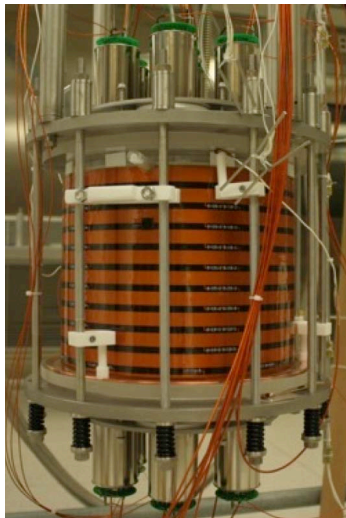


Figure 2.11: The DarkSide-10 inner detector. The sensitive argon volume is enclosed by the cylinder and seen by PMTs both from top and bottom; the black and orange strips are the field rings.

Italy. The detector performance is in a relatively stable phase after problems were exposed, diagnosed and fixed. The detector's response to electron recoil events is studied with  $^{39}\text{Ar}$  and external gamma ray sources; the best scintillation light yield is measured to be  $\sim 9$  p.e./keV at null field [100], representing the highest value ever reported by argon detectors. Its ability to detect nuclear recoils is investigated with an Americium-Beryllium (AmBe) neutron source, and preliminary studies have been carried out on the electron recoil background rejection power of the scintillation pulse shape discrimination and of the scintillation to ionization discrimination.

Based on the success of DarkSide-10, the first DarkSide detector with WIMP detection sensitivity, DarkSide-50, has been constructed and will be commissioned in LNGS soon (late 2013). The basic design is the same as the 10 kg prototype detector, but the sensitive volume is increased to  $\sim 50$  kg and the low- $^{39}\text{Ar}$  underground argon will be used. All the building materials have been pre-screened for low radioactivity and the assembly was done in a radon-free cleanroom (class 100). The PMTs are also upgraded to a lower radioactivity model Hamamatsu R11065-20 <sup>12</sup> and the PMT

---

<sup>12</sup>DarkSide is currently experiencing technical problems with the R11065-20 PMTs and may switch



number is increased to 38 (19 on the top and 19 on the bottom). The DarkSide-50 TPC is housed inside a 4 m diameter stainless steel sphere filled with boron-loaded liquid scintillator, which serves as an active neutron veto [133]. The neutron veto detector, in turn, is contained in a 11 m diameter cylindrical water Cherenkov detector. This graded shielding setup is illustrated in Fig. 2.12. The scintillator and water shielding detectors are also expected to host the DarkSide-G2 detector, a two phase TPC containing 3.3 tons of underground argon in the sensitive volume (2.8 tons fiducial), after the completion of DarkSide-50 measurement.

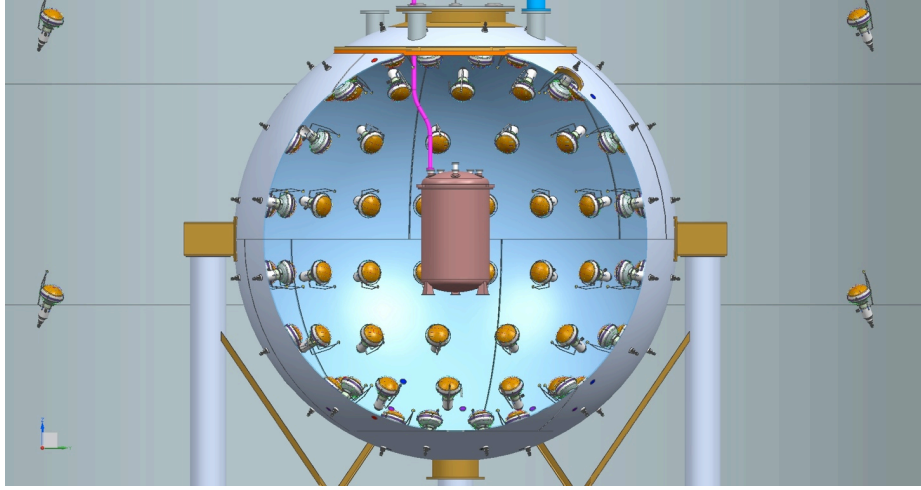


Figure 2.12: A schematic of the DarkSide-50 detector (the cylinder in the middle) along with the liquid scintillator neutron veto detector (the sphere with PMTs) and the water Cherenkov detector (the volume with PMTs outside the sphere).

### 2.4.2 The Active Neutron Veto Detector

As has been discussed, the DarkSide-50 TPC will be contained in a liquid scintillator detector to suppress the neutron backgrounds. Neutrons are believed to be the most dangerous background in all dark matter detectors because they can scatter from argon nuclei and produce nuclear recoils in the same way as WIMP particles.

---

back to the R11065 model for the first measurement.

Dark matter detectors are usually located deep underground, where the neutron flux is greatly reduced compared to the Earth’s surface. However, neutrons can also be produced underground in two ways: 1) neutrons from cosmic muon spallation and 2) fission neutrons and  $(\alpha, n)$  neutrons rising from the decays of U and Th. The former process can be enhanced in high atomic number materials, such as lead used in gamma ray shielding, but the flux goes down quickly as the depth increases. The latter rises from the detector components and rocks around the experiment, which becomes the dominant neutron source at large depths.

Passive neutron shielding is commonly used in low background experiments. Low atomic number material, such as water and polyethylene, can be used to slow down neutrons; high neutron capture cross section materials like boron and gadolinium can be added to the neutron moderators to increase the shielding power against neutrons. Large dark matter detectors may also use the neutron multiple scattering process to reject neutrons<sup>13</sup>, but this rejection power is expected to be very low in small detectors at the currently sub-ton scales. As for the passive shielding scheme, it is not effective in attenuating high energy cosmogenic neutrons, and it couldn’t reduce the neutron background emerging from the detector components.

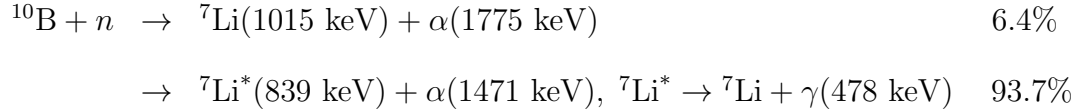
The neutron background in the DarkSide experiment is handled with a scintillator veto detector surrounding the argon TPC [133]. If a neutron deposits a detectable amount of energy in the veto before or after scattering with argon atoms in the TPC, the resulted argon nuclear recoil will be associated with the neutron event and rejected from the WIMP analysis. This active veto scheme doesn’t require the neutrons to be removed as in the case of passive shielding; it equivalently reduces the neutron attenuation length to the neutron interaction length and gives 1 m of scintillator veto a similar shielding power to  $\sim 4$  m of water. Besides, in the case that a neutron produces an argon nuclear recoil and then gets captured by the detector

---

<sup>13</sup>The mean free path of MeV level neutrons is several centimeters in liquid argon, and they are the most dangerous background to produce low energy nuclear recoils.

components, the capture gamma rays may also get recorded by the veto detector and helps reject the neutron background. To enhance the neutron detection efficiency in the veto detector, the DarkSide experiment uses a high scintillation efficiency scintillator Pseudocumene (PC) that is loaded with a high neutron capture cross section material trimethyl-borate (TMB). The PC scintillator is also used in the Borexino solar neutrino experiment and has exhibited excellent stability and scintillation properties [134].

The boron isotope  $^{10}\text{B}$  exists at a relative abundance ratio of 20% in natural boron, and it has a very high capture cross section ( $\sim 4,000$  barns) for thermal neutrons.



The  $(n, \alpha)$  capture channel is believed to be superior to the traditional  $(n, \gamma)$  channels in neutron detections because alpha particles are highly localized and can be fully contained in compact detectors. On the contrary, capture gamma rays usually have very high energies and are only efficiently captured in large detectors. The scintillation of alpha and lithium in PC is known to be quenched; their combined scintillation output is measured to be equivalent to 50-60 keV (gamma ray energy not included) electron events [135, 136]. At least 20-30 photoelectrons are expected to be detected by the veto PMTs at a conservative light yield value of 0.5 p.e./keV, which has been confirmed by an independent neutron measurement with this scintillator mixture<sup>14</sup>.

DarkSide-50 will be the first dark matter detector using a large volume of low- $^{39}\text{Ar}$  argon as the target, and also the first one with an active neutron veto system. In 3 years' operation (100 kg·yr exposure), the DarkSide-50 detector is anticipated to

---

<sup>14</sup>Optical simulations predict a higher light yield of 0.8-0.9 p.e./keV, and the simulation method has been verified with measurements using a 20 L chamber filled with the scintillator mixture. This 20 L scintillator chamber was also used in the neutron capture measurement.

achieve a sensitivity of  $1\text{--}2 \times 10^{-45} \text{ cm}^2$  for WIMPs at the mass of 100 GeV. Thanks to the virtue of noble liquid technology, the DarkSide-G2 detector can be built using the same techniques as DarkSide-50. The G2 detector will reach a sensitivity of  $2 \times 10^{-47} \text{ cm}^2$  in 5 years' operation (14 ton·yr exposure), and covers a large fraction of the WIMP parameter space predicted by common supersymmetry theories.

## Chapter 3

# The Low Background Liquid Argon Detector

The  $^{39}\text{Ar}$  measurement at the University of Bern indicated that argon extracted from certain underground sources has a low  $^{39}\text{Ar}$  content, which could make very large argon-based WIMP dark matter detectors possible. To further investigate the effects of the residual  $^{39}\text{Ar}$  content in underground argon on argon-based WIMP experiments, a more precise evaluation of the  $^{39}\text{Ar}$  concentration becomes necessary.

As discussed in Sec. 2.3.4, the sensitivity of the Bern measurement was mainly limited by the size of the argon sample. Only a few grams of argon was contained in the sensitive volume, and the recorded energy spectrum was background dominated. To improve the signal to background ratio and to pursue a higher  $^{39}\text{Ar}$  sensitivity, argon in a condensed phase should be used. A low background detector, taking advantage of the well-developed liquid argon scintillation technology, was proposed for this measurement.

A low background experiment should minimize the contamination both from external background radiation and from internal component radioactivity. Construction material of the detector components need to be carefully screened for low radioac-

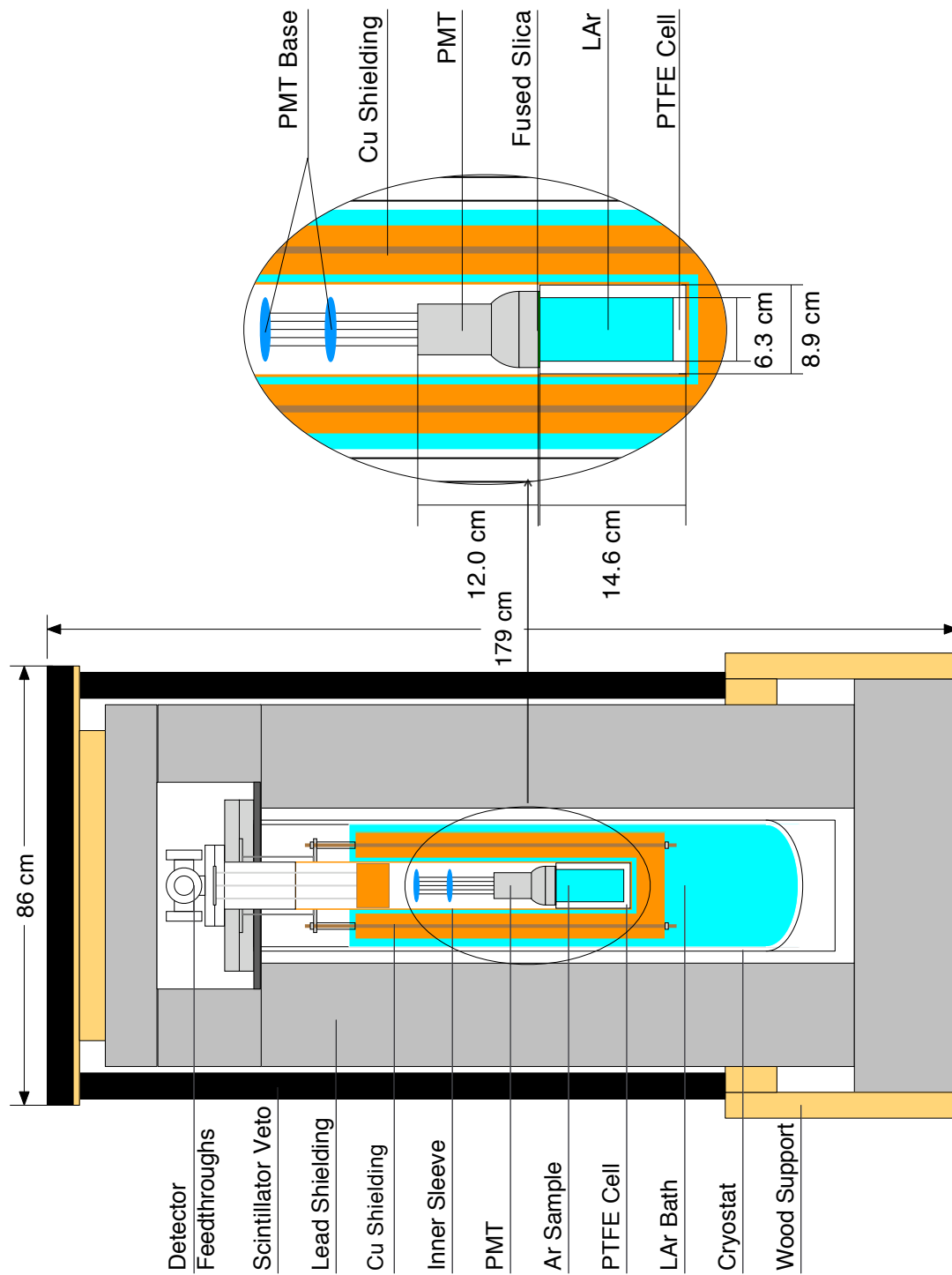


Figure 3.1: A schematic diagram of the low background detector. The active volume of liquid argon is surrounded by a PTFE cell coated with WLS, and viewed by a low background PMT. Copper and lead shielding reduces external backgrounds, and an external liquid argon bath provides cooling for the inner detector.

tivity, and relatively high radioactivity parts should be separated from the sensitive volume. In addition, a shielding system has to be implemented to suppress external backgrounds including environmental gamma rays, cosmogenic and radiogenic neutrons. Underground locations are often used because they offer reduced fluxes of cosmic rays and cosmogenic neutrons.

For the  $^{39}\text{Ar}$  measurement, a low background detector with passive shielding was designed and built. The design of the detector changed somewhat as upgrades were carried out during the course of running, but the main features can be seen in Fig. 3.1, which shows the detector in the configuration used in the 2011 measurement. The detector contained 0.56 kg of liquid argon as the active volume in a 2.5-inch inner diameter, 5.25-inch high “cup” made of highly crystalline PTFE. The inner surfaces of the PTFE container and the fused silica top window were coated with  $\sim 300 \mu\text{g}/\text{cm}^2$  of p-Terphenyl to shift the 128 nm ultraviolet argon scintillation light into the visible range. The photons were detected by a low background 3-inch photomultiplier tube (PMT) above the cup. The cup and PMT were enclosed within a 3.5-inch diameter copper and stainless steel sleeve, which was sealed at the top by a Conflat flange. The side and bottom of the sleeve were surrounded by 2 inches of oxygen-free high conductivity (OFHC) copper shielding; a loose-fitting 2.5-inch thick copper plug was inserted into the sleeve above the PMT to complete the inner shielding.

## 3.1 Inner Detector Components

### 3.1.1 Wavelength Shifter and Reflector

As discussed in Sec. 2.1, the argon scintillation light is in the ultraviolet region. The so-called second continuum light that is critical to the pulse shape discrimination method in argon-based detectors has a peak around 128 nm in its emission spectrum. Collection of UV light at this wavelength is extremely difficult for a few reasons:

1) few materials reflect vacuum UV light because the high photon energy is strongly ionizing; 2) PMTs are widely used in scintillation experiments, but only a few window materials are transparent to vacuum UV light. Lithium fluoride and magnesium fluoride have cutoff wavelengths around 105 nm and 120 nm respectively, but they are very expensive. Quartz, as used in the Hamamatsu R11065 PMTs cuts off light below the wavelength of 180 nm; 3) Common PMT photocathode materials are most sensitive to visible light. For example, the R11065 tube has a peak quantum efficiency at 420 nm. As a result, the argon scintillation light needs to be converted to longer wavelength to be effectively reflected and collected.

Photo-fluorescent materials that absorb short wavelength photons and emit long wavelength photons can be used as wavelength shifters (WLSs). The wavelength shifting process starts with the excitation of the fluorescent molecules into high energy electronic levels after the absorption of incident radiation. In a condensed medium like a solid or a liquid, collisions between molecules rapidly lead to the relaxation of vibrational energy and leave the molecules in the lowest vibrational level of the first excited electronic state, which is usually a spin singlet state denoted as  $S_1$ . If this  $S_1$  state can remain  $10^{-9}$  s or longer, fluorescent is emitted during the molecule relaxation to the vibrational levels of the ground state. The non-radiative loss of the vibrational energy leads to the conversion of incident light toward longer wavelengths. The spread of the absorption spectrum is determined by the vibrational energy levels of the (first) excited electronic state, while the fluorescent spectrum displays the vibrational spacing of the ground state [137]. Therefore, if these vibrational energy levels have similar structures, a reflection symmetry between the absorption and emission spectra can result, as observed in some scintillators.

Many organic materials exhibit appropriate properties to be qualified as WLSs. A WLS is characterized by its absorption spectrum, emission spectrum, quantum



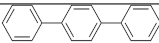
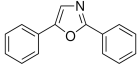
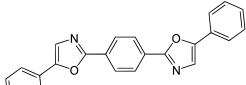
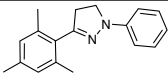
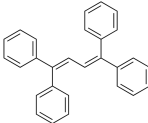
WLS Name	Molecular Formula	Chemical Structure	Abs. Peak	Emis. Ave.	Decay Time
PTP	$C_{18}H_{14}$		275nm	342nm	0.9 ns
PPO	$C_{15}H_{11}NO$		305nm	370nm	1.5 ns
POPOP	$C_{24}H_{16}N_2O_2$		355nm	415nm	1.3 ns
PMP	$C_{18}H_{20}N_2$		295nm	415nm	3 ns
TPB	$C_{28}H_{22}$		345nm	473nm	1.7 ns

Table 3.1: Basic properties of commonly used WLS chemicals [137–139].

efficiency and time response. Generally speaking, high quantum efficiency and fast fluorescence decay time are preferred to preserve the statistics and the time profile of the primary scintillation process. As for the spectrum preference, an experiment seeks the maximal absorption of primary scintillation light and best match between the emission spectrum and the spectrum response of the light detection devices used. Large separations between the absorption and emission spectra are preferred because they reduce the self-absorption effect, and in some cases a secondary WLS can be used to reduce light loss due to self-absorption.

Commonly used WLSs include p-Terphenyl (PTP), 1,1,4,4-Tetraphenyl-1,3-butadiene (TPB), 1-phenyl-3-mesityl-2-pyrazoline (PMP), 2,5-Diphenyloxazole (PPO), and 1,4-bis(5-phenyloxazol-2-yl) benzene (POPOP). Some basic photo-physical properties of these chemicals are summarized in Tab. 3.1, and their absorption/emission spectra are shown in Fig. 3.2. Spectrum data for PTP, PPO and POPOP are taken from Ref. [140], while data from Ref. [139] are used for PMP and Ref. [137] for TPB. Slight differences are observed between measured spectra due to different solvent and different solute concentration. Quantum yields are also reported at different values

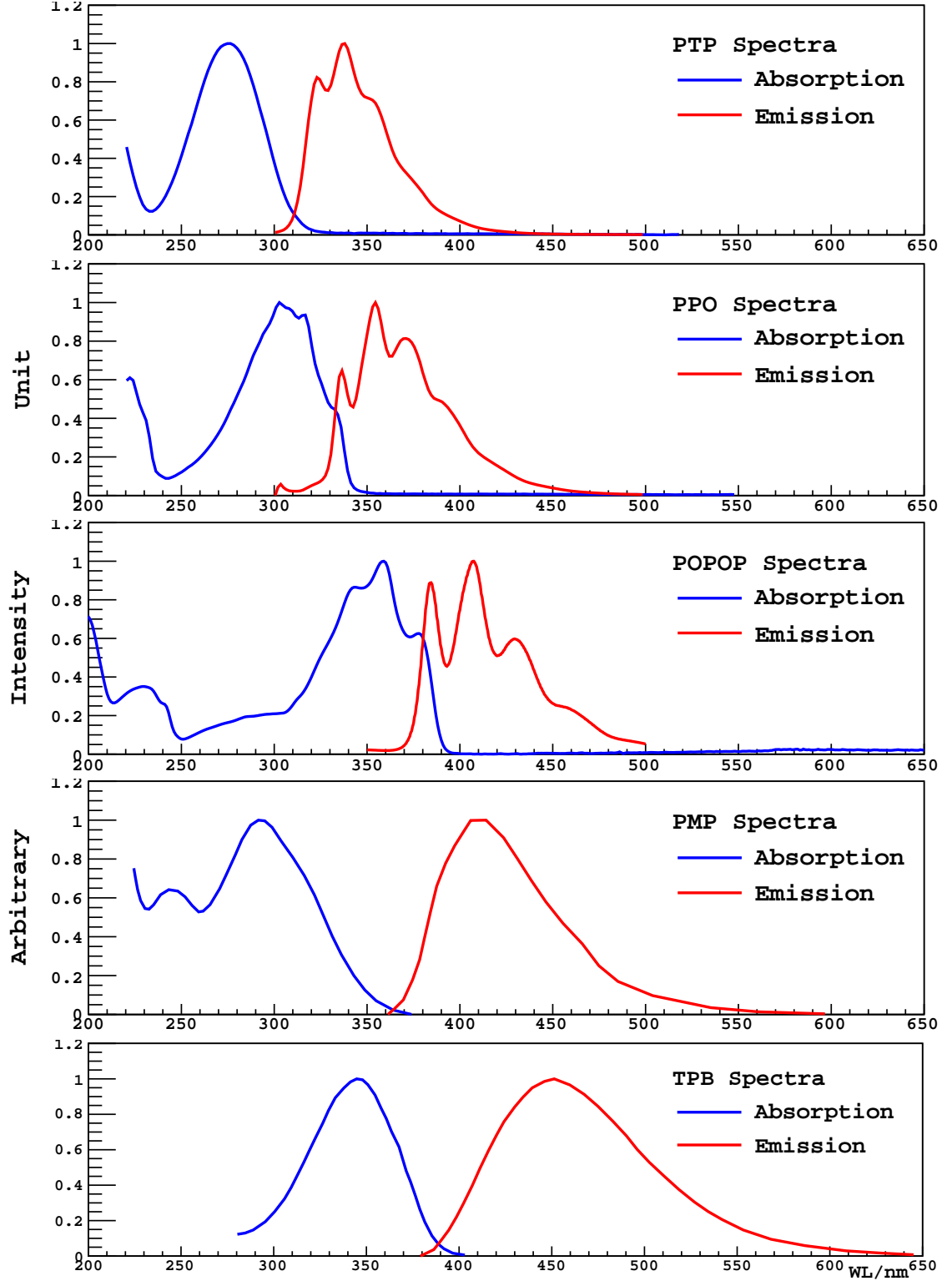


Figure 3.2: The absorption and emission spectra of commonly used WLSs. Data are collected from Ref. [137,139,140]. Both absorption and emission peaks are scaled to unit to better preserve the mirror symmetry.

in Ref. [137, 139, 140] possibly due to the differences in experimental conditions such as excitation wavelengths, chemical purity, and solvent materials, and the values are not included in this summary.

The reflectors that are interesting to this argon scintillation experiment include Spectralon, 3M Vikuiti Enhanced Specular Reflector (ESR) film, and highly crystalline PTFE (Teflon). Spectralon, which is a PTFE-based thermoplastic resin, gives the highest diffusive (Lambertian) reflectance of any known material over a large window of wavelength (UV-Vis-NIR). The nominal reflectance for thick Spectralon reflectance material ( $\gtrsim 1\text{cm}$ ) is  $>99\%$  from 400 to 1500 nm and  $>95\%$  from 250 to 2500 nm, according to the manufacturer Labsphere [141]. On the contrary, the non-metallic, multi-layer polymer ESR film manufactured by the 3M company is a specular reflector that maintains 98% reflectance across the visible light spectrum [142]. PTFE, which is well known for its high thermal stability and low friction coefficient, also provides a high diffusive reflection over a wide range down to  $<300\text{nm}$ . Since it is a bulk reflector, longer wavelength light has a higher transmission probability, and its reflectivity gradually drops as the wavelength increases. Usually thick PTFE parts are used to achieve high reflectance. Beside functioning as a good reflector, PTFE is also widely used in low background experiments because of its low radioactivity <sup>1</sup>.

The reflectivity of commonly used reflectors has been extensively studied, and a compilation of measurement is given in Ref. [145]. The reflectivity reported for Spectralon, 3M foil and PTFE tapes are shown in Fig. 3.3. The measured reflectivity is generally consistent with the values reported by the manufacturers, but were lower for some wavelengths. The reflectance of several other reflectors used by DarkSide and other dark matter search experiments, including Tetratex film (TTX), Tyvek film and Lumirror film, are also measured in Ref. [145].

The 3M ESR film exhibits a cutoff in reflectivity for short wavelengths below

---

<sup>1</sup>The U, Th, K contents in some raw PTFE powder are reported to be very low [143], but the lead content may be relatively high [144].

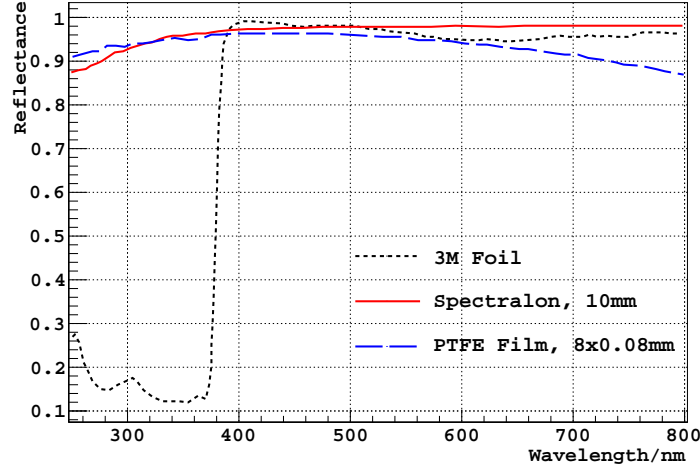


Figure 3.3: Reflectance of Spectralon, 3M foil and PTFE tapes measured by Ref. [145].

395 nm, and a similar effect is observed around 325 nm for Lumirror. To avoid unnecessary light loss due to this cutoff effect, the choice of reflector has to be made considering the choice of WLS, and vice versa. For example, if 3M foil is to be used in an argon scintillation detector, WLSs with longer emission wavelength such as TPB is preferred. On the other hand, if PTP is chosen as the WLS, Spectralon or PTFE gives a better overall light collection performance.

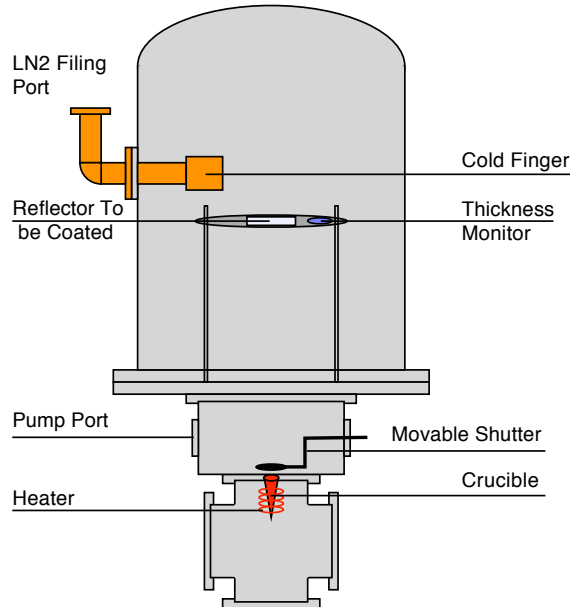


Figure 3.4: The vacuum evaporation system used for WLS coatings.

WLSs can be coated onto reflector surfaces by vacuum evaporation, or by painting or spraying the WLS solution with a volatile solvent; the former is believed to produce coatings with better uniformity than the latter [146]. A vacuum evaporation system, as illustrated in Fig. 3.4 has been constructed by the Princeton group and is used for WLS coating in this experiment. The evaporation chamber can be pumped down to a typical vacuum level of  $10^{-6}$  mbar in a few hours by a turbo-molecular pump that exhausts into a mechanical pump. Then liquid nitrogen is applied to the cold trap (cold finger), which removes residual moisture from the chamber and reduces the pressure down to  $10^{-7}$  mbar. At this pressure level, the WLS chemical (inside a Pyrolytic Boron Nitride (PBN) crucible (16 ml)) is heated by a Sorensen heating unit, and this process is controlled by a Eurotherm 2216 PID controller. Once the desired temperature (150C for PTP and 200C for TPB) is reached, the shutter is opened and a coating begins to form on the reflector; the coating thickness is measured in real time by a crystal thickness monitor. A detailed operating procedure of this vacuum evaporation system can be found in Appendix B.

The optimum coating thickness, at which the highest overall conversion efficiency is observed, is reported to be  $\sim 100 \mu\text{g}/\text{cm}^2$  for TPB and  $200\text{-}400 \mu\text{g}/\text{cm}^2$  for PTP [147]. In practice we usually aimed for  $\sim 300 \mu\text{g}/\text{cm}^2$  in the case of PTP, and  $100\text{-}200 \mu\text{g}/\text{cm}^2$  for TPB (in case of under-thickness due to non-uniformities).

### 3.1.2 PhotoMultiplier Tube

Choosing an appropriate PMT is crucial for the experiment to achieve a high light collection efficiency and a low radioactive background. When the detector was first constructed, a Hamamatsu R6233-100 super-bialkali Photomultiplier tube [148] was used because of its high quantum efficiency ( $\sim 35\%$  at 350 nm). However, the tube was not rated for cryogenic operation, nor was it low in radioactivity. A 26" long 3" diameter acrylic light guide was used to separate the PMT from the liquid argon

volume, so the PMT could be maintained at room temperature and its background contribution to the sensitive volume was also reduced.

Several early measurements suffered significant light loss in the light guide despite of the use of reflector wraps. In addition, the high outgassing rate from the acrylic posed a problem to argon purity, as it would seriously quench the slow component of argon scintillation. Fortunately a high quantum efficiency, low radioactivity, cryogenic PMT (model Hamamatsu R11065) became available, so the R6233-100 PMT was replaced and the acrylic light guide removed.

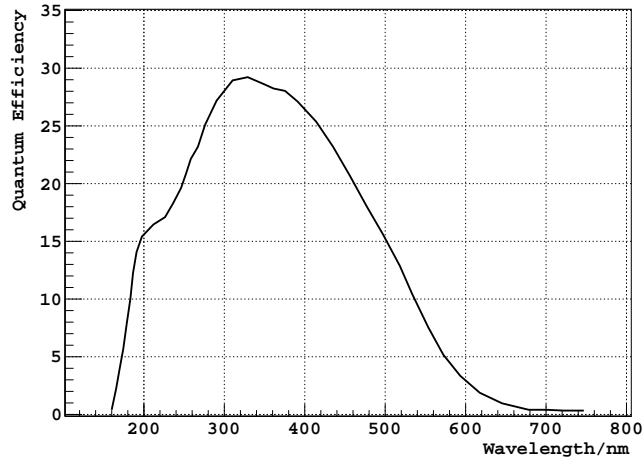


Figure 3.5: The spectral response of R11065 PMTs reported by Hamamatsu.

The Hamamatsu PMT R11065 has a high quantum efficiency ( $\sim 30\%$ ) special bialkali photocathode and a 3" diameter synthetic silica window. The 12-stage dynodes and other parts are encapsulated in a kovar metal case. The kovar alloy is well known for its low thermal expansion rate ( $5 \times 10^{-6}/^\circ\text{C}$ ), which makes it robust against thermal shocks. The feedthrough for the leads to the dynodes is made of another low thermal expansion ( $3 \times 10^{-6}/^\circ\text{C}$ ) material, borosilicate glass. The radioactivity of 3 sample R11065 tubes was measured with a low background high purity germanium gamma ray detector at Gran Sasso National Laboratory, and the results are reported in Tab. 3.2.

Decay Chain	Measurement Point	R11065 (mBq)	R11065-10 (mBq)
$^{232}\text{Th}$	$^{228}\text{Ra}$	$6 \pm 1$	$< 2.2$
	$^{228}\text{Th}$	$6 \pm 1$	$< 1.1$
$^{238}\text{U}$	$^{234}\text{Th}$	$190 \pm 40$	$< 70$
	$^{234m}\text{Pa}$	$80 \pm 40$	$< 62$
	$^{226}\text{Ra}$	$18 \pm 1.2$	$4.2 \pm 0.6$
$^{235}\text{U}$	$^{235}\text{U}$	$8 \pm 2$	$< 1.7$
$^{40}\text{K}$	$^{40}\text{K}$	$79 \pm 10$	$17 \pm 5$
$^{60}\text{Co}$	$^{60}\text{Co}$	$8.8 \pm 5.4$	$< 0.7$
$^{54}\text{Mn}$	$^{54}\text{Mn}$	$1.3 \pm 0.4$	$< 0.34$

Table 3.2: The measured radioactivity of a Hamamatsu R11065/R11065-10 PMT.

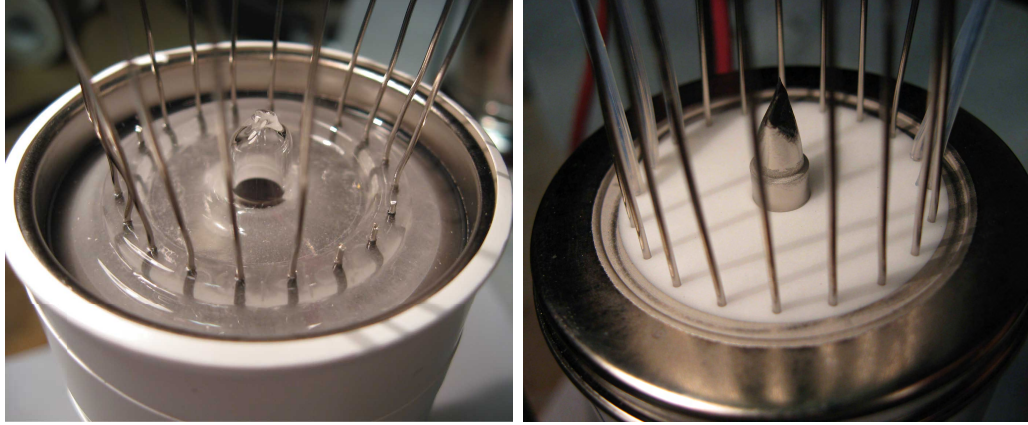


Figure 3.6: Comparison of the PMT feedthroughs. left: borosilicate glass feedthrough on a R11065 PMT; right: high purity ceramic feedthrough on a R11065-10 PMT

Further investigation into the PMT radioactivity revealed that the borosilicate feedthrough was a significant source of background. Then a modified version R11065-10 was developed where the borosilicate glass piece was replaced with high purity ceramic plate. The measured radioactivities of the new R11065-10 tubes are compared to that of the R11065 tubes in Tab. 3.2.

Although the modified R11065-10 tubes were measured to have low radioactivity level, they were found to fail high voltage tests in pure argon gas. The dielectric strength of argon gas is approximately 5 times smaller than that of air, or nitrogen, and this makes high voltage systems vulnerable in argon-rich environment. Electric

breakdown was observed at an anode voltage of  $\lesssim 1500$  V, and it was believed to happen around the anode lead. As shown in Fig 3.6, the surface of the ceramic plate near the edge is metalized to make a seal with the kovar case. However, since the kovar case shares the cathode potential, this joint brings the photocathode potential barely 1 mm away from the anode potential and may cause the breakdown.

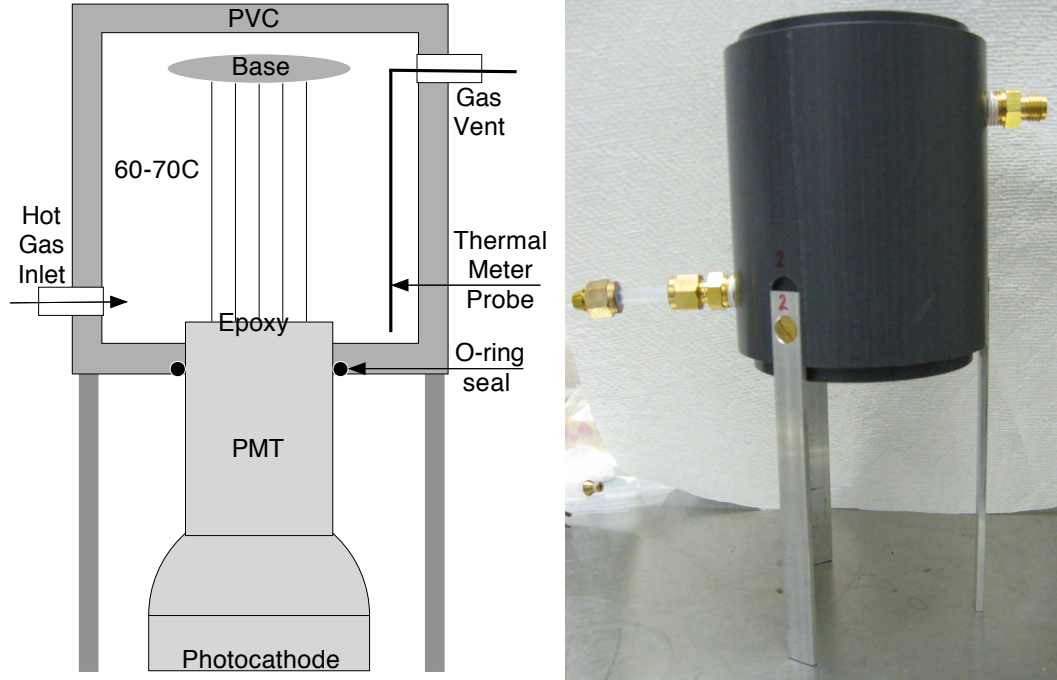


Figure 3.7: Customized oven to cure epoxy on the ceramic feedthrough of a R11065-10 PMT. left: schematic of the system; right: a picture of the oven.

Hamamatsu Japan planned to increase the space between the leads and the metal rim to 2.5 mm in a newer PMT model, but such a tube was not readily available. Instead, a temporary solution of coating the conducting part of the ceramic plate and the kovar leads with a thin layer of low outgassing rate, cryogenic epoxy (Masterbond EP29LPSP [149]) was made.

The cryogenic epoxy requires a minimum temperature of 55 C to cure, but the R11065-10 PMT is only rated up to 50 C (operation and storage). Above 50 C, part of the photocathode may evaporate and cause the quantum efficiency to decrease. To



address this problem, a customized oven was built to cure the epoxy. As illustrated in Fig 3.7, the rear end of the PMT with the epoxy layer was sealed in a PVC cell, and hot nitrogen gas flowed from a heating tube into the bottom of the oven. The flow rate of the nitrogen gas and the power of the heating tube were regulated to maintain a stable temperature of 60-70 C inside the oven, and the PMT window measured room temperature during this curing process. This epoxy coating survived cryogenic tests and enabled the PMT to function at 1600V in pure argon gas.

Decay Chain	Ceramic Plate		Kovar Case	
	Mass Con.	Rate	Mass Con.	Rate
U	10 ppb	2.47 mBq/PMT	0.2 ppb	0.37 mBq/PMT
Th	10 ppb	0.81 mBq/PMT	<0.01 ppb	<6.1 $\mu$ Bq/PMT
K	<1000 ppb	<0.62 mBq/PMT	6 ppb	<0.03 mBq/PMT

Table 3.3: The radioactive isotopes in parts of a R11065-10 tube measured by GDMS.

It is worth noting that although the ceramic feedthrough significantly reduces the PMT background, it is still responsible for most of PMT radioactivity. One sample R11065-10 PMT was dissected and sent to Evans Analytical for GDMS analysis. The U, Th, K levels in different components are listed in Tab 3.3. Higher purity synthetic ceramic feedthrough is currently under development in a collaborative effort between Princeton University and the OxiMaTec GmbH Company in Germany, and a purity level of <2.5 ppb U, <1.4 ppb Th and 8 ppm K has been achieved.

### 3.1.3 High Voltage and Signal Readout System

The operation of a PMT requires a high voltage divider and a readout circuit, which are usually integrated on a circuit board (PMT base). In order to minimize the amount of underground argon used in the measurement, the liquid argon level was set to be slightly above the PMT window. As a result the PMT base had to be

exposed to the low-dielectric strength argon gas, which put the high voltage system at the risk of electric breakdown.

Printed Circuit Board (PCB) bases have been designed for the DarkSide R11065 PMTs to be used in liquid argon, but they were tested to spark in argon gas at  $\sim 1000$  V in high voltage tests. Fig. 3.8 shows a picture of the DarkSide PMT base. The material used is FR4 (successor of G10) grade glass-reinforced epoxy laminate, which is flame resistant and provides excellent electrical insulation. But the compact size of the surface mount components makes this design vulnerable to voltage breakdown. Coating the boards with cryogenic epoxy improved the working voltage to  $\sim 1300$  V, which did not suffice safe PMT operations in this experiment.

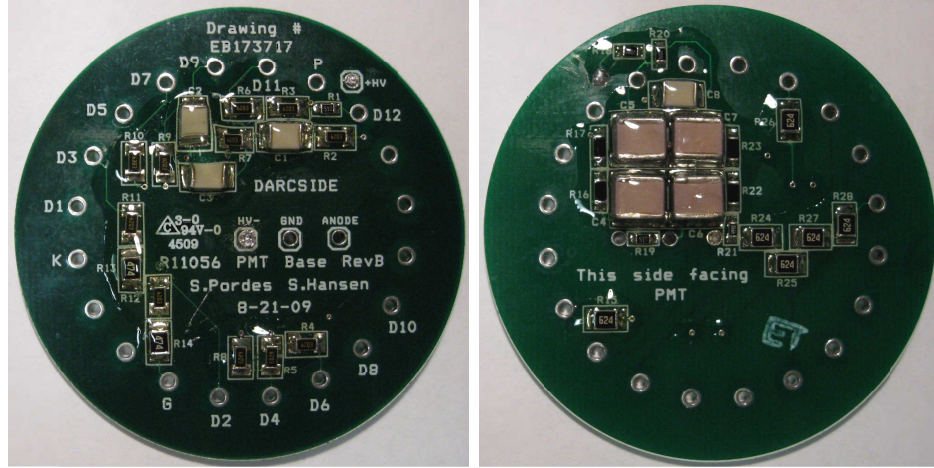


Figure 3.8: The front and back of a positive high voltage PCB board for R11065 PMTs.

Motivated by the idea that increasing the physical size of the electronic components can improve the robustness of the high voltage system in argon gas, we decided to build a customized PMT base with regular size cryogenic components. The circuit design followed that of the DarkSide R11065 PMT bases, as shown in Fig. 3.9.

A PMT circuit consists of a high voltage divider and a signal readout system. The voltage divider circuit distributes voltage among the dynodes and creates an interstage potential gradient. This voltage difference drives the photocathode electron signal

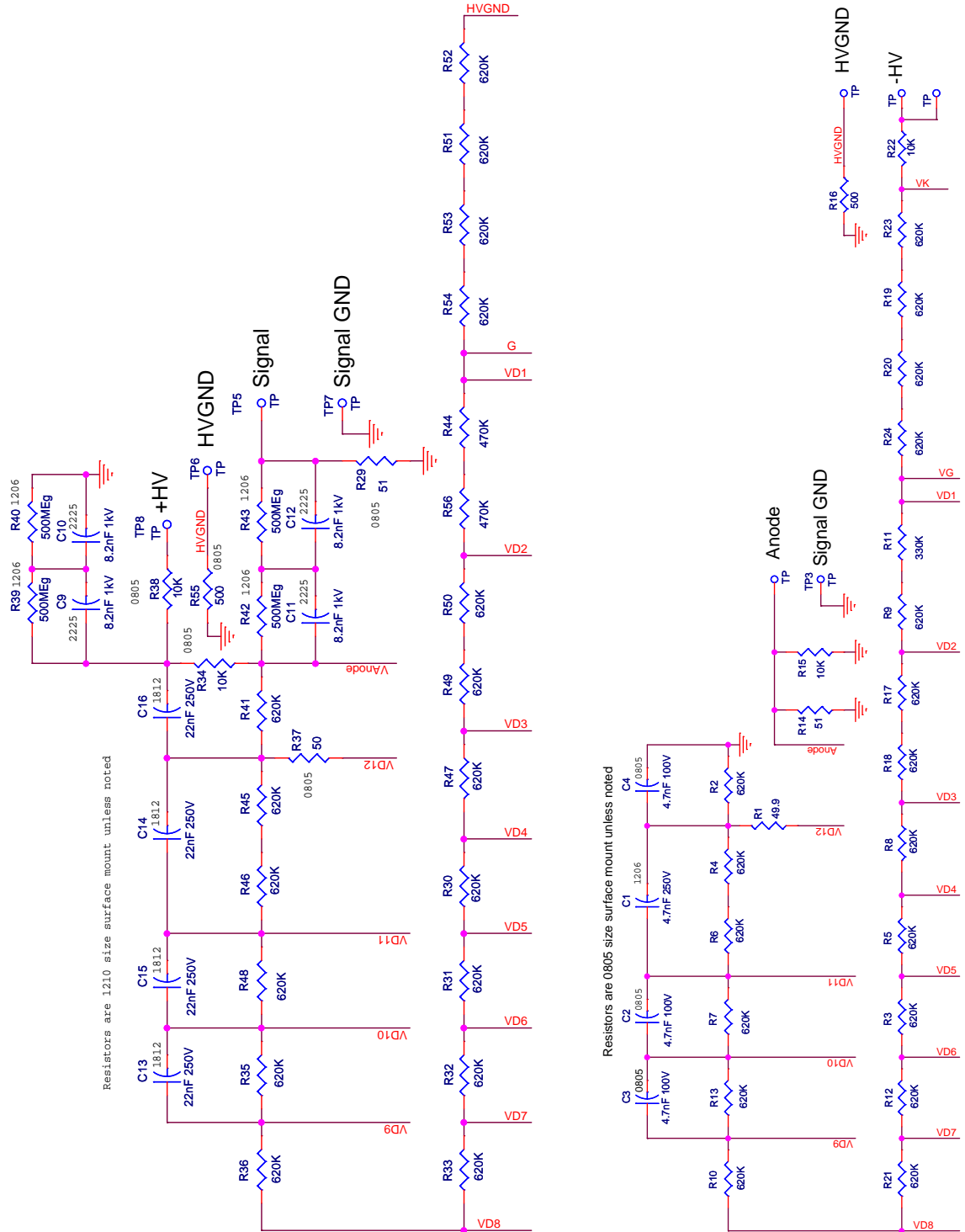


Figure 3.9: High voltage divider circuits designed by DarkSide collaborators at the FNAL for Hamamatsu R11065 PMTs. left: a positive HV scheme; right: a negative HV scheme.

toward the anode and amplifies it at each dynode. The simplest voltage dividing system is a resistor chain. What is more, a chain with equal interstage resistance yields the highest overall gain if a certain total voltage is given. However, the oversimplified model has to be complicated in practice [150].

1. To efficiently collect the primary photoelectrons, the voltage between the photocathode and the focusing grid needs to be increased. Similarly increasing the voltage across the first a few stages can improve the secondary emission probability, which, in turn, improves the output signal-to-noise ratio, pulse height dispersion, and also the electron transit time spread.
2. Exposing a PMT to a large number of photons in a short period of time can draw plenty of charge from the last dynodes and may alter the chain voltage distribution. For example, a voltage of  $\sim 1500$  V applied to the resistor chain in Fig. 3.9 creates a chain current around 0.1 mA, while a pulse of 10 primary photoelectrons in 10 ns requires a current of 0.01 mA from the last dynode at a gain of  $10^6$ . This fast current could change the voltage distribution on the dynodes and cause the overall gain to drop. A common solution is to mount decoupling capacitors in parallel to the last a few dynodes. These capacitors can supply charge to the dynodes during arrival of pulses and recharge outside the duty cycles. In this way the interstage voltages can be maintained at a stable level during operations.
3. If a high secondary electron density is created in the last stages, the electric field can be partially screened and cause the gain to drop. This is called the space charge effect and be mitigated by increasing the interstage voltage of the last dynodes, usually called a tapered chain scheme.

If a positive high voltage scheme is adopted, as illustrated in the circuit in the left of Fig 3.9, the photocathode is at ground potential, and photoelectrons are drifted

towards the anode that is at positive high voltage. Therefore, a high pass filter circuit (R29, C11-C12) is required to separate the output pulse signal from the high voltage. The high resistance R42-R43 are introduced to guarantee an equal voltage distribution between C11 and C12 for safe operations.

Noise from various sources needs to be filtered to improve the output signal quality. For fast pulse operations, damping resistors (R37 in the positive circuit) are usually installed at the last dynode(s) to suppress “ringing” at time scales of nanoseconds. In addition, the undesired ground loop current can be reduced by introducing a dissipative resistor (R55) between the high voltage ground and the signal ground. Furthermore, high frequency noise from the high voltage supply/cable or from the last dynodes can be passed to ground via a filter circuit (R39-R40, C9-C10).

The capacitors C9-C12 and the resistors in parallel (R39-40, R42-43) have to take half of the cathode-anode voltage and are most likely to cause the electric breakdown in the test of the PCB bases in argon gas. To reduce the risk of voltage breakdown for the customized base, capacitors of large dimensions from the CryoCircuits Inc were used exclusively in the base construction, as shown in Fig 3.10. This feature helped the base survive high voltage tests up to 2000 V in argon gas. In order to reduce the increased level of radioactive background from the increased size capacitors, the two filter circuits were mounted away (3”) from the resistor chain.

In addition to the increasing dimension of components, the value of the termination resistor (R29) was also increased in the customized base. The principle of impedance match requires the input/output impedance of electronics to have the same value, conventionally chosen to be 50 Ohm, to that of data transmission cables. In this way, the signal reflection is minimized, but the cost is that half of the charge collected from the dynode is dissipated on the termination resistor. A 1MOhm termination resistor was used in the customized base and directs essentially all anode charge to the 50 Ohm transmission cable. No noticeable reflection noise was observed

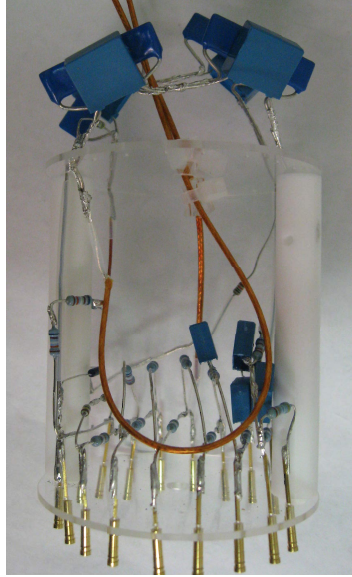


Figure 3.10: A positive high voltage divider board made of cryogenic components mounted on stress-relieved acrylic disks; the diameter of the disks is 2.5".

presumably because the matched impedance between the transmission cable and the data acquisition system suppressed the returning signal.

The customized base was used in the 2011 measurement. Later on, negative high voltage tests on the R11065 PMTs were carried out by the DarkSide collaboration, and the successful result suggested an alternative solution to the electric breakdown problem. In a negative high voltage scenario, the anode is at ground potential and no high pass filter is needed for signal readout. What's more, since the high frequency noise from the last dynodes has a direct path to ground, there is no need for a filter circuit either. Therefore, the possibility of high voltage breakdown in argon gas is significantly reduced even for a PCB base. However, extreme care has to be taken to ensure safe operations at negative high voltage because the kovar case shares the photocathode voltage and is at high voltage.

Typical FR4 or G10 PCBs have a high radioactivity level and thus are not ideal for low background applications. The DarkSide collaborators at Fermi National Accelerator Laboratory (FNAL) designed a new Cufion PCB board where copper traces

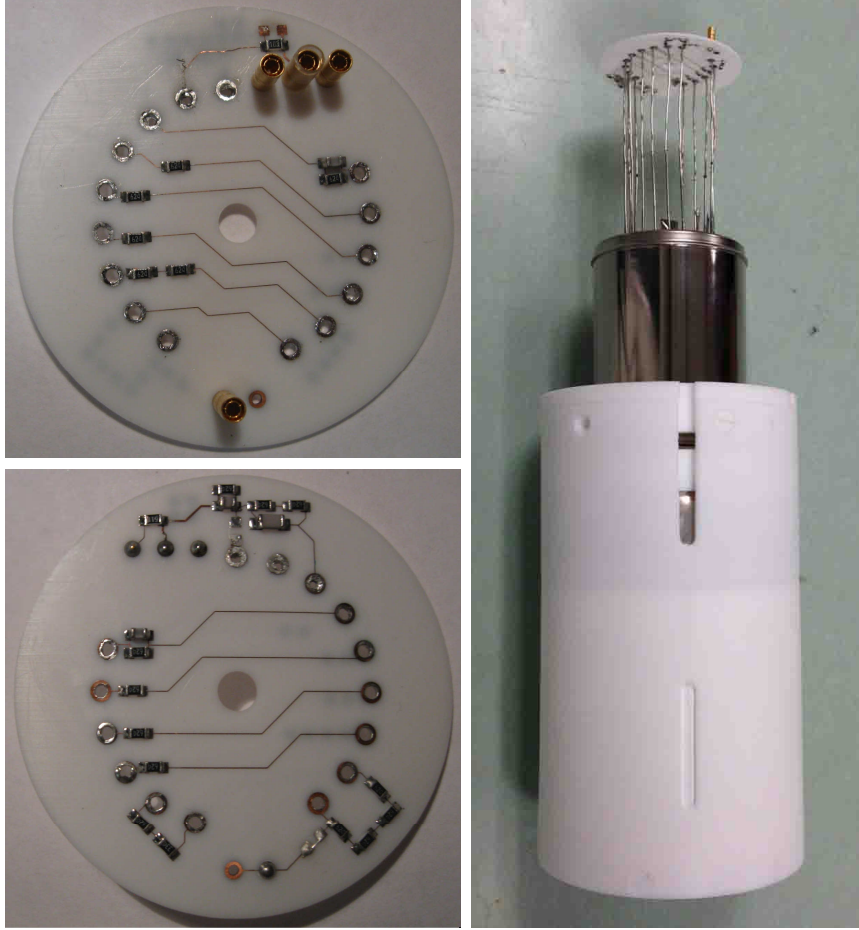


Figure 3.11: Left: a cuflon negative high voltage board for R11065 PMTs; Right: the inner detector (2012) with a PTP-coated Spectralon cell, a R11065-10 PMT and a cuflon base.

were printed on thin Teflon sheets, as shown in Fig 3.11. Thanks to the low radioactivity level of Cuflon and the small size of surface-mount components, this new system would have a much lower background than the customized base.

A few sample cuflon bases were tested in argon gas up to the maximum rated voltage (1800 V), and no electric breakdown was observed. A Cuflon board was used with a low background R11065-10 PMT in the 2012 underground argon measurement; the inner detector setup is shown in Fig 3.11, which also has a Spectralon scintillation cell with PTP coating.

## 3.2 Shielding from Backgrounds

### 3.2.1 Gamma Ray Shielding

The omnipresence of primordial radioactive isotopes results in a wide range of radiation backgrounds, of which gamma rays are among the most dangerous because of the high penetrating power. The continental crust contains approximately 2 ppm of U, 10 ppm of Th and 20,000 ppm of K, which produce a flux of approximately 10 gamma rays/cm<sup>2</sup>/s above 50 keV at 1 m above ground [119]. Sensitive volumes of low background experiments have to be shielded from these gamma ray contaminations.

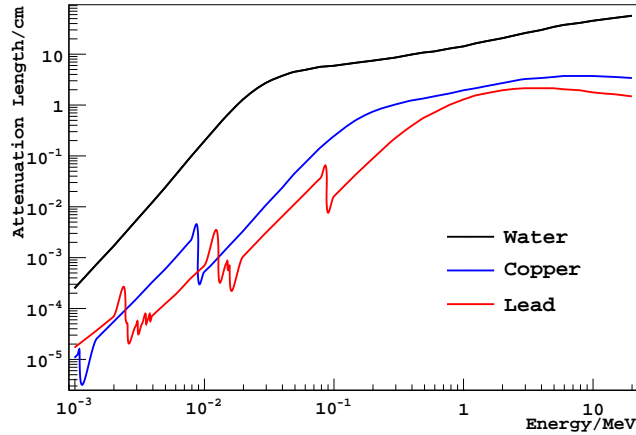


Figure 3.12: Gamma ray attenuation length in water, copper and lead, data from NIST X-Ray Mass Attenuation Coefficients table [151].

Gamma rays interact with matter mainly through 3 channels: 1) the photoelectric effect, in which a low energy gamma ray is absorbed by an atom and the energy transfer frees an orbital electron. The cross section can be approximated as  $\sigma_{P.E.} \propto Z^{4-5}/(\hbar\omega)^{3.5}$ . 2) Compton scattering, where one gamma ray transfers part of its energy to a (near-)free electron. The effective scattering cross section scales with the electron density, or the atomic number  $Z$ :  $\sigma_{C.S.} \propto Z$ . 3) pair production, where an electron-positron pair is produced by a high energy gamma ray ( $>1.02$  MeV) in the Coulomb field of a heavy nucleus. Its cross section is proportional to  $Z^2$  of the



absorber material. Fig. 3.12 shows the gamma ray attenuation length in lead, copper and water at different energies [151], and high atomic number materials like lead and copper are widely used in gamma ray shielding. The highest energy naturally occurring gamma ray (2.6 MeV from  $^{208}\text{Tl}$ ) has an attenuation length at the level of centimeters in lead. 8" of lead shielding, as is used in the low background detector, can suppress this gamma ray rate by at least 3 orders of magnitude.



Figure 3.13: Gamma ray shielding of the low background detector. Left: the lead castle; the wall thickness is 8" around the detector sensitive volume, 6" around the flanges and feedthroughs, and 4" to the top. Right: the outer copper shielding that hangs inside the lead castle; another 2.5" thick copper plug closes the top inside the inner detector cylinder.

The U and Th levels in lead are typically low, but the intrinsic lead radioactivity  $^{210}\text{Pb}$  (22 yr half-life) could be high.  $^{210}\text{Pb}$  decays to  $^{210}\text{Bi}$  by emitting a low energy electron (and a gamma ray), with a decay energy of  $\sim 64$  keV. These low energy radiations hardly escapes the self-absorption of lead, but the energetic electrons (1.16 MeV end point) from  $^{210}\text{Bi}$  decay can produce bremsstrahlung gamma rays and characteristic X-rays, which may emerge from the lead surface. Since low energy gamma

rays are subject to strong self-absorption, the spectrum of lead gamma rays emerging from the surface exhibits a peak around 170 keV [119]. The concentration of  $^{210}\text{Pb}$  in commercial lead ranges from the Bq/kg level up to a few kBq/kg, while the lowest reported value is less than 20 mBq/kg for antique Roman lead. A lead brick sample from the low background detector shielding was measured with a silicon detector at the University of Alabama to have approximately  $64 \pm 7$  Bq/kg of  $^{210}\text{Pb}$  [152].

In order to attenuate the residual gamma rays from the lead, 2" of oxygen-free high-conductivity (OFHC) copper was installed between the lead castle and the inner detector. Electrolytic copper is known to be one of the highest purity materials available because it has a high reduction potential and can be effectively separated from radionuclides during electrolysis. However, neutron activation in copper may produce radioactive isotopes including  $^{56-58}\text{Co}$ ,  $^{60}\text{Co}$ ,  $^{54}\text{Mn}$ ,  $^{59}\text{Fe}$ , and etc [153]. So copper exposed to cosmic rays or other neutron sources could contribute non-negligible backgrounds in low radioactivity experiments.

### 3.2.2 Muon Veto

High energy particles from the Sun and from the galaxies, which consist of  $\sim 90\%$  protons and  $\sim 10\%$  alpha particles, constantly bombard the Earth's top atmosphere at a rate of  $\sim 1000/\text{m}^2/\text{s}$ . These primary cosmic particles can produce massive secondary cosmic rays by collision with atoms in the atmosphere. For example, a single high energy particle may spall atomic nuclei and generate a hadronic cascade, the components of which, in turn, may produce more electromagnetic sub-showers. As the shower reaches the ground, it can extend over a large area (miles). Most of the hadronic components of the secondary cosmic ray are stopped by the atmosphere, but the penetrating particles including muons and neutrons may reach the ground. The intensities of the secondary cosmic ray components at sea level are estimated to be charged pions : protons : electrons : neutrons : muons  $\simeq 1 : 13 : 340 : 480 :$

1420 [119], with a muon flux of 100-200 /m<sup>2</sup>/s. More information about cosmic rays can be found in the review article Ref. [154].

Of all cosmic ray components, muons are particularly interesting. The half life of muons is  $\tau=2.2\mu s$ , so a naive estimate of muon path  $c\tau \sim 660$  m is far less than the depth of the atmosphere ( $\sim 10$ -100 km). However, muons are produced with high kinetic energies, and the relativistic correction enables them to travel many kilometers in the Earth frame. High energy charged particles lose energy mainly through ionization and radiation, but the radiation (bremsstrahlung) energy loss of muons is suppressed by the large mass (106 MeV). Muons typically lose a few MeV of energy for every g/cm<sup>2</sup> of interaction length, and can penetrate the atmosphere and also into the continental crust. Detailed discussion of muon interactions with matter can be found in Ref. [155].

A variety of backgrounds can be induced by cosmic rays in a detector [156]. 1) Prompt interactions: electrons and protons can be stopped in the detector shielding, but muons may go through the shielding and hit the sensitive volume. 2) Cosmic bremsstrahlung: muons can produce showers of particles in the shielding and thus give rise to event rate in the detector volume. 3) Delayed events: neutrons can be produced by muons in (high atomic) materials like lead, and they can excite or be absorbed by some nuclei which later decay, resulting in delayed signals.

Although cosmic ray muons cannot be stopped by passive shielding, active veto systems can be used to tag events that are in time coincidence with muons. 2" of EJ-200 plastic scintillator panels, manufactured by ELJEN Technology and loaned by FNAL to Princeton University, are installed around the lead shielding of the low background detector. Events in the inner detector that are in time coincidence with veto signals are attributed to muon interactions and are discarded. It is estimated that at least  $\sim 10$  MeV of ionizing energy would be deposited by a muon event in the veto panels. The energy is subsequently converted into scintillation light, and



Figure 3.14: The muon veto panels mounted outside the lead shielding.

two Hamamatsu R550 PMTs are mounted diagonally on each panel to collect this light. The PMT signals are fed into LeCroy 623B amplitude discriminator channels, which produce 50 ns long logic pulses if the preset threshold is passed. A LeCroy fan-in/fan-out module takes all the discriminator outputs and uses logical operations to determine if a veto trigger shall be sent out. The veto signal is then passed to the data acquisition system and is recorded along with the inner detector signal.

A conservative trigger algorithm is used in the veto system. The discrimination threshold on each veto PMT channel is individually set to yield a signal rate about twice the estimated muon rate on surface. For example, the dimension of the top scintillator panel is 34" by 34", and the estimated muon passing rate is  $\sim 150/\text{s}$  while horizontally placed; so the discrimination level for each PMT on this panel is set to yield approximately 300 Hz of veto signals. At this threshold level, gamma rays from a  $^{22}\text{Na}$  source can be observed, which indicates a threshold at the level of 1 MeV. The fan-in/fan-out module is configured to be a logic OR so that a veto signal is generated whenever at least one PMT sees a valid signal. In this way, we hope to minimize the

unvetoed muon rate while the dead time is at a relatively low level. All 5 veto panels produce a typical veto rate of 1000 Hz - 2000Hz, and result in a dead time of  $\leq 1\%$  with a veto window of a few microseconds.

### 3.2.3 KURF Laboratory

As has been discussed, cosmic ray muons cause background contamination in all experiments because they are almost impossible to shield against. An active muon veto system can suppress the cosmogenic backgrounds that are in time coincidence with a prompt muon signal, but has little effect on delayed cosmogenic events. In addition, cosmogenic neutrons activations on detector components may produce gamma rays seconds, or even days, after the associated muon event. There is no practical way for these events to be tagged and rejected. What's more, the muon veto efficiency may be affected by the system coverage, the signal collection efficiency, and statistical fluctuations. Even if the veto efficiencies is high, the un-vetoed cosmogenic event rate can be significant with the large cosmic ray flux at surface.

Low background experiments can be housed at underground locations to suppress the cosmic ray background. The dense continental crust ( $\sim 3\text{g/cm}^3$ ) serves as a more effective shield against muons compared to the atmosphere. The overall interaction depth of the 10-100 km high atmosphere is  $\sim 1000\text{g/cm}^2$ , which is comparable to only 3 meters of typical rock. The average muon energy is  $\sim 4\text{GeV}$  at sea level and the typical energy loss is estimated to be  $\sim 2\text{MeV}/(\text{g/cm}^2)$ , so muons are expected to be attenuated at a scale of  $\sim 2\text{kg/cm}^2$  [119]. Reduction factors of many orders of magnitude in the cosmic muon flux have been reported in underground laboratories such as LNGS and SNO. Fig 3.15 shows the estimated (and measured) muon flux for different depths of overburden.

The Kimballton Underground Research Facility (KURF) [158] is hosted by the Lhoist North America (LNA) Kimballton mine in Ripplemead, VA. The experimen-

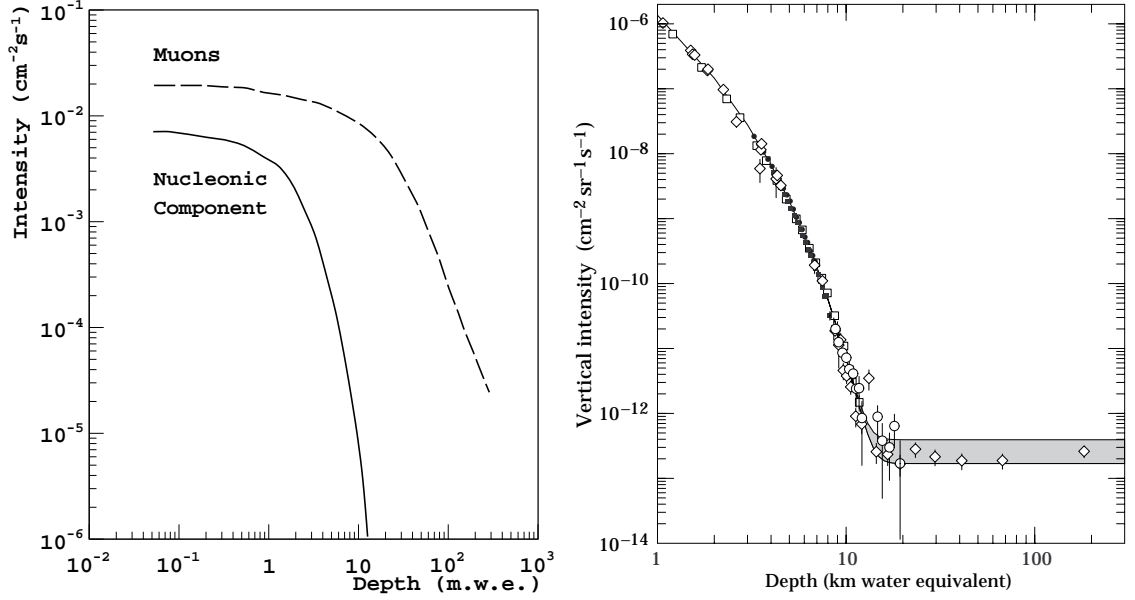


Figure 3.15: Left: Qualitative illustration of muon flux at moderated depth; the nucleonic component contains  $>97\%$  secondary neutrons [119]. Right: a compilation of muon flux measurements in large-depth underground locations; the shaded region represents the neutrino induced muon flux above 2 GeV energy [157].

tal hall, as shown in Fig. 3.16, is located at the 14th level of the mine, with  $\sim 1700$  ft of limestone overburden above it. This is equivalent to  $\sim 1450$  meters of water shielding and is expected to suppress the cosmic muon flux by 4 orders of magnitude. The airborne radon concentration in the laboratory was measured to be  $\sim 37$  Bq/m<sup>3</sup> in winter times and  $\sim 122$  Bq/m<sup>3</sup> in summer times [159], which is comparable to the typical values at surface laboratories. The KURF lab also features drive-in access, providing convenient transportation for personnel and equipments. The lab is administrated by Professor R. Bruce Vogelaar and Doctor S. Derek Rountree from the physics department of Virginia Polytechnic Institute and State University in Blacksburg, VA. Many users of the lab, including the Princeton  $^{39}\text{Ar}$  measurement group, also contributed to the upgrading and maintenance of the lab.

The cosmic ray muon flux in the KURF experimental hall was measured with two of the muon veto scintillator panels operated in coincidence mode. The two 29"x50" panels were placed horizontally with one on top of the other, separated by

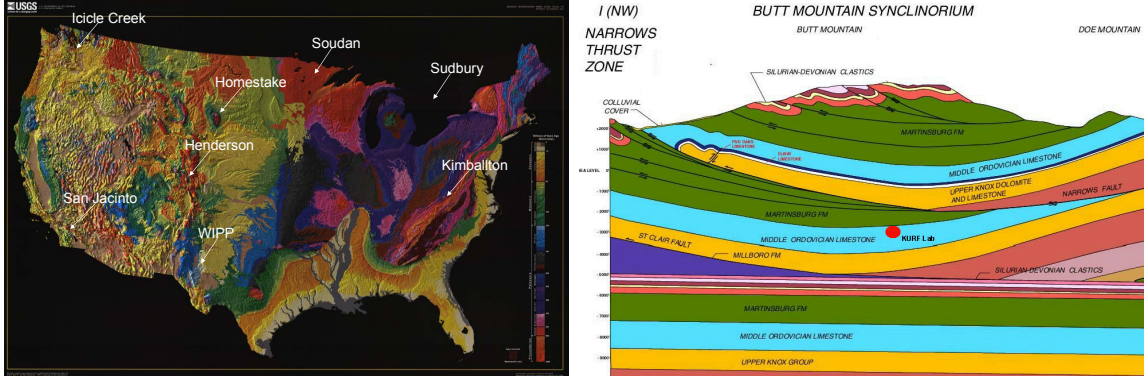


Figure 3.16: Left: the location of KURF along with other US underground facilities; Right: The Butt Mountain synclinorium and the position of the KURF experimental hall.

approximately 6". The discrimination levels on the PMT output signals were set at very low values so that each scintillator panel yielded a signal rate orders of magnitude higher than the expected muon rate. In this case the real muon coincidence rate is negligible compared to the trigger rate, and the false coincidence rate can be estimated as the product of trigger rates from both panels:

$$\begin{aligned}
 R_{F.C.} &= R_{P,1} \cdot R_{P,2} \cdot \tau \\
 &= 78.7 \text{ Hz} \times 89.4 \text{ Hz} \times 2\mu s \\
 &= 1.41 \times 10^{-2} \text{ Hz}
 \end{aligned}$$

where the coincidence window is set to be  $2 \mu s$ .

The false coincidence rate was also studied by examining the correlation of the trigger time in the two channels. A muon penetrating the two panels would lead to simultaneous signal triggers, while the trigger time difference of random coincidence events will spread out uniformly. From this approach, the false coincidence rate was estimated to be  $R_{F.C.} = 1.52 \times 10^{-2} \text{ Hz}$  for the same  $2 \mu s$  coincidence window, which is very close to the result from simple event rates calculation.

After the false coincidence events were statistically subtracted, the remaining

(“true”) coincidence event rate was calculated to be  $R_C = 1.20 \times 10^{-2}$  Hz, or  $1.27 \times 10^{-2}$  Hz/ $m^2$  if normalized by the surface area of the scintillator panels. A simple Monte Carlo simulation indicated that approximately 20% of muons would hit one panel and miss the other with the assumption of  $\cos^2\theta$  angular distribution for the residual muons at KURF. This correction factor of  $\sim 0.8$  brought the muon rate up to  $R_\mu = 1.6 \times 10^{-2}$  Hz/ $m^2$ , or  $R \simeq 1\mu/m^2/\text{min}$ . This value is approximately 10,000 times lower than the typical cosmic muon flux of 100-200 Hz/ $m^2$  at sea level, as expected from the previous estimation based on depth.

In addition, the uniformity of the light collection efficiency in the scintillator panels, and also the deviation of muon angular distribution from  $\cos^2\theta$  law at KURF, can lead to further corrections to the reported results. We assumed this measurement results to be accurate within a factor of 2. However, at the level of muon rate at KURF, other sources of background are believed to dominate, so this measurement of the muon flux is sufficient for background analysis.

## 3.3 Preparation of Argon for Measurements

### 3.3.1 Purification of Underground Argon

As discussed in Sec. 2.3.3, a VPSA unit was used to extract argon from the raw carbon dioxide gas at the Cortez site [127]. The gas product in the 2009-2010 operations contained  $\sim 70\%$  nitrogen,  $\sim 27.5\%$  helium, and  $\sim 2.5\%$  argon by volume, and it was improved to  $\sim 40\%$  nitrogen,  $\sim 55\%$  helium and  $\sim 5\%$  argon in 2011 runs. Further purification of the product gas using a cryogenic distillation column has been shown to reduce the nitrogen content by approximately 3 orders of magnitude and the helium content by more than 5 orders of magnitude [129].

Before the distillation column was commissioned, the argon product from the VPSA unit was purified with a zeolite column operated at Princeton University. The



zeolite system contains 18 kg of Zeochem’s Zeox Z12-07 zeolite in a 30L aluminum gas cylinder to absorb the nitrogen content in the gas mixture. This zeolite, consisting of beads with diameters between 0.4 mm and 0.8 mm, has a reported nitrogen adsorption capacity of at least 21 mL/g at STP. The gas to be processed was fed into the zeolite column at a flow rate of 10 L/min, producing an effluent stream of concentrated argon and helium. This enriched argon gas was then passed through a 6 L stainless steel bottle that was immersed in liquid nitrogen and filled with 2 kg of OVC 4x8 activated charcoal (manufactured by Calgon Carbon). This cryogenic charcoal trap captured the argon and allowed the helium to escape. During this process, a small fraction of argon was trapped in the zeolite column. It was recovered by purging the saturated zeolite column with helium; the desorbed gases were captured in another cryogenic charcoal trap for further reprocessing.

The argon gas processed by this system had a nitrogen concentration less than 1% by volume, as measured by a SRS UGA 300 residual gas analyzer. During the processing of a recent batch of underground argon from the Cortez site, we demonstrated that iterations of these processes can bring the nitrogen level below 0.1%.

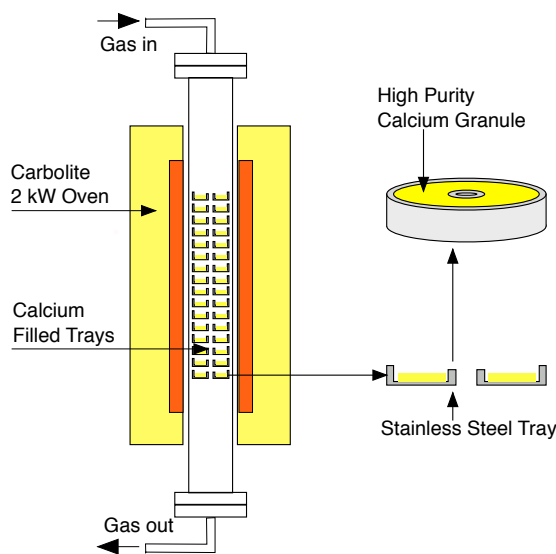


Figure 3.17: The hot calcium trap used for argon gas purification.

Further treatment of the argon gas from the zeolite column and that from the distillation column, involved the use of hot calcium to remove the remaining impurities. A calcium trap, illustrated in Fig. 3.17, held trays that were filled with granules of >98.0% purity calcium within a Conflat-sealed stainless-steel cylinder. The cylinder was first heated to above calcium’s melting point (842 degrees Celsius) for a short time to expose a fresh layer of calcium, and then the temperature was reduced slightly for the gettering actions. The argon gas flow through the hot calcium oven was controlled at  $\sim 1$  L/min to allow effective reactions between the calcium and the impurities. Stable solids such as calcium nitride were produced and remained in the trays, while argon passed directly through and got collected in a cryogenic charcoal trap. The cycles of refreshing by overheating the calcium could be repeated for several times until the calcium was largely consumed. Then the trap was opened, cleaned, and reloaded with fresh calcium.

### 3.3.2 The Detector Gas Handling System

Before the underground argon sample was filled into the low background detector for measurement, it was purified again in the detector’s gas handling system. The components of the system, shown in Fig. 3.18, were connected with copper/stainless steel tubing and Swagelok fittings (Conflat seals on the detector chamber). A Pfeiffer HLT 570 helium leak detector was used to ensure a leaking rate below  $10^{-8}$  mbar·L/s level in the system. The functionalities of the system include: 1) evacuate the detector to high vacuum levels to remove impurities; 2) purify the argon gas as it is filled into the detector; 3) condense the input argon gas into liquid phase and maintain a stable cryogenic condition; 4) recover the argon gas efficiently after each measurement.

A turbo-molecular pump (Pfeiffer Vacuum HiCube) was used to evacuate the gas plumbing and the detector chamber. Typical vacuum levels of  $10^{-6}$  mbar were obtained with several hours to a few days continuous pumping; purging the system

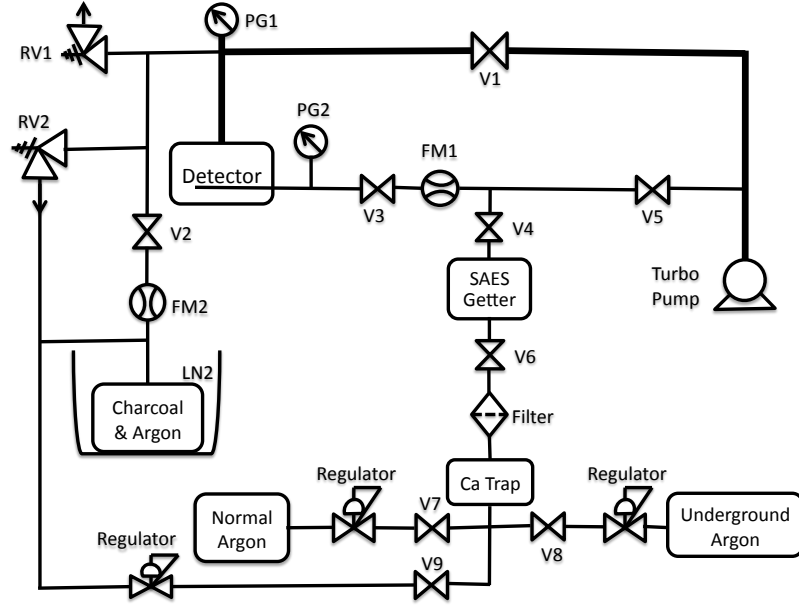


Figure 3.18: The gas handling system of the low background detector. The argon samples are purified as the detector is being filled, and can be fully recovered without loss with the liquid nitrogen cooled charcoal trap.

with high purity argon gas was found to be effective in speeding up this process. Usually 2-3 days of pumping/purging period were used before the  $^{39}\text{Ar}$  measurements to suppress the outgas from detector components. In some situations when quick detector assembly and filling were desired, the copper sleeve of the inner detector was baked to high temperatures ( $>100^\circ\text{C}$ ) while being pumped; meanwhile the inner parts were pumped in a separate vacuum chamber at room temperature to avoid re-evaporation of WLSs. A quick assembly and additional 2-3 hours of pumping were found to yield acceptable argon purities.

Once the vacuum reached the desired level, the filling process began. The calcium trap described earlier and a Mono-Torr zirconium metal getter were used to remove residual impurities such as water, oxygen, and nitrogen from the argon. The two purification units were usually turned on to warm up (including overheating the calcium) a few hours before the filling started. The argon gas was purified by the calcium oven, passed through a filter to remove particle contaminants from the oven,

and was then fed into the SAES getter. The SAES getter can absorb oxide and nitride impurities and form irreversible chemical bonds; it is reported to be capable of reducing impurities down to below 1 ppb level [160].

The inner detector and the copper shielding were cooled by a bath of commercial liquid argon in the double-wall cryostat. The liquid level in this bath was maintained by a Teragon LC10 liquid level controller, which read electric signals from two Teragon LS10-48 liquid level sensors and controlled a solenoid valve. The solenoid valve was mounted on a liquid argon storage tank and controlled the liquid argon flow to the cold bath. This liquid level system was designed for liquid nitrogen use, but was certified to work with liquid argon by the manufacturer. Because argon is usually used in the gaseous phase, the storage liquid argon tanks provided by Airgas are by default equipped with high value pressure relief valves (230 psi) to prevent argon gas from being wasted. Typical solenoid valves, however, are designed to operate at low pressures, as in the case of liquid nitrogen systems. Therefore, modification of reducing the relief pressure to 22 psi (as on regular liquid nitrogen tanks) was requested to Airgas for this experiment.

The detector chamber was pressurized to slightly above the atmospheric during the cooling process to minimize impurity contamination due to potential leaks under the thermal shock. As the system temperature dropped to liquid argon temperature, the clean argon gas started to condense and get collected in the bottom scintillation cell. The liquid level was monitored with two PT1000 thermal sensors that are mounted slightly above the top of the cell. The PT1000 sensors exhibit different resistance values at different temperature and are widely used as temperature sensors. They can also be used as liquid sensors because liquid argon conduct heat more efficiently than gaseous argon and thus is more effective in keeping the PT1000 sensors cold. The resistance value of PT1000 ( $\sim 1000$  Ohm at room temperature) was observed to decrease by a factor of 2 when there is a gas-to-liquid phase change.

After the liquid argon was filled into the detector, the purity would gradually drop due to the accumulation of impurities. But no argon recirculation and re-purification were attempted in this experiment for a few reasons: 1) most of our  $^{39}\text{Ar}$  measurements lasted less than a few weeks, and this moderate deterioration was tolerable; 2) the outgassing rate of the detector components such as PTFE and copper was low, and it was further reduced by the cryogenic temperature and the pumping/purging procedure; 3) a recirculation system required a boiler in the liquid volume and may introduce backgrounds to the sensitive volume. The degradation rate of argon scintillation light yield was measured to be less than 0.5% per day if the detector preparation was appropriate, and it was monitored and corrected in analysis.

Safety features were also implemented in this system. In case of power failure or liquid argon shortage, liquid argon in the detector may boil off, cause the pressure to build up, and create hazards. An emergency venting/recovering system was designed to address this possibility. The pressure relief valve RV2 (shown in Fig. 3.18) was programmed to direct the over-pressured argon gas ( $\gtrsim 20$  psia) into a activated charcoal trap cooled by liquid nitrogen<sup>2</sup>. Another pressure relief valve RV1 was set to vent argon directly into air to protect the experiment in case RV2 failed. The relief pressure of RV1 was set at  $\sim 30$  psia, well below the maximum operating pressure of 3 bar (44 psia) for the Hamamatsu R11065 PMT.

After the  $^{39}\text{Ar}$  measurements were completed, the charcoal trap was used to recover the underground argon gas. In this case the pressure relief valve RV2 was bypassed and argon in the inner detector was driven to flow directly into the charcoal trap that was under partial vacuum. The argon vapor pressure at liquid nitrogen temperature was  $\sim 0.3$  bar (4-5 psia), and this was further reduced by the absorption of charcoal. A partial vacuum of 5-10 psia was usually observed at a continuous argon gas flow rate of  $< 2$  L/min, and the value could drop to a few psia when the flow was

---

<sup>2</sup>This charcoal trap was baked and pumped to high vacuum before use, and was tested to be capable of absorbing kilograms of argon at cryogenic temperatures.

stopped. It is worth noting that the latent heat required to boil off liquid argon may cause the detector temperature to drop below the argon freezing point if the argon transfer rate was too high. Electrical heaters were used in some runs to heat up the argon bath and speed up the recovery process.

The recovered underground argon gas can be transferred from the charcoal trap into an aluminum gas bottle using similar principles. The trap was heated to 140-150 C and created a high pressure to drive the argon to flow into the liquid nitrogen-cooled gas bottle. The absence of mechanical compressors in the transferring processes reduced the possibility of impurities contaminations in the gas.

### 3.4 Data Acquisition System

During the main measurement campaign, data acquisition of the low background detector was carried out using CAEN V1720B waveform digitizers. A V1720 unit houses 8 channels of 12 bit, 250 MS/s waveform digitizers with an input range of 2 V; the V1720B sub-model is equipped with an extended buffer size of 10 MB. Up to 21 such V1720(B) units can be installed in a single CAEN VME8100 crate, and individual digitizer boards can communicate with each other via optical links. In this measurement we only used one V1720B digitizer board for the two data channels (one for the inner detector PMT and one for the logic veto signal). A data acquisition computer can control a digitizer board directly through a fiber-optic interface, but if there are multiple digitizer modules being used a VME crate controller can be used to communicate with all boards. Firmware of the digitizers was provided by CAEN, while the online and offline analysis software was developed by graduate students in the DarkSide collaboration, with Ben Loer making the major contribution.

As illustrated in Fig. 3.19, the output of the inner detector PMT was digitized directly. This signal also provided the trigger to the data acquisition system, deter-

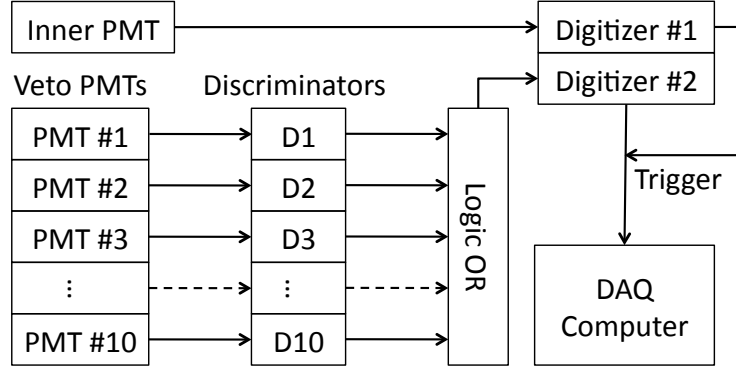


Figure 3.19: The data acquisition system of the low background detector. The inner PMT signal was digitized directly, while the veto PMT signals were discriminated and their logical OR was sent to a second digitizer channel.

mined by a voltage threshold and the pulse polarity. Typical trigger threshold in the underground measurements was at the order of a few photoelectrons, while it was set at higher values in the surface measurements to avoid excessive trigger rate rising from low energy backgrounds. Signals from the ten veto PMTs were processed by LeCroy 623B amplitude discriminators to produce 50 ns logic pulses, the logical OR of which was fed into a second digitizer channel. For each valid trigger, 15  $\mu\text{s}$  of data were recorded, beginning 5  $\mu\text{s}$  before the trigger time. Events with one or more veto signals in the pre-trigger window  $(-5-0 \mu\text{s})^3$  can be rejected as cosmogenic backgrounds, while delayed coincidence events separated more than 5  $\mu\text{s}$  apart were not vetoed. In the low muon environment at KURF, the application of the muon veto had no noticeable effect on the data; the veto was therefore disabled to avoid the (small) dead-time induced by random coincidences.

Before the CAEN system was acquired by the  $^{39}\text{Ar}$  measurement project, a Princeton Gamma Technology (PGT) Quantum Multiple Channel Analyzer (System 8000 MCA) was used in the data acquisition, as illustrated in Fig 3.21. Pulses from the inner PMT were integrated and amplified by an Ortec pre-amplifier (model 113),

<sup>3</sup>because of the relative delay of the veto signal in the logical operation modules, we allowed the veto signal to appear slightly after the inner PMT trigger.



Figure 3.20: The electronics rack and daq system. Left: the red front-panel crate on the top is the CAEN VME 8100 unit housing one CAEN V1720B digitizer board and one crate controller board; the two smaller units on top of VME crates are the DC power supply to the PT1000 sensors and the controller to the liquid argon level maintaining system; the rest are (from top to bottom): high voltage power supply to the inner PMT and (pre-)amplifiers, oscilloscope, logic modules for the veto signal processing, and HV distributor and HV power supply for the veto PMTs. Right: the data acquisition computer showing some online analysis results.

which was further boosted by an Ortec spectroscopy amplifier (model 672). The amplified pulse height was then digitized by the MCA to produce an energy spectrum. The MCA unit could take a gate signal to operate in coincidence or anti-coincidence mode, which allowed the selection or the rejection of the muon induced events. The muon gate signals were triggered by the logical OR of the discriminated veto signals in a gate generator. No scintillation waveform was saved, nor was the timing information. For waveform studies, a Tektronix Digital Phosphor Oscilloscope DPO7354 was used. The DPO7354 unit is a 4 channel, 40 GS/s sampling rate, 3.5 GHz band



width oscilloscope with many advanced functionalities. It is capable of recording up to 40,000 waveforms in a single acquisition in the fast-frame mode.

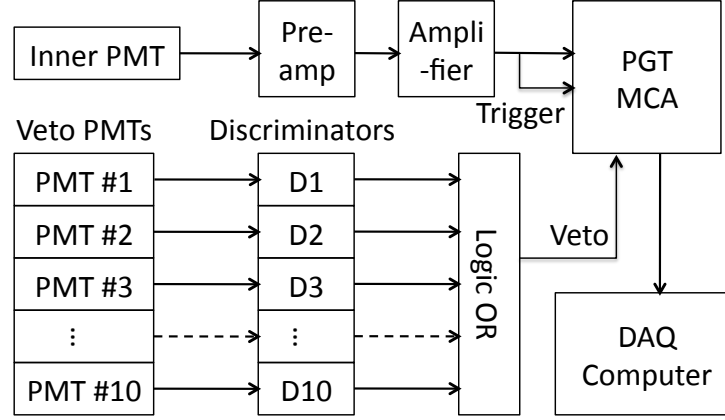


Figure 3.21: The DAQ system in the preliminary stage of the low background detector.

A system for monitoring the detector status was developed by Pablo Mosteiro and Dave Holtz for the  $^{39}\text{Ar}$  measurement. It provided remote access to the detector status during the underground operation at KURF. A MKS Type 740B Baratron Pressure Transducer and a NI SUB TC01 thermal meter probe were installed to monitor the pressure and temperature inside the detector. The pressure and temperature measurements were read into a National Instruments (NI) cRIO 9002 compact RIO real time controller and the values were displayed on a computer via LabView interface. The status of the liquid level controller system was also monitored by the LabView program, but no active control was attempted. History of the detector status was recorded automatically for later reference, and VNC connections were used to provide realtime remote access to this monitoring system.

# Chapter 4

## Measurements and Results

The measurement of  $^{39}\text{Ar}$  activity in the underground argon with the low background liquid argon detector was carried out in two major stages. The first stage involved the construction of the low background detector and a series of initial tests in a ground level laboratory in Princeton University from 2009 to 2010. Despite of a low light yield and a moderate level of background, the system revealed the first underground argon energy spectrum that clearly showed the low  $^{39}\text{Ar}$  concentration compared to that in atmospheric argon. Following the first measurement, substantial parts of the system were upgraded to achieve a lower background rate and a higher light yield. This stage of the measurement is referred as the main measurement campaign, which included both surface measurement in Princeton University and underground operations in the KURF laboratory. The most stringent upper limit of  $^{39}\text{Ar}$  content in the underground argon, 0.65% compared to the  $^{39}\text{Ar}$  in the atmosphere, was obtained from the 2011 underground measurement after identified backgrounds are subtracted. The 2012 underground campaign, though suffering from higher background from unidentified sources, confirmed the low  $^{39}\text{Ar}$  limit in the batch of underground argon to be used in the DarkSide-50 dark matter detector below 1-2% atmospheric value.

## 4.1 Preliminary Studies

This low background  $^{39}\text{Ar}$  counting project began in late 2009. At that time the design of the inner detector employed a 26" long acrylic light pipe to separate the room temperature-rated Hamamatsu R6233-100 PMT from the liquid argon sensitive volume, as illustrated in Fig. 4.1. The light guide also helped suppress the background radioactivity from the PMT at the cost of non-negligible light loss. The detector setup shown in Fig. 4.1 was configured to operate with an ultra-low radioactivity liquid scintillator during a preliminary study of the detector performance and background level. For liquid argon operations, the top flange was replaced by a 5-way cross to house necessary gas and electric feed-throughs.

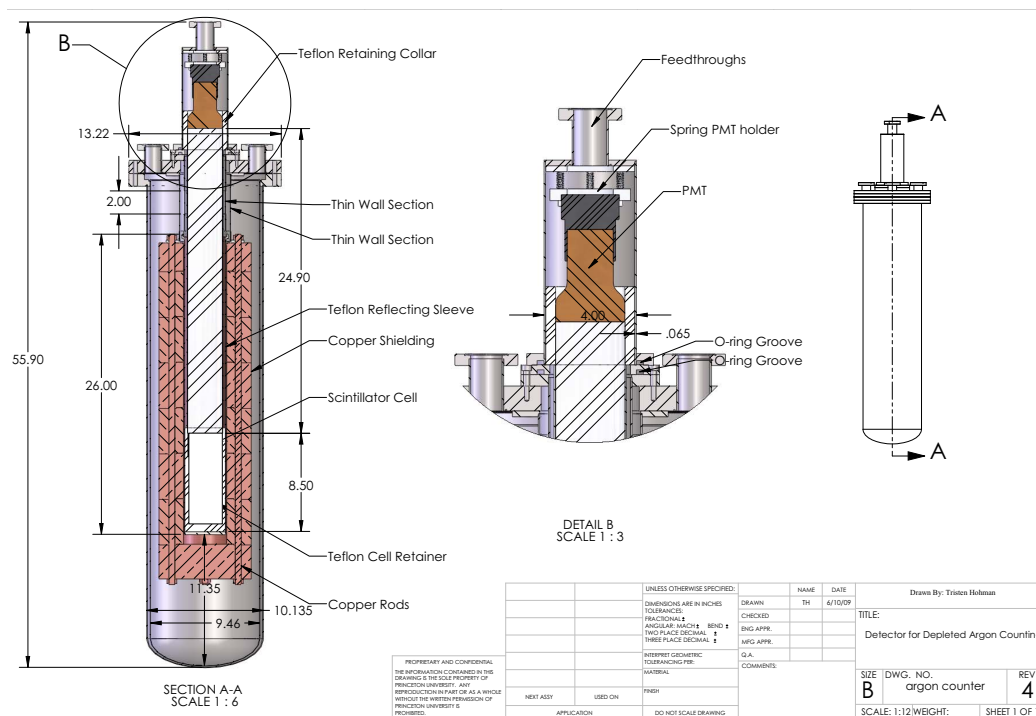


Figure 4.1: Schematic drawing of the original design of the low background argon detector. Compared to the “final” design in Fig. 3.1, a 26” long acrylic light guide is used along with a room temperature PMT Hamamatsu R6233-100; this schematic doesn’t include the gas and electric feed-throughs for liquid argon operation.

The data acquisition, as discussed in Sec. 3.4, was carried out with a PGT Sys-

tem 8000 Multiple Channel Analyzer (MCA). Signals from the R6233-100 PMT were integrated and amplified by an Ortec charge pre-amplifier and an Ortec spectroscopy amplifier before being recorded by the MCA. The Ortec amplifier has an adjustable gain up to 1,500, which makes it possible to study the system's single photoelectron (SPE) response and determine the absolute light yield for high gain PMTs like the Hamamatsu R11065. The SPE structure of the relatively low gain ( $\sim 10^5$ ) Hamamatsu R6233-100 PMT<sup>1</sup>, however, was not observed. So direct light yield measurements were not possible in some preliminary measurements.

#### 4.1.1 Background Study with Pseudocumene

Before the low background detector was tested with liquid argon, the detector background rate was evaluated with  $\sim 1$  kg of high purity liquid scintillator sealed in a fused silica cell. The liquid scintillator used was 1,2,4-trimethylbenzene, commonly known as pseudocumene or PC, which is also used in the solar neutrino experiment Borexino [161]. PC has a high scintillation yield of  $\sim 12$  photons/keV with a peak around 290 nm in the emission spectrum. The wavelength shifter (WLS) 2,5-diphenyloxazole (PPO) was dissolved at a concentration of 1.5 g/L to shift the PC light into longer wavelength ( $\sim 360$  nm) to increase the light collection efficiency. The Borexino scintillator was demonstrated to have an ultra low radioactivity level with 0.4 mBq/kg  $^{14}\text{C}$  and 0.2  $\mu\text{Bq/kg}$  of  $^{210}\text{Po}$ . The same quality scintillator was used to in this study.

Fig. 4.2 shows the energy spectra in the low background detector with the Borexino liquid scintillator. The energy scale was determined by fitting  $^{22}\text{Na}$  and  $^{137}\text{Cs}$  calibration spectra to the Monte Carlo simulated ones, assuming a linearity between the energy deposition and the observed photon numbers. A peak between 120 keV and 350 keV was observed in the un-vetoed energy spectrum, but was absent after the muon anti-coincidence cut was applied. This group of cosmogenic events were

---

<sup>1</sup>The maximal voltage rating for the Hamamatsu R6233-100 PMT is 1,500 V, but it was operated at 1,000 V to avoid high voltage breakdown in argon gas.

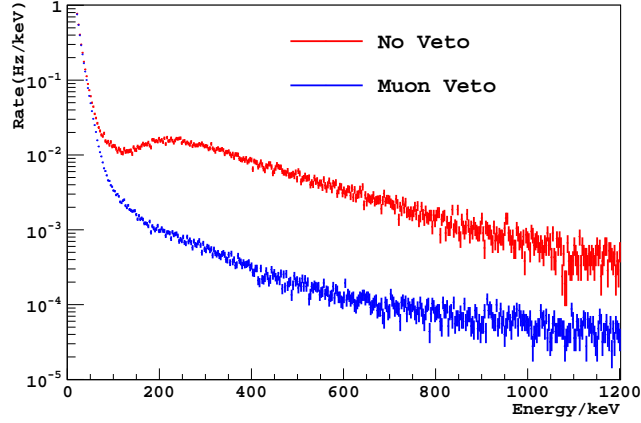


Figure 4.2: The background spectra taken with liquid scintillator in the preliminary stage of the low background detector with and without a muon veto system.

attributed to Cerenkov radiation induced by relativistic cosmogenic particles in the acrylic light guide because they disappeared after the light guide was eliminated in the second stage of the measurement.

Since the energy regions below 100 keV in both spectra were dominated by high rate background events, the energy threshold in this background estimation was set to be 100 keV. The event rate in the 100 keV - 800 keV energy window was integrated to be 5.4 Hz before muon veto and 0.36 Hz after muon veto, which confirmed that the dominant background had a cosmic ray origin. The background reduction factor due to the active muon veto was approximately 15, and more than half ( $\sim 2.8$  Hz) of the cosmogenic events appeared around the peak at 250 keV. If a similar background rate existed in the argon measurement, the expected  $^{39}\text{Ar}$  sensitivity would be  $\sim 40\%$  atmospheric with muon veto from a simple rate estimation. The sensitivity was limited by residual cosmic ray backgrounds at the Earth's surface.

The effect of the acrylic light guide in light collection was also evaluated with the liquid scintillator [162]. As illustrated in Fig. 4.3, the amount of light collected through the 26" long acrylic light guide was only  $\sim 40\%$  of that measured without a light pipe. However, since the aim of the low background detector was to measure the relative  $^{39}\text{Ar}$  abundance in underground argon compared to atmospheric argon,

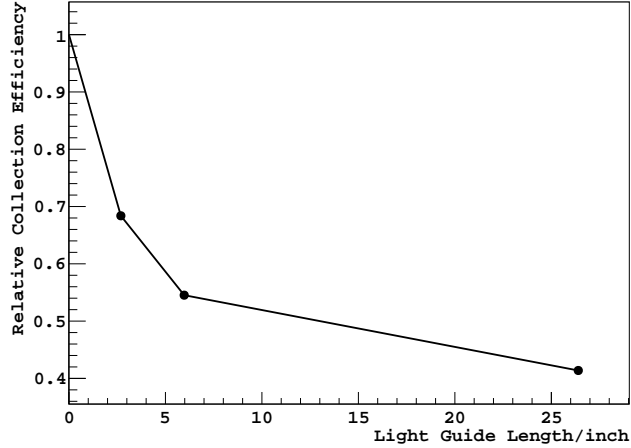


Figure 4.3: The relative light collection efficiency in the detector with different lengths of acrylic light pipe [162].

the absolute light yield was not critical. We comment that a higher light yield would improve the energy resolution of the detector appreciably.

#### 4.1.2 First Direct Evidence of $^{39}\text{Ar}$ Depletion

After the liquid scintillator tests, the low background detector was modified and tested for liquid argon operations. The first underground argon measurement took place in September 2010. A  $\sim 3/8$ " thick Teflon container with an aspect ratio of height:inner diameter  $\sim 3:1$  was used to contain the liquid argon sample (active mass  $\sim 1.15$  kg). The inner surface of the Teflon container was coated with the WLS Tetraphenyl Butadiene (TPB) at a thickness of  $200\text{--}300 \mu\text{g}/\text{cm}^2$  to shift the ultraviolet argon scintillation light into the visible region to be collected by the PMT.

Approximately 16 hours of atmospheric argon data (out of 2 days operation) and 28 hours of underground argon data (out of 4 days operation) were acquired with the muon veto system. Data with the veto system disabled were also collected to study the cosmogenic backgrounds. The operation time was limited because no automatic liquid argon level maintaining system was implemented at this time.

The recorded underground argon energy spectrum after muon anti-coincidence

cut is shown in Fig 4.4. This underground argon spectrum was observed for the first time, and it was clearly different from that of the atmospheric argon. The atmospheric argon data showed an excess of events below 800 keV, and this feature was attributed to the  $^{39}\text{Ar}$  decay electrons. The absence of such events in the underground argon spectrum confirmed its relatively low  $^{39}\text{Ar}$  activity.

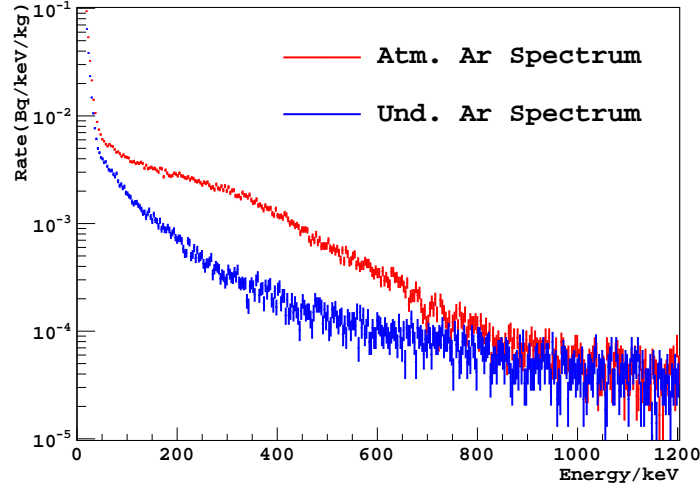


Figure 4.4: The energy spectra of underground argon and atmospheric argon observed in Sept. 2010 with the low background detector.

The event rate between 100 keV and 800 keV was 0.24 Hz/kg in the underground argon and 0.92 Hz/kg in the atmospheric argon data after muon veto cut. The rate difference of 0.68 Hz/kg in this energy window corresponded to a overall  $^{39}\text{Ar}$  activity difference of  $\sim 0.87$  Bq/kg, which corresponded to a limit of  $\sim 10\text{-}15\%$  on the  $^{39}\text{Ar}$  abundance in underground argon relative to atmospheric. However, the systematic uncertainties were believed to be large due to the smeared energy spectra. Spectrum fit was also attempted assuming a smooth background (two exponentials), which yielded  $\leq 5\%$   $^{39}\text{Ar}$  activities. The uncertainties, again, were difficult to determine, due to incomplete knowledge of backgrounds.

The residual event rate of 0.24 Hz/kg from 100 keV to 800 keV in the underground argon was comparable to that observed in the liquid scintillator (0.36 Hz for  $\sim 1$  kg). The exact mass and volume of the scintillator was not measured, so we could not

have a direct comparison. However, the event rate in the high energy region of the liquid scintillator data roughly agreed with that in 1 kg of liquid argon, as illustrated in Fig. 4.5; if we further assume the liquid scintillator spectrum represented the intrinsic detector background, the  $^{39}\text{Ar}$  activity in the underground argon spectrum was consistent with 0.

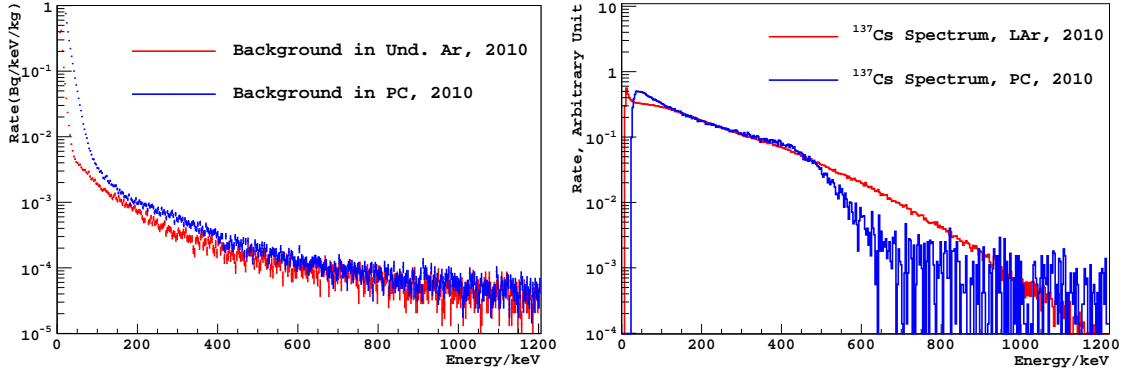


Figure 4.5: Left: comparison of the detector backgrounds measured with liquid scintillator and with underground argon; Right: comparison of the  $^{137}\text{Cs}$  calibration spectra taken with liquid scintillator and with liquid argon in Sept. 2010.

The slightly higher event rate in the liquid scintillator data at low energies was partially explained by the differences in sensitive volumes, masses and scintillation materials, and partially by the differences in electronic noise. The exponential noise spectrum at low energies was pushed down by approximately a factor of 2 in the liquid argon data. We believe this was due to an increase of light yield<sup>2</sup>. In addition, the configurations of the veto system were improved before the liquid argon measurement, so the rate of cosmogenic events that escaped the anti-coincidence system would be smaller. This may explain the reduced event rate between 200 keV and 400 keV, as indicated by Fig.4.5.

Although a higher light yield was observed in the liquid argon measurement, the energy resolution was considerably worse, as illustrated in Fig. 4.5. The Compton

<sup>2</sup>We comment that the absolute light yield of argon can be >2 times higher than that of liquid scintillator, but light loss is more significant in the liquid argon measurement due to variations in WLS efficiency and reflection efficiency.



scattering edge was clearly seen in the liquid scintillator data, but was not recognizable in the liquid argon data. A few factors were blamed for this difference.

1. The relatively small density of liquid scintillator and the low atomic number favored single Compton scattering of  $^{137}\text{Cs}$  gamma rays, and this gave rise to a clear Compton edge; while multiple scattering or even full energy deposition were likely to happen in liquid argon, which smeared the Compton edge.
2. The light collection efficiency in the PTFE container exhibited a large spatial variation due to light loss during the wavelength shifting process and reflections. A factor of  $\sim 2$  in light collection efficiency was observed between scintillation at the near-PMT end and the far-PMT end of the argon volume, as will be discussed in Sec. 4.2.2.
3. The light yield in the argon measurement degraded as impurities released by the detector components accumulated. And because the MCA system produced an energy spectrum for a run of events that extended a period of time, only run-level energy calibration was possible. The variation of light yield resulted in further smearing of energy spectrum.

The cosmogenic background in the liquid argon measurement was also studied. The energy spectrum with cosmogenic contamination is shown in Fig. 4.6. We didn't observed a peak structure around 200 keV like that in the scintillator data (Fig. 4.2); instead, a bump around 100 keV was visible in the spectral shape. If this bump feature had the same origin as the peak in the cosmogenic spectrum in the liquid scintillator measurement, the large shift in energy scale was suggesting that they were photon signals produced outside the active detector. For a photon background outside the scintillation cell, the apparent energy scale is calculated as:

$$E = \frac{\text{Number of Photons}}{\text{Light Yield}}$$

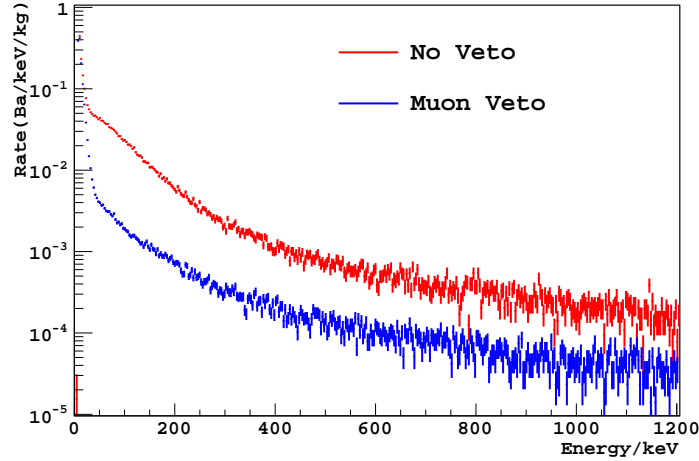


Figure 4.6: The background energy spectra in the low background detector (using underground argon) with and without the muon veto cut.

which appears at lower apparent energy for higher light yield. This argument also applied to the electronic noise in the very low energy regions. If we choose the same analysis window of 100-800 keV, the rate of the vetoed events was 1.81 Hz/kg, significantly lower than the value of  $\sim 5$  Hz in the liquid scintillator measurement. This confirmed the migration of some cosmogenic events out of the analysis window.

The lifetime of the slow component of argon scintillator was studied with a Tektronix oscilloscope. Usually 1,000 or more waveforms were averaged and a single exponential  $\chi^2$  fit was done in the time window of 1-7  $\mu$ s to estimate the lifetime. Typical values of 1.2-1.3  $\mu$ s were observed in the atmospheric argon run, and the values were 1.44-1.55  $\mu$ s in the underground argon measurement. The average lifetime degradation rate was at the level of  $\sim 0.1$   $\mu$ s/day, while it was observed to increase in the very beginning of the measurement ( $\sim 0.05$   $\mu$ s in the first 36 hours for the underground argon run).

## 4.2 Detector Upgrading

Based on the preliminary studies, we made substantial upgrades and carried out several tests with the low background detector from 2010 to 2011. Several detector components, including the PMT and the acrylic light pipe, the copper/lead shielding and muon veto, the WLS and reflector, as well as the data acquisition system, were modified or replaced to achieve a better performance.

### 4.2.1 Upgrade to Cryogenic PMTs

After the performance of the Hamamatsu R11065 PMTs was studied by the DarkSide collaboration, one such tube was acquired by the low background detector. This PMT model has a special bi-alkali photocathode that exhibits a high quantum efficiency ( $\sim 30\text{-}35\%$  at  $\sim 400\text{ nm}$ ) and can be stably operated at liquid argon temperature. It also has a high gain of  $\sim 10^6$  and a low radioactivity level, as discussed in Sec. 3.1. A custom-built high voltage divider and signal readout circuit was mounted on this PMT to avoid high voltage breakdown in argon gas. The acrylic light pipe became unnecessary and was removed from the system.

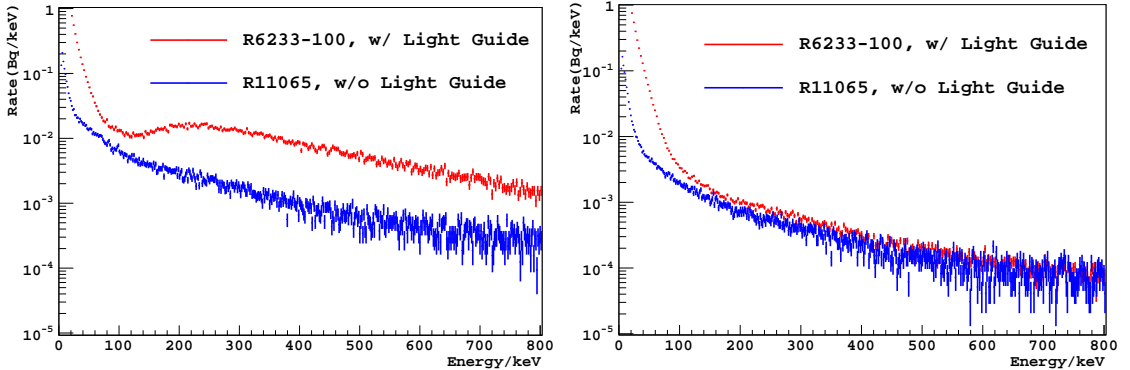


Figure 4.7: Background spectra taken with a R6233-100 PMT (with light guide) and with a R11065 PMT using liquid scintillator. Left: without muon veto; Right: with muon veto.

Fig. 4.7 shows the energy spectra taken with the R11065 PMT compared to that with the R6233-100 PMT using liquid scintillator. The event rate in the un-vetoed

spectrum was significantly reduced, especially around the bump feature at 200 keV. This improvement was attributed to the removal of the acrylic light guide and supported the Cerenkov radiation hypothesis of the events at the bump. In this new configuration, the event rate in the energy window of 100-800 keV was integrated to be 0.25 Hz and 0.96 Hz for the cases with and without muon veto cuts, compared to the values of 0.36 Hz and 5.4 Hz in the old setup.

The light collection efficiency, or equivalently the observed light yield value, was expected to increase by a factor of  $\gtrsim 2$  without the light pipe, based on the measurement in Fig. 4.3. This was confirmed by the suppression of electronic noise to lower apparent energy levels. As a result, a lower than 100 keV energy threshold was possible for the  $^{39}\text{Ar}$  analysis. We note that typical (gamma ray) backgrounds have decaying spectral shapes with increasing energy, while the  $^{39}\text{Ar}$  spectrum is rising below 200 keV, so the contrast may increase the  $^{39}\text{Ar}$  sensitivity for the spectral fit approach.

Following the removal of the acrylic light guide, the inner detector chamber was shortened; the copper-lead shielding and also the muon veto panels were adjusted to get a better coverage for the inner detector. A 2.5" thick copper plug was installed above the PMT base to achieve a  $4\pi$  copper coverage. During this process, all O-ring sealed flanges on the inner detector were replaced by Conflat flanges to reduce potential leaks from air during operation<sup>3</sup>.

### 4.2.2 Light Collection Study

The large spatial variation of the light collection efficiency in the argon container was blamed for the serious smearing of the energy spectrum, so the sources of the spatial dependence were investigated. The light source used in this study was a thin layer of WLS excited by a  $^{210}\text{Po}$  alpha source, as illustrated in Fig. 4.8. The WLS was

---

<sup>3</sup>The O-rings were not rated for cryogenic sealing purposes, and one of them was observed to leak when the liquid argon level got close to the top flange.

coated on a glass slide<sup>4</sup>, which was loosely pressed to a  $^{210}\text{Po}$  needle source using a spectralon clamp. The energy spectrum of the scintillation light, as shown in Fig. 4.8, consisted a of a low energy peak and a continuum up to a cutoff. The low energy peak rose from energy deposited by normal incidence alphas<sup>5</sup>, and the high energy cutoff corresponded to full energy deposition of alphas at large incident angles. A detailed discussion on the spectrum can be found in Sec. A.2.1.

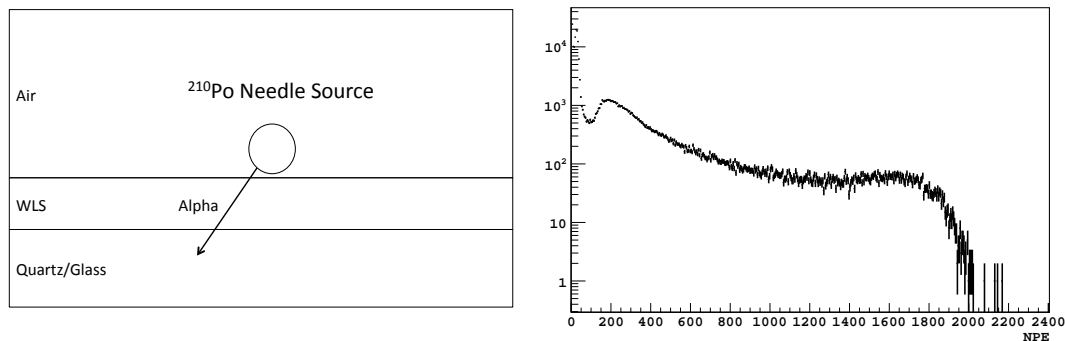


Figure 4.8: Left: the configuration of the light source used in the light collection efficiency study; Right: a typical energy spectrum taken with the alpha-WLS light source.

The light collection measurements were made in a dark box, with the alpha-WLS light source placed at different positions in the PTFE container. A variation factor of  $\sim 2$  was observed between the light collection efficiency at the bottom and the top of the container. As a control measurement, the PTFE cup was lined with a layer of 3M ESR film, which is know to give close to unit reflectivity over the TPB emission spectrum, and this configuration didn't show noticeable variations in light collections. However, once the 3M film was coated with TPB, the variation factor of  $\sim 2$  in light collection was observed again. In order to evaluate the effects of the glass slide, we also measured the light collection with the alpha source directly on the TPB coating of the 3M film. An increase of photon number by a factor of 2-3 was observed, but the spatial variation factor of  $\sim 2$  remained.

<sup>4</sup>Quartz slides were used in some measurements to reduce ultraviolet light loss.

<sup>5</sup>The alpha range in WLS is much larger than the coating thickness in this experiment.

Reflector Materials and WLS Configuration	Relative Light Collection Efficiency <sup>6</sup>	
	Middle/Top	Bottom/Top
PTFE, H:D~3:1, TPB coated	0.7	0.5
3M foil, H:D~3:1	~1	~1
3M foil, H:D~3:1, TPB coated	0.7	0.5
Special PTFE, H:D~2:1	-	0.8
Special PTFE, H:D~2:1, PTP coated	-	0.6

Table 4.1: The relative light collection efficiency for different reflector-WLS configurations.

These results were suggesting that the WLS coating was primarily responsible for the light loss. A explanation for the 3M film measurements was that the WLS changed the reflection type from specular to diffusive, which increased the average number of reflections and thus increased the light loss. The WLS quantum efficiency was also known to cause non-negligible light loss. The spatial variation in an uncoated PTFE cell (highly crystalline, mostly diffusive reflection, aspect ratio 2:1) was measured to be 1:0.8, but the variation increased to 1:0.6 after it was coated with WLS.

A optical simulation was used to cross check the measurement results. In the case of pure Lambertian reflection, an angular-independent reflectivity of 95% was found to induce a spatial variation of  $\sim 2$  at an aspect ratio of height:diameter=3:1. This equivalent reflectivity of 95% included both the light loss at the reflector interface and that in the WLS. The simulation also suggested that an aspect ratio to 2:1 could suppress the spacial variation to  $\sim 1:0.65$  and increase the overall light collection efficiency by 40-50%. We adopted this new aspect ratio in the upgrading to a highly crystalline PTFE cell at a cost of losing 1/3 of the active mass.

As reported by Ref. [147], the WLS chemical PTP is more transparent to its emission light and has a higher quantum efficiency, compared to TPB. Therefore, we switched from TPB to PTP in the hope of improving the light collection. Because the 3M ESR film exhibits a reflectance spectral cutoff around 350 nm, where the emission

---

<sup>6</sup>Uncertainty at the level of 5-10% should be expected in these reported values.

peak of PTP lies, we rejected the possibility of using 3M film as the reflector. A highly crystalline PTFE cell with height:diameter=2:1 was built for the new measurements. The light collection measurement was reported in Tab. 4.1, which approximately agreed with the simulation. The improvement of energy resolution with this new system could be seen in Fig. 4.9.

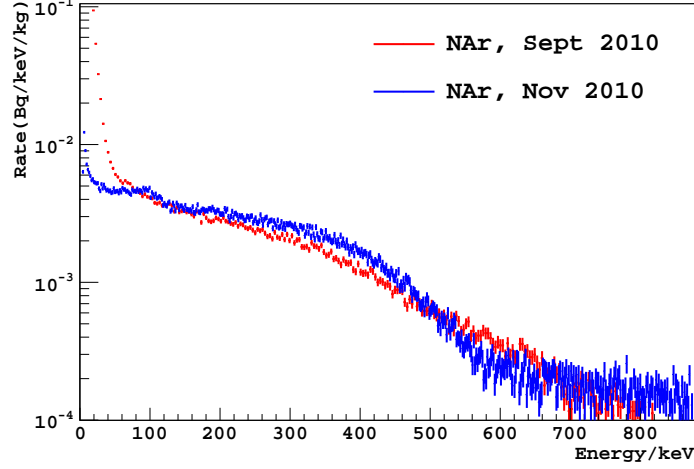


Figure 4.9: Comparison of the atmospheric argon spectra in the preliminary measurement and after upgrading. The upgrades include replacing the R6233-100 PMT with a R11065 PMT, removing the acrylic light guide, switching to PTP WLS, and reducing the argon container aspect ratio to height:diameter=2:1 using highly crystalline PTFE.

### 4.2.3 Investigation of Neutron Backgrounds

At a residual event rate at the level of  $\sim 10^{-3}$  Hz/keV/kg in the low background detector, cosmogenic neutron backgrounds may be significant. As we know, elastic neutron scattering can produce argon nucleus recoils, and these background could be rejected based on pulse shape discrimination. This possibility was studied using a 40 GS/s Tektronix oscilloscope to take waveform data in the fast-frame mode. The fast-frame mode enables users to take waveforms continuously, and tens of thousands of waveforms could be recorded in a single acquisition. The waveforms were saved in the text (.txt) format for offline pulse shape analysis.

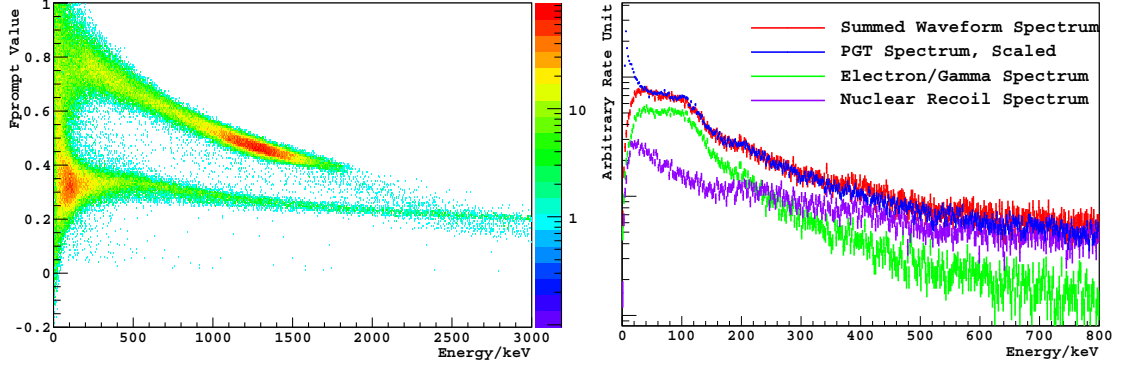


Figure 4.10: Left: the ratio of prompt argon scintillation to total scintillation for events at different energies, analyzed on the oscilloscope data; Right: spectra of the electron recoil and nuclear recoil events in the waveform data, compared to the MCA data.

The pulse shape analysis of the oscilloscope data, as shown in Fig. 4.10 (left), revealed two groups of events: one with a high fraction of prompt argon scintillation that was attributed to nuclear recoils and other high ionization events, and the other one with a low prompt fraction that came from electron recoils. The  $F_{\text{prompt}}$  parameter, defined as the fraction of argon scintillation light within 200 ns from the trigger<sup>7</sup>, was used to distinguish the two group of events. The higher  $F_{\text{prompt}}$  band exhibited a fast decreasing trend because of saturation effects; events with high  $F_{\text{prompt}}$  values had large prompt signal amplitudes, and they got truncated if they went beyond the range of the oscilloscope. Similar saturation happens to electron recoil events too, but at a larger energy scale because of the low  $F_{\text{prompt}}$  values.

The energy spectra of the electron recoil events and nuclear recoil events are shown in Fig. 4.10. The nuclear recoil rate went beyond the electron recoils at the energy of  $\sim 250$  keV and dominated the event rate in higher energy regions. As a result, a lower background rate can be obtained in the  $^{39}\text{Ar}$  measurement after the nuclear recoil events were rejected with the  $F_{\text{prompt}}$  parameter. However, dead time effect was observed in the oscilloscope data acquisition and not all valid triggers were recorded<sup>8</sup>,

<sup>7</sup>This time window is different from the 100 ns window used in the CAEN digitizer data analysis.

<sup>8</sup>We note it could be related to the oscilloscope settings. When the trigger was set at values less than half division of the oscilloscope voltage scale, almost no triggers were observed.



so no absolute background rate was directly derived in this analysis. We comment that the overall event spectrum of the waveform data matched the PGT data reasonably once the rates were scaled, and the high  $F_{\text{prompt}}$  backgrounds approximately counted for half of the residual event rate. It is worth noting that the “bump” structure around 100 keV electron recoil events in Fig. 4.10 was later identified to rise from inelastic neutron interactions, which couldn’t be rejected by pulse shape analysis but was significantly reduced by operating the detector underground.

Following the waveform study with the Tektronix oscilloscope, CAEN V1720B digitizers were acquired for waveform acquisition in the low background detector. A V1720B unit houses 8 channels of 12 bit 250 MS/s flash ADC waveform digitizers with 2 V dynamic input range, and can transfer data in real time to a data acquisition computer via fiber optic links. With a circular buffer design, the digitizer modules were rated for zero dead time operations.

## 4.3 Data Analysis in the Main Measurements

After the low background detector was upgraded, waveform signals from the inner detector PMT were directly digitized by the CAEN digitizers, and the muon veto signals were logically summed and then digitized by another channel of the digitizers. The data acquisition was triggered by a voltage threshold on the inner PMT channel, and  $15\ \mu\text{s}$  ( $-5 - 10\ \mu\text{s}$ ) of waveform data were recorded at each valid trigger. The unix timestamp and a nanosecond resolution trigger time were also recorded with each waveform. These raw data were processed offline to reconstruct the physical events.

### 4.3.1 Energy Calibration and Light Yield

In scintillation detectors, the event energy is usually estimated based on the total number of detected photons, or equivalently the integral of the scintillation waveform

in our case. In the low background detector data analysis, the integration was carried out by simply summing over all the digitizer samples after a flat baseline was subtracted. The baseline value was determined by the average of waveform values in the pre-trigger window after sparse pulses were removed<sup>9</sup>.

The translation from waveform integral to energy was realized by taking calibration with events of known energy. The calibration sources used in this project were  $^{137}\text{Cs}$ ,  $^{22}\text{Na}$  and  $^{39}\text{Ar}$ . The  $^{137}\text{Cs}$  source was used regularly to monitor the detector's energy response, while the  $^{22}\text{Na}$  source was only used in early measurements to check the linearity of liquid argon scintillation. When the detector was operated with atmospheric argon, the  $^{39}\text{Ar}$  electrons were also used as a calibration source.

In external gamma ray calibrations, the  $^{137}\text{Cs}$  and  $^{22}\text{Na}$  sources were introduced to a designated position outside the cryostat, at the same height as the center of the argon container. Because the gamma rays had to penetrate the cryostat, the liquid argon bath, the copper shielding (2"), the copper wall of the inner detector chamber, and the PTFE cell, before hitting the active argon volume, significant attenuation was expected. So strong gamma sources of  $10\mu\text{Ci}$  were used to increase statistics. The calibration spectra were then compared to Monte Carlo simulated spectra to estimate the detector's energy scale.

Typical  $^{137}\text{Cs}$  calibration spectra are shown in Fig. 4.11. A  $^{137}\text{Cs}$  nucleus decays to an excited state of  $^{137}\text{Ba}$  by nuclear beta decay, followed by the emission of a 661.7keV gamma rays with 85.1% branch ratio. The Compton edge of these gamma ray events was hardly recognizable due to multiple scatterings, and the Compton continuum region was also populated by interaction of gamma rays that had lost part of their energy in the shielding. Full energy deposition was unlikely because of the relatively small detector dimension of  $\Phi 2.5'' \times 5.2''$  compared to the attenuation length of  $\sim 4''$  of 661 keV gamma rays in liquid argon. Because of the broad energy

---

<sup>9</sup>A varying local baseline algorithm was also used in some situations, when the baseline exhibited irregular fluctuations at the time scale of microseconds or larger (usually due to electronic noise).

resolution, especially from the spacial variation of light collection, the end point of the  $^{137}\text{Cs}$  calibration spectra extended to 800 keV in this example.

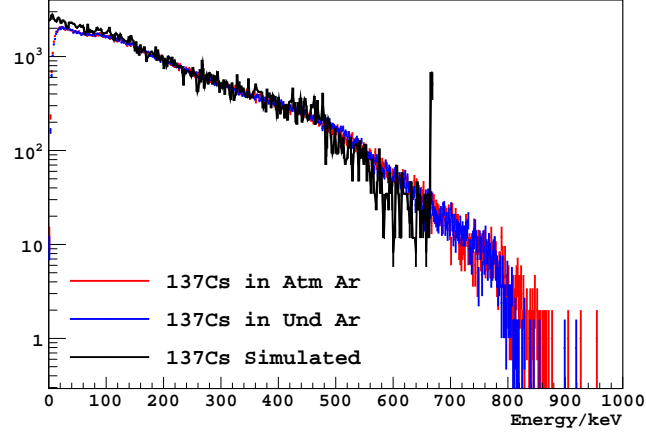


Figure 4.11: An example fit of two  $^{137}\text{Cs}$  calibration spectra – the energy scales of the two calibration runs differed by  $\sim 20\%$  before scaling; the Geant4 Monte Carlo simulated  $^{137}\text{Cs}$  energy spectrum is also plotted (without statistical smearing).

Besides broadening the energy spectrum, the varying light collection efficiency in the argon container also caused the observed  $^{137}\text{Cs}$  spectra to depend on the source positions. Although a calibration source holder was installed to ensure the same source position for all calibration measurements, the  $^{137}\text{Cs}$  calibrated energy scale was not well defined. As a result, the  $^{137}\text{Cs}$  calibration data were not used to determine the energy scale but to monitor the relative change during operation.

Given two  $^{137}\text{Cs}$  calibration measurements, the relative energy scale was determined by spectral comparison. One of the two  $^{137}\text{Cs}$  spectra was set to be the reference, and the other one was multiplied by a scaling factor and compared to the reference. Three algorithms were used in the comparison: 1) standard  $\chi^2$  test, 2) likelihood test [163], and 3) Kolmogorov-Smirnov test; the three approaches usually yielded results within 1% variation. This calibration method only considered the energy scale drift but ignored the change in resolution. Fig 4.11 show the energy spectra of two  $^{137}\text{Cs}$  calibration runs, the original energy scales of which differed by  $\sim 20\%$  but matched reasonably well after scaling.

The same calibration method was used on the  $^{39}\text{Ar}$  decay spectrum when the detector was operated with atmospheric argon. Because of the low  $^{39}\text{Ar}$  event rate ( $\sim 1\text{ Bq/kg}$  and  $\lesssim 1\text{ kg}$  active mass), usually hours of data were combined in the spectral comparison. This calibration agreed with the  $^{137}\text{Cs}$  calibration to better than 1% during stable operations. In addition, the  $^{39}\text{Ar}$  spectra were believed to give a better estimate of the detector's absolute energy scale because the  $^{39}\text{Ar}$  decay events were uniformly distributed within the active volume and their energy spectrum already included the effects of the spacial dependent light collection.

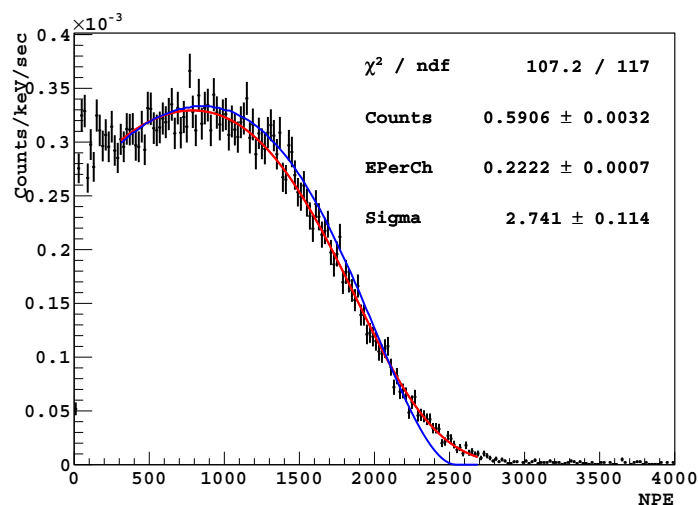


Figure 4.12: A fit of the subtracted  $^{39}\text{Ar}$  spectrum to the ideal one convolved with an Gaussian energy resolution function:  $\text{Gaus}(E, \sigma\sqrt{E})$ ; the red curve is the fit and the blue one shows the spectrum with perfect energy resolution.

During continuous data acquisitions, usually one  $^{137}\text{Cs}$  calibration run was taken every day. Then a continuous correction function (typically polynomials) was derived from the  $^{137}\text{Cs}$  calibrations, and from  $^{39}\text{Ar}$  calibrations if possible. This event-by-event correction was applied to both atmospheric and underground argon data to bring them to the same energy scale, and the difference between the atmospheric and underground argon spectra (live time normalized) was fitted to the ideal  $^{39}\text{Ar}$  spectrum with energy resolution. This fit determined both the energy scale and the energy resolution of the detector. For example, the fit shown in Fig 4.12 yielded an  $^{39}\text{Ar}$  rate of 0.59 Hz for

$\sim 0.56$  kg of argon, a light yield of 0.22 keV/p.e., or 4.5 p.e./keV in the conventional units, and an energy resolution function of  $\sigma(E) = (2.7\sqrt{E/\text{keV}})\text{keV}$ .

Besides the energy scale of a detector, another useful parameter describing the detector's performance is the light yield, defined as the number of photons detected for unit energy deposition. The light yield is important to understand the detector's energy resolutions. In the absence of instrumental noise, the energy resolution of a scintillation detector is restricted by the observed photon statistics:

$$\sigma(E) = E \sqrt{\frac{F}{N(E)}}$$

where  $N(E)$  is the photon number detected for energy deposition of  $E$  and  $F$  is the Fano factor [164]. This represents the ultimate energy resolution a detector could achieve. In the case of argon scintillation, the light yield is even more important in understanding the pulse shape discrimination power.

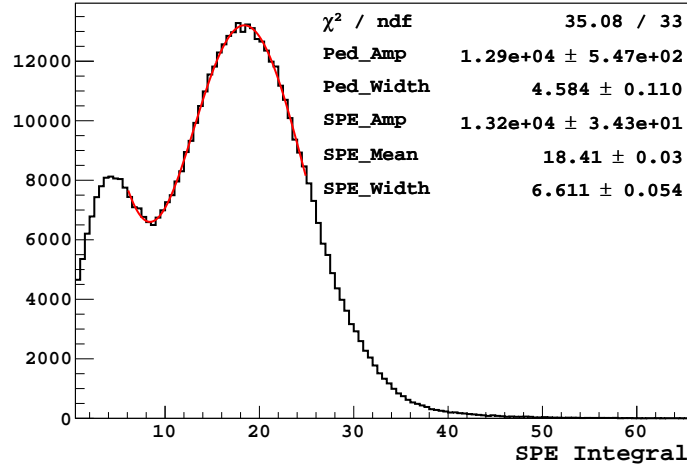


Figure 4.13: An example fit of a single photo-electron integral histogram to one Gaussian centered at 0 representing the pedestal and another Gaussian representing the SPE peak.

The light yield value can be calculated if the detector's response to single photon, or single photoelectron in our case, is measured. SPE data are usually acquired by sending controlled laser pulses to the PMT photocathode, but can also be studied by

picking out the small pulses in the tail of big pulses. We took the latter approach because we didn't implement a laser system in the low background detector. The selected pulses were then integrated to fill a histogram, as shown in Fig 4.13, which was then fitted to the expected SPE function:

$$f(x) = A_{spe} e^{-\frac{(x-\mu_{spe})^2}{\sigma_{spe}^2}} + A_{ped} e^{-\frac{x^2}{\sigma_{ped}^2}}$$

The first Gaussian peak represents the SPE integral and the second one centered at 0 represents the pedestal rising from baseline fluctuations. Due to the presence of multiple photon occupancy, the fit was carried out below where contributions from double photoelectron pulses became important. Similarly, we excluded the regions close to 0 in the fit because of the finite threshold in SPE pulse finding.

Typical light yields of 4-7 photo-electron (p.e.) per keV of energy deposition were observed in the low background detector. The best values were achieved by pumping and purging the inner detector chamber at high temperature for several cycles; at the same time the heat-sensitive components including the scintillation cell and the PMT were being pumped and purged at room temperature in a different vacuum chamber. Then the parts were quickly assembled in an argon-rich atmosphere for more pumping and purging cycles.

As impurities released from the inner detector components accumulated the argon purity degraded and the light yield decreased. As shown in Fig. 4.14, the typical degrading rate of light yield was around  $\sim 0.5\%$ /day in carefully prepared measurements, and this low rate was probably due to the low outgassing rate at cryogenic temperatures. For our average measurement periods of 1-2 weeks, the overall light yield degrading was not expected to be larger than 10%. No in-run purification of argon was implemented in the  $^{39}\text{Ar}$  measurements, and it was believed to be effective to monitor and correct the energy scale with calibration sources.

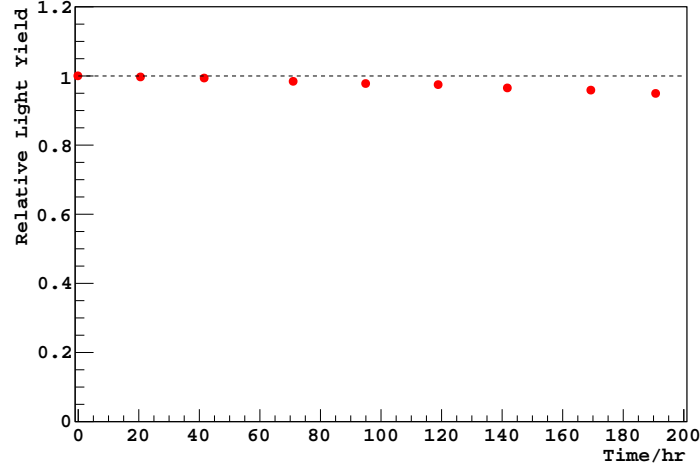


Figure 4.14: The relative light yield decrease in the atmospheric argon measurement in June 2011; this plot combined both the  $^{137}\text{Cs}$  calibration and  $^{39}\text{Ar}$  calibration; the errors are not explicitly shown because they are significantly smaller than 1%.

In addition to calculating the light yield, the SPE integral could also be used to estimate the gain of the photomultiplier tube. For example, the fit shown in Fig 4.13 yielded an SPE peak around 18 counts in a 12 bit CAEN digitizer with 2 V dynamic input range. Considering the 250 MHz sampling rate and the 50 Ohm input impedance, the charge collected by the CAEN 1720B digitizer channels is:

$$Q = \frac{18 \times 2V}{2^{12} \times 50\Omega \times 250 \text{ MHz}} \sim 7 \times 10^{-13} \text{ C}$$

With a MOhm termination resistor on the R11065 PMT base, essentially all anode charge was transferred to the 50 Ohm CAEN digitizer, so the gain is estimated as:

$$G = \frac{Q}{e} \sim 4.4 \times 10^6$$

which is at the same order of the nominal PMT gain ( $5 \times 10^6$ ).

It is worth noting that the gain of a PMT, and thus the integral of SPE pulses, is subjective to operating conditions. For example, the R11065 PMT gain with the customized base was observed to increased by 10-15% when it was cooled from room

temperature to liquid argon temperature. This was possibly due to the temperature dependence of base electronic components. Even at “stable” operation conditions, the gain could drift up to 5% within a few days. In addition, an empirical rule of the PMT gain dependence on the voltage is that the gain approximately increases by a factor of  $\sim 2$  for every 100 V increase of voltage.

### 4.3.2 Study of Slow Argon Scintillation

As discussed in Sec. 2.1, the argon scintillation light consists of a fast component and a slow component, and the ratio of the two strongly depends on the species of exciting particles. This property provides the basis of pulse shape discrimination that makes argon-based dark matter detection possible. However, the slow component of liquid argon scintillation can be highly quenched by electronegative impurities, in which case the light yield and the background rejection power degrade. So study of the slow component lifetime of argon scintillation is critical in monitoring the detector’s purity level and scintillation efficiency.

Because of the exponential decay of argon scintillation over time, the intensity of photons drops quickly. Even for high energy events that contain thousands of photons, the scintillation waveforms mostly consist of discrete photoelectron pulses after a few microseconds. Thousands of waveforms have to be summed/averaged to yield a continuous waveform for a statistically acceptable fit. In order to evaluate the goodness of fit and the uncertainties of the lifetime value, appropriate error bars need to be assigned to the summed/average waveform.

In the simplest situation where all waveforms to be analyzed have the same amplitude, the error bar at each sampling point can be computed statistically. Let  $a_i(t_j)$  denote the sample value at time  $t_j$  in the  $i$ th waveform, the averaged waveform and



associated error bars are:

$$\begin{aligned}\langle a(t_j) \rangle &= \frac{1}{N} \sum_i a_i(t_j) \\ \sigma(a(t_j)) &= \sqrt{\frac{1}{N} \sum_i (a_i(t_j) - \bar{a}(t_j))^2}\end{aligned}\tag{4.1}$$

In practice, however, we didn't have a mono-energetic signal with high enough rate to carry out this simple lifetime analysis, and often waveforms of very different amplitudes needed to be combined to yield enough statistics (keep in mind that the ultimate goal of this project was to reduce background and to achieve a low event rate). So it was desirable to appropriately propagate the the waveform uncertainties in the averaging process.

A straightforward way to combine the waveforms with different amplitudes is to take the direct sum  $S(t_j) = \sum_i a_i(t_j)$ , as in Eq. 4.1. Intuitively, this summed waveform can be interpreted as a single waveform with enormous photon statistics acquired by the system with a perfectly linear response. To evaluate the uncertainties in this sum, the equation can be rewritten as

$$S(t_j) = \sum_i a_i(t_j) = \sum_i \left( \frac{a_i(t_j)}{\sum_j a_i(t_j)} \cdot \sum_j a_i(t_j) \right)\tag{4.2}$$

which can be taken as the weighted average of the normalized waveform  $\frac{a_i(t_j)}{A_i}$ , with the weight  $A_i = \sum_j a_i(t_j)$  being the waveform integral. Equivalently, we can study the weighted average instead of the sum, and then the error at each bin is well defined.

$$\begin{aligned}\left\langle \frac{a(t_j)}{A} \right\rangle &= \frac{1}{\sum_i A_i} \sum_i \left( \left( \frac{a_i(t_j)}{A_i} \right) \cdot A_i \right) \\ \sigma\left( \frac{a(t_j)}{A} \right) &= \sqrt{\frac{1}{\sum_i A_i} \sum_i \left( \left( \frac{a_i(t_j)}{A_i} - \left\langle \frac{a(t_j)}{A} \right\rangle \right)^2 \cdot A_i \right)}\end{aligned}\tag{4.3}$$

We comment that the interpretation of this direct sum of waveforms as the weighted average of the normalized waveforms is only an approximation, and corrections can be made to this algorithm. However, when different approaches are taken to combine the waveforms, similar weighting mechanisms and uncertainty calculations are expected to be still valid.

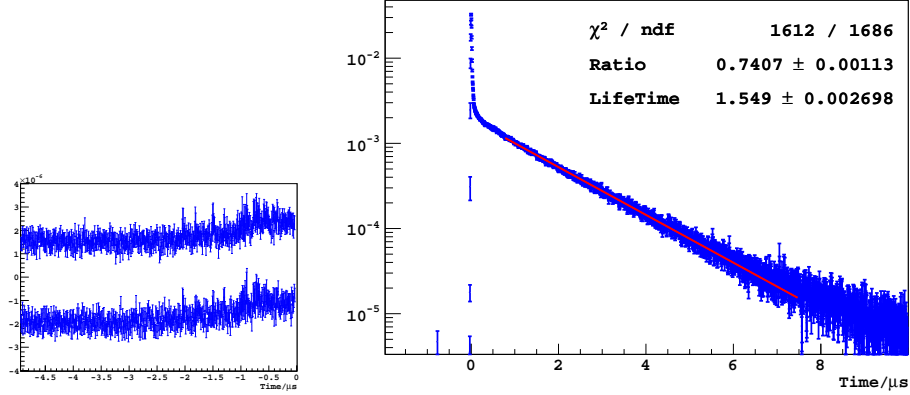


Figure 4.15: An example of the averaged electron recoil waveforms. left: zoomed-in picture of the pre-trigger baseline; right: an exponential fit to the slow component waveform.

Fig 4.15 shows an example of the averaged waveform over thousands of electron recoil scintillation events, where the exponential slow component is very prominent. A  $\chi^2$  fit was conducted in the time window of  $[0.75, 7.5] \mu\text{s}$ , and the lifetime was determined to be  $1.55 \mu\text{s}$ , with an amplitude of 74% compared to the total observed scintillation light.

An interesting phenomenon is that when many waveforms were averaged, the resultant baseline waveform before the trigger time split into two parallel sub-waveforms, as illustrated in Fig 4.15 (left). One possible explanation is that each of the 250 MHz CAEN V1720 digitizers consists of two 125 MHz sub-digitizers, the clocks of which were intentionally misaligned 4 ns apart to double the frequency. If this hypothesis is true, a slight offset between the ground potential of the two sub-digitizers could result in the double baseline phenomenon. However, in order for this hypothetical ground potential offset to survive the average over many waveforms, samples from

each sub-digitizers have to be aligned exactly in all waveforms. This is only possible if triggers from the two sub-digitizers are not distinguished in determining the data acquisition window. It would introduce a 4 ns uncertainty in the trigger time.

It is shown in Fig. 2.5 that the slow argon scintillation is very sensitive to the electronegative impurity level, while the fast component doesn't get significantly affected. Therefore, the light yield dependence on argon purity is dominated by the quenching of slow component. In this case the overall light yield can be estimated based on the observed slow component lifetime. Assuming the argon scintillation only consists of two independent exponential components,

$$f(t) = \frac{A_s}{\tau_s} e^{-\frac{t}{\tau_s}} + \frac{A_t}{\tau_t} e^{-\frac{t}{\tau_t}}$$

where the “A”s represent the scintillation amplitudes, the “ $\tau$ ”s represent the scintillation lifetimes, and the subscripts “s” and “t” stand for singlet (fast component) and triplet (slow component) respectively.

Fig. 2.5 also indicates that the initial intensity of the slow component scintillation (before the quenching effects start) is not affected by the impurity levels, which indicates that the ratio of  $A_t$  to  $\tau_t$  can be taken as a constant.

$$\frac{A_t}{\tau_t} = \frac{A_{t0}}{\tau_{t0}}, \quad A_t = \frac{\tau_t}{\tau_{t0}} A_{t0} \quad (4.4)$$

where  $\tau_{t0}$  and  $A_{t0}$  stand for the slow scintillation amplitude and lifetime at zero impurity level. Therefore, the total amount of light from both scintillation components, or equivalently the observed light yield, can be factored as a linear function of the slow component lifetime:

$$A = A_s + A_t = A_s + \frac{\tau_t}{\tau_{t0}} A_{t0} \propto 1 + \frac{A_{t0}}{A_s} \frac{\tau_t}{\tau_{t0}} \quad (4.5)$$

It's worth noting that if the light yield variation in an argon scintillation detector is exclusively resulted from the relaxation of the slow component, the light yield as a function of the slow component lifetime also depends on the ratio of fast-to-slow scintillation amplitude. As a result, the nuclear recoil energy in an argon detector can not be corrected based on gamma ray/electron calibrations if slow component relaxations are involved. Over-corrections of nuclear recoil energy can be caused by gamma ray calibrations, because nuclear recoils have a smaller slow component and the effect of slow component quenching is not as significant.

The light yield dependence on the lifetime of slow argon scintillation was studied with an  $^{241}\text{Am}$  source. The  $^{241}\text{Am}$  source was embedded in the bottom of the inner detector chamber (outside) to provide a real time calibration.  $^{241}\text{Am}$  nuclei decay to  $^{237}\text{Np}$  by emitting alpha particles of 5.6 MeV accompanied by a series of gamma rays. The most prominent gamma ray branch is at 59.5 keV (36% branch ratio) and was used to monitor the light yield drift. A typical  $^{241}\text{Am}$  spectrum is shown in Fig. 4.16, which was compared to the Monte Carlo simulated  $^{241}\text{Am}$  spectrum with a Gaussian resolution. The simulated spectrum with perfect energy resolution is also shown.

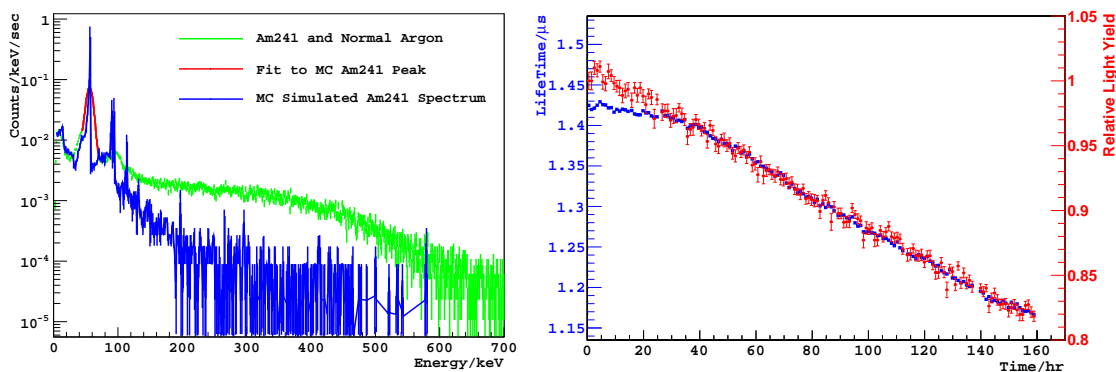


Figure 4.16: Left: the calibration spectra of  $^{241}\text{Am}$  gamma rays in atmospheric argon; Right: the degradation of light yield and slow component lifetime.

Approximately 200 hours of data were acquired with the  $^{241}\text{Am}$  source, which were combined in 1 hour bins in the analysis. The position of the 60 keV  $^{241}\text{Am}$  gamma

ray peak, and also the lifetime of the slow component scintillation were evaluated by  $\chi^2$  fits in the binned data. To reduce uncertainties from the averaging algorithm, only events around the 60 keV energy peak were included in the waveform study. The values of slow component lifetime and the relative light yield are shown in Fig. 4.16.

The degradation rate of the observed light yield was approximately  $\sim 2.95\%/day$ <sup>10</sup>. The lifetime values, however, exhibited a slower decreasing rate in the first 1.5 days and a faster rate afterwards. Similarly, the slow component amplitude relative to the fast (Fig. 4.17) showed a turnover point around 1 day, having increasing values before this point and decreasing values after this point. One hypothesis to explain the conflicting observations is that as the detector components released impurities into the argon volume, some impurities like water may prefer to condense on the cold surfaces of the argon container. As a result, the purity of argon degraded slowly, but the scintillation light was still absorbed by the impurities. After the water layer saturated the surface, all impurities came into the argon volume and a faster degradation in lifetime was resulted. We comment that during some measurements the slow component lifetime was observed to increase in the very beginning, and at the same time the light yield kept decreasing. To avoid complexity, data from the first 1.5 days were excluded from this analysis.

The assumption that the slow component amplitude (normalized to the fast component) is proportional to the slow component lifetime (Eq. 4.4) was first tested. The <sup>241</sup>Am data are shown in Fig. 4.17, and a proportionality was observed. The slope was determined to be  $A_t/A_s = 1.85\tau_t(\mu s)$ , corresponding to a ratio of 0.34 for the fast to slow scintillation amplitude at a lifetime of  $1.6 \mu s$ . This ratio was reported to be approximately 0.3 in Ref. [86], approximately consistent to our value. Plugging

---

<sup>10</sup>This value was larger than the typical values of  $<1\%$  due to a possible leak, so we took advantage of the large lifetime variation in this measurement for light yield study.

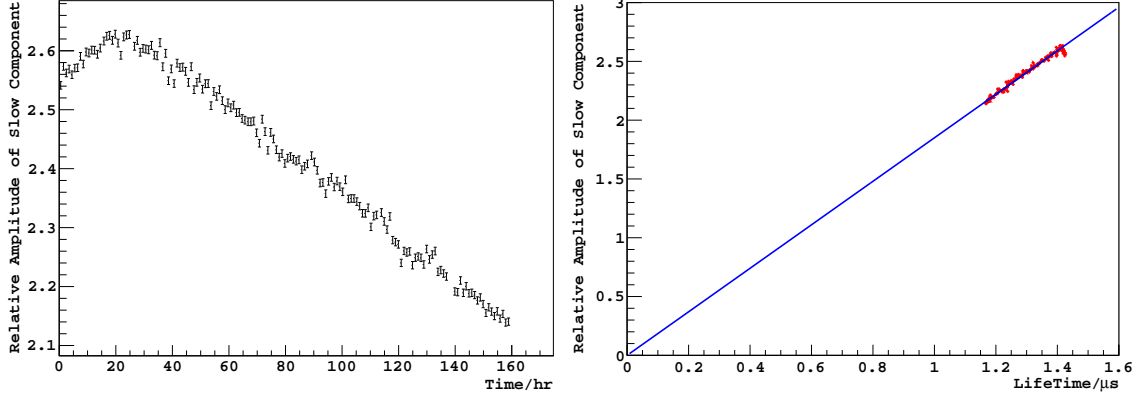


Figure 4.17: Left: the evolution of the slow component amplitude (normalized to the fast component amplitude) in the  $^{241}\text{Am}$  measurements; Right: The dependence of the slow component amplitude on the slow component lifetime.

the factor of 1.85 into Eq. 4.5, we can get an estimate of the light yield as:

$$\frac{A_t}{A_s} = 1.85\tau_t, \quad A = A_s + A_t \propto 1 + 1.85\left(\frac{\tau_t}{\mu s}\right) \quad (4.6)$$

This function agrees with the measured light yield data (Fig. 4.16) within 1.5% over the lifetime range of 1.15-1.4 $\mu\text{s}$  (the first 1.5 days of data were excluded), and the discrepancy may be large for lifetime values outside the fit window. Fitting the light yield to a linear function of the slow component lifetime returned a slope of 7.2 instead of 1.85; this difference was believed to rise from the light collection process. For example, a low lifetime value indicated a high impurity level in the detector, and the impurities can also absorb the scintillation light in addition to quenching the scintillation. Since Eq. 4.6 only considers the quenching effects, it underestimates the light yield dependence on the impurity level (slow component lifetime) of argon. We comment that the light yield and lifetime measurement with another detector in Princeton University<sup>11</sup> revealed a similar factor of  $A_t/A_s = 1.87\tau_s(\mu s)$ , but the observed light yield dependence on slow component lifetime was different, indicating

<sup>11</sup>This detector was dedicated to light yield study for the DarkSide project and was usually referred to as the 3" detector.

the light absorption process varies between experiments.

### 4.3.3 Data Quality and Cuts

In a rate counting experiment like the  $^{39}\text{Ar}$  measurement, it is critical to understand the event acceptance and the live time loss. While we made every effort to reduce the background event rate, we were also trying to maintain a high event acceptance level. As will be seen, the event loss due to hardware and software cuts were minimal in the low background detector.

The V1720 series digitizers were reported by CAEN to have 0 dead time with a circular memory buffer design. According to the data analysis with the DarkSide-10 detector, which used similar V1720(B) modules in a very intensive data acquisition situation ( $250\text{ }\mu\text{s}$  data acquisition window for 8 or 14 independent channels,  $>1,000\text{ Hz}$  while operated at surface), the system's dead time was predominately resulted from the write speed of the data-recording hard disk. This risk was significantly reduced in the low background detector because of its low event rate ( $\lesssim 1\text{ Hz}$  in the underground operations) and compact data size (2 channels  $15\text{ }\mu\text{s}$  data acquisition window). What's more, the digitizer model V1720B has an extended buffer size (10MS/ch).

However, anomalies such as system instabilities, data acquisition software failure, or hard drive communication errors, could result in unexpected loss of live time. Electronic noise and statistical effects such as event pileup could also cause some valid events to be rejected by the analysis software. The possibility of dead time in the low background detector data was studied from two approaches: the distribution of event time and the distribution of time interval between successive events. The former approach, being intuitive, tells if loss of live time at large time scales exist or not. The left figure in Fig. 4.18 shows a time spectrum of the event rate in a high rate  $^{137}\text{Cs}$  calibration run taken underground in July 2012. The average event rate was estimated to be  $169.2\text{ Hz}$ , and the instant rates at different times of the run were

within statistical fluctuations. If the data acquisition system was in a faulty state for a finite time, we would observe a drop in the event rate in this time window.

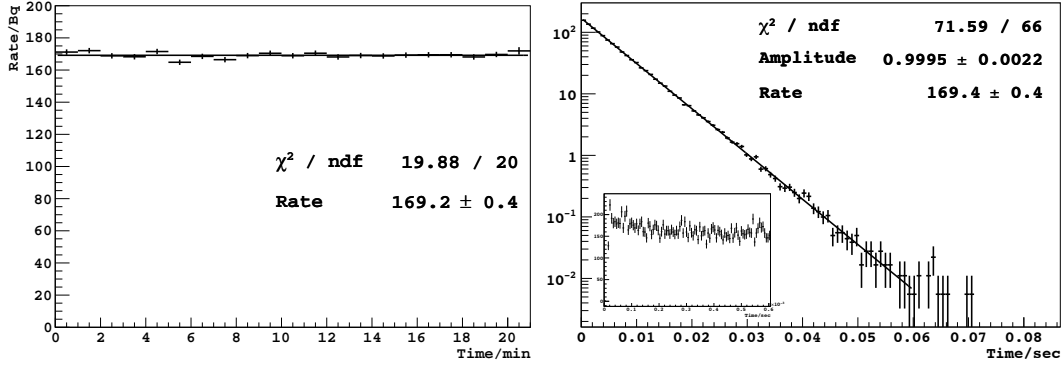


Figure 4.18: Dead time study of a  $^{137}\text{Cs}$  calibration run. Left: the event rate spectrum; Right: distribution of the time interval between successive events, and the insert figure shows the details of the first 600  $\mu\text{s}$ .

The limitation of this simple algorithm is that it doesn't help to identify systematic dead time. If the data acquisition system takes a certain time to recover from each acquisition, live time would be lost after every valid trigger; then the event rate would remain flat in time, but constantly lower than the true rate. The second approach of checking the time interval between successive events, however, allows such possibilities to be investigated. If a process causes a repeated live time loss, the observed time interval spectrum would exhibit a deficit at the relevant time scales. We will show that the expected distribution of the time interval between neighboring events is a simple exponential, depending on the average event rate  $\lambda$ .

For a group of events that occur randomly with certain probability  $\lambda$  in unit time, the expected number of events in a time interval  $\tau$  is  $\lambda\tau$ , and the observed events number in this time window follows the discrete Poisson distribution:

$$P(k; \lambda\tau) = \frac{e^{-\lambda\tau} (\lambda\tau)^k}{k!}$$



The probability for at least one event to occur before  $t = \tau$  is:

$$P(k > 0; \lambda\tau) = \sum_{k>0} P(k; \lambda\tau) = 1 - P(0; \lambda\tau) = 1 - e^{-\lambda\tau}$$

which could be equivalently interpreted as the probability for the first occurrence time  $t$  to be smaller than  $\tau$ :

$$P(t < \tau; \lambda) = 1 - e^{-\lambda\tau}$$

which is a cumulative probability distribution function. Taking the derivative, we will get the differential distribution function  $f(t)$  for the first occurrence time  $t$ , which is also the interval between two subsequent events.

$$f(t) = \lambda e^{-\lambda t}$$

The figure on the right of Fig. 4.18 shows an example of the exponential distribution on the same  $^{137}\text{Cs}$  calibration data set. The slope  $\lambda$ , or the rate parameter of the Poisson distribution, was fitted to be 169.4 Hz, which agreed excellently with the previous rate calculation. The insert figure shows the time interval distribution for the first 600  $\mu\text{s}$ , which allows us to study the possibility of dead time at small time scales. No statistically significant deficit was observed in the spectrum after 10  $\mu\text{s}$ , which was the end of the data acquisition window after each trigger. The absence of dead time in the high rate  $^{137}\text{Cs}$  calibration run indicated that it was even less likely for the low rate  $^{39}\text{Ar}$  measurements to have significant dead time.

However, the time interval spectrum in Fig. 4.18 (right) reveals a deficit in the first 10  $\mu\text{s}$ . This is an effective dead time due to analysis techniques. Pulses that arrive within the 10  $\mu\text{s}$  acquisition window of another event, usually referred to as pileup events, were excluded from the analysis. Typical argon scintillation waveforms

last for 7-8  $\mu s$ , so two pulses within a  $10\mu s$  time window usually had significant overlap and were difficult to unfold. Even if the two pulses can be separated, the later one is usually not fully contained in the  $10\mu s$  acquisition window. In addition, the pileup events rate was estimated to be insignificant and sophisticated analysis was not necessary. For example, the  $10\mu s$  acquisition window in the 170 Hz  $^{137}\text{Cs}$  calibration run lead to a loss of live time at the level of

$$\text{Dead Time} = \text{Rate} \times \text{Time Window} = 170\text{Hz} \times 10\mu s = 1.7 \times 10^{-3} = 0.17\%.$$

As for the  $^{39}\text{Ar}$  measurement runs, the typical rate was  $\lesssim 1$  Hz, which translated into a dead time of  $\lesssim 1 \times 10^{-5}$ , essentially negligible. As a result, no attempt to resolve the pileup events were made, and overlapping pulses would be rejected in the analysis.

As has been discussed, the event time distribution can be altered by live time loss at large scales (minutes or longer), but is blind to systematic dead time occurring at small scales (at  $\mu s$  level). On the contrary, the time interval distribution approach tracks repeated systematic dead time, but doesn't help occasional loss of live time. For example, if the data acquisition system crashes or suspends for a while, it only contributes one insignificant data point to the time interval distribution and may get overlooked. So it is important to combine both approaches for a complete study on the dead time issue.

Besides the data acquisition process, dead time can also be caused in the analysis by applying software cuts. An explicit software cut was the validation of baseline. Because the waveforms recorded by the CAEN V1720B digitizers carried an offset (baseline) it had to be subtracted before useful analysis could be done. The baseline was usually assumed to be a constant offset from 0, and was determined by the flat waveform section before the trigger. Small pulses, if existing in this window, were excluded from the baseline calculation. Typical distributions of baseline mean and

variance within a data run are shown in Fig. 4.19. A baseline was considered bad if it exhibited larger than normal fluctuations or if its mean value drifted at unreasonably large rates. In typical data runs approximately 1 out of  $10^5$  waveforms were rejected for having invalid baselines, and visual checks identified that most of the failing ones were not physical events.

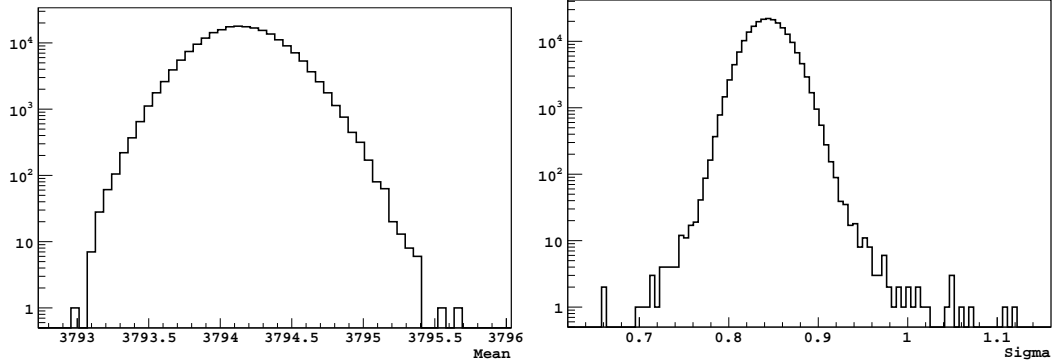


Figure 4.19: The mean digitizer baseline value and the standard deviation in an atmospheric argon run taken at KURF, the units are in digitizer sample counts.

A drifting baseline algorithm was also investigated. It calculated a locally averaged baseline and allowed this average to vary at relatively large time scales (microseconds or longer). This method was helpful in reducing electronic noise in some waveform studies. With this algorithm, even fewer waveforms failed the validation check because of the additional flexibility. However, due to its high computation demand and poorly understood uncertainty, this algorithm was not used in the  $^{39}\text{Ar}$  analysis.

Other software cuts applied in the analysis included a pulse height cut and a pulse shape discrimination cut. The former requires the signal amplitude to not saturate the digitizer, and also to pass a certain threshold to reject electronic noise. The PMT gain and the cuts were configured in a way that the  $^{39}\text{Ar}$  analysis window of 50-800 keV was not impacted. The pulse shape discrimination cut was to reject nuclear recoil and other heavy ionization backgrounds; the cut efficiency and acceptance will be discussed as we analyze the specific data sets.

### 4.3.4 Monte Carlo Simulation

As shown in the energy calibration discussion, Monte Carlo simulation played an important role in understanding the detector's performance when direct calculations were not possible. The simulation tool used in this project was the Geant4 package [165, 166], a toolkit to simulate the passage of particles through matter. Geant4 is capable of handling complicated detector geometries and allows users to specify the materials to be used and the physics processes to be included. The particle tracking and navigating processes are handled by the Geant4 core, but users are allowed to take control at various stages, including run level (`G4UserRunAction`), event level (`G4UserEventAction`), particle level (`G4UserStackingAction`), track level (`G4UserTrackingAction`) and interaction level (`G4UserSteppingAction`).

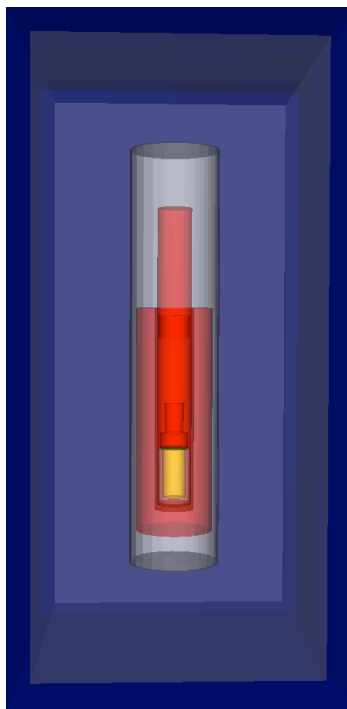


Figure 4.20: The simplified detector geometry used in the Geant4 simulation.

The geometry of the key components of the low background detector was programmed in the Geant4 simulation, but many approximations were taken. For exam-

ple, the inner detector chamber was simplified to a hollow copper cylinder with two end caps, while the top flanges and feedthroughs were ignored. Similarly the cryostat and the veto panels were approximated as a cylinder and a box respectively. Geometries of the inner detector components were followed to the best of our knowledge.

In many calibration simulations and radioactive background simulations, radioactive decays were involved. However, the time tracking algorithm in native Geant4 was found to be incapable of maintaining necessary time resolution at large time values. Geant4 records all time information in the unit of nanoseconds, and the global time, defined as the time in the laboratory frame since the start of the event, can get too large to be sensitive to nanosecond variations. For example, a double accuracy variable can represent numbers ranging from  $10^{-308}$  to  $10^{308}$ , but it could not differentiate  $10^{16}+1$  from  $10^{16}$ . The global time in Geant4 is defined as a double accuracy variable, and its value can exceed  $10^{16}$  ns (116 days) if long lived radionuclides are simulated. When this happens, two interactions separated by nanoseconds may be mistaken as simultaneous and the analysis is biased.

We solved this problem by defining an upper limit for the global time. Every time a new particle was pushed into the particle stack, its global time was compared with this limit in the `G4UserStackingAction` class. If the limit was exceeded, the particle was terminated in the current event after the particle information was stored. Then these stored particles would be regenerated as primary particles in the next event. Because the time limit was at the level of 100 days, no interactions other than radioactive decays would be affected by this fix.

The output of the Geant4 simulation was interaction information (or hit in the Geant4 terminology) that happened in the sensitive volumes. In order to compare with physical events, the saved hit information had to be clustered according to the detector's expected response to particle interactions. For example, the low background detector was blind to the position of scintillation events, so interactions that

occurred at different positions in the argon volume, such as multiple gamma ray scattering, needed to be combined. On the contrary, the detector was able to resolve events separated by several microseconds, and such Geant4 hits had to be resolved as different events even if they were produced by the same primary particle.

Besides simulating the calibration sources, the Geant4 tool was also used to simulate the detector backgrounds in the  $^{39}\text{Ar}$  measurements. The radioactivity of various detector components were measured or estimated, and these values were extrapolated into detector background in the  $^{39}\text{Ar}$  analysis region using the Geant4 simulation tool. This will be discussed in Sec. 4.5.1.

## 4.4 The Main Measurement Campaign

As the low background detector was under upgrading in early 2011, it was operated and tested for several cycles in Princeton University. During this time, the analysis techniques discussed in the Sec. 4.3 were developed. We also developed a few approaches to estimate the  $^{39}\text{Ar}$  content in the underground argon sample based on the atmospheric argon and underground argon data acquired during these operations.

In summer 2011 the detector was relocated to the Kimballton Underground Research Facility (KURF laboratory) in Ripplemead, VA. The rocks above the KURF lab provided a 1450 meters of water equivalent shielding against cosmic rays, and the muon flux in the lab was measured using the plastic muon veto panels to be  $\sim 1 \mu/m^2/s$ , or  $\sim 10,000$  times lower than that at surface. The first  $^{39}\text{Ar}$  measurement at KURF took place from May 2011 to June 2011, using an early (2009) underground argon sample from the Cortez site. The data yielded an upper limit of 0.65% on the  $^{39}\text{Ar}$  content in the underground argon compared to atmospheric after identified backgrounds were subtracted.

Then the low background detector was upgraded again in the hope of reducing

backgrounds that were identified in the 2011 measurement, and a new measurement campaign was launched in 2012. A  $\sim 1$  kg sample of underground argon taken from a batch of  $\sim 100$  kg processed by a fractional distillation column [129] in Fermilab was used in the 2012 measurement, and this batch was to be used in the DarkSide-50 dark matter detector. A low  $^{39}\text{Ar}$  level was confirmed, but the limit was higher than the 2011 measurement because of unidentified backgrounds.

In each of the measurement campaigns, the detector was first filled with high purity atmospheric argon ( $\geq 99.9997\%$  before being purified by the detector's gas handling system) manufactured by AirGas East to study the detector performance, which also set the reference for the  $^{39}\text{Ar}$  study. Then the detector was warmed up, pumped and purged before the underground argon sample was filled. To keep consistent background levels for the  $^{39}\text{Ar}$  analysis, no change other than the gas sample was made between the two measurements.

#### 4.4.1 The Measurement at Surface

Approximately 94 hours of atmospheric argon data and 376 hours of underground argon data were acquired in the surface measurement campaign from Feb 2011 to March 2011. Typical light yield values ranged from 6-6.5 p.e./keV, and the slow component lifetime was observed between  $1.45\mu\text{s}$  and  $1.55\mu\text{s}$ . The detector operation was very stable, as illustrated in Fig. 4.21 (left). The slow component lifetime in the underground argon measurement increased sharply in the first two days, and then decreased very slowly at a rate of  $0.004\mu\text{s}/\text{day}$ . The light yield was decreasing at a rate of  $\sim 0.4\%/ \text{day}$  for 18 days.

The trigger rate in the underground argon runs was approximately 3.7 Hz, and 2.5 Hz of them had one or more muon veto signals. The distribution of veto signal time relative to the inner PMT trigger time is shown in Fig. 4.21. The prominent peak at time 0 was attributed to prompt interaction of cosmic muons or other high energy

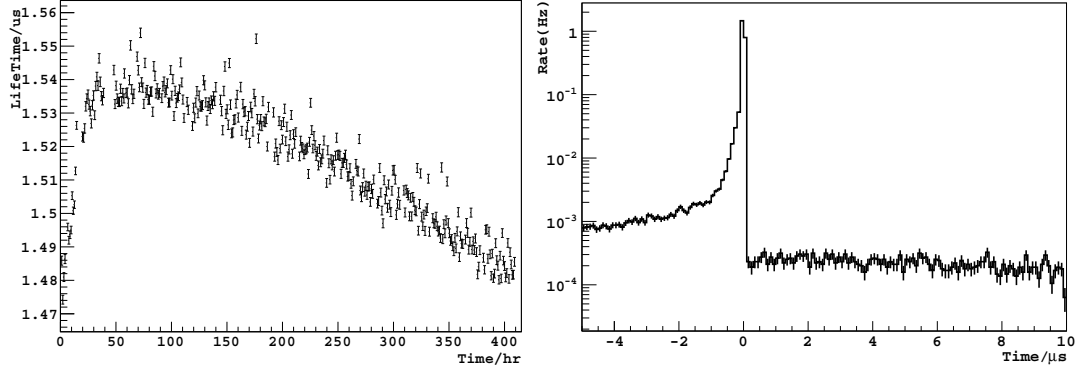


Figure 4.21: Left: the lifetime of the slow component argon scintillation observed in the underground argon measurement in March 2011; Right: the arrival time of muon veto signals relative to the trigger time of the inner PMT signal.

particles with argon, and the flat part of the spectrum after time 0 was explained as false coincidences. Events with veto signals between  $-5\mu\text{s}$  and 0 included both false coincidences and delayed coincidences, and were rejected in the analysis. Dead time due to the  $5\mu\text{s}$  veto window was estimated to be  $\sim 1\%$  at an average veto rate of  $\sim 2000\text{ Hz}$ , and the false coincidence rate was calculated to be  $\sim 0.5\%$  of the valid veto rate.

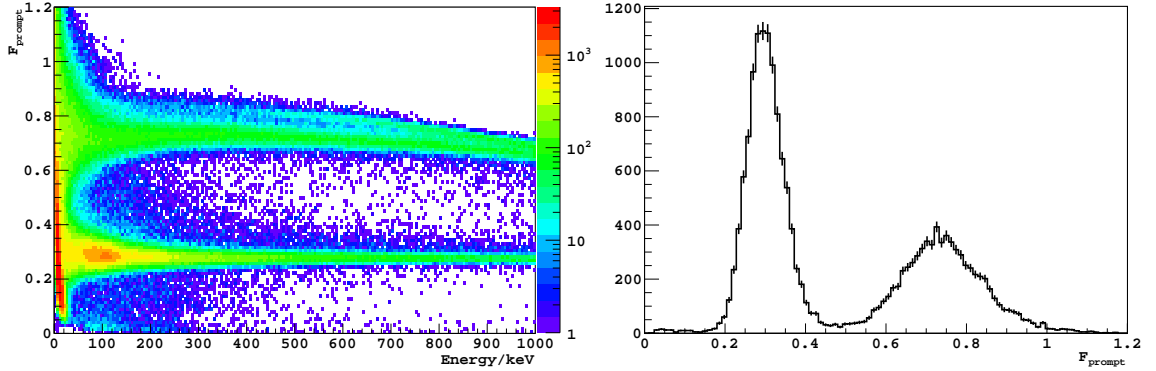


Figure 4.22: Left: the  $F_{\text{prompt}}$  value at different energies measured in the March 2011 underground argon measurement. The upper band was attributed to nuclear recoils and other heavily ionizing particles; the lower band was attributed to electron recoil events. Right: The  $F_{\text{prompt}}$  distribution for events at the energy around 50 keV.

The  $F_{\text{prompt}}$  distribution of underground argon data after the muon veto cut is shown in Fig. 4.22 (left). The  $F_{\text{prompt}}$  parameter was defined to be the fraction of



argon scintillation light in the first 100 ns after the trigger, which was reported to be most sensitive to interacting particle species. Similar to the data acquired with the Tektronix oscilloscope shown in Fig. 4.10, two groups of events with distinctive  $F_{\text{prompt}}$  values were observed. The events with higher  $F_{\text{prompt}}$  values included neutron induced argon nuclear recoils and other heavily ionizing particles, and the lower  $F_{\text{prompt}}$  ones were electron recoil events. The  $F_{\text{prompt}}$  values in the upper band decreased after 600 keV because they saturated the digitizer; similar saturation effect also happened to the lower band but at much higher energies. Unlike direct dark matter search experiments that reject electron recoils and retain nuclear recoil events, we retained the electron recoil events for the  $^{39}\text{Ar}$  analysis.

The  $F_{\text{prompt}}$  cut was chosen to reject as many nuclear recoil events as possible and retain a high electron recoils acceptance. Because the  $F_{\text{prompt}}$  discrimination power decreases at low energies [102, 167], we chose an analysis threshold of 50 keV to avoid significant signal loss and background contamination. The  $F_{\text{prompt}}$  cut was set at 0.5, independent of energy, which yielded an electron recoil acceptance of  $>99.9\%$  at 50 keV and a background rejection efficiency of  $>99\%$  according to Gaussian fits. At higher energies the  $F_{\text{prompt}}$  discrimination power was expected to be higher. We note that the events in the upper band with decreasing  $F_{\text{prompt}}$  values after 600 keV were rejected by a digitizer saturation cut.

The underground argon spectra with and without cuts are shown in Fig. 4.23. The atmospheric argon spectrum with both muon cut and PSD cut are also plotted as a reference. The event rate in the underground argon data before any cuts was 1.75 Hz/kg from 50 keV to 800 keV, and it was reduced to 0.38 Hz/kg after the muon veto cut was applied. The pulse shape discrimination cut brought the rate further down to 0.26 Hz/kg, where approximately half of the events were associated with the bump structure around 100 keV. This bump structure was observed in the atmospheric argon spectrum, and it was later identified to rise from inelastic neutron scattering

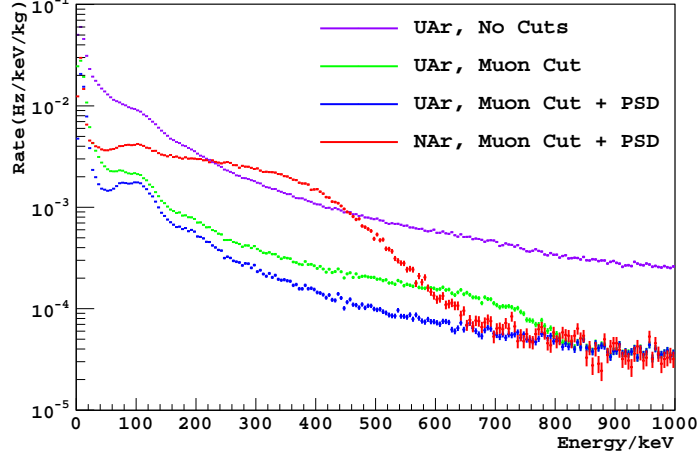


Figure 4.23: The underground argon (UAr) spectrum measured in March 2011, with different cuts; the atmospheric argon (NAr) spectrum with cuts is also shown. The underground argon spectrum with only muon cut decreased sharply around 700-800 keV because the digitizer saturation cut removed most of the high  $F_{\text{prompt}}$  events.

with  $^{19}\text{F}$  nuclei in PTFE.

A simple estimation of  $^{39}\text{Ar}$  activity in the underground argon sample can be made by comparing the rate with that of the atmospheric argon. The event rate between 50-800 keV in the atmospheric argon data was measured to be 1.13 Hz/kg, 0.87 Hz/kg higher than that in the underground argon. Based on the ideal  $^{39}\text{Ar}$  spectrum, 89.8% of the decay events occur in the 50-800 keV energy window, from which we can derive an overall  $^{39}\text{Ar}$  rate difference of 0.97 Hz/kg between the atmospheric and underground argon. We comment that a perfect energy resolution was assumed in this estimation, but in practice a finite energy resolution would cause events to spread out. Considering the rising spectrum shape of  $^{39}\text{Ar}$  decays around 50 keV, events would be lost to lower observed energy on average, so the difference of  $^{39}\text{Ar}$  activity between the atmospheric argon and underground argon could be  $\geq 0.97$  Bq/kg. Since the  $^{39}\text{Ar}$  activity in atmospheric argon was reported to be  $\sim 1$  Bq/kg, the  $^{39}\text{Ar}$  level in the underground argon sample was consistent with 0.

The background in these measurements was also studied. Fig. 4.24 (left) shows the  $F_{\text{prompt}}$  distribution of events rejected by the muon veto coincidences. The events

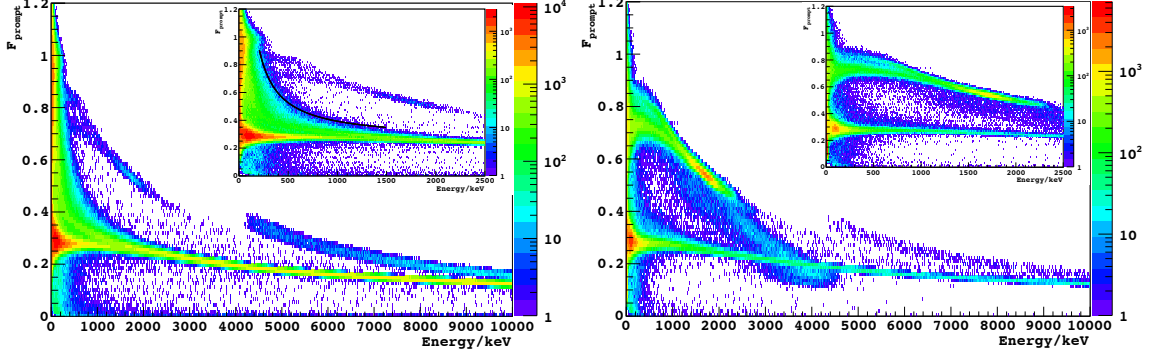


Figure 4.24: Left: the  $F_{\text{prompt}}$  distribution of events in coincidence with muon veto signals; Right: the  $F_{\text{prompt}}$  distribution of events without muon coincidence signals; the insert figures show the distribution below 2.5 MeV.

that saturated the digitizer are also shown, so the  $F_{\text{prompt}}$  values in the upper band noticeably decrease as energy goes up. It can be seen that most of these cosmogenic backgrounds lie in the electron recoil band, but the  $F_{\text{prompt}}$  distribution extended up to  $F_{\text{prompt}} \sim 1$  at low energies. The unit  $F_{\text{prompt}}$  events were usually assumed to be Cherenkov radiations, and the events with  $F_{\text{prompt}}$  values between the electron recoil band and the Cherenkov radiation band were explained as mixtures of the two types. A simple model to predict the effective  $F_{\text{prompt}}$  value of such mixture events could be described as

$$F'_p(E') = \frac{E \times F_p(E) + E_C}{E + E_C} = \frac{(E' - E_C) \times F_p(E' - E_C) + E_C}{E'}$$

where  $E$  is the energy of the electron recoil event,  $E_C$  is the equivalent Cherenkov radiation energy,  $E' = E + E_C$  is the apparent energy of the mixed event,  $F_p(E)$  is the  $F_{\text{prompt}}$  value of electron recoil events, and  $F'_p(E')$  is the effective  $F_{\text{prompt}}$  value for the mixed energy  $E'$ . An example of the model predicted  $F'_p(E')$  curve is shown in Fig. 4.24 (insert of the left plot), which followed the data reasonably.

In addition to the electron recoils and Cherenkov radiations, there is also a group of high energy events (500-2500 keV electron equivalent energy, or  $\text{keV}_{ee}$ ) with high

$F_{\text{prompt}}$  values. The spread of these events was very similar to that of the events without muon coincidences, as shown in Fig. 4.24 (right). The rate of these events was approximately 1% of that without veto signals, which was consistent with random muon coincidence rate. High  $F_{\text{prompt}}$  value cosmogenic events also existed in very high energy windows from 4000 keV<sub>ee</sub> up to 10000 keV<sub>ee</sub> (saturation effects were not corrected, and the real energy could be higher), but they were effectively removed by applying the muon veto cut.

The high  $F_{\text{prompt}}$  events from 500 keV<sub>ee</sub> to 2500 keV<sub>ee</sub> (uncorrected) were found to dominate the residual events in high energy regions after muon veto cut. A peak structure can be observed at  $\sim 1700$  keV<sub>ee</sub> with  $F_{\text{prompt}} \sim 0.55$ , shown in Fig. 4.24 (right). The energy can be corrected to  $\sim 3000$  keV<sub>ee</sub> if we assume an unbiased  $F_{\text{prompt}}$  value of 0.75, as that for very low energy events. Because of the high rate ( $\sim 0.2$  Hz/kg), these events were attributed to cosmic ray interactions. Cosmic rays are the most prevalent background next to environmental gamma rays at the Earth's surface, but gamma rays were expected to be highly attenuated by the lead shielding and copper shielding in the low background detector. Even if gamma rays penetrate the shielding and hit the detector they would appear in the electron recoil band. We comment that this cosmic ray explanation was confirmed by the underground measurement, where the rate of these events were significantly reduced. Since these events couldn't be efficiently rejected by the muon veto system, they were believed to originate from neutral cosmic ray particles, or delayed muon interactions.

One possible explanation of these high  $F_{\text{prompt}}$  events was argon nuclear recoil induced by high energy cosmogenic neutrons. If this is the case, the observed electron equivalent energy needed to be corrected with a relative quenching factor of 0.25-0.3 to obtain the original nuclear recoil energy [59, 168, 169], which would be  $\sim 10$  MeV. Kinematic calculations dictate that a neutron can not transfer more than  $\sim 10\%$  of its kinetic energy to an argon nucleus in an elastic scattering, and this would lead

to a neutron energy of  $\geq 100$  MeV. Cosmogenic neutrons at such high energy are known to exist [170], but only at insignificant rates. What's more, in the case of low energy elastic neutron-nuclei scattering, the nuclear recoil spectrum is flat below the maximum allowed energy transfer

$$E_R \leq 4E_n m_n M / (m_n + M)^2$$

where  $E$  is the incident neutron energy, as illustrated in Fig. 4.25. Generally we don't expect such a prominent peak in the nuclear recoil spectrum<sup>12</sup>.

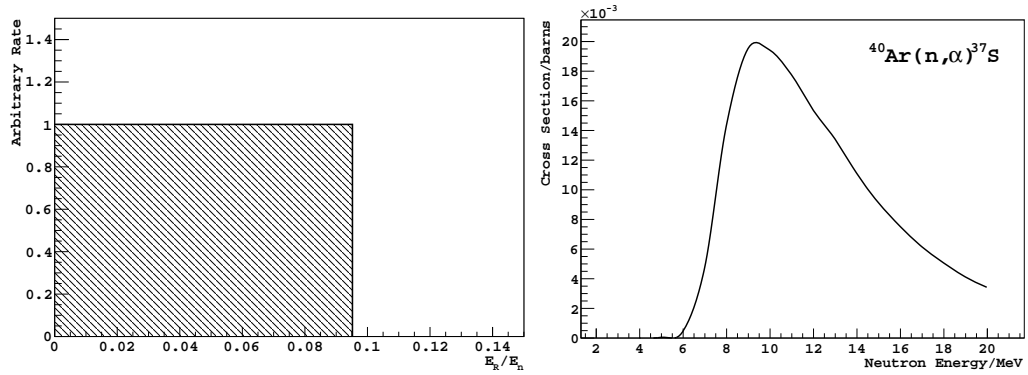


Figure 4.25: Left: the illustrative energy spectrum of recoiled argon nuclei from elastic scattering with mono-energetic neutrons; the scattering is assumed to be isotropic and at low energies; Right: the cross section of  $(n, \alpha)$  reaction on  $^{40}\text{Ar}$ .

An alternative possibility was ions produced by neutron interactions in argon. Alpha particles or protons can be produced by  $(n, \alpha)$  or  $(n, p)$  reactions in argon, and their scintillation don't get seriously quenched as nuclear recoils. As shown in the surface background study in Sec. A.3.2, alpha decays can produce similar high  $F_{\text{prompt}}$  events. In this scenario, the peak at  $\sim 3$  MeV may be explained as  $\sim 3$ -4 MeV for alpha particles or protons<sup>13</sup>, which is a reasonable energy scale for neutron interaction products. For example, the cross section resonance in Fig. 4.25 (right)

<sup>12</sup>The nuclear form factor may induce peaks in the recoil energy spectrum, but the amplitude is not expected to be so significant.

<sup>13</sup>If alphas and protons have a smaller  $F_{\text{prompt}}$  value than that of nuclear recoils (0.75 as we used in this correction), the particle energy could be even lower, like 2-3 MeV.

could produce an alpha peak in the MeV range. However, the cross section for such interactions does not seem to be large enough to account for the observed event rate. We comment that the rate of these high  $F_{\text{prompt}}$  events was similar to that of the inelastic neutron scattering on  $^{19}\text{F}$  in PTFE, but the  $^{19}\text{F}$  scattering cross section is hundreds of times larger. Therefore, the origin of these events remains unknown.

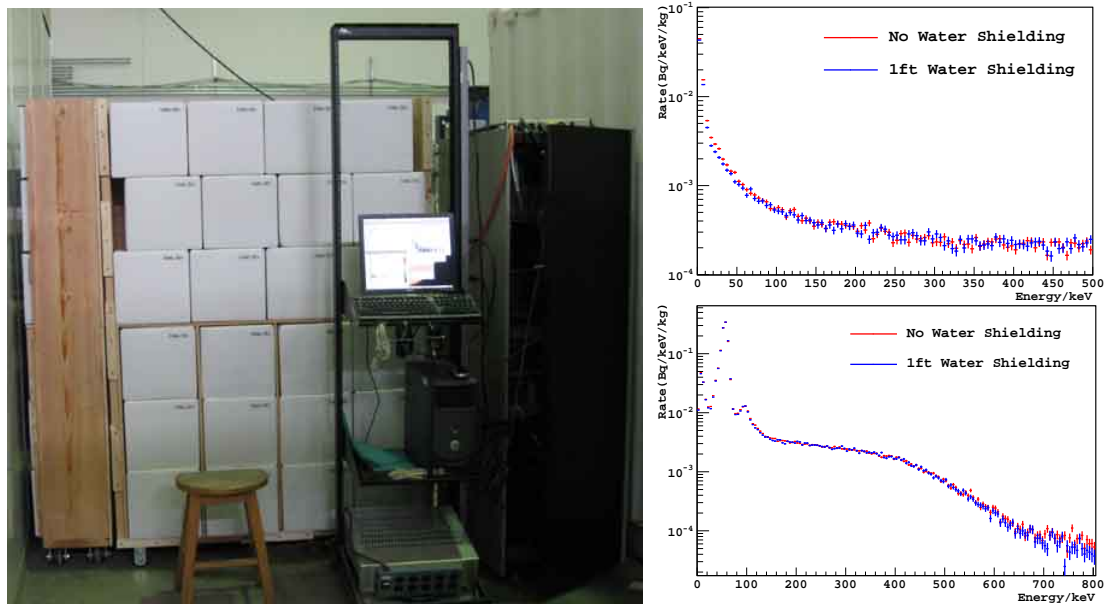


Figure 4.26: Left: a picture of the low background detector with 1ft of water shielding on the side; the top was not installed when the picture was taken. Right, the high  $F_{\text{prompt}}$  value (nuclear recoils and other heavy ionizations) events spectra (top) and the electron recoil event spectra (bottom) with and without water shielding.

Because various backgrounds in the low background detector were believed to associate with neutrons, 1 ft of water shielding was installed around the detector during one measurement in an attempt to reduce neutron backgrounds, as illustrated in Fig 4.26. The water shielding reduced the high  $F_{\text{prompt}}$  events rate by  $3.6 \times 10^{-2} \text{ Hz/kg}$  below 100 keV, while making little difference at higher energies. The spectrum of the reduced events had an exponential decay shape with a decay energy scale of  $\sim 17 \text{ keV}_{ee}$ , and they were attributed to neutron induced nuclear recoils. The high  $F_{\text{prompt}}$  events at higher energy were not significantly affected, indicating that

they were produced by very high energy neutrons<sup>14</sup> or other cosmic ray particles. We were not able to study the effects of the water shielding on the inelastic neutron scattering rate on  $^{19}\text{F}$  (110 keV) because the calibration  $^{241}\text{Am}$  gamma rays were dominating the electron recoil spectrum below 250 keV. The rate reduction of high energy electron recoils was minimal ( $\sim 1 \times 10^{-3}$  Hz/kg/100keV).

#### 4.4.2 Measurement at KURF - 2011

Different approaches, including rate analysis, background simulation and spectral fits, were attempted to evaluate the  $^{39}\text{Ar}$  activity in the underground argon sample from Princeton measurements, but the sensitivity was restricted by the high cosmic ray flux. The low background detector was then relocated to the Kimballton Underground Research Facility (KURF) in Ripplemead, VA. The limestone above the underground laboratory provided  $\sim 1450$  meters of water equivalence shielding against cosmic rays, and the cosmic muon rate was measured to be  $\sim 10,000$  times lower than that at surface. The level of airborne radon concentration in the lab was reported to be comparable to the surface values.



Figure 4.27: Left: a mine forklift lifting lead bricks for the detector shielding; Right: the lab F250 truck loaded with two liquid argon dewars; from left to right: Prof. R. Bruce Vogelaar, Geoffrey Lou Guray, and Dave Holtz.

<sup>14</sup>The mean free path of 10 MeV neutrons is approximately 10 cm in water, and the MeV neutrons are expected to be affected by the water shielding. This disfavored the neutron origin for these high  $F_{\text{prompt}}$  high energy events.

We received generous help from the Lhoist mining company both in personnel and in equipment as the detector parts were transported underground. After the detector was initially set up with help from the mining company, the transport of equipment and materials, such as liquid argon, was carried out with a pickup truck owned by Virginia Tech. Fig. 4.27 (right) shows a picture of two storage liquid argon cryostats on the pickup truck, and a tailgate lift was used to load and unload the cryostats. Extreme care had to be taken while driving on the unpaved road in the non-luminated tunnels, where the traffic was dominated by heavy duty mine trucks. The water shielding was not used in the underground measurements due to transporting and lifting limitations.

The first  $^{39}\text{Ar}$  measurement at KURF took place from June 2011 to July 2011. The underground argon sample measured was extracted from the Cortez site in 2009, which was also used in the measurements in Princeton University. Approximately 200 hours of atmospheric argon data and 150 hours of underground argon data were collected in this campaign.

Electric breakdown in the inner detector chamber was observed when the R11065 PMT was operated at a typical voltage of 1300-1400 V<sup>15</sup>, so a reduced voltage of 1200 V was used in these measurements. As a result, it was difficult to distinguish the single photo-electron (SPE) pulses from baseline fluctuations in the waveforms, and the absolute light yield was not directly measured. Estimations of light yield were made based on the PMT gain dependence on operation voltages and was cross checked with the slow component lifetime. The light yield value was approximately 5p.e./keV, and the degradation rate was measured to be  $\leq 0.5\%$  per day. The compromised light yield and lifetime ( $\sim 1.32\mu\text{s}$ ) values were possibly due to the exposure of the inner detector components to the dusty mine atmosphere during assembly, and the pumping /purging time was also limited in the underground operations.

---

<sup>15</sup>The problem was possibly due to a faulty high voltage feedthrough. The problem didn't show up in the 2012 measurement when the feedthrough was replaced.



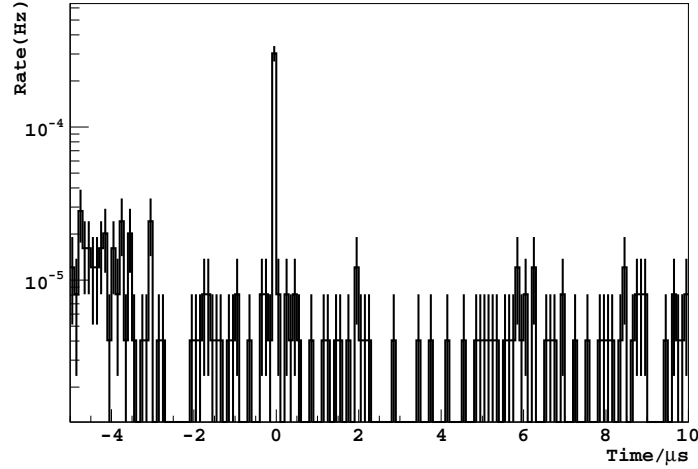


Figure 4.28: The arrival time of muon veto signals relative to the inner PMT trigger time at KURF. The low muon rate can be seen by comparing to the surface data (Fig. 4.21).

The trigger rate in this measurement was approximately 0.04 Hz in the underground argon runs and 0.6 Hz in the atmospheric argon runs. The valid muon veto coincidence rate was estimated to be  $3.2 \times 10^{-4}$  Hz from the spectrum of the muon arrival time in Fig. 4.28, which was less than one percent of the trigger rate in the underground argon data. Compared to the muon coincidence rate of 2.4 Hz at surface, the reduction factor was calculated to be  $\sim 7,500$ , which was consistent with the independent muon flux measurement ( $\sim 10,000$ ). Because of the low muon rate, the anti-coincidence cut was not applied in the analysis to avoid dead time.

The event rate in the (50, 800) keV energy window was integrated to be  $3.7 \times 10^{-2}$  Hz/kg in the underground argon data, and the pulse shape discrimination reduced the value to  $3.3 \times 10^{-2}$  Hz/kg. This residual event rate was approximately 50 times lower than the raw surface rate (1.75 Hz/kg), or  $\sim 8$  times lower than the surface rate with both muon veto cut and PSD cut applied (0.26 Hz/kg). The rate comparison confirmed that the residual event were primarily due to sources other than cosmic rays; otherwise, the event rate would decrease by a similar factor of 7,500-10,000 as the muon flux rate, instead of  $\sim 50$  as observed.

Compared to the underground argon energy spectra measured at surface, the

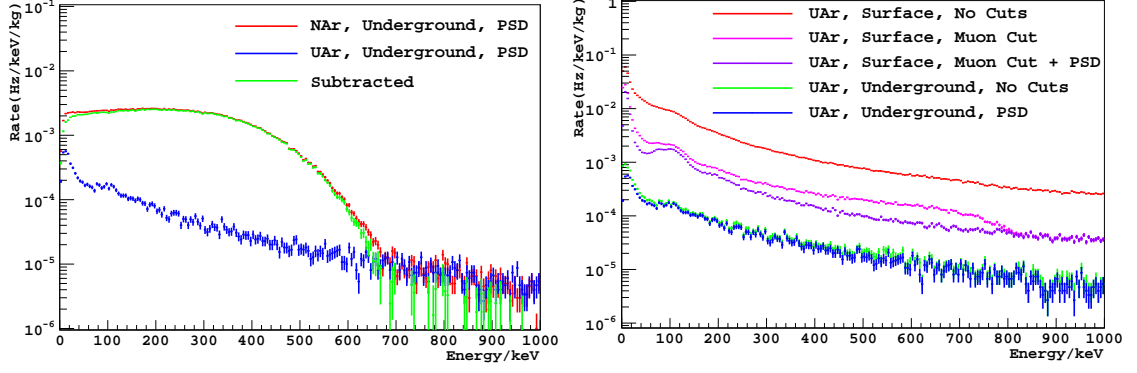


Figure 4.29: Left: the energy spectra of atmospheric argon and underground argon taken at KURF in June 2011; nuclear recoil events were rejected; Right: comparison of the underground argon spectra taken at surface and underground.

peak structure around 100 keV electron recoil events was significantly reduced. This peak was attributed to the inelastic scattering of fast neutrons with fluorine in the PTFE parts, which produced gamma rays at 87.3 keV, 109.9 keV and 197.1 keV. If the gamma rays lost part of their energy before going into the argon volume (back scattering), they could produce a very broad peak region as observed. This inelastic neutron scattering hypothesis was also confirmed with data from an  $^{252}\text{Cf}$  neutron calibration measurement, as will be discussed later in this section.

The residual event rate in the atmospheric argon data after PSD cut was 0.93 Hz/kg in the same energy window of (50, 800) keV, approximately 0.90 Hz/kg higher than the underground argon rate. Keep in mind that 89.8% of  $^{39}\text{Ar}$  decay events occur in this energy window with a perfect energy resolution, the rate difference was consistent with the nominal  $^{39}\text{Ar}$  activity of  $\sim 1$  Bq/kg in atmospheric argon, and the  $^{39}\text{Ar}$  concentration in the underground argon could be 0. However, we didn't calculate the  $^{39}\text{Ar}$  activity in the underground argon using this method because of the large uncertainty in the atmospheric argon activity (1 Bq/kg,  $\sim 8\%$ ). This method was also subjected to the uncertainty in the volume of the argon container (0.56 kg, 2-3%), and the uncertainty in the detector energy resolution (undetermined).

The ratio of the underground argon event rate to the atmospheric argon rate, on

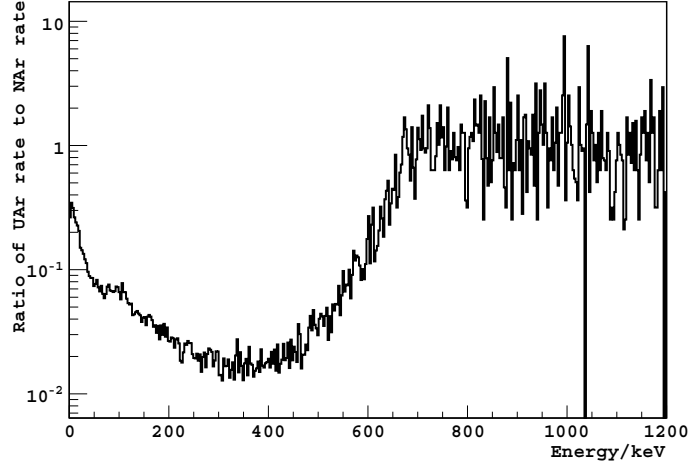


Figure 4.30: The ratio of the event rate in the underground argon to that in atmospheric argon for data taken at KURF in June 2011.

the contrary, was robust against these uncertainties, and was used in the  $^{39}\text{Ar}$  analysis. Fig 4.30 shows the ratio of the two energy spectra in different energy regions. The plot indicated that the best energy window to obtain an  $^{39}\text{Ar}$  limit was from 300 to 400 keV. The residual event rate in this energy window was  $(3.34 \pm 0.11)$  mHz/kg in the underground argon data, which was  $(1.71 \pm 0.05)\%$  of that in atmospheric argon. With a conservative assumption that all the residual events in the underground argon spectrum were due to  $^{39}\text{Ar}$  decays, this ratio can be taken as an estimate of the relative  $^{39}\text{Ar}$  activity in underground argon compared to atmospheric. However, the measured event rate in underground argon was known to include background events, this estimate must be taken only as a conservative upper limit.

An example of the backgrounds in the  $^{39}\text{Ar}$  measurement was an  $^{252}\text{Cf}$  neutron source. At the last day of the measurement, we were informed that a weak  $^{252}\text{Cf}$  neutron source ( $\sim 5000\text{n/s}$ ) stored in the KURF lab was blamed for inducing backgrounds in another KURF experiment<sup>16</sup>. The  $^{252}\text{Cf}$  source was stored approximately 45 ft away from the low background detector and was not considered as a significant source of background. However, after the  $^{252}\text{Cf}$  source was removed from the

<sup>16</sup>The experiment that reported neutron contamination was  $\sim 10$  ft away from the  $^{252}\text{Cf}$  source.

lab, the event rate in the low background detector dropped from  $3.3 \times 10^{-2}$  Hz/kg to  $\sim 2.6 \times 10^{-2}$  Hz/kg in the (50, 800) keV window, and the rate from 300 keV to 400 keV dropped by  $\sim 40\%$  to  $1.9 \times 10^{-2}$  Hz/kg. Unfortunately, the detector was scheduled to shut down, and continuing operations was not a possible option. As a result, only 4 hours of  $^{252}\text{Cf}$ -free data were acquired. The energy spectrum is shown in Fig. 4.31 (left), along with the data having the  $^{252}\text{Cf}$  contamination.

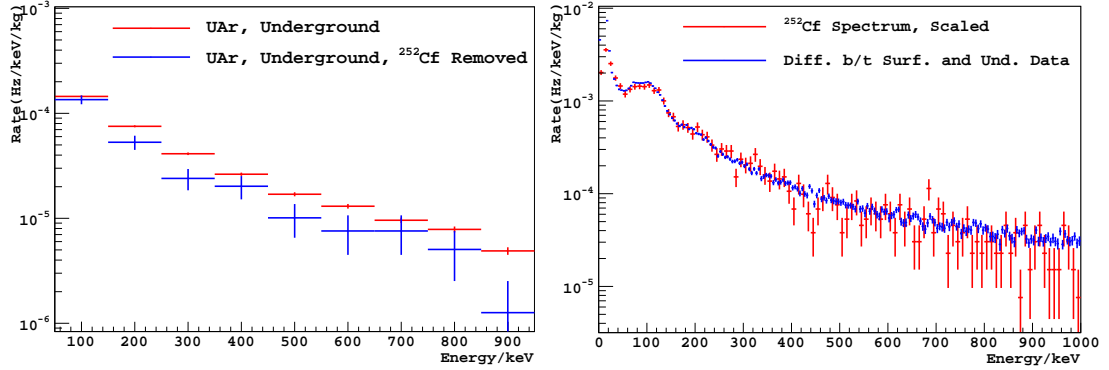


Figure 4.31: Left: the comparison of the underground argon data with and without the  $^{252}\text{Cf}$  source contamination; Right: the spectrum taken with the  $^{252}\text{Cf}$  source  $\sim 2$  ft away from the low background detector, compared to the difference of the electron recoil spectra at surface and underground.

To study the  $^{252}\text{Cf}$  contamination events, we also acquired data with the  $^{252}\text{Cf}$  source very close ( $\sim 2$  ft) to the low background detector. The neutron induced electron recoil event spectrum is shown in Fig. 4.31 (right). A prominent peak was observed around 100 keV, which confirmed the hypothesis of inelastic neutron scattering with  $^{19}\text{F}$  in PTFE. High energy electron recoils were also produced by the neutron source, and they were explained as gamma rays emerging from neutron capture on various detector components.

We have discussed a similar peak structure in the electron recoil background in surface measurements, but it was not observed in the underground measurements, as shown in Fig. 4.29 (right). The difference of the electron recoil spectra measured at surface and underground is compared to the  $^{252}\text{Cf}$  neutron induced spectrum in

Fig. 4.31. The two spectra have been scaled to have the same rate from 250 keV to 800 keV. The two spectra have almost identical shapes at all energies, which indicates that a large fraction of the electron recoil backgrounds in surface measurements are also due to neutrons. The  $\sim 100$  keV energy peak is slightly smaller in the  $^{252}\text{Cf}$  data, possibly due to a less significant fast neutron component in the  $^{252}\text{Cf}$  neutrons compared to cosmogenic neutrons.

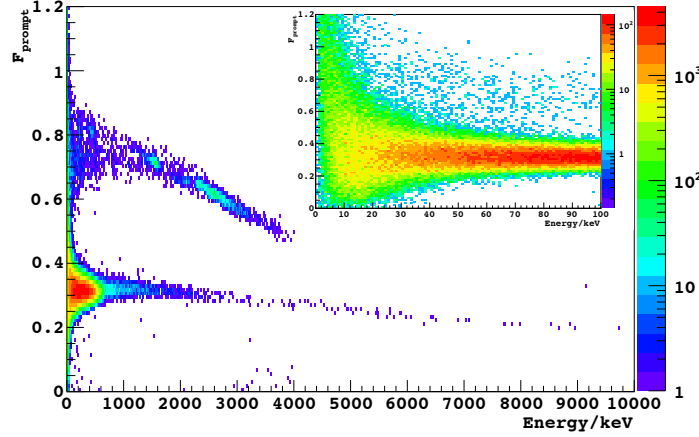


Figure 4.32: The  $F_{\text{prompt}}$  and energy distribution of the atmospheric argon data taken at KURF in June 2011; the insert figure shows the distribution below 100 keV.

Although the high  $F_{\text{prompt}}$  backgrounds have been rejected by the pulse shape discrimination method, it is important to compare the rate at surface and underground to understand their origin. The  $F_{\text{prompt}}$  distribution of the atmospheric argon data in the KURF measurement is shown in Fig 4.32, where two peaks are observed in the top  $F_{\text{prompt}}$  band. The first one, with a rate of  $\sim 2 \times 10^{-3}$  Hz/kg, had an apparent energy of 1500 keV $_{ee}$  at  $F_{\text{prompt}} \sim 0.71$ . The energy can be corrected to  $\sim 1750$  keV $_{ee}$  if we assumed an unbiased  $F_{\text{prompt}}$  value of 0.75. The second peak, with a rate of  $\sim 6 \times 10^{-3}$  Hz/kg, has a apparent energy of 2600 keV $_{ee}$  at a  $F_{\text{prompt}}$  value of 0.62, which can be corrected to 3950 keV $_{ee}$  at  $F_{\text{prompt}} \sim 0.75$ .

The overall rate of these high  $F_{\text{prompt}}$  events decreased by a factor of  $\sim 25$  in the underground measurements compared to the surface measurements. This significant

reduction indicated that these events may be related to cosmic rays. The rate reduction factor of  $\sim 25$  compared to that of the muons (7,500-10,000), however, required other production mechanisms than cosmic rays to exist underground. We comment that remaining cosmic muons tend to have higher average energies at deeper locations, and thus have higher neutron yields [171], but this correction was not expected to explain the dramatic difference between the muon reduction factor of  $\sim 10,000$  and the high  $F_{\text{prompt}}$  events reduction factor of  $\sim 25$ .

The origin of these high energy, high  $F_{\text{prompt}}$  events is still not known, and we will summarize all that we have learned. These events did not arrive in time coincidence ( $5\mu\text{s}$  window) with muon veto signals, but got significantly reduced in underground measurements. They are possibly due to cosmogenic neutral particles like neutrons, and the rate is close to that of the inelastic neutron scattering with PTFE in surface measurements. However, these events didn't get significantly reduced by 1 ft of water shielding, and were not efficiently produced by  $^{252}\text{Cf}$  neutrons. If they rise from neutron induced nuclear recoils, the nuclear quenching effect and kinematics would require the original neutrons to have high flux with  $\gtrsim 100\text{ MeV}$  energy, and it couldn't explain the prominent peak structure. Another possibility is neutron induced alphas or protons, but the interaction cross section doesn't seem to explain the rate. In addition, sources other than cosmic rays may exist because the event rate doesn't scale down with the muon flux in the underground measurements.

We comment that these events were also observed in another liquid argon detector operated in Princeton in 2013. The high  $F_{\text{prompt}}$  event rate per unit mass was a few times lower than that in the low background detector, but can be taken as consistent given the different detector configurations and shielding. This detector had two PMTs, both of which detected such high  $F_{\text{prompt}}$  events with comparable signal amplitude; this excluded the possibility of PMT/electronics effects as sources of such signals. An AmBe neutron source used in the calibration might have produced

events in this window, but the result was inconclusive due to low statistics.

#### 4.4.3 Measurement at KURF - 2012

Following the 2011 measurement at KURF, the low background was upgraded again in the hope of further reducing background and improving light collection. The modifications were made based on the background analysis of the 2011 data, as will be discussed in Sec. 4.5.1.

1. A new PMT model R11065-10 was made available by Hamamatsu, which had a lower radioactivity level than R11065. However, the PMT was found to spark in argon gas, and a cryogenic epoxy coating with unknown radioactivity was used to fix the problem.
2. We modified the detector's high voltage feedthrough by adding mylar films and epoxy to enhance its high voltage performance; it was tested to work in pure argon gas up to 2000 V. We also switched to a negative high voltage PMT base, which worked in argon gas and had a low radioactivity.
3. We replaced the highly crystalline PTFE argon container with a Spectralon cell with an aspect ratio of height:diameter  $\approx 1:1$  to improve the light collection.

This measurement campaign began in July 2012 and ended in August 2012. Approximately 40 kg·hr of data were collected for both atmospheric argon and underground argon. The underground argon sample used was a  $\sim 0.4$  kg sample from a batch of  $\sim 100$  kg that was extracted from the Cortez site in 2011 and was processed by a distillation column at Fermilab. This batch of underground argon was to be used in the DarkSide-50 dark matter detector, which was going to be the first dark matter detector utilizing low  $^{39}\text{Ar}$ -activity argon and an active neutron veto.

As suggested by the 2011 data, the muon veto system was not used in this measurement, and we confirmed with the KURF lab administrative that no artificial

neutron sources existed in the lab area. The R11065-10 PMT was operated stably at a voltage of 1400 V, which yielded clean single photoelectron pulses. The light yield was measured to be  $\sim 5.4\text{p.e./keV}$  in the atmospheric argon run and  $\sim 20\%$  lower in the underground argon run<sup>17</sup>. The measured slow component lifetime value ranged between  $\sim 1.2\text{-}1.35\mu\text{s}$ .

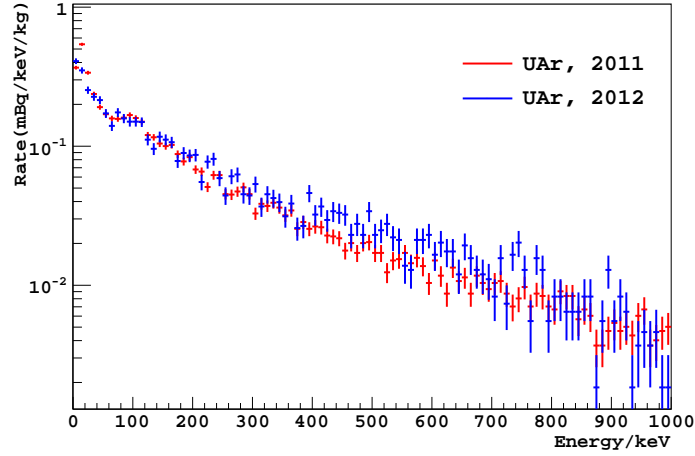


Figure 4.33: Comparison of the underground argon spectrum measured in 2012 with that in 2011; the rates have been corrected by sensitive masses.

The recorded underground argon spectrum from this measurement is shown in Fig 4.33, compared to that of the 2011 measurement. The two spectra were very similar both in shape and in rate. A slight rate decrease was observed around 110 keV in the 2012 data, possibly due to the removal of the  $^{252}\text{Cf}$  neutron source. However, the event rate in the 2012 measurement was higher than that of 2011 measurement in energy regions higher than 200 keV.

The residual event rate in the underground argon after pulse shape discrimination was  $3.7 \times 10^{-2} \text{ Hz/kg}$  in the (50, 800) keV energy window, and  $3.9 \times 10^{-3} \text{ Hz/kg}$  in the (300, 400) keV energy window, compared to the 2011 values of  $3.3 \times 10^{-2} \text{ Hz/kg}$  and  $3.3 \times 10^{-3} \text{ Hz/kg}$  respectively. Due to the slightly different spectral shape, we chose a different energy window of 280-380 keV for a rate analysis. A conservative  $^{39}\text{Ar}$  limit

<sup>17</sup>The underground argon processed by the distillation column had a nominal purity of 99.9%, and we purified this gas for a few cycles before the light yield reached this value.



of 2.0% could be obtained by comparing the event rate in the underground argon and atmospheric argon, assuming all residual events in the underground argon were  $^{39}\text{Ar}$  decays. Again, the detector backgrounds were ignored and thus the result must be taken as a conservative upper limit.

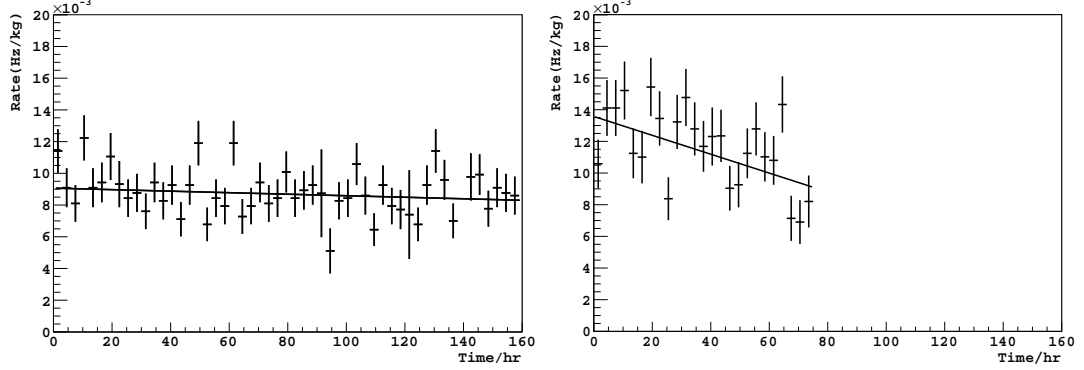


Figure 4.34: Left: the event rate from 300 keV to 800 keV in the 2011 measurement; Right: the event rate in the same energy window in the 2012 measurement.

The origin of the additional electron recoil background in the 2012 measurement was not identified, but the background event rate was found to decrease with time. The event rate between 300 and 800 keV was found to decrease by  $\sim 30\%$  in 70 hours according to a linear fit, as illustrated in Fig. 4.34. The 2011 rate in the same energy window, also shown in Fig. 4.34, was statistically stable; the time dependence was  $\lesssim 8\%$  in 160 hours. If we assume the decrease of event rate was due to radon contamination, the  $^{39}\text{Ar}$  limit obtained from rate comparison could be reduced to  $\sim 1\%$ . However, no conclusion has been made due to the low statistics.

In addition to the contamination in electron recoil events, the high  $F_{\text{prompt}}$  event rate also increased compared to 2011 data. Fig. 4.35 shows the  $F_{\text{prompt}}$  distribution for the atmospheric argon data taken in the 2012 measurement, which had a similar structure to that of the 2011 data (Fig. 4.32). The digitizer saturation effect was observed at lower energies compared to the 2011 measurement because of the higher PMT voltage (higher gain) used. The event rate at the first high  $F_{\text{prompt}}$  peak was

estimated to be  $\sim 1.5 \times 10^{-2}$  Hz/kg, and the second had a rate of  $\sim 4 \times 10^{-3}$  Hz/kg. The total event rate was approximately 2 times higher than that of the 2011 measurement, which had a rate of  $\sim 2 \times 10^{-3}$  Hz/kg and  $\sim 6 \times 10^{-3}$  Hz/kg respectively.

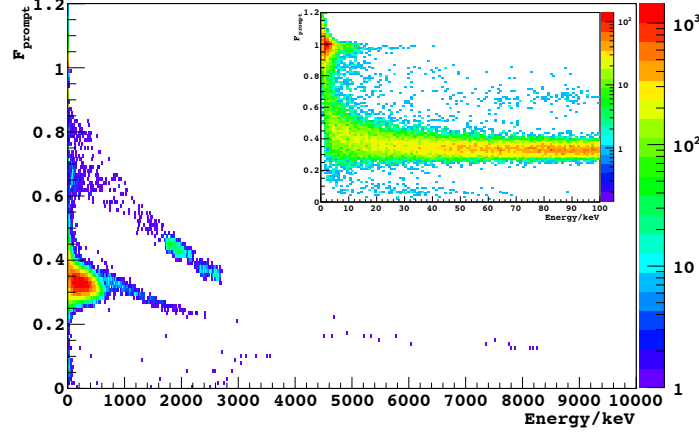


Figure 4.35: The  $F_{\text{prompt}}$  and energy distribution of the atmospheric argon data taken in 2012; the insert figure shows the distribution below 100 keV.

Similar to the electron recoil events, the rate of these high  $F_{\text{prompt}}$  events also decreased with time, by approximately 50% over 70 hours, as shown in Fig. 4.36. The rate of these events was relatively stable in the 2011 measurement and also in the surface measurements. The atmospheric argon rate in the 2012 data was  $\sim 30\%$  lower than that in the underground argon, but had a similar decreasing trend<sup>18</sup>. The decreasing rate in both high and low  $F_{\text{prompt}}$  event was unlikely to be due to hardware problems because the rates of decreasing were different. In addition, the atmospheric argon data had a stable  $^{39}\text{Ar}$  rate though the high  $F_{\text{prompt}}$  event rate was decreasing. This observation suggested that radon and its progeny could be one source of these events, as alpha particles are good candidates to these high  $F_{\text{prompt}}$  events. However, it is unlikely for the underground argon to have a similar radon content with the atmospheric argon; or if the radon emerged from the inner detector parts, they had to be recharged to the same level between the atmospheric

<sup>18</sup>The high  $F_{\text{prompt}}$  event rates in underground and atmospheric argon were very similar in the surface measurements and in the 2011 measurements.

and underground argon measurements.

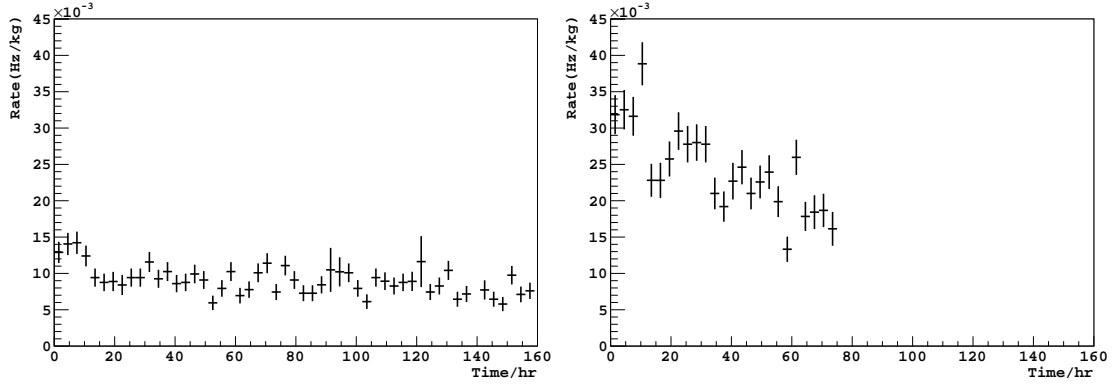


Figure 4.36: Left: the high  $F_{\text{prompt}}$  event rate above  $1000 \text{ keV}_{ee}$  in the 2011 underground argon measurement; Right: the event rate in the 2012 underground argon measurement.

The insert figure of Fig. 4.35 shows the  $F_{\text{prompt}}$  distribution for energies below  $100 \text{ keV}$ , where there is a group of events around  $F_{\text{prompt}} \sim 1$ , which was not observed in the 2011 measurement (Fig. 4.32). The  $F_{\text{prompt}} \sim 1$  events are usually attributed to Cherenkov radiation of charged particles in the quartz window of the PMT, and other possibilities include scintillation signals in the WLS and PMT after pulses resulted by ionization of residual gas in the PMT case. But none of these possibilities have been identified. The event rate was estimated to be  $1\text{--}2 \times 10^{-2} \text{ Hz}$  in  $\sim 0.42 \text{ kg}$  of liquid argon.

Despite of the various unknown backgrounds in the 2012 measurement, we confirmed the low  $^{39}\text{Ar}$  activity in the batch-processed underground argon to be used in the DarkSide-50 dark matter detector. The DarkSide-50 detector is expected to yield the ultimate  $^{39}\text{Ar}$  content measurement in this batch.

## 4.5 $^{39}\text{Ar}$ Analysis

We have shown that a conservative  $^{39}\text{Ar}$  limit of  $\sim 2\%$  can be obtained by comparing the underground argon spectrum with the atmospheric one and assuming that all the

residual events in the underground argon were due to  $^{39}\text{Ar}$  decays. However, various backgrounds were known to exist in the detector, as indicated by the presence of events outside the  $^{39}\text{Ar}$  energy window. A more stringent limit on the  $^{39}\text{Ar}$  activity in underground argon can be obtained by evaluating the background radioactivity and subtracting their contributions from the observed events rate. The data from the 2011 measurement were used in this analysis because of its consistently low background rate. The event rate in the following discussion will not be scaled by argon mass ( $\sim 0.56$  kg) to avoid additional uncertainties in the volume calculation.

#### 4.5.1 External Background Study

The first background source considered in this study is the  $^{252}\text{Cf}$  neutron source. The electron recoil event rate in the low background detector was observed to drop by 20-40% in different energy windows after the source was removed from KURF lab, but only 4 hours of  $^{252}\text{Cf}$ -free data were acquired. The  $^{39}\text{Ar}$  sensitivity from the  $^{252}\text{Cf}$ -free data was limited by statistics. For example, only 15 events were observed in the 300-400 keV energy window, which could be translated to an event rate of  $1.06 \pm 0.27$  Hz (or  $\sim 1.9 \pm 0.51$  Hz/kg). The statistical uncertainty could be reduced to  $\sim 7\%$  by expanding the analysis window to (50, 800) keV, but we would lose the sensitivity from spectral shapes. Therefore, we estimated the electron recoil background in the 300-400 keV window induced by the  $^{252}\text{Cf}$  source using a combined analysis technique to reduce the uncertainties.

The neutron contamination spectrum, defined as the electron recoil energy spectrum produced by the  $^{252}\text{Cf}$  source at its storage location ( $\sim 45$  ft away from the detector), was obtained by subtracting the  $^{252}\text{Cf}$ -free data from the  $^{252}\text{Cf}$ -contaminated data. Due to the low statistics of the  $^{252}\text{Cf}$ -free data set, these events were grouped in 100 keV bins, and only data from 50 keV to 950 keV were considered. Fig. 4.37 shows this subtracted neutron contamination spectrum along with the neutron calibration

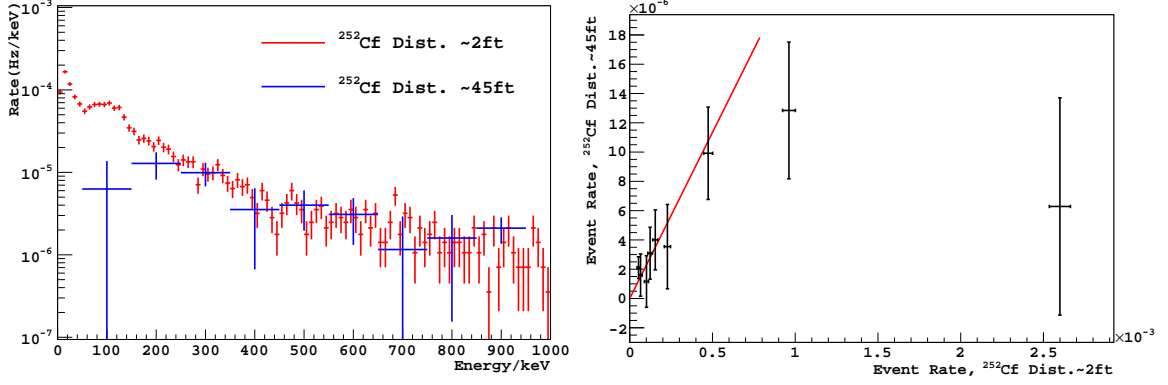


Figure 4.37: Left: Comparison of the neutron contamination spectrum ( $^{252}\text{Cf}$  source  $\sim 45$  ft) and the neutron calibration spectrum ( $^{252}\text{Cf}$  source  $\sim 2$  ft), the latter has been scaled to match the rate of the former; Right: event rate comparison between the two neutron spectra in corresponding energy bins; the 2 bins below 250 keV were excluded from the fit.

spectrum, defined as the electron recoil spectrum induced by the  $^{252}\text{Cf}$  neutron source when it was placed  $\sim 2$  ft away from the detector. The two spectra agreed reasonably above 250 keV, but deviated significantly at lower energies. As discussed in Fig. 4.31, inelastic scattering between fast neutrons and  $^{19}\text{F}$  nuclei in PTFE lead to emission of gamma rays around 100 keV and 200 keV, while thermal neutron capture on various detector components produced high energy gamma rays and were responsible for the continuous electron recoil spectrum. As a result, when the  $^{252}\text{Cf}$  neutron source was very close to the low background detector the neutrons had a large fast component and produced a significant peak around 100 keV via inelastic scatterings.

If the high statistics neutron calibration spectrum can serve as the reference shape for the neutron contamination events above 250 keV, the neutron contamination rate in a small energy window  $[x, y]$  can be calculated by scaling from the rate in a large window  $[X, Y]$ .

$$R_{con}([x, y]) = R_{con}([X, Y]) \frac{R_{cal}([x, y])}{R_{cal}([X, Y])}$$

The contamination rate in the energy window of [250, 950] keV is:

$$R_{con}([250, 950] \text{ keV}) = ((6.78 \pm 0.11) - (4.24 \pm 0.55))\text{mHz} = (2.54 \pm 0.56)\text{mHz}$$

And the contamination rate in the [300,400] keV window can be estimated as:

$$R_{con}([300, 400] \text{ keV}) = (2.54 \pm 0.56) \frac{231 \pm 15.2}{769 \pm 27.7} = (0.78 \pm 0.18) \text{ mHz}$$

An alternative method is to determine the scaling factor between the two spectra and then scale down the calibration neutron rate in the region of interest to estimate the contamination rate.

$$R_{con}([x, y]) = R_{cal}([x, y]) \frac{R_{con}([X, Y])}{R_{cal}([X, Y])}$$

The scaling factor  $R_{con}([X, Y])/R_{cal}([X, Y])$  could be estimated using both spectral shapes and event rates. The event rates in the corresponding energy windows of both spectra are shown in Fig. 4.37 (right), and a scaling factor  $(2.27 \times 10^{-2} \pm 4.54 \times 10^{-3})$  was returned by a fit. The scaling factor indicated that the  $^{252}\text{Cf}$  source produced  $\sim 50$  times more capture gamma rays in its calibration position ( $\sim 2$  ft away) than that at its storage position ( $\sim 45$  ft away). A solid angle estimation predicted a neutron flux difference of  $\sim 500$  times, but the high neutron flux was expected to have a small thermal component at the calibration position and this may explain the difference. Using this scaling factor, a neutron contamination rate of  $(0.82 \pm 0.17) \text{ mHz}$  was obtained in the energy window of 300-400 keV.

The neutron contamination rate estimated from the two approaches were consistent, and we chose the second one in the analysis because it took advantage of the spectral shapes and had smaller uncertainties. After the  $^{252}\text{Cf}$  contamination events were subtracted from the underground argon data in the energy window of (300,400) keV, the residual rate was  $(1.05 \pm 0.18) \text{ mHz}$ . The value was very close to the rate of  $(1.06 \pm 0.27) \text{ mHz}$  directly measured in the  $^{252}\text{Cf}$ -free data set but the uncertainty level was improved.

Decay Chain	Measurement Point	PMT (mBq)	Base (mBq)	Cu (mBq/kg)
$^{232}\text{Th}$	$^{228}\text{Ra}$	$6 \pm 1$	$41 \pm 2.8$	-
	$^{228}\text{Th}$	$6 \pm 1$	$45 \pm 4.7$	-
$^{238}\text{U}$	$^{234}\text{Th}$	$190 \pm 40$	$25 \pm 3.7$	-
	$^{234m}\text{Pa}$	$80 \pm 40$	$< 149$	-
	$^{226}\text{Ra}$	$18 \pm 1.2$	$32 \pm 1.9$	-
$^{235}\text{U}$	$^{235}\text{U}$	$8 \pm 2$	$1.4 \pm 0.4$	-
$^{40}\text{K}$	$^{40}\text{K}$	$79 \pm 10$	$65 \pm 9.3$	-
$^{60}\text{Co}$	$^{60}\text{Co}$	$8.8 \pm 0.8$	$< 1.2$	$2.1 \pm 0.19$
$^{57}\text{Co}$	$^{57}\text{Co}$	-	-	$1.8 \pm 0.4$
$^{58}\text{Co}$	$^{58}\text{Co}$	-	-	$1.7 \pm 0.09$
$^{56}\text{Co}$	$^{56}\text{Co}$	-	-	$0.2 \pm 0.03$

Table 4.2: The radioactivity values used in the background analysis; the copper values were the saturated cosmogenic activities at Gran Sasso (need to be scaled to reflect the sea level condition); primordial radioactivity in the copper was not included.

Other detector backgrounds considered in this analysis included the radioactivity of the R11065 PMT and the high voltage divider board, and cosmogenic activities in the copper shielding. All radioactivity measurements were made using low-background, high-purity germanium detectors at the Low Background Counting Facility [172] of the Gran Sasso National Laboratory (LNGS). The parts measured were not the specific units used in the low background detector, but units of the same model<sup>19</sup>. The measurement values, as summarized in Tab. 4.2, were taken in the Geant4-based simulation to predict the background rate in the detector volume.

In addition to the uncertainties in the measured radioactivity and the statistical uncertainty in the simulation, we also included uncertainties from other sources. A 25% uncertainty was suggested by the authors who made the measurements to account for the distribution of radioactivity inside the PMT. When the measurement was made the location of radioactivity in the PMT case was not known and an uniform

---

<sup>19</sup>The PMTs used in the radioactivity measurement were 3 Hamamatsu R11065 units, and we took the average radioactivity values in our analysis; the PMT board components measured were purchased from CryoCircuits, and the same batch was used to build the low background detector PMT board; we didn't have a dedicated copper measurement, but assume a similar activity to that reported in Ref. [153].

distribution was assumed. The copper sample measured by the authors of Ref. [153] was exposed to the cosmic rays at LNGS (altitude 985 m above sea level), and the activities were scaled down by a factor of 2.1 to reflect the lower cosmic ray flux at sea level. The copper used in the low background detector shielding was stored at surface in Princeton for at least 4 years before moving underground, while the nuclide  $^{60}\text{Co}$  has a live time of 5.3 years (the longest in the table), so an equilibrium may not have been reached. Therefore, a 25% uncertainty was included to account for the uncertainties in the copper exposure history, the variations in the cosmic ray flux with latitude, and the (small) overburdens covering our copper during exposure. Additionally, we include a 5% uncertainty to account for approximations made in the Monte Carlo geometry for all radioactivity simulations.

With all uncertainties discussed included, the Monte Carlo simulation predicted a background rate of  $(0.29 \pm 0.08)$  mHz from the PMT,  $(0.07 \pm 0.02)$  mHz from the PMT base, and  $(0.36 \pm 0.11)$  mHz from the copper shielding. The values are summarized in Tab. 4.3, which summed up to  $\sim 70\%$  of the background after the  $^{252}\text{Cf}$  contamination was subtracted. We note that the primordial radioactivity in copper and the radioactivity in the PTFE parts were not included in this analysis because they were not measured. These levels were typically low, and vary from sample to sample. This fact added to the conservativeness of the  $^{39}\text{Ar}$  result.

Source	$^{252}\text{Cf}$	PMT	Base	Copper
Rate (mHz)	$0.82 \pm 0.17$	$0.29 \pm 0.08$	$0.07 \pm 0.02$	$0.36 \pm 0.11$

Table 4.3: The expected background rate in 300 - 400 keV $_{ee}$  from different sources.

Another background is electron recoil events induced by neutrons via inelastic scattering and capture gamma ray emissions. Neutrons can be produced at underground locations by cosmic rays or  $(\alpha, n)$  reactions, but were not measured directly in



KURF. If the high energy ( $>1000 \text{ keV}_{ee}$ ) events in the high  $F_{\text{prompt}}$  band in Fig. 4.24 and Fig. 4.32 gave an estimate of the neutron flux, the residual neutron rate in the KURF lab was  $\sim 25$  times lower than that at surface. If we further assume that the difference between the underground electron recoil spectrum and the surface measurements (with muon veto cut, shown in Fig. 4.31) were exclusively due to neutrons, it can be used to estimate the electron recoil event rate induced by residual neutrons at KURF. A rough estimation yielded a value of  $\sim 0.35 \text{ Hz}$ , which might explain the event rate unexplained by Tab. 4.3, but we didn't include this background in the analysis because of the unknown uncertainties.

## 4.5.2 Radioactivity in the Argon Sample

While the external detector backgrounds were expected to be identical in the atmospheric argon measurements and in the underground argon measurement, radioactivity in the measured argon samples might be different. The most important radioactivity for the  $^{39}\text{Ar}$  analysis was  $^{85}\text{Kr}$  and also possible  $^{39}\text{Ar}$  produced by cosmic rays when the underground argon was stored at surface.

Krypton is also a noble gas, next to argon in the noble family. Krypton presents in air at a much lower concentration of  $\sim 1 \text{ ppm}$  by volume, compared to  $\sim 1\%$  for argon. The boiling point of krypton is  $115.8 \text{ K}$ ,  $28.5 \text{ K}$  higher than that of argon ( $87.3 \text{ K}$ ). In commercially produced argon from liquid air distillation, the relative krypton concentration can be reduced by orders of magnitude, but may still present at small concentrations because of their similar physical and chemical properties.

The krypton isotope  $^{85}\text{Kr}$  is a beta emitter with an endpoint energy of  $687 \text{ keV}$ , very close to that of  $^{39}\text{Ar}$  ( $565 \text{ keV}$ ).



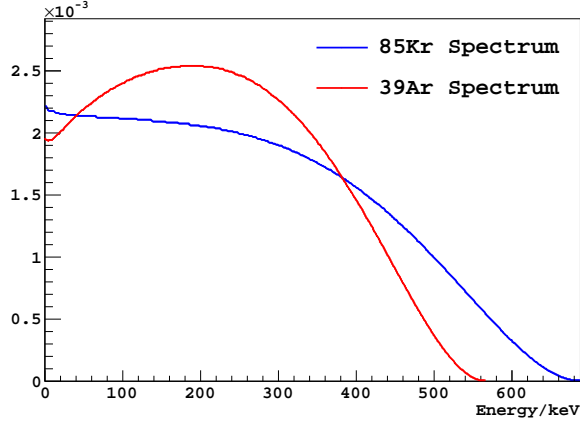


Figure 4.38: The normalized  $^{85}\text{Kr}$  spectrum compared with the normalized  $^{39}\text{Ar}$  spectrum.

$^{85}\text{Kr}$  is mainly produced by fission processes of uranium and plutonium. When a heavy atom splits, it usually produces two large fission fragments and a few neutrons.  $^{85}\text{Kr}$  can be produced in such processes with a fission yield of about 0.3%. Because of its short half life of 11 years, the presence of  $^{85}\text{Kr}$  in the atmosphere was believed to be negligible before the nuclear era, and its current concentration in air is primarily attributed to anthropogenic sources. It is estimated that up to mega-curies of  $^{85}\text{Kr}$  was released into the atmosphere each year after World War Two, and its concentration in the atmosphere is at the level of  $1 \text{ Bq/m}^3$ . Note the radioactivity of  $^{39}\text{Ar}$  in air is at the level of  $0.01 \text{ Bq/m}^3$ .

Due to the similar spectrum shape of  $^{85}\text{Kr}$  and  $^{39}\text{Ar}$ , krypton in argon could be mistaken as  $^{39}\text{Ar}$  signals. As a result, its presence in the underground argon sample could artificially lift the estimated  $^{39}\text{Ar}$  level, while its presence in the atmospheric argon reference sample would lead to a falsely large  $^{39}\text{Ar}$  depletion. The krypton level in the high purity atmospheric argon was measured by the manufacturer (Airgas East) to be less than 40 ppb, below the apparatus's detection limit. At this level of krypton and a typical  $^{85}\text{Kr}/\text{Kr}$  ratio of 15 ppt [116], the  $^{85}\text{Kr}$  decay rate in the reference sample was less than 1.8% of the  $^{39}\text{Ar}$  decay rate. We included a systematic uncertainty to account for this potential background because we assumed all the difference in the

atmospheric and the underground argon spectrum was due to  $^{39}\text{Ar}$  decays. As for the underground argon sample, the level of krypton was expected to be extremely low because no efficient underground krypton production mechanism was known<sup>20</sup>. In any case,  $^{85}\text{Kr}$  in the underground argon sample would be conservatively considered as  $^{39}\text{Ar}$  in the analysis.

Another potential background in the underground argon sample was  $^{39}\text{Ar}$  produced by neutron activation during storage time. The specific underground argon sample used in the 2011 measurement was extracted and processed in 2009, and before being taken underground for the measurement it had been exposed to cosmic rays at the Earth's surface for 2-3 years, which was approximately 1% of its half life. Considering the approximate equilibrium of  $^{39}\text{Ar}$  concentration in the atmosphere (production rate  $\approx$  decay rate), the  $^{39}\text{Ar}$  content produced in the underground argon sample would have been  $\sim 1\%$  if the neutron flux at surface were the same as that in the atmosphere.

Fortunately, however, the cosmogenic neutron flux at the Earth's surface is a few orders of magnitude lower than the average value in the atmosphere [173], which suggested that  $^{39}\text{Ar}$  production in the underground argon sample during storage time would be much smaller than the previously estimated value of 1%. A calculation using the COSMO code [174] confirmed that the equilibrium  $^{39}\text{Ar}$  activity in argon stored on surface is only 1.7 mBq/kg, approximately 3 orders of magnitude smaller than the atmospheric value of 1 Bq/kg. So after three years of surface exposure the  $^{39}\text{Ar}$  activity will be at the level of a few percent of 1 mBq/kg, well below the expected detection sensitivity of this experiment.

---

<sup>20</sup>The isotope  $^{85}\text{Kr}$  can be produced in fissions, but its rate may be suppressed by the short half life and low fission yield, similar to the case of atmospheric concentration before nuclear age.

### 4.5.3 $^{39}\text{Ar}$ Limits with Background Subtracted

To evaluate the  $^{39}\text{Ar}$  concentration in the underground argon sample, we subtracted the identified backgrounds from both the underground argon data and the atmospheric argon data, and assumed that the residual events originated from  $^{39}\text{Ar}$  decays in the underground argon and in the atmospheric argon. Only the backgrounds from known sources were subtracted, as summarized in Tab. 4.3, while the radioactivity from the PTFE parts and the primordial radioactivity in the copper shielding, and also the residual neutron backgrounds were not included. We comment that if certain background content remains in the data after the subtraction, it would add to the conservativeness of the analysis.

	Rate(mHz), (300, 400) keV
Atmospheric Ar (AAr)	$108.78 \pm 0.39$
Underground Ar (UAr)	$1.87 \pm 0.06$
Estimated Background	$1.54 \pm 0.23$
$^{85}\text{Kr}$ in AAr	$< 1.83$
AAr, Background Subtracted	$107.2 \pm 1.9$
UAr, Background Subtracted	$0.32 \pm 0.23$

Table 4.4: A summary of the background subtraction analysis. The upper limit of  $^{85}\text{Kr}$  rate in the atmospheric argon is used as its uncertainty. To convert these rates into activities per unit mass, an argon mass of  $0.56 \pm 0.03$  kg can be used.

After the backgrounds were subtracted, an event rate of  $(0.32 \pm 0.23)$  mHz remained in the energy window of 300-400 keV in the underground argon, compared to a rate of  $(107.2 \pm 1.9)$  mHz in the atmospheric argon, as summarized in Tab. 4.4. The ratio of the two rates can be interpreted as the relative  $^{39}\text{Ar}$  concentration in the two argon samples. A 95% C.L. upper limit of 0.65% on the relative  $^{39}\text{Ar}$  activity in the underground argon was derived, which implies a reduction factor of  $\sim 150$  in the  $^{39}\text{Ar}$  activity in the 2009 underground argon sample compared to the atmospheric.

The summarized background spectrum from identified sources is compared with the measured spectrum in Fig. 4.39. The backgrounds account for approximately

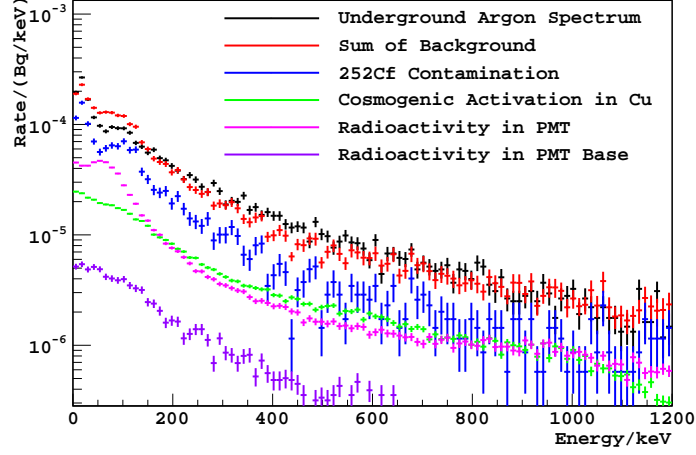


Figure 4.39: The expected background spectra from the identified background sources compared to the observed spectrum; we used the  $^{252}\text{Cf}$  neutron calibration spectrum in place of the neutron contamination spectrum, and this is responsible for the excess of summed background over the observed spectrum around 100 keV.

80% of the residual event rate in the underground argon data above 250 keV, and the spectral shape closely resembles the observation. Because the  $^{252}\text{Cf}$  neutron calibration spectrum is used in place of the very low statistics neutron contamination spectrum, an excess of events can be observed in the summed background spectrum around 100 keV. As has been discussed, this feature is due to the inelastic scattering between high energy neutrons and the  $^{19}\text{F}$  nuclei in PTFE. The general agreement between the expected background spectrum and the observed spectrum confirmed the validity of this background analysis.

# Chapter 5

## Discussion on the low- $^{39}\text{Ar}$ Argon

We developed a low background liquid argon detector to measure the  $^{39}\text{Ar}$  activity in argon extracted from underground sources. The background rate in the detector was  $<4\text{ mHz/kg}$  in the 300-400  $\text{keV}_{ee}$  energy range when operated in the KURF underground laboratory. We report no observation of  $^{39}\text{Ar}$  in argon gas extracted from the Doe Canyon  $\text{CO}_2$  field in Cortez, Colorado, and set an upper limit of 0.65% on the  $^{39}\text{Ar}$  activity relative to atmospheric argon. This limit is approximately 10 times lower than the best earlier results [121] and, to the best of our knowledge, demonstrates the highest sensitivity to  $^{39}\text{Ar}$  in argon yet obtained. We note if this argon gas originates from the Earth's mantle, the  $^{39}\text{Ar}$  concentration could be as low as  $\sim 0.1\%$  of atmospheric value. We will investigate the implication of this low- $^{39}\text{Ar}$  argon in direct dark matter search experiments, and also discuss its potential application in coherent neutrino scattering detectors. Preliminary results have been presented in conference talks [175, 176], and a paper draft can be found in Ref. [177].

### 5.1 Implication for Dark Matter Experiments

This  $^{39}\text{Ar}$  measurement result represents an important milestone in argon-based direct dark matter searches. The extraordinarily low  $^{39}\text{Ar}$  activity will substantially lower

the background rate in argon-based dark matter detectors if this underground argon is used. This could enable two phase argon Time Projection Chambers (TPCs) to operate without significant  $^{39}\text{Ar}$  induced pile-up at multi-ton scales, and improve argon detectors' sensitivity to WIMP-nucleus interactions at a given exposure. It also has potential capability in the detection of low mass WIMPs.

We will focus on the  $^{39}\text{Ar}$  electron backgrounds in this analysis, though electron recoil backgrounds may also be produced by cosmic rays, environmental gamma rays, and detector radioactivity in an argon-based dark matter detector. These backgrounds can be efficiently suppressed by operating the detector in an appropriate underground location, implementing adequate (passive and active) shielding and choosing radio-pure material to construct the detector. The prevalent gamma ray backgrounds may have multiple-site interactions and are usually concentrated close to the detector surfaces, so the rate may get further reduced in the analysis. Indeed, a Geant4 Monte Carlo simulation of the DarkSide-50 detector, which uses  $\sim 50$  kg of underground argon as its detecting medium, confirms the  $^{39}\text{Ar}$  electrons as the most important source of residual electron recoil backgrounds; the  $^{39}\text{Ar}$  rate is estimated to be comparable to all other major background sources combined. It is worth noting as the the detector size increases in future experiments, the surface-to-volume ratio, and thus the external background rate per unit target mass, will decrease, while the  $^{39}\text{Ar}$  background will become more important.

### 5.1.1 Pulse Shape Discrimination in Argon

Although the  $^{39}\text{Ar}$  decay rate is many orders of magnitude higher than the expected WIMP rate in argon-based experiments, it may get sufficiently rejected by the scintillation pulse shape discrimination (PSD) method to allow sensitive WIMP detection. Therefore, the efficiency of the PSD method has to be carefully studied before a valid dark matter analysis can be carried out. In this work we will use the statistical

$F_{\text{prompt}}$  model in Ref. [167] to study the energy dependence of the PSD method and its effect on direct WIMP detection experiments.

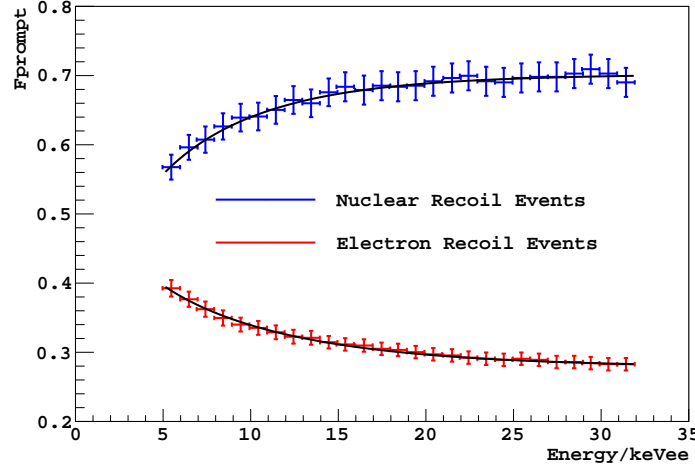


Figure 5.1: The  $F_{\text{prompt}}$  values for nuclear recoil events and for electron recoil events measured by Ref. [167]; the energy unit is in electron equivalent energy and a correction factor of 0.29 needs to be applied to obtain the nuclear recoil energy. The black curves are the analytical functions used in this analysis.

As discussed in Sec. 2.1, electron recoils and nuclear recoils have different fractions of prompt scintillation light, thus the parameter  $F_{\text{prompt}}$  can be used to discriminate between the two groups of events. As illustrated in Fig. 5.1, nuclear recoils, with high ionization densities, have larger  $F_{\text{prompt}}$  values than electron recoils. As the energy goes down the  $F_{\text{prompt}}$  separation between the two group of events gets smaller. This is usually explained by the changes of ionization energy density at low energy (the value is expected to increase for electron recoils and to decrease for nuclear recoils), but statistical effects may also play a role, as will be discussed. Due to the converging  $F_{\text{prompt}}$  values and the decreasing photon statistics at low energies, the PSD discrimination power would deteriorate.

The photon numbers of the prompt scintillation and the late scintillation are modeled as independent Gaussian distributions in Ref. [167]; the mean and width are denoted as  $\mu_p, \mu_l$  and  $\sigma_p, \sigma_l$  respectively. In simple Poisson statistics,  $\mu_p = (\mu_p + \mu_l)\hat{f}_p = \mu_t\hat{f}_p$ ,  $\mu_l = \mu_t(1 - \hat{f}_p)$ ,  $\sigma_p^2 = \mu_p$  and  $\sigma_l^2 = \mu_l$ . But in experiments, additional



uncertainties (noise) also add to the spread of these Gaussian distributions.

$$\begin{aligned}\sigma_p^2 &= \mu_p + \sigma_{p,add}^2 \\ \sigma_l^2 &= \mu_l + \sigma_{l,add}^2\end{aligned}\tag{5.1}$$

The additional uncertainties may come from the finite width of the PMT's single photon response, the waveform integration algorithm, or electronics noise. Most of these uncertainty sources may be significantly reduced for low energy events in large dark matter detectors with many PMTs, where photon occupancy at each PMT is low and single photon counting becomes possible.

The distribution of the  $F_{\text{prompt}}$  values can be calculated as the ratio of two correlated Gaussian distributions:  $G(\mu_p, \sigma_p)$  for the prompt light and  $G(\mu_p + \mu_l, \sqrt{\sigma_p^2 + \sigma_l^2})$  for the total light. An approximate formulation of the distribution function is given by Ref. [167] as<sup>1</sup>:

$$g_{f_p}(x) = \frac{\sigma_l^2 \mu_p x + \sigma_p^2 \mu_l (1-x)}{\sqrt{2\pi} [\sigma_l^2 x^2 + \sigma_p^2 (1-x)^2]^{3/2}} \exp \left\{ -\frac{[\mu_l x - \mu_p (1-x)]^2}{2[\sigma_l^2 x^2 + \sigma_p^2 (1-x)^2]} \right\} \tag{5.2}$$

which was reported to agree well with the exact form in the authors' original work. So this approximate formula is used in this analysis.

The authors of Ref. [167] fit the measured  $F_{\text{prompt}}$  distributions of the electron recoil data and nuclear recoil data to the  $F_{\text{prompt}}$  distribution function, and used the fit functions to estimate the probability for an electron recoil event to pass the mean nuclear recoil value ( $\sim 50\%$  acceptance). This probability is defined as the electron recoil contamination (ERC), and its energy dependence is shown in Fig. 5.2(left).

The fit to Eq. 5.2 also provided estimates of the free parameters; the variances  $\sigma_p^2, \sigma_l^2$  were found to be  $\sim 1.3$  and  $\sim 2.2$  times higher than the Poisson statistical

---

<sup>1</sup>We note the formulae in Ref. [167] and Ref. [102] both have typos. The formula presented here were calculated from the original paper (Ref. [178]) and were tested with simulations.

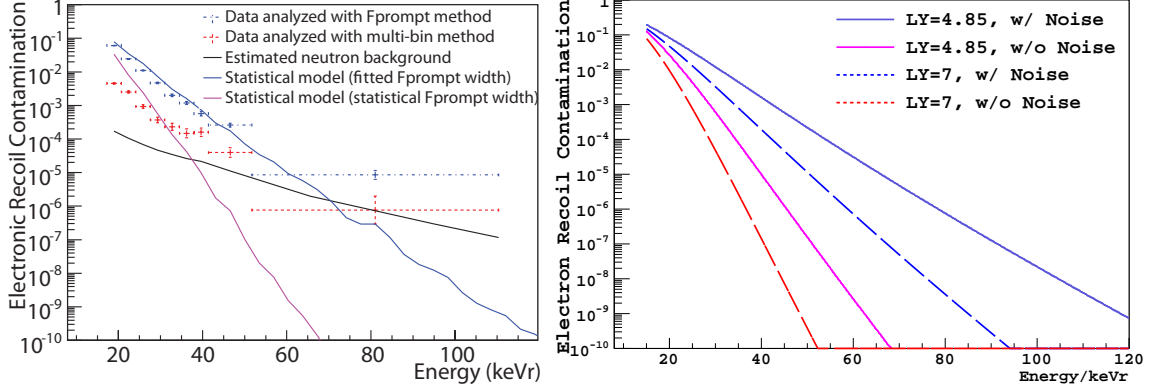


Figure 5.2: Left: the electron recoil contamination (ERC) probability reported in Ref. [167]; the result of the multi-bin method is incorrect in this figure but doesn't affect our analysis; Right: the ERC probability calculated in this work.

predictions  $\mu_p, \mu_l$  respectively. Because the authors didn't report the  $\mu_p, \mu_l$  values determined by the fit, we used that obtained by simple Gaussian fits (shown in Fig. 5.1); the factors 1.3 and 2.2 were also used to reflect the contribution from noise. The ERC probability we calculated (right of Fig. 5.2) generally agrees with the original work, but the values in some regions are slightly higher, possibly due to the differences in the  $\mu_p, \mu_l$  and  $\sigma_p^2, \sigma_l^2$  values. We also present the ERC probability at a higher light yield value of 7 p.e./keV<sub>ee</sub> compared to 4.85 p.e./keV<sub>ee</sub> in Ref. [167]. This is a typical light yield value of the DarkSide experiment<sup>2</sup>, and should be achievable in other argon detectors. The ERC rate calculated at 7 p.e./keV<sub>ee</sub> is noticeably better than that at 4.85 p.e./keV<sub>ee</sub>, and will be used in this analysis.

However, the above model (Eq. 5.2) doesn't consider the spread of the observed energy. Due to statistical and systematical fluctuations, the observed event energy estimated from photon numbers could be higher or lower than the deposited energy. We have ignored this energy spread and applied a uniform  $F_{\text{prompt}}$  cut (the 50% nuclear recoil acceptance cut is a function of energy) in calculating the ERC rate. So Monte Carlo simulation was used to evaluate this effect.

<sup>2</sup>DarkSide has achieved an electron recoil light yield of  $\sim 9$  p.e./keV at null drift field [100], and the value may drop by half when an electric field is applied; the nuclear recoil light yield is not expected to significantly vary with the field.

Fig. 5.3 (left) shows the mean  $F_{\text{prompt}}$  distribution of simulated electron recoil events (with noise) at an energy deposition of  $10 \text{ keV}_{ee}$ . The  $F_{\text{prompt}}$  mean takes the simulated value of 0.34 at the observed energy of  $10 \text{ keV}_{ee}$ , but the value is slightly higher at lower observed energy and lower at higher observed energy. This was found to be a result of the non-Poisson variances in the prompt/late photon numbers. Simulations revealed that the  $F_{\text{prompt}}$  values stayed approximately flat with respect to observed energies when  $\sigma_{p,l}^2 = \mu_{p,l}$ . In the case of  $\sigma_p^2/\mu_p < \sigma_l^2/\mu_l$ , as is in the case of electron recoils ( $\sigma_p^2/\mu_p \sim 1.3, \sigma_l^2/\mu_l \sim 2.2$ ), the  $F_{\text{prompt}}$  values have a trend shown in Fig. 5.3, and the curve flips about the expected  $F_{\text{prompt}}$  value for  $\sigma_p^2/\mu_p > \sigma_l^2/\mu_l$ . For a continuous energy spectrum, the positive and negative  $F_{\text{prompt}}$  offsets may cancel out and result in a flat (but broader)  $F_{\text{prompt}}$  distribution. This compensation scheme breaks down in the vicinity of 0 because there are no events from negative energy deposition to balance out the  $F_{\text{prompt}}$  offsets induced by positive energy events. This effect may be responsible for part of the rising  $F_{\text{prompt}}$  values for low energy electron recoils, and might also partially explain the dropping nuclear recoil  $F_{\text{prompt}}$  if  $\sigma_p^2/\mu_p > \sigma_l^2/\mu_l$  were met.

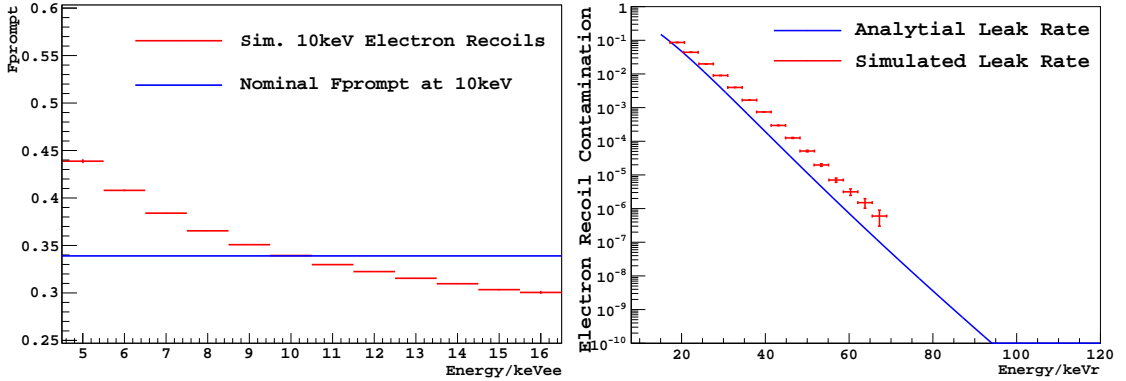


Figure 5.3: Left: the  $F_{\text{prompt}}$  distribution of simulated electron recoil events at an energy deposition  $10 \text{ keV}_{ee}$ ; Right: The simulated ERC rate compared to the analytical model (Eq. 5.2); note that the energy scale is the deposited energy, and the leakage events are mostly observed at lower energies. In both plots we assume a light yield of  $7 \text{ p.e./keV}_{ee}$ .

$F_{\text{prompt}}$  prefers to take a larger value for observed energies below the energy

deposition, and the  $F_{\text{prompt}}$  cut that defines 50% nuclear recoils acceptance drops at low energy, so a higher than predicted ERC rate can result, as illustrated in Fig. 5.3 (right). However, since the observed energy of the leakage events are mostly below the deposited energy, this ERC curve needs to be shifted to lower energies in an experiment, with the offset value of the shift determined by the electron recoil spectrum. The analytical model result in Fig. 5.2 could also carry a smaller offset, which may explain the better than predicted PSD power observed in Fig. 5.2 (left).

To sum up, the argon PSD efficiency depends on a variety of experimental parameters such as the light yield, the electronic noise level and the background spectral shape; the background rejection power is expected to vary from experiment to experiment. We note that the DarkSide experiment has predicted a better background rejection power using this  $F_{\text{prompt}}$  model by reducing the electronic noise [179], and alternative PSD methods have been shown to yield better discrimination powers [167]. However, we will stick to the simple analytical PSD model in this illustrative analysis and restrict to the  $^{39}\text{Ar}$  electron background.

### 5.1.2 Event pile-up in Two Phase Argon TPCs

A two phase argon TPC such as the DarkSide detector, collects both the scintillation and ionization signals induced by WIMP-nucleus collisions. On the one hand, the two phase operation enables the TPCs to gain background rejection power in addition to the PSD. For example, the ionization signals carry information of the event positions (the x-y position is indicated by the projection of the ionization signal and the z position can be estimated by the drift time), and help reject the surface related backgrounds. In addition, the scintillation-to-ionization ratio can help distinguish nuclear recoil events from electron recoil backgrounds, and combining the scintillation and ionization signals can provide a better estimate of the event energy.

On the other hand, the two phase scheme can cause serious pile-up problems

in large argon TPCs. In a typical liquid argon TPC, the ionization electrons are drifted by an electric field towards the gas phase and get detected. The height of a cylindrical liquid argon detector with 1 ton volume is approximately 97 cm at a unit diameter-to-height ratio<sup>3</sup>; this corresponds to a maximum drift time of  $\sim 500 \mu\text{s}$  at a typical drift velocity of a few mm/ $\mu\text{s}$  for  $\sim \text{keV}/\text{cm}$  drift field [113]. Considering the  $\sim 1 \text{ Bq/kg}$   $^{39}\text{Ar}$  activity in atmospheric argon, approximately 50% of the  $500 \mu\text{s}$  data acquisition windows would contain at least one  $^{39}\text{Ar}$  decay event. This pile-up effect poses serious challenges to the experiments. For example, uncertainties may be brought in during the process of pairing up ionization and scintillation signals, so the background rejection power from scintillation-to-ionization comparison may be compromised. If these events occur very close in time, resolving their energies and positions is also difficult. As a result, a large fraction of the TPCs' operation time would be effectively dead at 1 ton scale.

$^{39}\text{Ar}$ Levels	$M_{\text{Ar}}$ , 50% D.T.	TPC height	drift time
atmospheric	1 ton	1.0 m	$500 \mu\text{s}$
5% atmospheric	10 ton	2.1 m	$1000 \mu\text{s}$
0.65% atmospheric	45 ton	3.4 m	$1700 \mu\text{s}$
0.1% atmospheric	180 ton	5.5 m	$2700 \mu\text{s}$

Table 5.1: The estimated mass of two phase argon TPCs that have  $\lesssim 50\%$  dead time from  $^{39}\text{Ar}$ . An equal diameter-height ratio and an electron drift velocity of  $2 \text{ mm}/\mu\text{s}$  are used.

However, it is usually believed that multi-ton detectors are required to scan the predicted parameter space of WIMP candidates. A seemingly possible solution is to build a short TPC that has a smaller drift time, but this method is only expected to suppress pileup effect by factors of a few. In addition, such a design will have a larger surface area and require more PMTs, which could make the experiment more costly and induce more backgrounds.

---

<sup>3</sup>The aspect ratio of equal diameter and height gives the minimum surface area at a given cylindrical volume, and the surface is usually responsible for a large fraction of the backgrounds.

This pile-up problem can be mitigated by using argon with a low  $^{39}\text{Ar}$  activity. Taking the 1 ton cylindrical argon TPC as example, the probability for an  $^{39}\text{Ar}$  decay to appear in the 500  $\mu\text{s}$  drift window is only  $\leq 0.3\%$  for the underground argon ( $\leq 0.65\%$   $^{39}\text{Ar}$  compared to the atmospheric). If we assume  $^{39}\text{Ar}$  is the only background in an argon detector, we can calculate the TPC mass that gives  $\lesssim 50\%$  dead time for different  $^{39}\text{Ar}$  levels; this will give us an illustration of the effects of  $^{39}\text{Ar}$ . Denote  $d$  and  $h$  as the diameter and height of the TPC,  $v$  as the typical electron drift velocity,  $\rho$  as the liquid argon density of  $1.4\text{ g/cm}^3$ , and  $R$  as the  $^{39}\text{Ar}$  activity relative to the atmospheric value, we will have the equation

$$\frac{h}{v} \frac{\pi d^2 h}{4} \rho \frac{1\text{Bq}}{1\text{kg}} R = 50\%$$

The TPC mass limits are calculated for different  $^{39}\text{Ar}$  activities, as summarized in Tab. 5.1. The usage of underground argon can increase the maximum size of argon TPCs from  $\sim 1$  ton to at least 45 tons. We note that the actual  $^{39}\text{Ar}$  activity in the underground argon could be as low as 0.1% atmospheric, and this would further increase the mass limit to 180 tons.

Fig. 5.4 shows the expected WIMP sensitivity of argon TPCs (1 year exposure) with  $^{39}\text{Ar}$  concentrations and sizes that are listed in Tab. 5.1. We have applied a dead time of 50% that includes some contributions from backgrounds other than  $^{39}\text{Ar}$  (The  $\sim 50\%$  time loss in the above discussion only applies to the maximum drift time, while most events have much smaller drift time values.). Besides the exposure, the dark matter sensitivity calculation also requires an estimate of the energy threshold values in the WIMP search, which will be discussed in detail in Sec. 5.1.3. We comment that we used a conservative PSD efficiency function and left out the scintillation-to-ionization discrimination power in this calculation; so the result is conservative and only serves illustration purposes. The WIMP parameter spaces predicted by a few

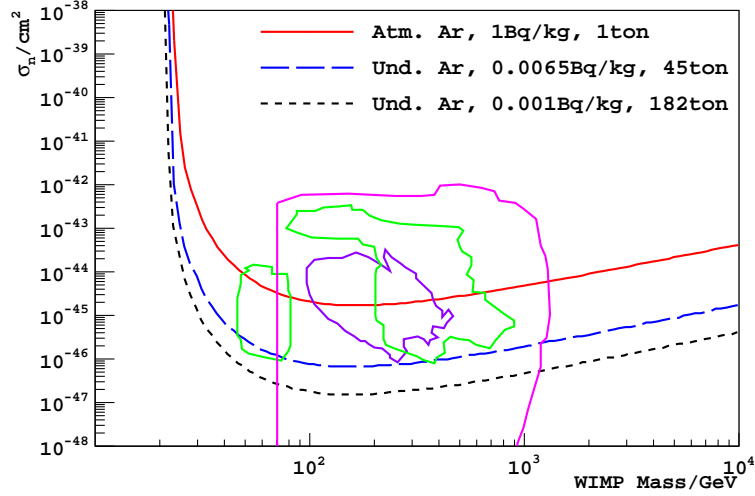


Figure 5.4: The expected WIMP sensitivity of a argon TPC (1 year exposure) with  $^{39}\text{Ar}$  concentration and size values as summarized in Tab. 5.1. The contours show the LHC-constrained WIMP parameter spaces predicted by various theories: phenomenological MSSM [180](pink), and cMSSM [181,182] (purple and green).

supersymmetric theories (restrained by LHC results) are also shown.

### 5.1.3 Improved WIMP sensitivity in Argon Detectors

Besides increasing the maximum possible size of argon TPCs, the use of underground argon can also increase the WIMP sensitivity of argon detectors (both two phase and single phase) at a given exposure. Single phase argon scintillation detectors don't have serious pile-up problems until the active mass reaches  $\sim 100 \text{ ton}^4$ , but they can also benefit from a low WIMP detection energy threshold that is made possible by the low  $^{39}\text{Ar}$  electron recoil background rate.

Tab. 5.2 summarizes the estimated energy threshold in an argon scintillation detector that yields  $\lesssim 0.1$  misidentified  $^{39}\text{Ar}$  event in 1 ton·yr exposure. For a Poisson distribution with an expected event rate of  $\lesssim 0.1$ , the probability of observing 0 events is  $\gtrsim e^{-0.1} \approx 90\%$ , and we take this rate limit as an assumption for null result. In the calculations, we first multiplied the  $^{39}\text{Ar}$  electron spectrum with the PSD rejection ef-

<sup>4</sup>We have assumed a data acquisition window at the level of  $\sim 10 \mu\text{s}$ .

efficiency at 50% nuclear recoil acceptance (Fig. 5.3), and then integrated the resultant function over different energy regions to get the expected rate. We comment that the PSD power is very high at high energies that the misidentified event rate doesn't significantly change for  $^{39}\text{Ar}$  levels different by a few orders of magnitude, and the effect is only significant at low energies. Lower electron recoil background rate can enable the detector to take a lower energy threshold and thus increase its capability of detecting WIMP interactions.

$^{39}\text{Ar}$ Levels	$E_{th}$ w/ noise from Ref. [167]		$E_{th}$ stat. only	
	$E_{ee}$	$E_{nr}$	$E_{ee}$	$E_{nr}$
atmospheric	24.3 keV	83.8 keV	13.5 keV	46.6 keV
5% atmospheric	20.9 keV	72.0 keV	12.0 keV	41.4 keV
0.65% atmospheric	18.7 keV	64.5 keV	11.0 keV	37.9 keV
0.1% atmospheric	16.7 keV	57.6 keV	10.1 keV	34.8 keV

Table 5.2: The estimated energy threshold in an argon detector that yields  $\lesssim 0.1$  misidentified  $^{39}\text{Ar}$  event in 1 ton·yr exposure. The nuclear recoil acceptance is set to be  $\sim 50\%$ .

The dark matter sensitivity of a null-result experiment is usually represented with a 90% exclusion curve. This curve gives the combination of WIMP-nucleon interaction cross section and WIMP mass to yield the expected 90% upper limit of the WIMP interaction rate. For example, if 0 event is observed, the 90% upper limit of WIMP interaction rate is estimated to be 2.3 from Poisson statistics. In other words, for a Poisson distribution  $P(k, \lambda)$  with an expected event rate of  $\lambda$ , the probability to observe one or more events  $P(k > 0, \lambda) = 1 - e^{-\lambda}$  is greater than 90% for  $\lambda > 2.3$ . If a finite event number is observed and the background level in the experiment is known, the Feldman-Cousins method can be used to calculate the classical (from frequentist's view instead of Bayesian) confidence interval/limits [183]. We used the micrOMEGAs software [184] to calculate the WIMP interaction rates.

Fig. 5.5 shows the projected sensitivities of an argon-based dark matter detector in



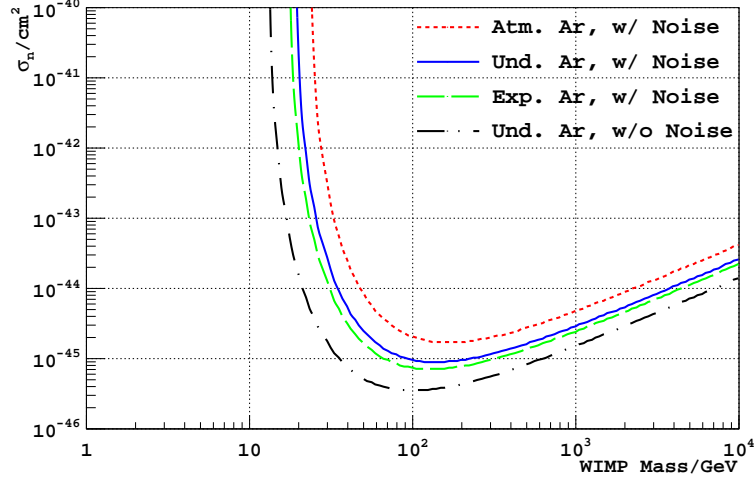


Figure 5.5: The estimated WIMP dark matter sensitivity of an argon detector with 1 ton·yr exposure (50% acceptance). The  $^{39}\text{Ar}$  level in the underground argon is assumed to be the upper limit value of 0.65% and the expected  $^{39}\text{Ar}$  level is 0.1%. We assume no observation of WIMPs events above the energy thresholds listed in Tab. 5.2.

1 ton·yr exposure assuming no observation of WIMP events. We show the sensitivity curves for atmospheric argon, for the underground argon with an  $^{39}\text{Ar}$  limit of 0.65% atmospheric, and for the expected 0.1%  $^{39}\text{Ar}$  level in the underground argon; the differences are resulted from the different energy threshold values as listed in Tab. 5.2. For heavy WIMP ( $\gtrsim 100$  GeV), the projected sensitivity using the underground argon (0.65%  $^{39}\text{Ar}$  compared to atmospheric) is approximately 2 time better than that using atmospheric argon. This corresponds to an increase of the WIMP interaction rate by  $\sim 2$  with the lower energy threshold. As for low mass WIMPs below 100 GeV, the improvement is more prominent ( $\sim 50$  times increase in sensitivity for 30 GeV WIMPs) because light WIMPs only induce nuclear recoil events at low energies, and the lowered energy threshold makes the detection of such events possible.

We also show the sensitivity curve using underground argon but excluding the additional noise in the PSD analysis. This may be achieved in large dark matter detectors where many PMTs are installed so single photon counting method can be used in low energy events. As a result the uncertainties from the PMT's single

photoelectron pulse spread and from the waveform baseline noise can be eliminated. This would increase the underground argon detector’s sensitivity by a factor of  $\sim 2\text{-}3$  for heavy WIMPs and up to  $\sim 100$  for lighter WIMPs.

We comment that the sensitivity prediction presented in Fig. 5.5 is to illustrate the effects of different  $^{39}\text{Ar}$  activities, and the real WIMP sensitivity of an argon detector depends on many experimental parameters. For example, the microClean experiment has achieved a PSD power a few times better than the simple  $F_{\text{prompt}}$  method with the multi-bin method [167]. The DarkSide-10 experiment also significantly improved the  $F_{\text{prompt}}$  discrimination efficiency by reducing the electronic noise and defining an energy-dependent nuclear recoil acceptance [179]. This improvement enables the DarkSide-50 detector to expect an energy threshold as low as 20 keV nuclear recoil energy (with a low nuclear recoil acceptance  $< 5\%$ ) using the underground argon (assuming its current upper limit). The DarkSide-50 experiment is expected to have a dark matter sensitivity of  $1 \times 10^{-45} \text{ cm}^2$  for 100 GeV WIMPs in 100 kg·yr exposure, 1/10 of that assumed in this analysis.

#### 5.1.4 Argon in Light WIMP Detections

Several experiments including DAMA [38], CoGeNT [44, 45], CRESSTII [56] and CDMSII [52] have reported possible signals of light WIMP ( $\sim 10 \text{ GeV}$ ) interactions at the cross section level of  $10^{-42} - 10^{-39} \text{ cm}^2$ . Argon detectors, however, are usually considered as insensitive to light WIMPs. For example, the argon nuclear recoil energy from collision with  $\sim 10 \text{ GeV}$  WIMPs is expected to be  $\lesssim 20 \text{ keV}$ , while few argon detectors can achieve such a low threshold. As illustrated in Fig. 5.5, even for detectors using the underground argon with  $\sim 150$  times less  $^{39}\text{Ar}$  activity, the detection of light WIMPs is still unlikely at the cross section of  $10^{-40} \text{ cm}^2$ .

The limitation of argon-based detectors in low mass WIMP detection rises from the requirement of zero background, and thus may be avoided if backgrounds are allowed.

Light WIMPs are expected to have a high flux, and the interactions mostly have low energy transfers, so the signal rate at low energies may be significant compared to the residual background rate. In this scenario, interactions of light WIMPs can be identified by comparing the expected background event rate with what is observed, or by a rate modulation analysis like that of DAMA and CoGeNT. In this sense, argon may be used in the search for light WIMPs and provide an independent test of the existing WIMP claims.

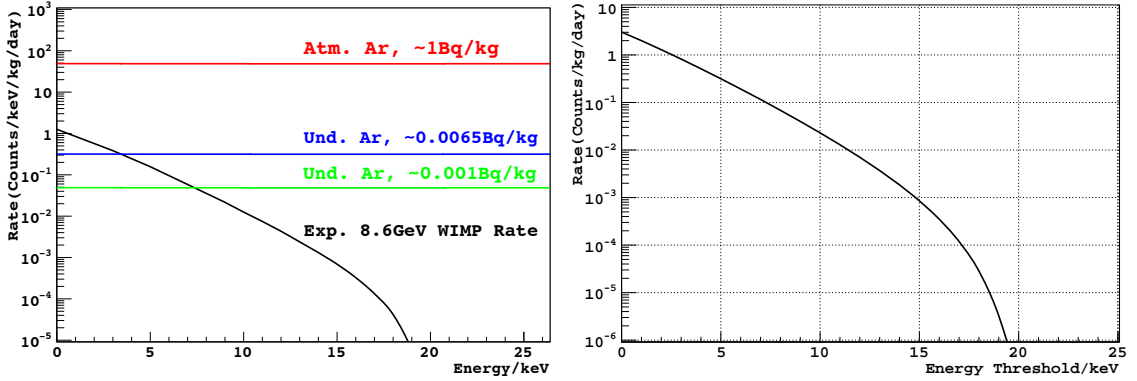


Figure 5.6: Left: The expected argon nuclear recoil energy spectrum induced by 8.6 GeV WIMPs at a nucleon scattering cross section of  $1.9 \times 10^{-41} \text{ cm}^2$ , compared to the expected  $^{39}\text{Ar}$  rate. We have assumed a quenching factor of 0.29 for nuclear recoils relative to electron recoils; Right: the integrated light WIMP signal rate above a certain energy threshold.

Fig. 5.6 (left) shows the expected argon nuclear recoil spectrum induced by 8.6 GeV WIMPs at a spin-independent WIMP-nucleon scattering cross section of  $1.9 \times 10^{-41} \text{ cm}^2$ . The  $^{39}\text{Ar}$  background spectra at different  $^{39}\text{Ar}$  concentration levels are also shown, where we have used a quenching factor of 0.29 to convert the  $^{39}\text{Ar}$  electron recoil energy to equivalent nuclear recoil energy. We don't discriminate between nuclear recoil events and electron recoil events in this analysis, which makes the result conservative. As can be seen, the expected WIMP interaction events are overwhelmed by the  $^{39}\text{Ar}$  electrons in atmospheric argon even at the lowest energy, but the rate is significantly higher than that of  $^{39}\text{Ar}$  in underground argon (assuming an  $^{39}\text{Ar}$  activity at the upper limit of 0.65%) below 3 keV. The overall WIMP event rate below

10 keV is calculated to be comparable to that of the total  $^{39}\text{Ar}$  rate ( $\sim 3/\text{kg}/\text{day}$ ) in underground argon. If the actual  $^{39}\text{Ar}$  activity in the underground argon is  $\sim 0.1\%$  of the atmospheric value, the WIMP events would dominate the  $^{39}\text{Ar}$  background up to  $\sim 8$  keV and allow a larger WIMP search window.

Therefore, the underground argon may be used in the detection of light WIMPs if the rate of other electron recoil backgrounds can be suppressed to below that of  $^{39}\text{Ar}$ . Actually argon has its advantages over germanium and xenon in light WIMP detection because argon nuclei can pick up more kinetic energy from collisions with light WIMPs. The challenges in such experiments are the suppression of electron recoil backgrounds and the estimation of nuclear recoil energy at very low energy scales. The former is believed to be achievable in a radio-pure detector like DarkSide-50; Monte Carlo simulations have shown that  $^{39}\text{Ar}$  is the dominant source of residual electron recoil backgrounds in DarkSide-50, which is equipped with a high efficiency scintillator veto. As for the latter, an argon nuclear recoil experiment (DarkSide-SCENE) is ongoing at the Norte Dame University using a neutron beam, and may shed light on the argon quenching factors at very low energies.

## 5.2 Potential Application in CNS Detection

The underground argon also has its potential application in fields other than direct dark matter detections. The possibility of detecting very low energy nuclear recoils with low- $^{39}\text{Ar}$  argon opens the possibility of detecting Coherent Neutrino Scattering (CNS) with argon. The CNS process, which has long been predicted by the Standard Model of particle physics, can test standard and non-standard neutrino interaction models, but has not been observed.

A neutrino of any flavor can scatter off a nucleus via neutral current interaction and transfer part of its energy to the nucleus. The maximum nuclear recoil energy is

$2k^2/(M_T + 2k)$ , or approximately  $2k^2/M_T$  for relatively low neutrino energy, where  $k$  is the incident neutrino energy. Typical recoil energy varies from keV to tens of keV depending on the target mass and the neutrino energy. At such a low energy transfer, all the nucleons in the nucleus interact with the neutrino coherently, as in the case of low energy WIMP-nucleus interactions. The coherent interaction cross section for a spin-less nucleus like argon is calculated to be [185,186]:

$$\begin{aligned}
\frac{d\sigma}{dE} &= \frac{G_F^2}{2\pi} \frac{(N - (1 - 4\sin^2\theta_W)Z)^2}{4} F^2(2M_T E) M_T \left(2 - \frac{M_T E}{k^2}\right) \\
\sigma &\sim 0.4 \times 10^{-44} N^2 \left(\frac{k}{\text{MeV}}\right)^2 \text{cm}^2 \\
\langle E \rangle &= \frac{1}{3} E_r^{\text{max}} \approx 716 \frac{k/\text{MeV}}{A} \text{eV}
\end{aligned} \tag{5.3}$$

where  $G_F$  is the Fermi coupling constant,  $\theta_W$  is the weak mixing angle,  $N$  and  $Z$  are the neutron number and proton number of the target nucleus,  $M_T$  is the target nucleus mass, and  $F$  is the nuclear form factor at momentum transfer  $2M_T E$ . The coherent condition is largely satisfied for neutrino energies up to 50 MeV.

Typical CNS interaction cross sections are at the level of  $\sim 10^{-39} \text{cm}^2$ , significantly larger than that of the charged current interactions such as inverse beta decay of proton ( $\sim 10^{-40} \text{cm}^2$ ) and elastic scattering with electrons ( $\sim 10^{-43} \text{cm}^2$ ) in the same neutrino energy region [185]. If the cross section and the nuclear recoil spectrum of CNS can be accurately measured, it will provide useful information about the weak mixing angle, the neutrino magnetic moment, and other neutrino physics beyond the Standard Model. Since the interaction is blind to neutrino flavors, it measures the total neutrino flux, and can constrain neutrino mixing parameters and also sterile neutrinos physics by combining with charged current interaction measurements. This process is also proposed to monitor nuclear reactor operations.

The CNS interaction rate for stopped-pion neutrinos<sup>5</sup> with a few target nuclei

---

<sup>5</sup>This neutrino source includes 29.9 MeV  $\nu_\mu$  from  $\pi^+$  decay, and  $\bar{\nu}_\mu \nu_e$  neutrinos at the energy of tens of MeV level from  $\mu^+$  decays.

including argon is calculated in Ref. [185]. Assuming a neutrino flux of  $\sim 1 \times 10^7 \nu/s/cm^2$ , the expected CNS rate from the 29.9 MeV  $\nu_\mu$  is approximately 7,000 /ton/yr in argon, and the rate above an energy threshold of 20 keV is  $\sim 2,000$ /ton/yr. At the same neutrino flux, the  $\bar{\nu}_\mu \nu_e$  neutrinos contribute a higher rate of 18,000 /ton/yr, or 9,000 /ton/yr above 20 keV. This event rate and energy threshold are expected to be within the reach of modern low background detectors, if a low energy threshold and a low background are achieved.

Ref. [186] proposes a two phase liquid argon TPC aiming to detect CNS from reactor neutrinos. Because of the low neutrino energy from reactors, the average energy of CNS nuclear recoil events is very low, approximately 200 eV. No efficient scintillation signals can be observed at this energy level, and the detector is designed to collect the ionized electrons by drifting the electrons with an electric field and detecting them in a gas phase. Assuming a neutrino flux of  $\sim 6 \times 10^{12} \nu/s/cm^2$ , the expected CNS rate is 56 /kg/day, 29% of which are expected to produce at least one ionized electron based on a Monte Carlo simulation. The fraction can be increased to 36% if the 1% of xenon doping is added to the argon volume.

Fig. 5.7 shows the Monte Carlo simulated CNS nuclear recoil spectrum induced by a reactor neutrino flux of  $\sim 6 \times 10^{12} \nu/s/cm^2$  in argon. The gamma ray backgrounds are sampled from certain levels of U, Th, K contents in 20 cm of concrete wall, and the neutron background is assumed to be  $\sim 10^5 /m^2/s$  with an  $1/E$  spectral shape from thermal energy up to 20 MeV. It can be seen from the figure that with adequate shielding (2 cm of lead and 10 cm of borated polyethylene) the gamma ray and neutron background can be suppressed to several times lower than the CNS rate, but the  $^{39}\text{Ar}$  background overwhelms the CNS signal if atmospheric argon is used.

Nevertheless, if the underground argon is used in this experiment, the  $^{39}\text{Ar}$  background rate will be greatly reduced and bring the overall background rate below the expected CNS rate. The authors have built a prototype argon TPC with 140 g of

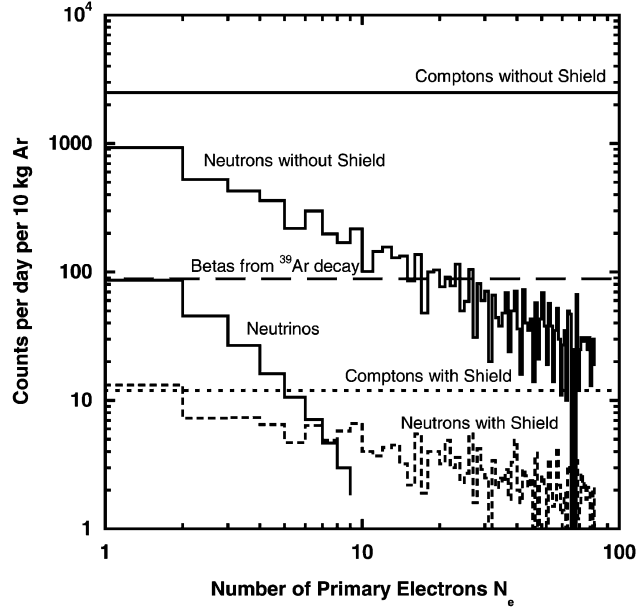


Figure 5.7: The simulated CNS nuclear recoil spectrum from reactor neutrinos compared to that of various backgrounds [186]. The gamma ray backgrounds are assumed to originate from 20 cm of concrete wall with certain U/Th/K contents, and the neutron backgrounds used have a  $1/E$  spectrum from thermal energy up to 20 MeV.

active mass, and have successfully observed single electron ionization signals [187]. A 10 kg detector has been proposed, which will be installed close to a nuclear power plant in an attempt to detect CNS signals. The authors have expressed interests in our underground argon, but no implementation plan has been made yet.

It is worth noting that CNS events can be an irreducible background to WIMP dark matter experiments. The flux of ambient neutrinos including solar neutrinos, atmospheric neutrinos, geo-neutrinos and reactor neutrinos, is estimated to be at the level of  $\sim 10^{10} \nu/s/cm^2$  [188]. Most of them are populated at low energies ( $<1$  MeV) and don't produce nuclear recoil events above 1 keV in medium atomic number elements. The solar  $^8B$  neutrinos, on the contrary, may extend beyond 10 MeV energy and have a high flux of  $\sim 10^6 \nu/s/cm^2$ ; they can be a serious background to dark matter experiments. The potential CNS nuclear recoil backgrounds have been studied by a few authors [188, 189], and tens of CNS nuclear recoils are expected in 1 ton·yr

exposure if keV level energy thresholds are achieved<sup>6</sup>. As for argon-based WIMP detectors, the relatively high energy thresholds of  $\gtrsim 20$  keV used in current experiments cut off most of the neutrino contamination, but as the detection technology continues improving, the ultimate sensitivity will be restricted by the neutrino backgrounds.

### 5.3 Discussion on Argon Isotopes

The electron capture decay of  $^{40}\text{K}$  is primarily responsible for the terrestrial production of the stable argon isotope  $^{40}\text{Ar}$ . The importance of this process can be seen from the large  $^{40}\text{Ar}/^{36}\text{Ar}$  ratio of 295.5 in the atmosphere compared to the solar value of  $3 \times 10^{-4}$  [115]. The total  $^{40}\text{Ar}$  produced since the Earth's accretion can be calculated based on the estimated  $K$  concentration in the bulk Earth; approximately 50% of the radiogenic  $^{40}\text{Ar}$  is found in the Earth's atmosphere, with the rest remaining underground [115].

The radioactive argon isotope  $^{39}\text{Ar}$  is mainly produced in the atmosphere by cosmogenic neutrons:  $^{40}\text{Ar}(n, 2n)^{39}\text{Ar}$ . The interaction cross section is most significant for neutron energy higher than 10 MeV.  $^{39}\text{Ar}$  has a half life of 269 yr, and decays by emitting electrons up to 565 keV energy. The presence of  $^{39}\text{Ar}$  poses a serious problem to direct dark matter detection experiments that use atmospheric argon as the target material. A reasonable approach to solve the  $^{39}\text{Ar}$  problem is to seek underground sources of argon that are shielded from cosmic rays. Note that neutrons may also be produced deep underground by fission and  $(\alpha, n)$  processes, but fortunately the radiogenic neutrons usually have energies lower than 10 MeV. Combining the low neutron flux with the low mass fraction of  $^{40}\text{Ar}$  in the bulk Earth, the  $^{40}\text{Ar}(n, 2n)^{39}\text{Ar}$  process is negligible underground.

However, alternative  $^{39}\text{Ar}$  production processes, including negative muon capture

---

<sup>6</sup>The contamination from reactor neutrinos depends on the relative locations of the reactors and the detectors, and the readers are referred to Ref [190] for such an example analysis.



and (n, p) process on  $^{39}\text{K}$ , as well as (n,  $\alpha$ ) reaction on  $^{42}\text{Ca}$ , can be significant. Negative muon capture on  $^{39}\text{K}$  is reported to dominate the  $^{39}\text{Ar}$  production at shallow underground sites ( $<1,800$  m.w.e.), while the muon induced neutron production rate is lower by approximately 2 orders of magnitude over all depths [117]. The muon capture production decreases quickly at large depth, where the  $^{39}\text{K}(\text{n}, \text{p})^{39}\text{Ar}$  process takes over. The  $^{42}\text{Ca}(\text{n}, \alpha)^{39}\text{Ar}$  process is a subdominant production channel because of its relatively high energy threshold compared to the  $^{39}\text{K}(\text{n}, \text{p})^{39}\text{Ar}$  process. Ref. [117] calculated the  $^{39}\text{Ar}$  and  $^{40}\text{Ar}$  production rate at different depth for typical rock composition. The results show that the  $^{39}\text{Ar}/^{40}\text{Ar}$  ratio in argon from deep underground sources can be similar to, or 1-2 orders of magnitude lower than, the atmospheric ratio, depending on the rock porosity and the argon diffusion and transportation properties. At shallow depths, the  $^{39}\text{Ar}/^{40}\text{Ar}$  ratio can be a few orders of magnitude higher than the atmospheric value, primarily due to the production by negative muon capture on  $^{39}\text{K}$ .

The prediction of the  $^{39}\text{Ar}$  activity in underground argon gets more complicated if we consider the argon recycled from the atmosphere to underground by dissolving in ground water. As a result, large uncertainties are observed for the  $^{39}\text{Ar}/^{40}\text{Ar}$  ratio measured in underground argon samples. Relative  $^{39}\text{Ar}$  concentrations ranging from 20 times lower to 16 times higher than the atmospheric value have been reported [110, 116]. The rock type is also found to play an important role in affecting the  $^{39}\text{Ar}/^{40}\text{Ar}$  ratio, with granite typically having a high  $^{39}\text{Ar}$  production rate.

The Earth's mantle, on the contrary, has a U and Th concentration 2-3 orders of magnitude lower than that of the crust. The neutron flux from ( $\alpha$ , n) process and thus the  $^{39}\text{K}(\text{n}, \text{p})^{39}\text{Ar}$  production rate can be greatly reduced. As a result, the  $^{39}\text{Ar}$  concentration in the mantle is expected to be much lower than that in the crust. Argon gas samples have been extracted from the middle ocean ridge basalts (MORB), which were derived by partial melting of the upper mantle, but no  $^{39}\text{Ar}$  measurements

have been reported. A study of the isotope ratios of rare gases extracted in the CO<sub>2</sub> gas fields in the US southwest indicated that these gases may be derived from the Earth’s upper mantle, exhibiting consistent relative isotope abundances with MORB gases [124–126]. Our underground argon is extracted from the same area, so it may also have a mantle origin, which might explain the extraordinarily low <sup>39</sup>Ar activity.

It is worth noting that the <sup>40</sup>Ar concentration in the Earth’s mantle calculated from the MORB <sup>3</sup>He/<sup>40</sup>Ar ratio and the derived MORB <sup>3</sup>He concentration couldn’t account for the total <sup>40</sup>Ar amount underground. This indicates that there may be an <sup>40</sup>Ar reservoir in the deep mantle [115]. If this is the situation, we can expect a steady flow of <sup>40</sup>Ar continuously from the mantle, which will be beneficial to many argon-based experiments. We comment that our early effort of extracting argon from the Bravo Dome CO<sub>2</sub> gas fields in Bueyeros, NM was discarded because of a rise in the <sup>39</sup>Ar concentration. This is explained by possible leaks of air into the gas well as the well pressure decreases.

The stable argon ratio <sup>40</sup>Ar/<sup>36</sup>Ar of 13,300 in our underground argon gas is consistent with the values measured with the MORB mantle gases, which range from 300 to 40,000 [191, 192]. No significant production of <sup>36</sup>Ar in the Earth’s mantle is known, and its existence is explained as either recycled air, an accretionary signature, or a combination of the two [115]. So the large variability of the <sup>40</sup>Ar/<sup>36</sup>Ar ratio in the MORB gases may reflect a mixing between the mantle argon and atmospheric argon. We note that Ref. [115] mentions that argon gas with a dominating crustal signature can also have a high <sup>40</sup>Ar/<sup>36</sup>Ar at the level of 10,000, but the crustal argon measurements by Ref. [116] all have <sup>40</sup>Ar/<sup>36</sup>Ar ratios around 300.

By contrast, the argon from the National Helium Reserve [121] has a measured <sup>40</sup>Ar/<sup>36</sup>Ar ratio of 1,640, between atmospheric and mantle values. The low <sup>39</sup>Ar limit compared to expected levels from the crust [116, 118], and the intermediate value of the <sup>40</sup>Ar/<sup>36</sup>Ar ratio may suggest that the source of the gas is deeper than the crust.

However, the argon from the National Helium Reserve was separated from natural gas that is expected to be biotic, and therefore crustal in origin. We note that noble gases in crustal fluids can show a mantle signature, particularly in regions that may be undergoing tectonic extension [193], but alternative hypotheses also exists for the origin of natural gas [194].

Besides  $^{39}\text{Ar}$  and  $^{40}\text{Ar}$ , other isotopes of argon include  $^{36}\text{Ar}$ ,  $^{37}\text{Ar}$ ,  $^{38}\text{Ar}$ ,  $^{41}\text{Ar}$  and  $^{42}\text{Ar}$ , of which  $^{36}\text{Ar}$ ,  $^{38}\text{Ar}$  and  $^{40}\text{Ar}$  are stable. Most of these argon isotopes are produced by muon spallation or neutron induced reactions on K, Ca, Cl isotopes as well as  $^{40}\text{Ar}$ , while some of them such as  $^{38}\text{Ar}$  and  $^{42}\text{Ar}$  can also be produced by alpha particle interactions on the same elements. Of the radioactive isotopes,  $^{37}\text{Ar}$  and  $^{41}\text{Ar}$  are short lived (35 days for  $^{37}\text{Ar}$  and 110 min for  $^{41}\text{Ar}$ ), and are usually not considered as serious backgrounds for underground experiments. The relatively long lived  $^{42}\text{Ar}$  decays to  $^{42}\text{K}$  by emitting electrons up to 600 keV with a half life of 33 years, and the subsequent  $^{42}\text{K}$  decay produces electrons with an endpoint of 3.5 MeV. The  $^{42}\text{Ar}$  abundance has been reported to be lower than  $6 \times 10^{-21}$  [195], which corresponds to a negligible decay rate at the level of  $\sim 1 \times 10^{-4}$  Bq/kg.

# Appendices

# Appendix A

## Surface Background Study

Direct WIMP dark matter detection experiments search for low energy nuclear recoil events as possible evidences for WIMP interactions. Various backgrounds such as elastic neutron collisions and surface alpha activities, however, can also produce nuclear recoils; the former has been discussed in Sec. 2.4.2, while the latter has not been addressed. Radon progeny can attach to the surfaces of detector components; when an alpha decay occurs the daughter nucleus can gain a recoil energy up to a few hundred keV and mimic a WIMP signal. This background has to be efficiently suppressed in a dark matter detector to allow sensitive WIMP detection.

### A.1 Surface Alpha Decay Backgrounds

Radon is naturally present in air at an activity of tens of Bq/m<sup>3</sup>. Daughter nuclides of radon decays are usually ionized at production, so they can attach to various surfaces due to static charges. Radon may also emanate from the decays of U and Th impurities in bulk materials and rise to the surface. The surface alpha activity due to radon daughters can be a few Bq/m<sup>2</sup> at normal conditions [196]<sup>1</sup>, and may be

---

<sup>1</sup>Ref. [196] reported values at the level of 100-200 Bq/m<sup>2</sup>, but the investigated samples were exposed to air with hundred times higher radon concentrations (1-3 kBq/m<sup>3</sup>) than normal values.

suppressed down to less than  $10 \alpha/m^2/\text{day}$  in low background experiments that are constructed in radon-free environments [197].

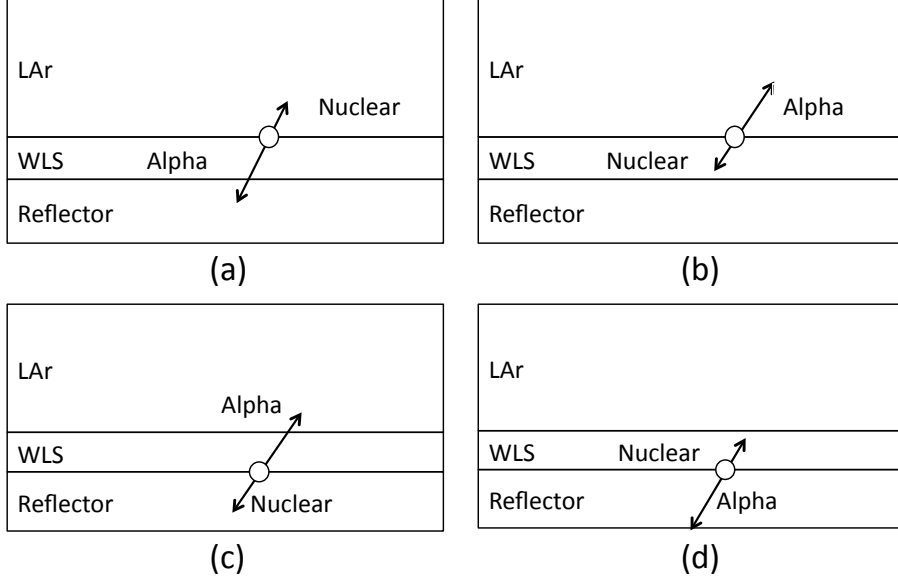


Figure A.1: Illustration of the possible configurations of surface alpha activities.

Wavelength shifting chemicals are commonly used in argon scintillation detectors to convert argon scintillation photons from UV to the visible range, so alpha emitters may exist at both the reflector surfaces and the wavelength shifter (WLS) surfaces, as illustrated in Fig. A.1. Configuration (a) is the most dangerous background in a dark matter detector because the recoiled nucleus hits the liquid argon volume directly. Take the prevalent surface background  $^{210}\text{Po}$  ( $\sim 5.3 \text{ MeV}$  alpha energy, 138 days half life) as an example, the recoil energy of the  $^{206}\text{Pb}$  nuclide is estimated to be  $\sim 103 \text{ keV}$ , which is right in the WIMP search window of some dark matter detectors. Even at a suppressed surface activity of  $\sim 10 \alpha/m^2/\text{day}$ , this surface background rate would be at the level of 10,000/year in a 1-ton argon detector<sup>2</sup>, orders of magnitude higher than the expected WIMP interaction rate. In case (b) the decay alpha hits liquid argon, and its high energy would lift this event way above typical WIMP energy windows. Case (c) is similar to case (b) because it is very likely for the alpha

<sup>2</sup>For a 1 ton LAr detector with unit diameter-to-height ratio, the total surface area is  $\sim 5 \text{ m}^2$ .

particles to penetrate the WLS layer and deposit a large kinetic energy in the liquid argon volume. For example, the 5.3 MeV alpha particles from  $^{210}\text{Po}$  decays have an expected range of  $\sim 4\text{ mg/cm}^2$  in organic chemicals, and can mostly penetrate the WLS coating at a typical thickness of  $0.1\text{--}1\text{ mg/cm}^2$  in argon experiments. In addition, the alpha energy deposition in the WLS would also produce photons<sup>3</sup> and adds to the argon scintillation. Case (d) is unlikely to be a background because nuclear recoil scintillations in WLSs are usually heavily quenched and could fall below the energy threshold of WIMP experiments. In two-phase TPCs, case (d) events can also be rejected because no ionization signals exist in liquid argon.

Nuclear recoil backgrounds due to surface alpha activities may be mitigated using a few techniques. One approach is to install a charge intercept ring near the TPC anode to block the ionization signals from surface backgrounds and reject the associated scintillation signals. Similarly if event positions can be estimated in a detector, software position cuts can be applied to reject the surface events. In this study we will investigate a new method to reject surface nuclear recoils using the concurrent alpha scintillation signals in the WLS. The photons produced by alphas can add to the nuclear recoil signal and may lift the overall energy of this background event to above the WIMP energy window; if the alpha scintillation in the WLS has a distinctively different waveform from that of nuclear recoils in liquid argon, pulse shape discrimination methods can also be used to reject the surface backgrounds.

## A.2 WLS Scintillation

Since the focus of this study is to use the alpha scintillation signals in the WLSs to reject the nuclear recoil backgrounds due to surface activities, the scintillation properties of the commonly used WLSs have to be thoroughly studied. We will discuss

---

<sup>3</sup>We note that the scintillation yield of organic scintillators is a few times lower than that of liquid argon, and alpha scintillation is highly quenched.

the alpha-induced scintillation in TPB and PTP WLSs both at room temperature and at cryogenic temperatures using a needle  $^{210}\text{Po}$  alpha source.

### A.2.1 Room Temperature Measurements

The alpha source used in these measurements is a  $^{210}\text{Po}$  needle source. The eye of the needle has a gold surface, and the  $^{210}\text{Po}$  nuclides (from a  $^{210}\text{Po}$  solution) adhere to the gold. During the measurements this needle source was pressed slightly against a WLS (TPB or PTP) layer that was coated onto a glass slide, as illustrated in Fig. A.2; the two pieces were clamped together using Spectralon fixture. The scintillation from this “light source” was collected using a Hamamatsu R11065 photomultiplier tube (PMT) and a Spectralon cell was used to enhance reflections.

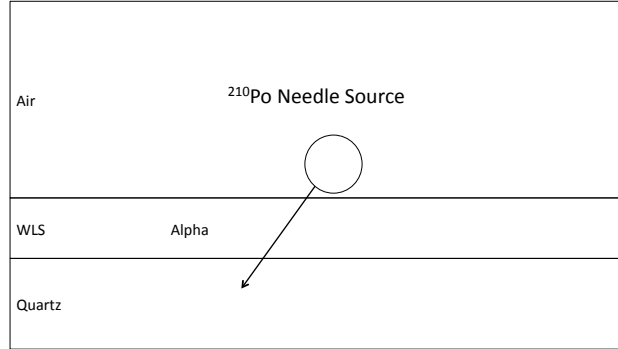


Figure A.2: The alpha-in-WLS scintillation measurement at room temperature.

As the  $^{210}\text{Po}$  nuclides decay, approximately half of the emitted alpha particles hit the WLS and make scintillation light. Alphas mostly undergo small angle scattering in the WLS and have near-straight paths. The minimum path length is the thickness of the WLS coating, which would lead to a low energy spectral cutoff. Actually because a large fraction of the alpha particles have path lengths close to this minimum, a prominent peak can be observed in the low energy region, as illustrated in Fig. A.3. The alphas with larger incident angles would produce more photons, up to a high energy cutoff that corresponds to the full alpha energy deposition in the WLS.



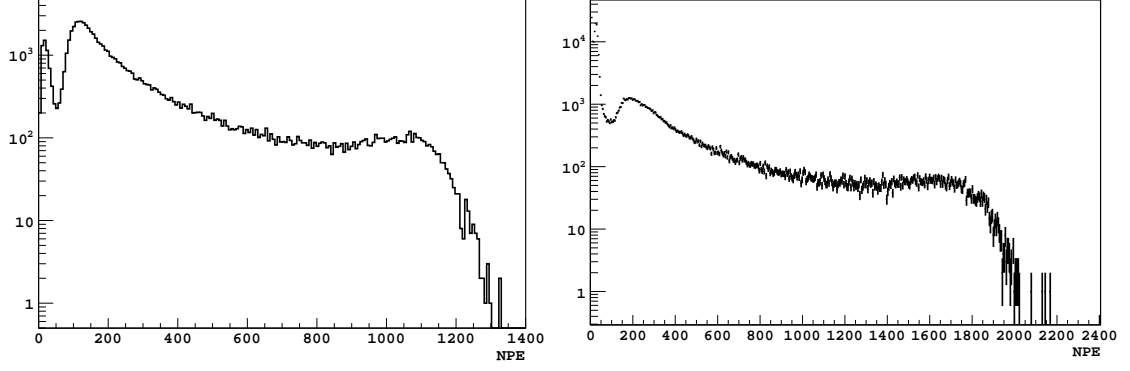


Figure A.3: The scintillation spectra of  $^{210}\text{Po}$  alpha particles in WLSs at room temperature; Left:  $329\ \mu\text{g}/\text{cm}^2$  TPB; Right:  $373\ \mu\text{g}/\text{cm}^2$  PTP.

The thickness of the WLS coatings used in the measurements were  $329\ \mu\text{g}/\text{cm}^2$  for TPB and  $373\ \mu\text{g}/\text{cm}^2$  for PTP. In the TPB measurement (Fig. A.3 left), approximately 120 photoelectrons were observed at the low energy peak, and about 1150 photoelectrons are observed at the high energy cutoff; the numbers of photons in the PTP measurements (Fig. A.3 right) were  $\sim 180$  and  $\sim 1850$  for the two peaks respectively. The energy depositions of the  $5.3\ \text{MeV}$   $^{210}\text{Po}$  alpha particles in the TPB and PTP layers are estimated to be  $290\ \text{keV}$  and  $330\ \text{keV}$  respectively. Therefore, the relative scintillation efficiency of TPB and PTP is calculated to be  $(120\text{p.e.}/290\text{keV})/(180\text{p.e.}/330\text{keV}) \sim 0.76$  for normal incident alphas (the low energy peak) and  $(1150\text{p.e.}/5.3\text{MeV})/(1850/5.3\text{MeV}) \sim 0.64$  for the full alpha energy deposition (the high energy cutoff). We comment that the WLS thickness values may not be accurate and large uncertainties may exist in the calculations.

The efficiency of organic scintillators under alpha excitations is known to be quenched relative to electron excitations, and the quenching factor depends on the alpha energy. This is the reason why the full alpha energy peak produced only  $\sim 10$  times more photons than the normal incident alpha peak<sup>4</sup> instead of the energy ratio of  $\sim 5.3\ \text{MeV}/300\ \text{keV} \sim 18$ . The alpha quenching factors for TPB and PTP are not

<sup>4</sup>Alphas with large incident angles have to travel relatively long distances in air before hitting the WLSs, so the observed “full” energy peak is lower than the true value.

known, but we may use the empirical quenching formula for the Borexino scintillator [198] as an estimate.

$$Q_\alpha(E) = 20.3 - 1.3 \frac{E}{\text{MeV}} \quad (\text{A.1})$$

Eq. A.1 describes the overall quenching effects of an alpha particle as it gradually loses kinetic energy and makes scintillation light in the Borexino scintillator, so it includes the contribution of the quenched alpha scintillation at different alpha energies. The differential quenching factor for a small energy loss  $\Delta E$  at the alpha energy  $E$  can be derived as:

$$Q_\alpha^d(E) = \frac{\Delta E}{\frac{E+\Delta E}{Q_\alpha(E+\Delta E)} - \frac{E}{Q_\alpha(E)}} = \frac{1}{20.3} \left( 20.3 - 1.3 \frac{E}{\text{MeV}} \right)^2 \quad (\text{A.2})$$

The differential quenching factor for the  $^{210}\text{Po}$  alphas  $Q_\alpha^d(5 - 5.3 \text{ MeV})$  is estimated to be  $\sim 9.1$ , but the value increases as the alpha energy decreases, so an overall quenching factor  $Q_\alpha(5.3 \text{ MeV}) \sim 13.4$  is resulted. In this case the observed scintillation energy of the full alpha energy  $5.3 \text{ MeV}/Q_\alpha(5.3 \text{ MeV})$  is only  $\sim 11.6$  times higher than that of the minimum energy deposition of  $\sim 300 \text{ keV}/Q_\alpha^d(5 - 5.3 \text{ MeV})$ , approximately consistent with the observed value of  $\sim 10$ . Uncertainties in this estimation may rise from the inappropriate quenching function and the alpha energy loss in air.

To sum up,  $^{210}\text{Po}$  alphas can produce a minimum of 100-200 photoelectrons in 300-400  $\mu\text{g}/\text{cm}^2$  of TPB or PTP at room temperature. If the same result can be obtained for surface alpha events in a liquid argon detector, the alpha scintillation photons may be interpreted as an equivalent nuclear recoil energy (in argon) of  $\sim 50$ -100 keV if we assume an argon light yield of 6-7 p.e./keV<sub>ee</sub> and a nuclear quenching factor of 0.25-0.3. Combining with the  $\sim 100 \text{ keV}$   $^{206}\text{Pb}$  nuclear recoil energy in liquid argon from a surface  $^{210}\text{Po}$  decay, the total (equivalent) energy of this surface event would be  $\gtrsim 150$ -200 keV. Since WIMP induced nuclear recoils are expected to concentrate in

low energy regions, such surface backgrounds may be efficiently rejected by choosing an appropriate WIMP energy window.

### A.2.2 Cryogenic Measurements

The above measurements have been made at room temperatures, but argon-based dark matter detectors are usually operated at cryogenic conditions; it is not necessary for the WLS scintillation efficiency to stay the same, so cryogenic alpha scintillation measurements are necessary to investigate the surface background rejection possibility. The same system described in Sec. A.2.1 was cooled down to liquid nitrogen temperature using the low background liquid argon detector described in Ch. 3. The detector chamber was filled with nitrogen gas during the measurements.

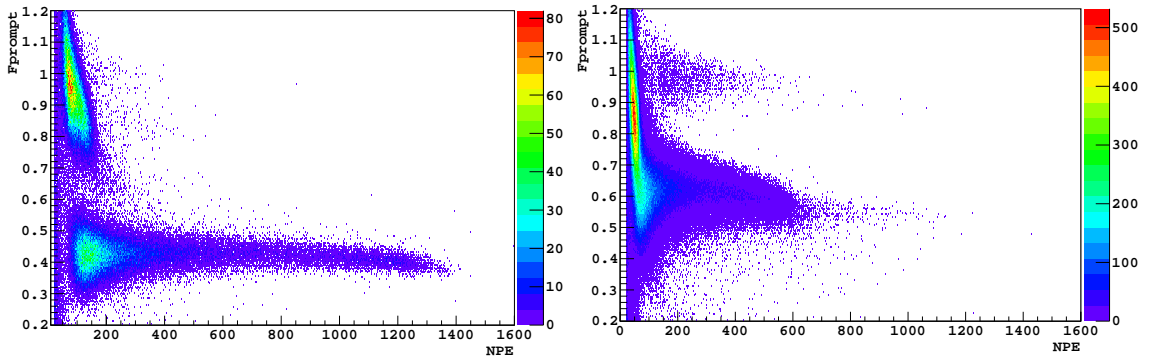


Figure A.4: The  $F_{\text{prompt}}$  distribution and scintillation spectra of TPB; Left: room temperature measurement; Right: liquid nitrogen temperature measurements. The lower  $F_{\text{prompt}}$  events are attributed to TPB scintillations.

Because the PTFE cell of the low background detector was coated with PTP, it was lined with 3M ESR film in the TPB measurement to avoid possible light adsorption effects. The measured  $F_{\text{prompt}}$  distribution and the scintillation spectra at room temperature and liquid nitrogen temperature are shown in Fig. A.4; the  $F_{\text{prompt}}$  parameter is defined as the fraction of scintillation photons within 100 ns of the trigger time and the events in the lower  $F_{\text{prompt}}$  band are attributed to

alpha scintillations <sup>5</sup>. The low energy normal incident peak and the high energy full energy cutoff were observed at  $\sim 70$  p.e. and  $\sim 600$  p.e. respectively at liquid nitrogen temperatures, which were approximately half of the values at room temperature. In addition, the  $F_{\text{prompt}}$  value of the alpha-induced TPB scintillation increased from  $\sim 0.4$  at room temperature to  $\sim 0.6$  at cryogenic temperature. We note this  $F_{\text{prompt}}$  observation may be in contradiction to that reported in Ref. [199].

Although we attributed the observed decrease of TPB scintillation photon number to a drop of TPB scintillation efficiency at cryogenic temperatures, it might also be caused by changes in the reflector. PTFE is estimated to contract by approximately 2-3% from room temperature to liquid nitrogen temperature, and this contraction may produce wrinkles in the 3M film and cause the light collection efficiency to drop. However, this effect may not be able to make  $\sim 50\%$  difference because 3M film has almost perfect reflection for TPB emission light, and it does not explain the increase of the  $F_{\text{prompt}}$  values of the scintillation signals at low temperatures.

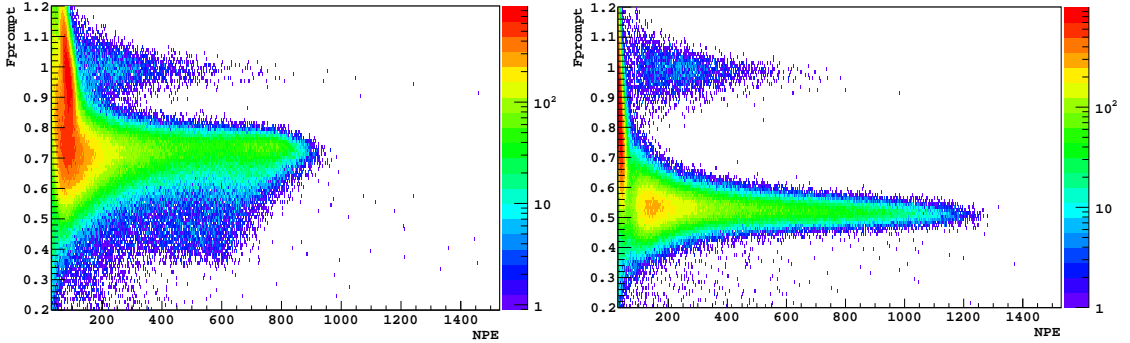


Figure A.5: The  $F_{\text{prompt}}$  distribution and scintillation spectra of PTP; Left: room temperature measurement; Right: liquid nitrogen temperature measurements.

To the contrary of TPB, the alpha scintillation in PTP was enhanced at cryogenic temperatures. The normal incident peak and the full energy cutoff increased from  $\sim 80$  p.e. and  $\sim 780$  p.e. at room temperature to  $\sim 140$  p.e. and  $\sim 1150$  p.e. at liquid

<sup>5</sup>The higher  $F_{\text{prompt}}$  events are blamed as backgrounds; the energy scale and  $F_{\text{prompt}}$  values are observed to change with environmental conditions (surrounding gas specie, pressure, etc), but they do not vanish when the system was operated in vacuum.

nitrogen temperature. We comment that the photon numbers at room temperature were less than that reported in Sec. A.2.1 due to the light collection in the PTFE cell: the light collection efficiency at the bottom of the cell is only  $\sim 50\%$  of that at the top<sup>6</sup>, as studied in Sec. 4.2.2. The changes in the  $F_{\text{prompt}}$  distributions in the PTP measurements were also to the opposite of the TPB measurements: the  $F_{\text{prompt}}$  values decreased from  $\sim 0.7$  to  $\sim 0.5$  at liquid nitrogen temperature.

A brief comparison between TPB and PTP can be made based on the above measurements. 1) The scintillation efficiency of TPB is approximately 70% of that of PTP at room temperature. 2) The TPB scintillation efficiency was observed to drop by a factor of  $\sim 2$  at cryogenic temperatures while that of PTP was observed to increase by a factor of  $\sim 2$ . This makes the TPB scintillation efficiency only  $\sim 20\%$  of PTP at cryogenic temperatures. 3) The scintillation waveform of TPB light has a low  $F_{\text{prompt}}$  value at room temperature, but at cryogenic temperatures it approaches the nuclear recoil waveforms in liquid argon; the PTP scintillation, to the contrary, has a high  $F_{\text{prompt}}$  value at room temperature but shifts to low  $F_{\text{prompt}}$  values at cryogenic temperatures. Therefore, the WLS PTP is expected to yield more surface background rejection power than TPB both by producing copious alpha scintillation light and by altering the nuclear recoil scintillation waveform.

### A.3 Surface Background Measurements

Based on the above analysis, in situ measurements were attempted to validate the possibility of rejecting surface backgrounds by taking advantage of the alpha scintillation in the WLS. Since  $^{210}\text{Po}$  is the most prevalent surface radioactivity, an ideal experiment would collect  $^{210}\text{Po}$  onto the surface of WLS coatings and measure the alpha decay signals inside a liquid argon detector. Such surface  $^{210}\text{Po}$  activities can

---

<sup>6</sup>This measurement indicates that the light collection efficiency at the bottom of the PTFE cell is  $\sim 80/180$  of that in a Spectralon cell.

be obtained by exposing a WLS layer to radon gas, but it may take a very long time for  $^{210}\text{Po}$  to accumulate due to its long half life ( $\sim 138$  days); the equilibrium rate is also suppressed by the long lifetime of  $^{210}\text{Pb}$  (22 yr). In addition, the  $^{210}\text{Po}$  decay rate will very low and ultra-low background measurements are required.

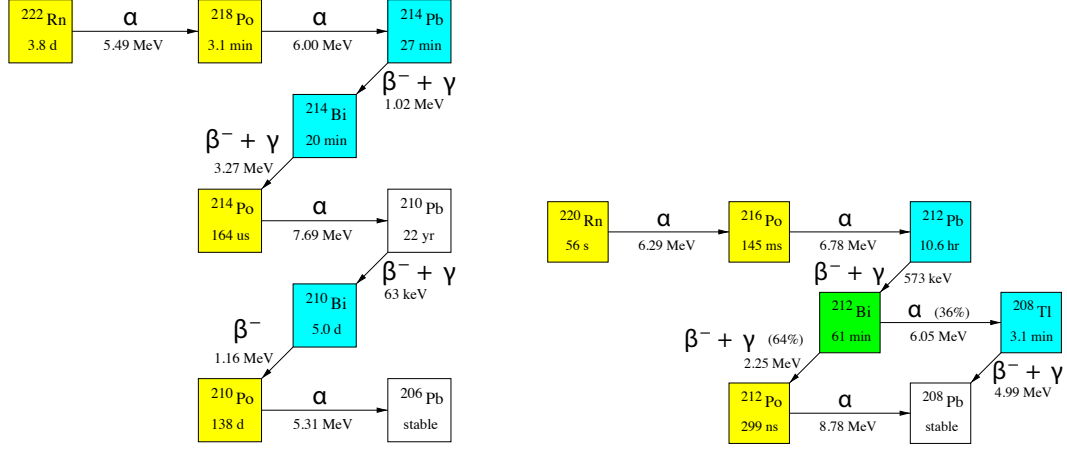


Figure A.6: The radon decay chains; only the significant decay channels are shown [198].

The difficulties with the surface  $^{210}\text{Po}$  scheme may be avoided by using the nuclide  $^{214}\text{Po}$ . The precursors of  $^{214}\text{Po}$  have half lives of 20-30 minutes (27 min for  $^{214}\text{Pb}$  and 20 min for  $^{214}\text{Bi}$ ) and it allows  $^{214}\text{Po}$  to build up within a few hours of exposure to radon gas. This lifetime value, meanwhile, may provide several hours of work time before the  $^{214}\text{Po}$  rate dies away. For example, a  $\sim 10^6$  Bq  $^{222}\text{Rn}$  source is available at Princeton University, and if a fraction of the  $^{214}\text{Pb}$  and  $^{214}\text{Bi}$  can be collected, the surface alpha rate would drop to the level of 1 Hz in  $\sim 10$  hours. More importantly, the short lifetime of  $^{214}\text{Po}$  ( $164\mu\text{s}$ ) opens the possibility of using  $^{214}\text{Bi}$ - $^{214}\text{Po}$  coincidence to reduce the background rate in the measurements.

### A.3.1 Radon Collection

Most radon daughters are positively charged at formation and thus can be collected onto negatively charged surfaces [200]. A radon collection system, as illustrated in

Fig. A.7, was constructed to collect radon daughters onto the WLS coatings using high voltages. The system was operated in a radioactive fume hood at negative pressures.

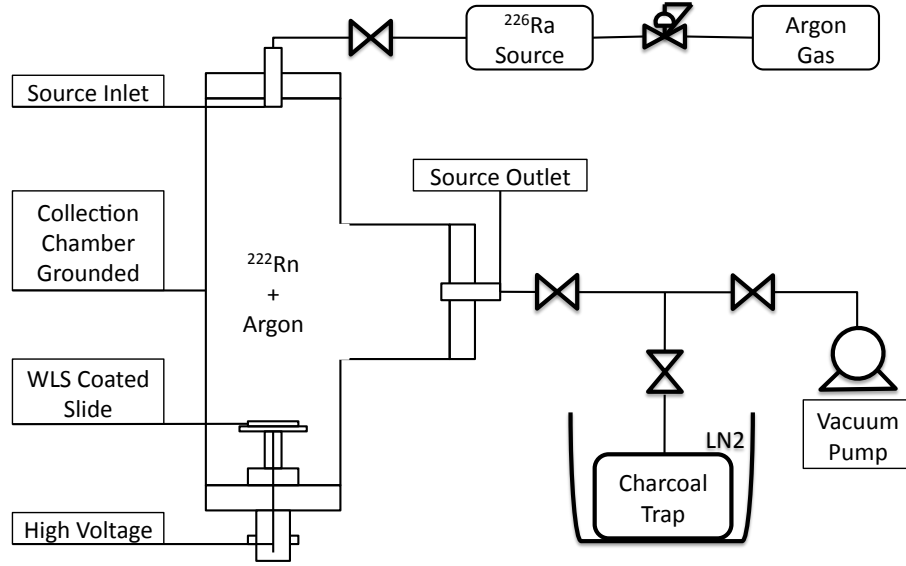


Figure A.7: The radon collection system used to collect radon daughters onto the surface of WLSs. Argon is used to push radon gas to flow from the source to the collection chamber, where a high voltage is applied to facilitate radon daughter collection. The residual radon gas can be recovered into a charcoal trap.

The  $^{222}\text{Rn}$  gas in this system is supplied by a dry powder  $^{226}\text{Ra}$  source (Pylon RN-1025). Argon gas is used to push the emanated radon to flow from the source capsule into the collection chamber that has been evacuated using a vacuum pump. A high voltage (1000 V) is applied to the metal plate that supports the WLS coated quartz slide to facilitate the deposition of the radon daughters. The collection process usually lasts 2-3 hours for the  $^{214}\text{Pb}$  and  $^{214}\text{Bi}$  contents to build up to equilibrium levels. After the collection process completes, the residual radon and argon gas in the chamber is recovered into a liquid nitrogen-cooled charcoal trap to minimize the radioactivity released into the environment. The recovered radon gas can be refilled into the chamber for subsequent collections.

A few radon deposition tests were made with this system to study the  $^{214}\text{Po}$  collection efficiency. Fig. A.8 shows the measured alpha scintillation rate on a WLS

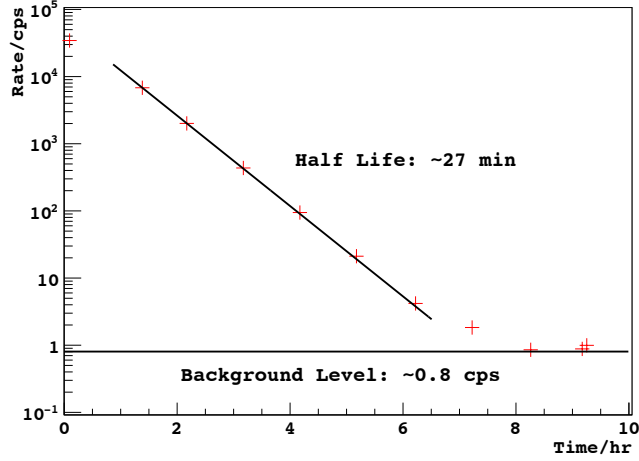


Figure A.8: The alpha decay rate on the WLS coating after radon collection.

sample after radon collection. This rate was calculated on the WLS scintillation events produced by normal incident alphas, so it only reflects a portion of the overall  $^{214}\text{Po}$  decay rate. The half life of the decay rate was fitted to be  $\sim 27$  min, consistent with that of the  $^{214}\text{Pb}$  nuclide. Since it took approximately 7-8 hours for the  $^{214}\text{Po}$  alpha event rate to drop to the background level, useful data may be acquired for the surface background study if the WLS slide and the detector could be assembled and prepared for data taking within 5-6 hours.

### A.3.2 Bi-Po Coincidence Measurements

The low background liquid argon detector was used in the surface background measurements. To reduce the system preparation time after radon collection, a special operating procedure was developed. The low background detector was first pumped down for a few days to remove the gas impurities, and as soon as the radon collection process was completed the detector chamber was filled with high purity argon gas and was opened briefly for a quick assembly of the radon-deposited, WLS-coated quartz slide into the scintillation cell. Then the detector was closed, pumped down for 1-2 hours, cooled down to liquid argon temperature in 1-2 hours, and filled with high



purity argon in another  $\sim 1$  hour. Usually data acquisition started 5-6 hours after the radon collection and reasonable argon purities was obtained.

Because of the short lifetime of  $^{218}\text{Po}$  and the long lifetime of  $^{210}\text{Pb}$ , the observed radon daughter events  $\sim 6$  hours after radon collection were mostly  $^{214}\text{Pb}$ ,  $^{214}\text{Bi}$  and  $^{214}\text{Po}$  decays. The beta decay of  $^{214}\text{Bi}$  and the alpha decay of  $^{214}\text{Po}$  occur very close in time (half life  $\sim 164\mu\text{s}$ ), so time coincidence method can be used to select the  $^{214}\text{Po}$  alpha events for the surface backgrounds study. Based on the difference in the scintillation waveforms, the recorded events were divided into gamma-like events (low  $F_{\text{prompt}}$  value) and alpha-like events (high  $F_{\text{prompt}}$  value); if an alpha-like event occurred within 1 ms after a gamma ray-like event, the two events were assumed to be a valid  $^{214}\text{Bi}$ - $^{214}\text{Po}$  coincidence. The time intervals between the coincidence pairs were fitted to an exponential with a half life value around  $160\mu\text{s}$ .

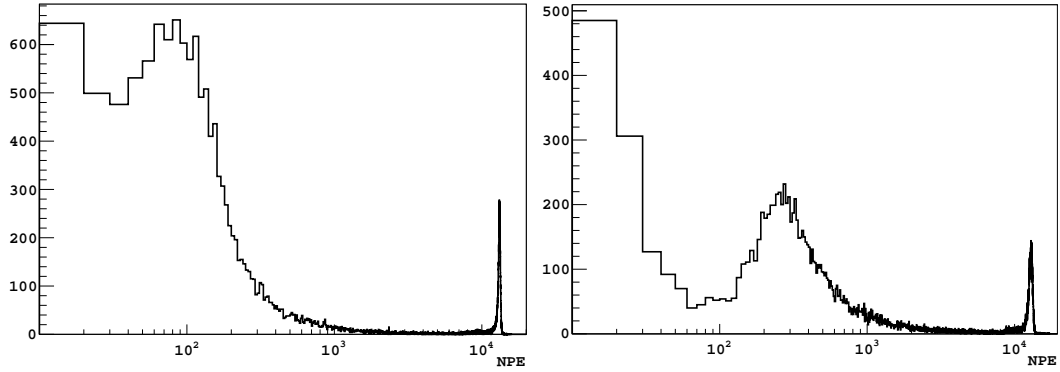


Figure A.9: The surface  $^{214}\text{Po}$  alpha decay event energy spectrum in the TPB measurement (left) and in the PTP measurement (right).

The WLS chemicals TPB and PTP were both investigated in this study. The energy spectrum of the  $^{214}\text{Po}$  alpha events in the TPB measurement is shown in Fig. A.9 (left). Two peaks were observed and were attributed to the configurations (a) and (b) in in Fig. A.1 respectively. The low energy peak around  $\sim 80$  p.e. includes the contributions from the alpha scintillation in the TPB coating and from the associated nuclear recoil scintillation in liquid argon. The minimum energy deposition of the

$^{214}\text{Po}$  alphas (7.7 MeV) in  $329\ \mu\text{g}/\text{cm}^2$  of TPB was estimated to be  $\sim 220\ \text{keV}$  with a differential quenching factor of  $\sim 5.35$  (Eq. A.2). Compared to the cryogenic TPB measurement results in Sec. A.2.2 ( $\sim 70\ \text{p.e.}$  for  $\sim 290\ \text{keV}$  energy deposition at  $\sim 9.1$  quenching), it can be estimated that approximately 40 photoelectrons were produced by the alphas<sup>7</sup> and the other 40 p.e. could be attributed to the recoil  $^{210}\text{Pb}$  nucleus ( $\sim 146\ \text{keV}$ ). As for the PTP measurement (Fig. A.9 right), the low energy peak appears at  $\sim 250\ \text{p.e.}$ . The alpha energy deposition was estimated to be  $\sim 250\ \text{keV}$  with a similar differential quenching factor of  $\sim 5.35$ ; scaled from the cryogenic PTP measurement results of  $\sim 140\ \text{p.e.}$  for  $\sim 330\ \text{keV}$  energy at a differential quenching factor of  $\sim 9.1$ ,  $\sim 180\ \text{p.e.}$  were expected from the alphas. The rest of the photons ( $\sim 70$ ) were attributed to the recoiled  $^{210}\text{Pb}$  nucleus.

The volume-averaged light yield values for electron recoils in the two measurements were estimated to be  $\sim 5.3\ \text{p.e.}/\text{keV}$  based on  $^{137}\text{Cs}$  calibrations; if we assume a relative scintillation efficiency of  $\sim 25\text{--}29\%$  for nuclear recoils,  $\sim 200\ \text{p.e.}$  could be expected from the  $\sim 146\ \text{keV}$   $^{210}\text{Pb}$  nucleus. However, only  $\sim 40\text{--}70\ \text{p.e.}$  were associated with the nuclear recoil signals. The discrepancy may be partially explained by the poor light collection efficiency at the bottom of the low background detector cell, and the photon collection efficiency in the TPB measurement may also be affected by the PTP coating on the PTFE cell. But other factors such as the thickness of the WLS coating and the quenching factors also carry large uncertainties, so more accurate measurements have to be made to clarify the observed results.

The  $F_{\text{prompt}}$  distributions of the  $^{214}\text{Bi}$ - $^{214}\text{Po}$  coincidence events in the TPB and PTP measurements are shown in Fig. A.10. Events in the high  $F_{\text{prompt}}$  band are attributed to the surface alpha events, and the  $F_{\text{prompt}}$  values drop at high energies due to the saturation of the digitizer by the large prompt pulses. The full alpha energy peaks (including small contribution from the nuclear recoil scintillation in WLS) are

---

<sup>7</sup>A light collection efficiency of  $\sim 5/9$  is applied, which is estimated from the PTP measurements ( $\sim 180\ \text{p.e.}$  in a Spectralon cell compared to  $\sim 80$  at the bottom of the low background detector cell).

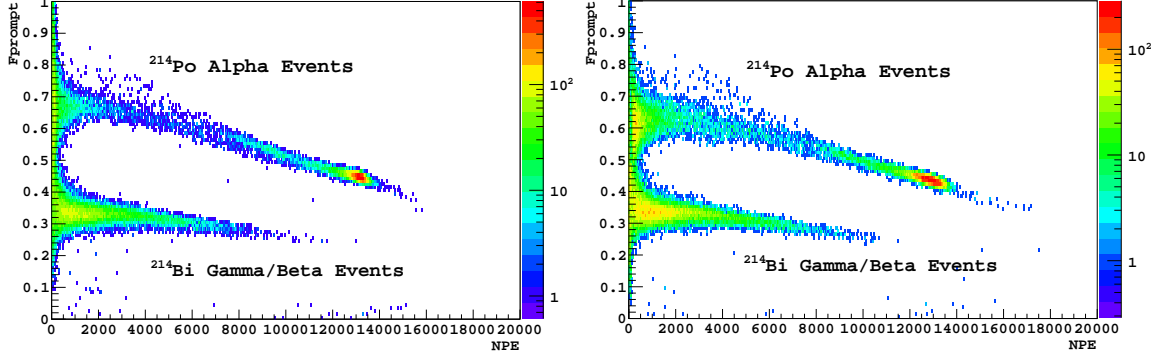


Figure A.10: The  $F_{\text{prompt}}$  distribution of the  $^{214}\text{Bi}$ - $^{214}\text{Po}$  coincidence events in the TPB measurement (left) and in the PTP measurement (right).

observed at  $\sim 13,000$  p.e., which may be corrected to  $\sim 25,000$  if we assume a no-saturation  $F_{\text{prompt}}$  value of  $\sim 0.7^8$ . The expected photon number produced by alpha scintillation in liquid argon is approximately 35,000 at a light yield of  $\sim 4.6$  p.e./keV (7/8 of that of electron recoils), and the lower observation may be explained by the light loss at the bottom of the cell and possible non-linear effects in the PMT and in the readout electronics. But since the alpha scintillation in liquid argon is so prominent they can be unambiguously identified and used to estimate the rate of surface alpha background activities.

### A.3.3 Summary

Despite of the possible inconsistencies, PTP seems to be more efficient than TPB in producing scintillation photons under alpha excitation at cryogenic conditions, and thus has a higher chance to lift the surface nuclear recoil backgrounds to above WIMP search energy windows. In addition, the scintillation waveforms of PTP have smaller prompt components than TPB, which make them more distinguishable from pure nuclear recoil events. For example, the  $F_{\text{prompt}}$  value of the surface contamination events in the TPB measurement was found at  $\sim 0.67$ , while it was  $\sim 0.61$  for the PTP

<sup>8</sup>A lower PMT voltage was used in one measurement and showed a slightly saturated  $F_{\text{prompt}}$  value of  $\sim 0.65$ , so we assume the no-saturation  $F_{\text{prompt}}$  value to be  $\sim 0.7$ .

measurement. We remind the readers that the  $F_{\text{prompt}}$  value of nuclear recoil events in liquid argon has a high value around  $\sim 0.7\text{-}0.8$ .

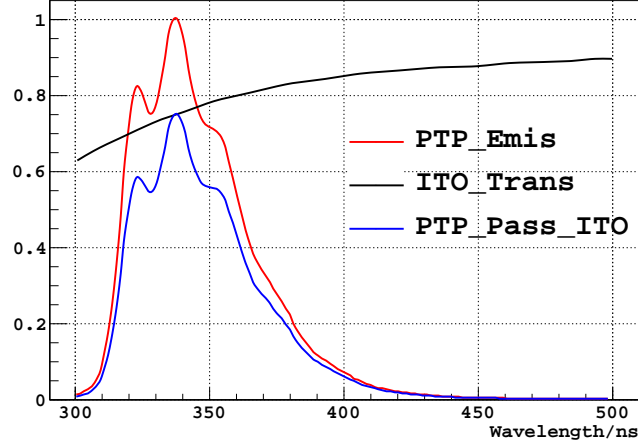


Figure A.11: The transmittance of a  $\sim 150 \text{ \AA}$  ITO coating, and its effect on the PTP emission light. The ITO transmittance was measured by the Evaporated Coatings Inc.

However, we comment that the application of PTP in argon scintillation experiments has not been as well studied as that of TPB. Since TPB is currently widely used, the detector setup of some experiments may disfavor the use of PTP. For example, the DEAP experiment uses acrylic light guides, which allow TPB light to go through but may partially block the shorter-wavelength PTP light; for similar reasons PTP may not be an option for an experiment using the 3M ESR film as the reflector. The DarkSide experiment uses a transparent conducting material Indium-Tin-Oxide that has a decreasing transmittance at short wavelengths on the cathode/anode plates, so PTP is not preferred in this design. Fig. A.11 shows the transmittance of  $\sim 150 \text{ \AA}$  ITO to near-UV light, and it reduces the PTP light output by  $\sim 25\%$  on average, which is approximately twice higher than that of TPB. But if a grid-coating ITO layer at the same thickness is feasible, the loss of PTP light can be reduced to  $\sim 1.2\%$  for 5% ITO coverage or  $\sim 2.3\%$  for 10% ITO coverage, which may make the use of PTP possible in the DarkSide detector.

# Appendix B

## Evaporation Procedures

The following list is the developed operating procedure of the Princeton vacuum evaporation system that has been described in Sec. 3.1.1.

1. Preparations before Operating the System.
  - Gather the necessary parts: wavelength shifter chemicals, nitrile gloves, Kimwipe paper towels, argon/nitrogen gas bottle, liquid nitrogen, etc.
  - Clean the reflector parts to be evaporated; sand the surface if needed.
  - Weigh the parts and measure the dimensions (for thickness calculation).
2. Opening the Evaporator Chamber (assume there is a previous evaporation).
  - Check the pressure in the evaporator chamber (use the mechanical gauge beside the shutter valve and TC2). You may open the evaporation chamber only when the pressure is about 1 atm; in the case of (partial) vacuum you may risk lifting the whole system, or breaking the lifting hoist.
  - Make sure the cold finger is warm, otherwise moisture would condense on it when open to air. Make sure there is no more liquid nitrogen in the cold finger; wait for a few hours after it is empty.

- Lift the bell jar with the pulley chain by 1-2 feet; use caution and keep the cover balanced when lifting.
- Put on latex gloves, and take the metal plate out of the chamber; use caution when tilting/flipping the plate so that the parts mounted on the plate, if any, do not fall off.
- Weigh the coated parts if possible and calculate the coating thickness (later); store the coated parts properly.
- Mount the new parts to be evaporated on the metal plate using appropriate fixtures; double check the orientation of the parts.
- Refill the crucible with wavelength shifter chemical; if a different chemical is to be used, clean the crucible with methanol and dry it before filling.
- Check the remaining lifetime of the thickness monitor crystal.
- Mount the metal plate onto the rods inside the chamber, and check the positioning of the thickness monitor.
- Close the evaporation chamber carefully and make sure the o-ring is in place; put vacuum grease on the o-ring if it is dry.

### 3. Pumping Down the Evaporation Chamber.

- Power on the pump station if it is not already on.
- Check the shutter valve to make sure it is widely open; check the valves to the gas filling line.
- Turn on the pump by pressing the button “Start/Stop Reset”, and check the chamber pressure on TC2.
- After the pressure drops below  $1 \times 10^{-3}$  torr, check if the turbo pump is at its full speed (56k rpm).

- Start the emission gauge by pressing the button “Chan” 5 times until it says “TC2 BA2” and then hit “Emis”.
- Wait until the chamber pressure reaches  $3 \times 10^{-6}$  torr; it usually takes about 2 hrs if there's no leak.
- Pour liquid nitrogen into the cold finger; be careful, it may spill out!
- The chamber pressure should drop to  $5\text{-}6 \times 10^{-7}$  torr in about 10 min; maintain the liquid nitrogen level in the cold finger.

#### 4. Start the Evaporation Process.

- Close the shutter to block the crucible (close all the way and back for a few turns, so it doesn't isolate the volume close to the pressure gauge in case it outgases/leaks slightly.)
- Power on the thickness monitor, the temperature controller, and the heater if they are not already on.
- Turn on the cooling water to the heater and to the thickness monitor; check the water valves at the wall to make sure water is flowing.
- Set the temperature to the desired values ( $\sim 200^\circ\text{C}$  for TPB and  $\sim 150^\circ\text{C}$  for PTP); Raise the temperature set point value slowly to avoid large overshoot.
- After the temperature reaches the desired value, wait for 30 seconds, zero the thickness monitor and open the shutter valve all the way.
- Watch the deposition rate and the cumulated thickness on the thickness monitor; estimate the actual rate/thickness with the calibrated conversion factors; raise the temperature slightly if the rate is too low.
- Record the evaporation conditions: chamber pressure, crucible temperature, average deposition rate, total deposited thickness, duration of evap-

oration, etc.

- Keep an eye on the chamber pressure; add more liquid nitrogen to the cold finger if necessary.
- Close the shutter valve all the way when the thickness monitor reading reaches the desired value.
- Lower the set point temperature on the heater controller to 0C.
- Turn off the emission gauge.
- Turn off the turbo pump.
- Turn off cooling water when the temperature drops to room temperature.
- Wait for 10-20 min for the turbo pump to slow down, then you can slightly open up the valve connecting the turbo pump and the gas bottle to let a little argon/nitrogen in and further slow down the turbo pump. Only let gas into the chamber if under tight schedule, and use caution to make sure the turbo pump is not damaged.
- After the turbo stops, fill more argon/nitrogen into the chamber; open the shutter slightly to monitor the pressure with the mechanical gauge.
- Close the valve to stop the flow when the pressure reaches 1 atm; DO NOT over-pressurize the chamber, otherwise it may pop!
- Wait for a few hours for the cold finger to warm up.

5. Consult Item 2 on opening the evaporator chamber.

Note: the approximate conversion factor between the mass thickness value and the actual thickness is:  $1 \mu\text{g}/\text{cm}^2 \approx 100 \text{ \AA}$ .

TPB melting point: 196-209C, flash point:  $\sim 253\text{C}$ , boiling point: 495C.

PTP melting point:  $\sim 212\text{C}$ , flash point:  $\sim 207\text{C}$  (sublimes), boiling point: 389C.



# Appendix C

## Useful Online Resources

This is a compilation of some online resources that can be useful in research. Note that some of the websites/software are maintained by individuals and may not have been verified to yield correct results. Use your own best judgement.

### **Nuclear Data and Decay Radioactivity.**

The LBNL Isotopes Project Home Page

<http://ie.lbl.gov/>

LBNL Isotopes Project - LUNDS Universitet WWW Table of Radioactive Isotopes

<http://ie.lbl.gov/toi/>

The Berkeley Laboratory Isotopes Project's Exploring the Table of Isotopes

<http://ie.lbl.gov/education/isotopes.htm>

The Lund/LBNL Nuclear Data Search

<http://nucleardata.nuclear.lu.se/toi/>

Periodic Table linked to ToRI data of known isotopes for each element

<http://nucleardata.nuclear.lu.se/toi/perchart.htm>

National Nuclear Data Center

<http://www.nndc.bnl.gov/>

NNDC Nuclear Structure and Decay Data

<http://www.nndc.bnl.gov/nudat2/>

NNDC Evaluated Nuclear Data File

<http://www.nndc.bnl.gov/exfor/endl00.jsp>

## **Interactions of Radiations with Matter.**

LBNL X-RAY DATA BOOKLET

<http://xdb.lbl.gov/>

X-Ray Mass Attenuation Coefficients and Mass Energy-Absorption Coefficients

<http://www.nist.gov/pml/data/xraycoef/index.cfm>

X-Ray Mass Attenuation Coefficients in Elemental Media

<http://physics.nist.gov/PhysRefData/XrayMassCoef/tab3.html>

X-Ray Mass Attenuation Coefficients in Compounds and Mixtures

<http://physics.nist.gov/PhysRefData/XrayMassCoef/tab4.html>

Stopping-Power and Range Tables for Electrons, Protons, and Helium Ions

<http://www.nist.gov/pml/data/star/index.cfm>

Stopping Powers and Ranges for Protons

<http://physics.nist.gov/PhysRefData/Star/Text/PSTAR.html>

Stopping Powers and Ranges for Helium Ions

<http://physics.nist.gov/PhysRefData/Star/Text/ASTAR.html>

Stopping Powers and Ranges for Electrons

<http://physics.nist.gov/PhysRefData/Star/Text/ESTAR.html>

SRIM Particle Interactions with Matter

<http://www.srim.org/>

Calculate the energy loss of a charged particle by ionization as it passes through many kinds of matter.

<http://meroli.web.cern.ch/meroli/EnergyLossCalculation.html>

## **Dark Matter Physics Related.**

Dark Matter Network Exclusion Diagram online tool

<http://pisrv0.pit.physik.uni-tuebingen.de/darkmatter/index2.html>

DAMNED Nuclear Recoil Event Spectra

<http://pisrv0.pit.physik.uni-tuebingen.de/darkmatter/spectra/index.php>

DAMNED Dark Matter Parameter Limit

<http://pisrv0.pit.physik.uni-tuebingen.de/darkmatter/limits/index.php>

MicrOMEGAs: a code for the calculation of Dark Matter Properties

<http://lapth.cnrs.fr/micromegas/>

Sensitivity Plots for Direct Detection of WIMP Dark Matter, UC Berkeley

<http://dendera.berkeley.edu/plotter/entryform.html>

LUX Dark Matter Online Tools

<http://dmtools.brown.edu/>

DarkSUSY, a fortran package for supersymmetric dark matter calculations

<http://www.fysik.su.se/~edsjo/darksusy/>

SuperBayeS, Supersymmetry Parameters Extraction Routines for Bayesian Statistics

<http://www.ft.uam.es/personal/rruiz/superbayes/index.php?page=main.html>

## **Material Radioactivity.**

the ILIAS database on radio-purity of materials

<http://radiopurity.in2p3.fr/>

The Conversion factors ppb U, ppb Th, ppm K to Bq/kg

<http://radiopurity.in2p3.fr/conversion.html>

SOURCES-4C, Calculating Alpha, N, Fission, Delayed Neutron Sources and Spectra

<http://www.oecd-nea.org/tools/abstract/detail/ccc-0661>

Calculation of the ( $\alpha$ , n) neutron yield induced by natural radioactivity in user's specified elements or compounds.

<http://neutronyield.usd.edu/>

COSMO: a program to estimate spallation radioactivity produced in a pure substance by exposure to cosmic radiation on the earth.

<http://www.cpc.cs.qub.ac.uk/>

Atomic and Nuclear Properties of Materials for more than 300 materials

<http://pdg.lbl.gov/2012/AtomicNuclearProperties/>

## **Scintillation Physics.**

The Liquid Scintillation Spectrometry International Library

<http://www.lsc-international.org/library.html>

PhotochemCAD, absorption and emission spectra for 150 diverse compounds

<http://omlc.ogi.edu/spectra/PhotochemCAD/index.html>

## **General about Physics.**

LUNDS University Physics and Web development links

<http://www.pixe.lth.se/links/index.asp>

Particle Data Group 2012 Review of Particle Physics

<http://pdglive.lbl.gov/listings1.brl?exp=Y>

Wayne Hu's Tutorial Page about CMB Cosmology

<http://background.uchicago.edu/index.html>

Ned Wright's Cosmology Tutorial

<http://www.astro.ucla.edu/~wright/cosmolog.htm>

## **Geant4 Related.**

The Geant4 Software Reference Manual

<http://geant4.cern.ch/bin/SRM/G4GenDoc.csh?flag=1>

Geant4 General Particle Source Users Manual

[http://reat.space.qinetiq.com/gps/new\\_gps\\_sum\\_files/gps\\_sum.htm](http://reat.space.qinetiq.com/gps/new_gps_sum_files/gps_sum.htm)

CERN Geant4 Webhome

<https://twiki.cern.ch/twiki/bin/view/Geant4/>

## **Miscellaneous.**

Computer Physics Communications Program Library

<http://www.cpc.cs.qub.ac.uk/>

MATPACK Numerical and Graphical Library

<http://www.matpack.de/>

Wolfram Mathematica Online Integrator

<http://integrals.wolfram.com/index.jsp>

SPICE, Simulation Program with Integrated Circuit Emphasis

<http://bwrce.eecs.berkeley.edu/Courses/IcBook/SPICE/>

A Few Softwares that can Digitize Data from Graphs and Plots

<http://getdata-graph-digitizer.com/>

<http://plotdigitizer.sourceforge.net/>

<http://digitizer.sourceforge.net/>

An Online Tool to Digitize Data from Graph

<http://arohatgi.info/WebPlotDigitizer/>

Science Journal Title Abbreviations

[http://images.webofknowledge.com/WOK46/help/WOS/A\\_abrvjt.html](http://images.webofknowledge.com/WOK46/help/WOS/A_abrvjt.html)

# Bibliography

- [1] V Trimble. Existence and nature of dark matter in the universe. *Annu. Rev. Astron.*, 25(1):425–472, 1987.
- [2] Jonathan Feng and Mark Trodden. Dark worlds. *Scientific American*, 303(5):38–45, November 2010.
- [3] Anne-Marie Weijmans et al. The shape of the dark matter halo in the early-type galaxy ngc 2974. *Monthly Notices of the Royal Astronomical Society*, 383(4):1343 – 1358, 2008.
- [4] J. Anthony Tyson and Philippe Fischer. Measurement of the mass profile of abell 1689. *The Astrophysical Journal Letters*, 446:L55, June 1995.
- [5] Douglas Clowe et al. A direct empirical proof of the existence of dark matter. *The Astrophysical Journal*, 648(2):L109–L113, September 2006.
- [6] Maxim Markevitch. Chandra observation of the most interesting cluster in the universe. *arXiv:astro-ph/0511345*, November 2005.
- [7] Robert Wilson. The 1978 nobel lecture on the discovery of cosmic microwave background radiation. [http://www.nobelprize.org/nobel\\_prizes/physics/laureates/1978/wilson-lecture.pdf](http://www.nobelprize.org/nobel_prizes/physics/laureates/1978/wilson-lecture.pdf).

- [8] NASA/WMAP Science Team. The detailed, all-sky picture of the infant universe created from nine years of wmap data. <http://map.gsfc.nasa.gov/media/121238/index.html>.
- [9] Dorothea Samtleben, Suzanne Staggs, and Bruce Winstein. The cosmic microwave background for pedestrians: A review for particle and nuclear physicists. *arXiv:0803.0834*, March 2008. *Ann.Rev.Nucl.Part.Sci.*57:245-283,2007.
- [10] Wayne Hu. *Wandering in the Background: A Cosmic Microwave Background Explorer*. PhD thesis, University of California at Berkeley, 1995.
- [11] G. Hinshaw et al. Nine-year wilkinson microwave anisotropy probe (WMAP) observations: Cosmological parameter results. *arXiv:1212.5226*, December 2012.
- [12] Planck Collaboration. Planck 2013 results. i. overview of products and scientific results. *arXiv:1303.5062*, March 2013.
- [13] Robert H. Sanders and Stacy S. McGaugh. Modified newtonian dynamics as an alternative to dark matter. *Annu. Rev. Astron.*, 40(1):263–317, 2002.
- [14] P. Tisserand et al. Limits on the macho content of the galactic halo from the EROS-2 survey of the magellanic clouds. *Astronomy and Astrophysics*, 469(2):387–404, July 2007.
- [15] J. Rich, D. Lloyd Owen, and M. Spiro. Experimental particle physics without accelerators. *Physics Reports*, 151(5-6):239–364, July 1987.
- [16] D. H. Perkins. *Particle Astrophysics, Second Edition*. OUP Oxford, December 2008.
- [17] Gerard Jungman, Marc Kamionkowski, and Kim Griest. Supersymmetric dark matter. *Physics Reports*, 267(5-6):195–373, March 1996.

- [18] D. O. Caldwell et al. Laboratory limits on galactic cold dark matter. *Phys. Rev. Lett.*, 61(5):510–513, August 1988.
- [19] Hsin-Chia Cheng, Jonathan L. Feng, and Konstantin T. Matchev. Kaluza-klein dark matter. *Phys. Rev. Lett.*, 89(21):211301, October 2002.
- [20] A. L. Maroto. Nature of branon dark matter. *Phys. Rev. D*, 69(4):043509, February 2004.
- [21] Scott Dodelson. *Modern Cosmology*. Academic Press, March 2003.
- [22] Gary Steigman, Basudeb Dasgupta, and John F. Beacom. Precise relic WIMP abundance and its impact on searches for dark matter annihilation. *Phys. Rev. D*, 86(2):023506, July 2012.
- [23] J. Ipser and P. Sikivie. Can galactic halos be made of axions? *Phys. Rev. Lett.*, 50(12):925–927, March 1983.
- [24] R. D. Peccei and Helen R. Quinn. Constraints imposed by CP conservation in the presence of pseudoparticles. *Phys. Rev. D*, 16(6):1791–1797, September 1977.
- [25] J R Primack, D Seckel, and B Sadoulet. Detection of cosmic dark matter. *Annu. Rev. Nucl. Part. Sci.*, 38(1):751–807, 1988.
- [26] Hai-Yang Cheng. Tabulation of astrophysical constraints on axions and nambu-goldstone bosons. *Phys. Rev. D*, 36(6):1649–1656, September 1987.
- [27] H. Peng et al. Cryogenic cavity detector for a large-scale cold dark-matter axion search. *Nucl. Instrum. Meth. A*, 444(3):569–583, April 2000.
- [28] P.F. Smith and J.D. Lewin. Dark matter detection. *Physics Reports*, 187(5):203–280, March 1990.



- [29] Qing-Hong Cao, Ian Low, and Gabe Shaughnessy. From PAMELA to CDMS and back. *Phys. Lett. B*, 691(2):73–76, July 2010.
- [30] J. D. Lewin and P. F. Smith. Review of mathematics, numerical factors, and corrections for dark matter experiments based on elastic nuclear recoil. *Astropart. Phys.*, 6(1):87 – 112, 1996.
- [31] Jonathan L. Feng, Jason Kumar, Danny Marfatia, and David Sanford. Isospin-violating dark matter. *Phys. Lett. B*, 703(2):124–127, September 2011.
- [32] J. Engel, S. Pittel, and P. Vogel. Nuclear physics of dark matter detection. *International Journal of Modern Physics E*, 01(01):1–37, March 1992.
- [33] the ILIAS dark matter online tool. <http://pisrv0.pit.physik.uni-tuebingen.de/darkmatter/>.
- [34] K. Hans Wedepohl. The composition of the continental crust. *Geochimica et Cosmochimica Acta*, 59(7):1217 – 1232, 1995.
- [35] R. Bernabei et al. New limits on WIMP search with large-mass low-radioactivity NaI(Tl) set-up at gran sasso. *Phys. Lett. B*, 389(4):757–766, December 1996.
- [36] Katherine Freese, Mariangela Lisanti, and Christopher Savage. Annual modulation of dark matter: A review. *arXiv:1209.3339*, September 2012.
- [37] R. Bernabei et al. On a further search for a yearly modulation of the rate in particle dark matter direct search. *Phys. Lett. B*, 450(4):448–455, March 1999.
- [38] R. Bernabei et al. New results from DAMA/LIBRA. *arXiv:1002.1028*, February 2010. *Eur. Phys. J. C* (2010) 67: 39-49.
- [39] R. Bernabei et al. The DAMA/LIBRA apparatus. *arXiv:0804.2738*, April 2008. *Nucl.Instrum.Meth.A*592:297-315,2008.

- [40] G. Bellini et al. Cosmic-muon flux and annual modulation in borexino at 3800 m water-equivalent depth. *J. Cosmol. Astropart. Phys.*, 2012(05):015, May 2012.
- [41] R. Bernabei et al. First results from DAMA/LIBRA and the combined results with DAMA/NaI. *Eur. Phys. J. C*, 56(3):333–355, August 2008.
- [42] P S Barbeau, J I Collar, and O Tench. Large-mass ultralow noise germanium detectors: performance and applications in neutrino and astroparticle physics. *J. Cosmol. Astropart. Phys.*, 2007(09):009–009, September 2007.
- [43] CoGeNT Collaboration. Experimental constraints on a dark matter origin for the DAMA annual modulation effect. *Phys. Rev. Lett.*, 101(25):251301, December 2008.
- [44] C. E. Aalseth et al. Results from a search for light-mass dark matter with a p-type point contact germanium detector. *Phys. Rev. Lett.*, 106(13):131301, March 2011.
- [45] C. E. Aalseth et al. Search for an annual modulation in a p-type point contact germanium dark matter detector. *Phys. Rev. Lett.*, 107(14):141301, September 2011.
- [46] Chris Kelso, Dan Hooper, and Matthew R. Buckley. Toward a consistent picture for CRESST, CoGeNT, and DAMA. *Phys. Rev. D*, 85(4):043515, February 2012.
- [47] CDMS Collaboration. Exclusion limits on the WIMP-nucleon cross section from the first run of the cryogenic dark matter search in the soudan underground laboratory. *Phys. Rev. D*, 72(5):052009, September 2005.

- [48] CDMS Collaboration. Search for weakly interacting massive particles with the first five-tower data from the cryogenic dark matter search at the soudan underground laboratory. *Phys. Rev. Lett.*, 102(1):011301, January 2009.
- [49] The CDMS II Collaboration. Dark matter search results from the CDMS II experiment. *Science*, 327(5973):1619–1621, March 2010.
- [50] CDMS Collaboration. Results from a low-energy analysis of the CDMS II germanium data. *Phys. Rev. Lett.*, 106(13):131302, March 2011.
- [51] CDMS Collaboration. Search for annual modulation in low-energy CDMS-II data. *arXiv:1203.1309*, March 2012.
- [52] CDMS Collaboration. Dark matter search results using the silicon detectors of CDMS II. *arXiv:1304.4279*, April 2013.
- [53] E. Aprile et al. The XENON100 dark matter experiment. *Astropart. Phys.*, 35(9):573–590, April 2012.
- [54] XENON100 Collaboration. Dark matter results from 225 live days of XENON100 data. *arXiv:1207.5988*, July 2012.
- [55] XENON10 Collaboration. Search for light dark matter in XENON10 data. *Phys. Rev. Lett.*, 107(5):051301, July 2011.
- [56] G. Angloher et al. Results from 730 kg days of the CRESST-II dark matter search. *arXiv:1109.0702*, September 2011.
- [57] D.Yu. Akimov et al. WIMP-nucleon cross-section results from the second science run of ZEPLIN-III. *Phys. Lett. B*, 709:14–20, March 2012.
- [58] EDELWEISS Collaboration. Search for low-mass WIMPs with EDELWEISS-II heat-and-ionization detectors. *Phys. Rev. D*, 86(5):051701, September 2012.

- [59] R. Brunetti et al. WARP liquid argon detector for dark matter survey. *New Astronomy Reviews*, 49:265–269, May 2005.
- [60] XENON100 collaboration. Limits on spin-dependent WIMP-nucleon cross sections from 225 live days of XENON100 data. *arXiv:1301.6620*, January 2013.
- [61] Berta Beltran and the Picasso Collaboration. Dark matter spin-dependent limits for WIMP interactions on  $^{19}\text{F}$  by PICASSO. *JPCS*, 203(1):012032, January 2010.
- [62] COUPP Collaboration. First dark matter search results from a 4-kg  $\text{CF}_3\text{I}$  bubble chamber operated in a deep underground site. *Phys. Rev. D*, 86(5):052001, September 2012.
- [63] David Tucker-Smith and Neal Weiner. Status of inelastic dark matter. *Phys. Rev. D*, 72(6):063509, September 2005.
- [64] R. Bernabei et al. Possible implications of the channeling effect in  $\text{NaI(Tl)}$  crystals. *Eur. Phys. J. C*, 53(2):205–213, November 2007.
- [65] the AMS Collaboration. First result from the alpha magnetic spectrometer experiment. <http://www.ams02.org/2013/04/first-results-from-the-alpha-magnetic-spectrometer-ams-experiment/>.
- [66] J. Chang et al. An excess of cosmic ray electrons at energies of 300-800GeV. *Nature*, 456(7220):362–365, November 2008.
- [67] Fermi LAT Collaboration. Measurement of the cosmic ray  $e^+e^-$  spectrum from 20 GeV to 1 TeV with the fermi large area telescope. *Phys. Rev. Lett.*, 102(18):181101, May 2009.
- [68] O. Adriani et al. An anomalous positron abundance in cosmic rays with energies 1.5-100GeV. *Nature*, 458(7238):607–609, April 2009.

- [69] AMS Collaboration. First result from the alpha magnetic spectrometer on the international space station: Precision measurement of the positron fraction in primary cosmic rays of 0.5-350 GeV. *Phys. Rev. Lett.*, 110(14):141102, April 2013.
- [70] H.E.S.S. Collaboration. Energy spectrum of cosmic-ray electrons at TeV energies. *Phys. Rev. Lett.*, 101(26):261104, December 2008.
- [71] V. Barger, Y. Gao, W.-Y. Keung, D. Marfatia, and G. Shaughnessy. Dark matter and pulsar signals for fermi LAT, PAMELA, ATIC, HESS and WMAP data. *Phys. Lett. B*, 678(3):283–292, July 2009.
- [72] Yi-Zhong Fan, Bing Zhang, and Jin Chang. Electron/positron excesses in the cosmic ray spectrum and possible interpretations. *International Journal of Modern Physics D*, 19(13):2011–2058, November 2010.
- [73] Christoph Weniger. A tentative gamma-ray line from dark matter annihilation at the fermi large area telescope. *J. Cosmol. Astropart. Phys.*, 2012(08):007–007, August 2012.
- [74] Gianfranco Bertone, Marco Cirelli, Alessandro Strumia, and Marco Taoso. Gamma-ray and radio tests of the  $e^+/-$  excess from DM annihilations. *J. Cosmol. Astropart. Phys.*, 2009(03):009–009, March 2009.
- [75] IceCube Collaboration. Multiyear search for dark matter annihilations in the sun with the AMANDA-II and IceCube detectors. *Phys. Rev. D*, 85(4):042002, February 2012.
- [76] S. Desai et al. Study of TeV neutrinos with upward showering muons in superkamiokande. *Astropart. Phys.*, 29(1):42–54, February 2008.

- [77] A Heister et al. Absolute mass lower limit for the lightest neutralino of the MSSM from  $e^+e^-$  data at  $s$  up to 209 GeV. *Phys. Lett. B*, 583(3-4):247–263, March 2004.
- [78] CDF Collaboration. Search for supersymmetry in  $pp^-$  collisions at  $\sqrt{s}=1.96\text{TeV}$  using the trilepton signature for chargino-neutralino production. *Phys. Rev. Lett.*, 101(25):251801, December 2008.
- [79] D0 Collaboration. Search for associated production of charginos and neutralinos in the trilepton final state using 2.3 fb $^{-1}$  of data. *Phys. Lett. B*, 680(1):34–43, September 2009.
- [80] CMS Collaboration. Search for supersymmetry at the LHC in events with jets and missing transverse energy. *Phys. Rev. Lett.*, 107(22):221804, November 2011.
- [81] ATLAS Collaboration. Searches for supersymmetry with the ATLAS detector using final states with two leptons and missing transverse momentum in proton-proton collisions. *Phys. Lett. B*, 709(3):137–157, March 2012.
- [82] Tadayoshi Doke, Akira Hitachi, et al. Absolute scintillation yields in liquid argon and xenon for various particles. *Japanese Journal of Applied Physics*, 41(Part 1, No. 3A):1538–1545, 2002.
- [83] Marlo Martin. Exciton self-trapping in rare-gas crystals. *J. Chem. Phys*, 54(8):3289–3299, April 1971.
- [84] E. Morikawa et al. Argon, krypton, and xenon excimer luminescence: From the dilute gas to the condensed phase. *J. Chem. Phys*, 91(3):1469–1477, August 1989.

- [85] R.T. Williams and K.S. Song. The self-trapped exciton. *Journal of Physics and Chemistry of Solids*, 51(7):679–716, 1990.
- [86] Akira Hitachi et al. Effect of ionization density on the time dependence of luminescence from liquid argon and xenon. *Phys. Rev. B*, 27(9):5279–5285, May 1983.
- [87] P. Moutard, P. Laporte, J.-L. Subtil, N. Damany, and H. Damany. Pressure effects on kinetics and decay processes in argon under selective photoexcitation. *J. Chem. Phys.*, 87(8):4576–4588, October 1987.
- [88] W. Krotz, A. Ulrich, B. Busch, G. Ribitzki, and J. Wieser. Third excimer continuum of argon excited by a heavy-ion beam. *Phys. Rev. A*, 43(11):6089–6094, June 1991.
- [89] Satoshi Suzuki and Akira Hitachi. Applications of rare gas liquids to radiation detectors. In *Charged Particle and Photon Interactions with Matter*, pages 879–922. CRC Press, December 2010.
- [90] A. Hitachi, T. Doke, and A. Mozumder. Luminescence quenching in liquid argon under charged-particle impact: Relative scintillation yield at different linear energy transfers. *Phys. Rev. B*, 46(18):11463–11470, November 1992.
- [91] John L. Magee and Jan-Tsyu J. Huang. Triplet formation in ion recombination in spurs. *The Journal of Physical Chemistry*, 76(25):3801–3805, December 1972.
- [92] M.G. Boulay and A. Hime. Technique for direct detection of weakly interacting massive particles using scintillation time discrimination in liquid argon. *Astropart. Phys.*, 25(3):179 – 182, 2006.
- [93] D.C. Lorents. The physics of electron beam excited rare gases at high densities. *Physica B+C*, 82(1):19–26, March 1976.

- [94] Tetsuhiko Takahashi, Susumu Himi, Masayo Suzuki, Jian-zhi Ruan(Gen), and Shinzou Kubota. Emission spectra from Ar-Xe, Ar-Kr, Ar-N<sub>2</sub>, Ar-CH<sub>4</sub>, Ar-CO<sub>2</sub> and Xe-N<sub>2</sub> gas scintillation proportional counters. *Nucl. Instr. Meth. Phys. Res.*, 205(3):591–596, February 1983.
- [95] R. Acciarri et al. Oxygen contamination in liquid argon: combined effects on ionization electron charge and scintillation light. *J. Instrum.*, 5(05):P05003, May 2010.
- [96] C Amsler, V Boccone, et al. Luminescence quenching of the triplet excimer state by air traces in gaseous argon. *J. Instrum.*, 3(02):P02001–P02001, February 2008.
- [97] R. Acciarri et al. Effects of nitrogen and oxygen contamination in liquid argon. *Nuclear Physics B - Proceedings Supplements*, 197(1):70–73, December 2009.
- [98] C Rubbia et al. Underground operation of the ICARUS t600 LAr-TPC: first results. *J. Instrum.*, 6(07):P07011–P07011, July 2011.
- [99] P. Benetti et al. First results from a dark matter search with liquid argon at 87k in the gran sasso underground laboratory. *Astropart. Phys.*, 28(6):495 – 507, 2008.
- [100] D. Akimov et al. Light Yield in DarkSide-10: a Prototype Two-phase Liquid Argon TPC for Dark Matter Searches. *arXiv:1204.6218*, 2012.
- [101] V Boccone and the ArDM collaboration. The ArDM project: A liquid argon TPC for dark matter detection. *JPCS*, 160:012032, April 2009.
- [102] M. G. Boulay et al. Measurement of the scintillation time spectra and pulse-shape discrimination of low-energy beta and nuclear recoils in liquid argon with DEAP-1. *arXiv:0904.2930*, April 2009.



- [103] Andrew Hime. The MiniCLEAN dark matter experiment. *arXiv:1110.1005*, October 2011.
- [104] the LBNE Experiment. <http://lbne.fnal.gov/>.
- [105] the LArTPC Experiment. <http://www-lartpc.fnal.gov/summary.htm>.
- [106] the GLACIER Experiment. <http://neutrino.ethz.ch/GLACIER/Welcome.html>.
- [107] Roxanne Guenette. The ArgoNeuT experiment. *arXiv:1110.0443*, October 2011.
- [108] C. M. Ignarra. MicroBooNE. *arXiv:1110.1604*, October 2011.
- [109] P. Benetti et al. Measurement of the specific activity of  $^{39}\text{Ar}$  in natural argon. *Nucl. Instrum. Meth. A*, 574(1):83 – 88, 2007.
- [110] H.H. Loosli. A dating method with  $^{39}\text{Ar}$ . *Earth Planet. Sci. Lett.*, 63(1):51 – 62, 1983.
- [111] W. H. Lippincott et al. Scintillation time dependence and pulse shape discrimination in liquid argon. *Phys. Rev. C*, 78:035801, Sep 2008.
- [112] The XENON100 Collaboration. Dark matter results from 100 live days of XENON100 data. *Phys. Rev. Lett.*, 107(13):131302, September 2011.
- [113] W. Walkowiak. Drift velocity of free electrons in liquid argon. *Nucl. Instrum. Meth. A*, 449(1-2):288–294, July 2000.
- [114] Dongming Mei et al. Argon depletion for a large scale dark matter detector, 2011. <http://meetings.aps.org/link/BAPS.2011.DNP.JG.1>.

- [115] Chris J. Ballentine and Greg Holland. What co<sub>2</sub> well gases tell us about the origin of noble gases in the mantle and their relationship to the atmosphere. *Philos. T. Roy. Soc. A.: Math., Phys. and Eng. Sci.*, 366, 2008.
- [116] B. E. Lehmann, S. N. Davis, and June T. Fabryka-Martin. Atmospheric and subsurface sources of stable and radioactive nuclides used for groundwater dating. *Water Resour. Res.*, 29(7):2027 – 2040, 1993.
- [117] D.-M. Mei et al. Prediction of underground argon content for dark matter experiments. *Phys. Rev. C*, 81:055802, May 2010.
- [118] H.H.Loosli, B.E. Lehmann, and W. Balderer. Argon-39, argon-37 and krypton-85 isotopes in stripa groundwaters. *Geochim. Cosmochim. Ac.*, 53:1825–1829, 1989.
- [119] G Heusser. Low-radioactivity background techniques. *Annu. Rev. Nucl. Part. Sci.*, 45(1):543–590, 1995.
- [120] D.-M. Mei, C. Zhang, and A. Hime. Evaluation of (alpha,n) Induced Neutrons as a Background for Dark Matter Experiments. *Nucl. Instrum. Meth.*, A606:651–660, 2009.
- [121] D. Acosta-Kane et al. Discovery of underground argon with low level of radioactive <sup>39</sup>Ar and possible applications to wimp dark matter detectors. *Nucl. Instrum. Meth. A*, 587(1):46 – 51, 2008.
- [122] H Loosli, Martin Heimann, and Hans Oeschger. Low-level gas proportional counting in an underground laboratory. *Radiocarbon*, 22(2), 1980.
- [123] Tanya Lyubetskaya and Jun Korenaga. Chemical composition of earths primitive mantle and its variance. *J. Geophys. Res-Planet*, 112, 2007.

- [124] T Staudacher. Upper mantle origin for harding county well gases. *Nature*, 325:605 – 607, 1987.
- [125] M. W. Caffee et al. Primordial noble gases from earth’s mantle: Identification of a primitive volatile component. *Science*, 285(5436):2115–2118, 1999.
- [126] Greg Holland and Chris J. Ballentine. Seawater subduction controls the heavy noble gas composition of the mantle. *Nature*, pages 186 – 191, 2006.
- [127] Henning O. Back et al. First Large Scale Production of Low Radioactivity Argon From Underground Sources. *arXiv:1204.6024*, 2012.
- [128] John C. Kayser and Kent S. Knaebel. Pressure swing adsorption: Experimental study of an equilibrium theory. *Chemical Engineering Science*, 41(11):2931 – 2938, 1986.
- [129] H. O. Back et al. First Commissioning of a Cryogenic Distillation Column for Low Radioactivity Underground Argon. *arXiv:1204.6061*, 2012.
- [130] P. Collon et al. Development of an AMS method to study oceanic circulation characteristics using cosmogenic  $^{39}\text{Ar}$ . *Nucl. Instrum. Meth. B*, 223-224:428–434, 2004.
- [131] W. Jiang et al.  $^{39}\text{Ar}$  detection at the  $10^{-16}$  isotopic abundance level with atom trap trace analysis. *Phys. Rev. Lett.*, 106, 2011.
- [132] the DarkSide Collaboration. <http://darkside-docdb.fnal.gov/cgi-bin/ShowDocument?docid=360>.
- [133] Alex Wright, Pablo Mosteiro, Ben Loer, and Frank Calaprice. A highly efficient neutron veto for dark matter experiments. *Nucl. Instrum. Meth. A*, 644(1):18 – 26, 2011.

- [134] G. Alimonti et al. The borexino detector at the laboratori nazionali del gran sasso. *Nucl. Instrum. Meth. A*, 600(3):568 – 593, 2009.
- [135] S.C. Wang et al. A feasibility study of boron-loaded liquid scintillator for the detection of electron anti-neutrinos. *Nucl. Instrum. Meth. A*, 432(1):111 – 121, 1999.
- [136] L. R. Greenwood and N. R. Chellew. Improved 10b-loaded liquid scintillator with pulse-shape discrimination. *Review of Scientific Instruments*, 50(4):466–471, 1979.
- [137] Isadore B Berlmán. *Handbook of fluorescence spectra of aromatic molecules*. Academic Press, New York, 1971.
- [138] H Gusten. PMP, a novel solute for liquid and plastic scintillation counting. In *Proceedings of the International Conference on Advances in Scintillation Counting*, pages 330–339, 1983.
- [139] Hans Gsten and Jeffrey Mirsky. PMP, a novel scintillation solute with a large stokes’ shift. In *Proceedings of the International Conference on New Trends in Liquid Scintillation Counting and Organic Scintillators*, pages 1–8, 1989.
- [140] the optical data from PhotochemCAD. <http://omlc.ogi.edu/spectra/PhotochemCAD/index.html>.
- [141] optical grade spectralon from Labsphere. <http://www.labsphere.com/uploads/datasheets/optical-grade-spectralon-product-sheet.pdf>.
- [142] the 3M Reflective Film. [http://solutions.3m.com/wps/portal/3M/en\\_US/Building-Trades/Construction/Product-Info/Product-Catalog/?PC\\_7\\_RJH9U52308ESC02DFLU60I0K05000000\\_nid=7358GD8CMRbeCNK67JJ2T1g1](http://solutions.3m.com/wps/portal/3M/en_US/Building-Trades/Construction/Product-Info/Product-Catalog/?PC_7_RJH9U52308ESC02DFLU60I0K05000000_nid=7358GD8CMRbeCNK67JJ2T1g1).

- [143] D.S. Leonard et al. Systematic study of trace radioactive impurities in candidate construction materials for EXO-200. *Nucl. Instrum. Meth. A*, 591(3):490–509, July 2008.
- [144] the ILIAS database on radiopurity of materials. <http://radiopurity.in2p3.fr/>.
- [145] M. Janecek. Reflectivity spectra for commonly used reflectors. *IEEE Trans. Nucl. Sci.*, 59(3):490–497, June 2012.
- [146] The ArDM Collaboration. Development of wavelength shifter coated reflectors for the ArDM argon dark matter detector. *J. Instrum.*, 4(06):P06001–P06001, June 2009.
- [147] C.H. Lally, G.J. Davies, W.G. Jones, and N.J.T. Smith. UV quantum efficiencies of organic fluors. *Nucl. Instr. Meth. Phys. Res. B*, 117(4):421–427, October 1996.
- [148] the Hamamatsu R6233-100 PMT. <http://www.hamamatsu.com/us/en/R6233-100.html>.
- [149] Master Bond Polymer System EP29LPSP. <http://www.masterbond.com/tds/ep29lpsp>.
- [150] Photomultiplier Tubes, Basics and Applications. [http://www.sales.hamamatsu.com/assets/pdf/catsandguides/PMT\\_handbook\\_v3aE.pdf](http://www.sales.hamamatsu.com/assets/pdf/catsandguides/PMT_handbook_v3aE.pdf).
- [151] NIST X-Ray Mass Attenuation Coefficients. <http://www.nist.gov/pml/data/xraycoef/index.cfm>.
- [152] Andreas Piepke. 210pb content measurement at the university of alabama. private communication, 2010.

- [153] M. Laubenstein and G. Heusser. Cosmogenic radionuclides in metals as indicator for sea level exposure history. *Appl. Radiat. Isot.*, 67:750 – 754, 2009.
- [154] J. F. Ziegler. Terrestrial cosmic ray intensities. *IBM Journal of Research and Development*, 42(1):117 –140, January 1998.
- [155] Donald E. Groom, Nikolai V. Mokhov, and Sergei I. Striganov. Muon stopping power and range tables 10 mev - 100 tev. *Atomic Data and Nuclear Data Tables*, 78(2):183–356, July 2001.
- [156] F. Pointurier, J. Laurec, X. Blanchard, and A. Adam. Cosmic-ray induced background reduction by means of an anti-coincidence shield. *Applied Radiation and Isotopes*, 47(9-10):1043–1048, September 1996.
- [157] Joseph A. Formaggio and C.J. Martoff. Backgrounds to sensitive experiments underground. *Annu. Rev. Nucl. Part. Sci.*, 54(1):361–412, 2004.
- [158] the Kimballton Underground Research Facility. <http://www.phys.vt.edu/~kimballton/kurf/pub/w.shtml?home/locations.jpg>.
- [159] P. Finnerty et al. Low-background gamma counting at the kimballton underground research facility. *Nucl. Instrum. Meth. A*, 642(1):65–69, June 2011.
- [160] the SAES gas purifier. <http://www.puregasproducts.com/ps4.htm>.
- [161] the Borexino Collaboration. The borexino detector at the laboratori nazionali del gran sasso. *Nucl. Instrum. Meth. A*, 600(3):568–593, March 2009.
- [162] Dave Holtz. A Low Background Detector for Measurements of  $^{39}\text{Ar}$  in Underground Argon for Dark Matter Detectors. Junior Paper, Princeton University, 2009.
- [163] Roger Barlow and Christine Beeston. Fitting using finite monte carlo samples. *Computer Physics Communications*, 77(2):219–228, October 1993.

- [164] M. Kase, T. Akioka, H. Mamyoda, J. Kikuchi, and T. Doke. Fano factor in pure argon. *Nucl. Instrum. Meth. A*, 227(2):311–317, November 1984.
- [165] the Geant4 Toolkit. <http://geant4.cern.ch/>.
- [166] Geant4 Collaboration. Geant4 a simulation toolkit. *Nucl. Instrum. Meth. A*, 506(3):250–303, July 2003.
- [167] W. H. Lippincott et al. Scintillation time dependence and pulse shape discrimination in liquid argon. *Phys. Rev. C*, 78(3):035801, September 2008.
- [168] D.-M. Mei, Z.-B. Yin, L.C. Stonehill, and A. Hime. A model of nuclear recoil scintillation efficiency in noble liquids. *Astropart. Phys.*, 30(1):12 – 17, 2008.
- [169] Dan Gastler et al. Measurement of scintillation efficiency for nuclear recoils in liquid argon. *Phys. Rev. C*, 85(6):065811, June 2012.
- [170] P Goldhagen et al. Measurement of the energy spectrum of cosmic-ray induced neutrons aboard an ER-2 high-altitude airplane. *Nucl. Instrum. Meth. A*, 476(1-2):42–51, January 2002. PMID: 12033224.
- [171] D.-M. Mei and A. Hime. Muon-induced background study for underground laboratories. *Phys. Rev. D*, 73(5):053004, March 2006.
- [172] C. Arpesella. A low background counting facility at laboratori nazionali del gran sacco. *Appl. Radiat. Isot.*, 47:991 – 996, 1996.
- [173] J. F. Ziegler. Terrestrial cosmic rays. *IBM J. Res. Dev.*, 40:19–39, 1996.
- [174] C.J. Martoff and P.D. Lewin. Cosmo - a program to estimate spallation radioactivity produced in a pure substance by exposure to cosmic radiation on the earth. *Comp. Phys. Comm.*, 72:96 – 103, 1992.

- [175] Jingke Xu. New measurement of  $^{39}\text{Ar}$  in underground argon with a low background liquid argon detector. In *APS April Meeting*, Atlanta, GA, April 2012.
- [176] Jingke Xu. Measurement of  $^{39}\text{Ar}$  in underground argon for dark matter experiments. In *The First KURF User Meeting*, Blacksburg, VA, June 2013.
- [177] J. Xu, F. Calaprice, C. Galbiati, A. Goretti, G. Guray, T. Hohman, D. Holtz, A. Ianni, M. Laubenstein, B. Loer, C. Love, C. J. Martoff, D. Montanari, S. Mukhopadhyay, A. Nelson, S. D. Rountree, R. B. Vogelaar, and A. Wright. A Study of the Residual  $^{39}\text{Ar}$  Content in Argon from Underground Sources. *arXiv:1204.6011*, 2012.
- [178] D. V. Hinkley. On the ratio of two correlated normal random variables. *Biometrika*, 56(3):635–639, December 1969.
- [179] Luca Grandi and Richard Saldanha. Discrimination measured in DS-10 and its impact on DS-50 projected sensitivity. Internal DarkSide Document 468-v3, 2012.
- [180] Alexandre Arbey et al. An update of the constraints on the phenomenological MSSM from the new LHC higgs results. *Phys. Lett. B*, 720(1-3):153–160, March 2013.
- [181] O. Buchmueller et al. Implications of initial LHC searches for supersymmetry. *Eur. Phys. J. C*, 71(5):1–13, May 2011.
- [182] C. Stenge et al. Updated global fits of the cMSSM including the latest LHC SUSY and higgs searches and XENON100 data. *J. Cosmol. Astropart. Phys.*, 2012(03):030, March 2012.
- [183] Gary J. Feldman and Robert D. Cousins. Unified approach to the classical statistical analysis of small signals. *Phys. Rev. D*, 57(7):3873–3889, April 1998.



- [184] MicrOMEGAs: a code for the calculation of Dark Matter Properties. <http://lapth.cnrs.fr/micromegas/>.
- [185] Kate Scholberg. Prospects for measuring coherent neutrino-nucleus elastic scattering at a stopped-pion neutrino source. *Phys. Rev. D*, 73(3):033005, February 2006.
- [186] C. Hagmann and A. Bernstein. Two-phase emission detector for measuring coherent neutrino-nucleus scattering. *IEEE Trans. Nucl. Sci.*, 51(5):2151–2155, 2004.
- [187] S. Sangiorgio et al. A prototype detector for observation of coherent neutrino-nucleus scattering at a nuclear reactor. Poster at Neutrino 2012 Conference, ID 195 - 3, 2012. [http://lartpc-docdb.fnal.gov/0008/000806/001/sangiorgio\\_neutrino2012\\_poster\\_v3.pdf](http://lartpc-docdb.fnal.gov/0008/000806/001/sangiorgio_neutrino2012_poster_v3.pdf).
- [188] Jocelyn Monroe and Peter Fisher. Neutrino backgrounds to dark matter searches. *Phys. Rev. D*, 76(3):033007, August 2007.
- [189] Louis E. Strigari. Neutrino coherent scattering rates at direct dark matter detectors. *New Journal of Physics*, 11(10):105011, October 2009.
- [190] A. J. Anderson, J. M. Conrad, E. Figueroa-Feliciano, K. Scholberg, and J. Spitz. Coherent neutrino scattering in dark matter detectors. *Phys. Rev. D*, 84(1):013008, July 2011.
- [191] Philippe Sarda, Thomas Staudacher, and Claude J. Allgre. 40ar36ar in morb glasses: constraints on atmosphere and mantle evolution. *Earth Planet. Sci. Lett.*, 72(4):357 – 375, 1985.
- [192] Bernard Marty and Franck Humbert. Nitrogen and argon isotopes in oceanic basalts. *Earth Planet. Sci. Lett.*, 152:101 – 112, 1997.

- [193] R.K. O’Nions and E.R. Oxburgh. Helium, volatile fluxes and the development of continental crust. *Earth Planet. Sci. Lett.*, 90(3):331 – 347, 1988.
- [194] Thomas Gold and Freeman J. Dyson. *The Deep Hot Biosphere: The Myth of Fossil Fuels*. Springer, May 2001.
- [195] V.D. Ashitkov et al. New experimental limit on the  $^{42}\text{Ar}$  content in the earth’s atmosphere. *Nucl. Instrum. Meth. A*, 416(1):179–181, October 1998.
- [196] E. O. Knutson, C. V. Gogolak, P. Scofield, and G. Klemic. Measurements of radon progeny activity on typical indoor surfaces. *Radiation Protection Dosimetry*, 45(1-4):313–317, December 1992.
- [197] J. Benziger et al. The nylon scintillator containment vessels for the borexino solar neutrino experiment. *Nucl. Instrum. Meth. A*, 582(2):509–534, November 2007.
- [198] Kevin McCarty. *The Borexino Nylon Film and the Third Counting Test Facility*. PhD thesis, Princeton University, 2006.
- [199] Tina Pollmann, Mark Boulay, and Marcin Kuniak. Scintillation of thin tetraphenyl butadiene films under alpha particle excitation. *Nucl. Instrum. Meth. A*, 635(1):127–130, April 2011.
- [200] S.K. Dua and P. Kotrappa. Comment on the charge on decay products of thoron and radon. *American Industrial Hygiene Association Journal*, 42(3):242–243, 1981.